Università degli Studi di Ferrara

DOTTORATO DI RICERCA IN FISICA

CICLO XXIX

COORDINATORE Prof. Vincenzo Guidi

New challenges in the spectral reconstruction of terrestrial gamma rays and reactor antineutrinos

Settore Scientifico Disciplinare FIS/07

Dottoranda
Dott.ssa Marica Baldoncini

Tutore
Prof. Fabio Mantovani

Anni 2014/2016

Contents

Overview

Life on Earth always coexisted and evolved in the presence of radioactivity, which acts as a driver for organism's adaptation and natural selection. We live under a radioactive sky, continuously exposed to cosmic radiation which brings messages from the faraway Universe, and we live on a radioactive Earth, which tirelessly shines mainly in alpha and beta particles, gamma rays and neutrinos. Starting from the last century, the scientific progress has driven humanity to discover, handle, manage and produce radioactivity. Human activities cause the release to the environment of radioactive materials which can derive from atmospheric nuclear weapon tests and peaceful applications of nuclear technology as well as from the enrichment in naturally occurring radionuclides associated to industrial processes.

Radioactivity on Earth reveals itself on multiple levels involving the type of emitted particles, the energy range, the length and time scales and each manifestation represents a distinctive probe, opening a window into different fields of knowledge. The multiform nature of radioactivity materializations populates the color palette of a kaleidoscope of spectral structures which can be deciphered as a superposition of fundamental shapes. As in gamma-ray spectroscopy the $\sim$ 1 MeV energy range is the theater where the ensemble of ^{40}K, ^{238}U and ^{232}Th rehearse, in electron antineutrino measurements the same energy range is inhabited by reactor antineutrinos and geoneutrinos. In this scenario, in order to get insights into the Earth's surface and interior, it is necessary to provide for gamma-ray and geoneutrino measurements an adequate understanding of the different spectral components as well as reliable procedures for reconstructing observed spectra.

An inclusive interpretation of manifold spectral structures is a key point in order to address the scientific and technological challenges posed by frontier experiments. Liquid scintillation technology is currently moving from the $\sim$kton scale of the KamLAND (Japan), Borexino (Italy) and SNO+ (Canada) experiments, operating in the long baseline regime ($\sim$200 km reactor-detector distance) to the $\sim$20 kton scale of the JUNO (China) and RENO50 (South Korea) detectors, characterized by a $\sim$50 km reactor-detector distance. Exploring a new baseline length scale implies digging into a new phase space of neutrino oscillation parameters and therefore facing the reconstruction of new reactor antineutrino spectral structures. At the same time, the broad scientific agenda of these multipurpose experiments pushes towards the management of spectral reconstruction techniques applicable to physics events coming from different particle interaction mechanisms and belonging to different energy ranges. A comprehensive approach towards the treatment of spectral shape features can play an important role also in the light of multisensorial detectors, as in the case of frontier mobile instruments

in which the integration of gamma-ray and neutron measurements is explored for nuclear proliferation monitoring applications.

Integrating information coming from distinctive probes can provide us pictures of the subject under investigation with multiple camera focal lenses. Gamma-rays yield their largest image of the Earth via the airborne spectroscopy method which, although having a lateral field of view of hundreds meters, allows us only to scratch the Earth's surface since gamma-rays typically come from the first tens centimeters of the top soil. Even if we can penetrate the geophysical structure of our planet down to the core by means of seismology, gathering access to the chemical composition of the deep Earth is much harder. The first victory in this scientific challenge has been conquered by the KamLAND experiment in 2005 via the detection of geoneutrinos, extraordinarily elusive particles able to traverse the Earth traveling thousands of kilometers almost without interacting. If from one side gamma-ray and geoneutrino spectroscopy are characterized by completely different detection mechanisms and spatial resolution scales, the emblematic example of the ^{214}Bi beta decay tells us that with the 609 keV gamma emission and with the emission of an electron antineutrino having 2.66 MeV maximum energy we have in our hands two distinct pair of glasses we can use to observe the radiating Earth.

Gamma-ray spectroscopy is an extremely powerful method for environmental monitoring thanks to photon's high penetration range and characteristic energy, which provides an unambiguous identification of the decayed isotope. Gamma-ray surveys can be performed from aircraft, unmanned aerial vehicles, field vehicles, on foot, in boreholes and in laboratories which implies that a variety of spatial scales is also accessible. In the last decades monitoring environmental radioactivity has become a urgent request of strategic importance concerning both the assessment of human exposure to ionizing radiation and the applications in the field of geosciences. Radiometric information over large areas can be attained via airborne gamma-ray spectrometry, which has been proved to be an excellent tool for mineral prospecting and geochemical mapping but also for emergency preparedness and homeland security, as in the case of nuclear fallout or location of lost radioactive sources.

The MeV energy scale involved in natural radionuclides decays well matches the performances of semiconductor and scintillation detector designed for gamma-ray spectroscopy measurements. On the other hand, just two beta transitions in the ^{238}U decay chain and two in the ^{232}Th decay chain give rise to measurable geoneutrinos, as the Inverse Beta Decay (IBD) reaction currently exploited in their detection has a 1.806 MeV energy threshold. Up to an antineutrino energy of $\sim$10 MeV it is also possible to observe in the spectral shape of IBD events a component due to antineutrinos produced by nuclear reactors, which are the strongest man made antineutrino sources. Nowadays there are about 440 commercial reactor cores which provide electricity to the developed countries and at the same time generate some 10^{20} $\bar{\nu}_e$/s.

This thesis illustrates the challenges and the objectives faced in the spectral reconstruction of gamma-rays coming from the Earth and antineutrinos produced by nuclear reactors, which constitute a severe source of background in geoneutrino studies.

During my PhD I went through several key aspects one encounters in the transition from measured gamma and electron antineutrino spectra to quantitative estimates of radioactive contents, which

break down into spectral reconstruction processes, detector calibration approaches and background modeling. The multidisciplinary nature of these studies stimulated me to propose operative solutions relying on highly versatile methods which involve χ^2 minimization analysis, Monte Carlo simulation and reconstruction of spectral shapes on the basis of individual templates.

The research activities I carried out during these years allowed me to be a member of a wide and heterogeneous network in which the theme of environmental radioactivity is seen under a large spectrum of lights, comprising both theoretical and experimental aspects. I participated to international conferences in the presence of highly diversified scientific communities and I spent formation periods abroad at the University of Maryland and at the Barcelona Supercomputing Center. These experiences were a driver for improving my hard skills as well as my communication skills and they stimulated me to tune languages and methods according to the surrounding context. I had the chance to give a talk at the JaPan Geoscience Union meeting (Japan), the Neutrino Geoscience Conference (Paris), the Topics in Astroparticle and Underground Physics conference (Turin), the Applied Antineutrino Physics conference (Virginia Tech) and the Workshop on Aero Gamma Spectrometry (Bad Schlema). In these occasions I had the opportunity of exposing the results of my studies to the international community but also of coming in contact with the new frontiers of the scientific and technological research in the field of geoscience and electron antineutrino detection. Indeed, electron antineutrino detection technology is becoming sufficiently mature to be employed in homeland security purposes, such as nuclear proliferation monitoring. This is a common ground between antineutrino and gamma-ray measurements: indeed, collaborations aimed at establishing an international network dedicated to the radiological emergency preparation are growing also in the field of airborne gamma-ray surveys, trying to build shared playgrounds concerning measurement techniques, data formats, integration of the results provided by multiple teams.

The contents of this thesis are included in 8 publications, both peer-reviewed papers and conference proceedings, among which 5 already published and 3 to be submitted to scientific journals. The writing of these publications involved the contribution of about 30 coauthors of 5 different countries belonging to different disciplines (Geology, Physics, Engineering, Chemistry) and to different international institutions. In the framework of these collaborations I was called to face not only scientific, but also cultural and language challenges. Each one of the following chapters deals with a specific case study and is introduced emphasizing my personal contributions.

Chapter 1 presents a worldwide reference model for the prediction of reactor antineutrino signals and spectra, which is fundamental for inferring the geoneutrino component from the measured inverse beta reaction events. I calculated the expected reactor signal at different locations corresponding respectively to current (KamLAND and Borexino), entering operation (SNO+ and JUNO) and proposed (RENO50, LENA and Hanohano) antineutrino liquid scintillation experiments. I addressed the problem of the uncertainty propagation by means of a Monte Carlo based approach and I highlighted the site dependent and time dependent nature of the uncertainty budget and hierarchy. I performed a multitemporal analysis of the expected reactor signal over a time lapse of ten years using reactor operational records collected in a comprehensive database published at `www.fe.infn.it/antineutrino`. As

the operational conditions of nuclear reactors continuously evolve, this model is of crucial importance for geoneutrino studies, especially for long baseline experiments, characterized by a reactor-detector distance of $\sim$ 200 km.

After 14 years and 10 years of data taking of the KamLAND and Borexino detectors, respectively, in July 2017 the class of long baseline liquid scintillation detectors will have a new active member, SNO+. Predicting the expected geoneutrino and reactor signals and spectra at SNO+ is the aim of the work presented in Chapter 2, with the purpose of highlighting crucial points that need further investigation for future refinements. I performed the reactor signal and spectra calculation and estimated their variability caused by the temporal evolution of the reactor fissile inventory: this point is indeed strictly related to the poor knowledge about the functioning of CANDU reactors, responsible for $\sim$55% of the total reactor signal at SNO+. The Huronian Supergroup geological reservoir has been identified as a major source of uncertainty in the prediction of the local contribution to the SNO+ geoneutrinos signal due to the 60% uncertainty on its expected signal. In the light of a better constraining of the geochemical model of this reservoir, I took care of the laboratory gamma-ray spectroscopy measurements on collected rock samples and I defined the statistical distributions describing the U and Th content. In order to address this type of analysis, having refined measurements of natural radionuclides abundances was mandatory, which required an accurate instrumental calibration for the different spectral components.

Chapter 3 discusses the feasibility of using certified reference materials for the full energy efficiency calibration of High-Purity Germanium (HPGe) detectors dedicated to the measurement of radioactivity in environmental samples. I was actively involved in the assessment of correction factors related to the intrinsic features of the specific gamma decays and I gave a decisive contribution in estimating by Monte Carlo simulation the self-absorption correction factor, which allows to account for variations in photon attenuation within the source material due to variations in sample chemical composition and density. The reliability of the HPGe performances is the foundation for the challenging construction of a sensitivity calibration procedure to be applied to scintillation detectors.

In Chapter 4 I adopted a sensitivity calibration of in-situ and airborne sodium iodide scintillators based on the application of the Full Spectrum Analysis (FSA) with Non Negative Least Square (NNLS) constraint. I handled the implementation of the FSA-NNLS method which lead to the determination of the ^{40}K, ^{238}U, ^{232}Th and ^{137}Cs fundamental spectral shapes. In performing this task I dealt with the delicate point of comparing in-situ measurements and laboratory measurements conducted for the characterization of natural calibration sites, which have heterogeneous fields of view and affected by different sources of uncertainty. I also performed Monte Carlo simulations for the reconstruction of a synthetic fundamental spectra, which opens the way to the investigation of a variety of environmental and instrumental variables, as well as to the reconstruction of airborne gamma-ray spectra without the introduction of height scaling factors.

In order to model the background spectral components of airborne gamma-ray measurements, dedicated calibration flights at different heights above the sea should be performed, which represent a challenge both from the point of view of the experimental measurement and of the data analysis. An

extensive airborne gamma-ray survey over a wide altitude range is presented in Chapter 5, which has the purpose of measuring the background gamma radiation originating from the aircraft materials and cosmic rays. I participated to the airborne measurement campaign and I developed a χ^2 statistical analysis aimed at separately determining the background contributions in the ^{40}K, ^{214}Bi (eU) and ^{208}Tl (eTh) photopeaks of interest. In performing this task I integrated the measured count rates in a cosmic energy window, on the basis of which I could also assess the cosmic effective dose to the human population.

While events in the cosmic energy window are easily detected, airborne gamma-ray measurements suffer for the presence of a phantom source in the atmosphere, ^{222}Rn. Chapter 6 examines the feasibility of distinguishing and quantifying the presence of radon in the atmosphere by means of airborne gamma-ray spectroscopy measurements performed over the sea in a broad range of altitudes. I was personally involved in the data acquisition and I statistically tested with the adoption of fit estimators two theoretical models respectively describing the expected count rate in the ^{214}Bi energy window excluding and accounting for the presence of atmospheric radon.

The last two chapters report the most recent efforts I performed and they are going to be submitted in the next weeks.

Chapter 1

Worldwide estimation of the reactor antineutrino signals and spectra

The existence of antineutrinos was first theorized in 1930 by Pauli, who attempted to explain the continuous electron energy distribution in beta decay as due to the emission of a third light, weakly interacting neutral particle. This prediction was confirmed in 1956 by Reines and Cowan in the Savannah River Experiment, in which Inverse Beta Decay (IBD) reactions caused by electron antineutrinos from nuclear reactors were observed for the first time (Cowan et al. 1956). From then on, antineutrinos from nuclear reactors have played a crucial role in exploring neutrino physics, with respect to both the standard three-flavor neutrino oscillations and possible signatures of non-standard neutrino interactions.

Reactor antineutrino physics is currently being explored on a short and a long baseline scale (i.e. on a reactor-detector distance of $\sim$1 km and of $\sim$200 km, respectively), which also means investigating two different phase spaces of the oscillation parameters. However. till now there is no direct indication about the neutrino mass hierarchy as well as on the absolute mass of the electron, muon and tau neutrinos: these are the open questions that under construction and future medium baseline ($\sim$ 50 km) reactor neutrino experiments want to address.

While IBD reactions occurring in short-baseline experiments are essentially due to antineutrinos produced by the single close-by reactor core, the signal measured by long baseline experiments is shared among reactor antineutrinos generated by the worldwide nuclear power plant industry and geoneutrinos produced by the U and Th deployed in the whole planet. As reactor antineutrinos constitute the dominant source of background for geoneutrino measurements, a global reference model for antineutrinos from reactors is fundamental for inferring the geoneutrino component of the overall signal detected at long baseline experiments. Moreover, as the prime example of the KamLAND detector highlights, the operational conditions of nuclear reactors continuously change, giving rise to sizable reactor signal variations over time.

In this framework, this study provides a reference worldwide model for antineutrinos from reactors,

in view of reactors operational records yearly published by the International Atomic Energy Agency (IAEA). The expected signal from commercial reactors is evaluated for ongoing (KamLAND and Borexino), planned (SNO+ and JUNO) and proposed (RENO-50, LENA and Hanohano) experimental sites.

This study gave me the opportunity to focus on the reactor signal calculation and in particular to the problem of the uncertainty propagation. Since an analytical uncertainty propagation is not feasible, I applied a Monte Carlo based method according to which each input quantity is randomly sampled with respect to its probability density function. This approach allowed me not only to assess the global uncertainty budget for the investigated experimental sites, but also to establish a hierarchy of the input quantities according to their contribution to the overall uncertainty.

In this study I also highlighted the site dependent and time dependent nature of the uncertainty budget and hierarchy, which are directly connected to the antineutrino luminosities, to the distance and type of reactors dominating the reactor signal, and not least to the modeling of the input quantities according to the state of the art knowledge. The reactor signals at long baseline experiments have been calculated and compared also according to different parametrization of the individual antineutrino spectra generated by the four dominant fissile isotopes. The parametrization of the reactor antineutrino spectrum triggered also a deeper investigation of the off-equilibrium corrections to be applied to the reference spectra both during the burning of the reactor and in terms of contributions coming from spent nuclear fuels stored in the cooling pools. I also handled the creation of the web page `www.fe.infn.it/antineutrino` from which a comprehensive database of reactor operational records collected from 2003 to 2015 can be freely downloaded.

1.1 Background

During the last 20 years the neutrino physics sector has been experiencing an exciting and fruitful life. The observation of reactor antineutrino disappearance by the KamLAND (KL) experiment in 2005 (Araki et al. 2005b) confirmed the neutrino oscillation as the mechanism behind the solar neutrino deficit identified in 2001 by the SNO experiment (Ahmad et al. 2001), opening the way to precise estimates of the oscillation parameters, as the recent determination of the non-zero value of θ_{13}. Moreover, recent results from reactors pointed out an apparent 6% deficit of electron antineutrinos, referred to as the reactor antineutrino anomaly, which could be compatible with the existence of a fourth (sterile) neutrino (Abazajian et al. 2012).

Short-baseline and long-baseline reactor experiments, characterized respectively by a reactor-detector distance small/long in comparison with a length scale on the order of 1 km, provided significant improvements in the accuracy of neutrino oscillation parameters (F. P. An et al. 2013; Ahn et al. 2012; Y. Abe et al. 2012; Gando et al. 2013). Thanks to the remarkable progresses in the neutrino field over the last decades, the possibility of applying neutrino detection technologies for safeguard purposes is seriously under investigation (Lasserre et al. 2010). In the neutrino puzzle, the feasibility of reactor antineutrino experiments at medium baseline is currently being explored with the

intent of probing neutrino oscillation parameters both at short and long wavelength and of potentially investigating interference effects related to the mass hierarchy (Capozzi et al. 2014a).

Concurrently, antineutrinos produced at nuclear reactors constitute a severe source of background for the detection of geoneutrinos, i.e. the electron antineutrinos produced in beta minus decays along the ^{238}U and ^{232}Th decay chains. As the energy spectrum of antineutrinos from nuclear reactors overlaps with the spectrum of geoneutrinos, a careful analysis of the expected reactor signal at specific experimental sites is mandatory to establish the sensitivity to geoneutrinos. Geoneutrinos are a real time probe of the Earth's interior as their flux at the terrestrial surface depends on the amount and on the distribution of ^{238}U and ^{232}Th naturally present in the crust and in the mantle, which are thought to be the main reservoirs of these radioisotopes (G. Fiorentini et al. 2007).

The first experimental evidence of geoneutrinos dates from 2005, when the KL Collaboration claimed the observation of four events associated with ^{238}U and five with ^{232}Th decay chains (Araki et al. 2005a). Recent results from the KL and Borexino (BX) experiments provided quantitative measurements of the geoneutrino signal (116^{+28}_{-27} observed events in a total live-time of 2991 days for KL (Gando et al. 2013) and from $23.7\ ^{+6.5}_{-5.7}(\text{stat})^{+0.9}_{-0.6}(\text{sys})$ geoneutrino events in 2056 days for BX (Agostini et al. 2015)), important for discriminating among different Earth compositional models. The crustal contribution to the geoneutrino signal can be inferred from direct geochemical and geophysical surveys, while the mantle contribution is totally model-dependent. A better discrimination among different compositional models of the Bulk Silicate Earth (BSE), referred to as cosmochemical, geochemical and geodynamical (Šrámek et al. 2013), can be attained by combining the results from several sites (Huang et al. 2013). Therefore, new measurements of geoneutrino fluxes are highly awaited from experiments entering operation, such as SNO+ (Maneira et al. 2013) and JUNO (F. An et al. 2016), or proposed to the scientific community, such as RENO-50 (Kim 2013), LENA (Wurm et al. 2012), Hanohano (Cicenas and Solomey 2012), Homestake (Tolich et al. 2006) and Baksan (Domogatsky et al. 2005).

Electron antineutrinos are currently detected in liquid scintillation detectors via the IBD reaction on free protons

$$\bar{\nu}_e + p \rightarrow n + e^+ \tag{1.1}$$

which has an energy threshold of 1.806 MeV. As the antineutrino detection depends on several experimental parameters (e.g. the fiducial volume), expressing both geoneutrino and reactor antineutrino signals in terms of detector independent quantities allows the comparison of signals measured at different experiments and originating from different sources. Therefore, event rates are quoted in Terrestrial Neutrino Units (TNU) (G. Fiorentini et al. 2007), corresponding to one event per 10^{32} target protons per year, which are practical units as liquid scintillator mass is on the order of one kton ($\sim 10^{32}$ free protons) and the exposure times are typically on the order of a few years.

Considering that the reactor antineutrino spectrum extends beyond the endpoint of that of the geoneutrinos, there can be a significant overlap between geoneutrino and reactor signals in the geoneutrino energy window (Fig. 1.1), where generally about 27% of the total reactor events are registered.

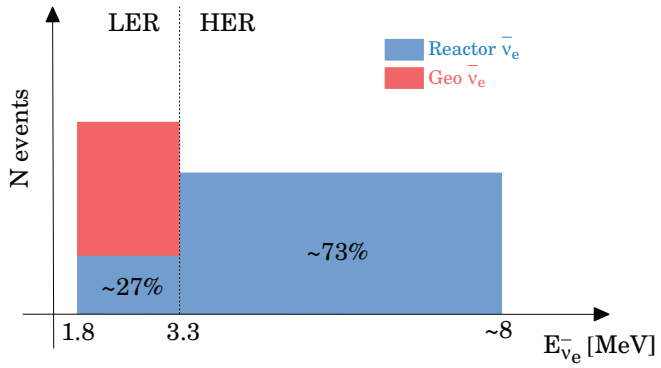

Figure 1.1: A sketch of the expected reactor signal in the Low Energy Region (LER) and in the High Energy Region (HER). The reactor signal in the HER is crucial for modeling the reactor contribution in the LER, and therefore for extracting information on geoneutrinos. The reactor contribution to the signal changes according to the different reactor operational conditions, while the geoneutrino component is time independent.

The boundaries of this energy range, also specified as Low Energy Region (LER), are defined by the detection reaction threshold and by the maximum energy of emitted geoneutrinos, occurring in the ^{214}Bi beta minus decay (3.272 MeV) (Gianni Fiorentini et al. 2010). The High Energy Region (HER) extends from the upper edge of the LER to the endpoint of the reactor antineutrino spectrum.

In this framework, modeling the predicted signal in the HER where only reactor events are expected, is of decisive importance for understanding the reactor contribution in the LER. In particular, the ratio R_{LER}/G between the predicted reactor signal in the LER (R_{LER}) and the expected geoneutrino signal (G) can be considered as a figure of merit for assessing the discrimination power on geoneutrinos at a specific location.

1.2 Inputs of the model

The dominating background in geoneutrino studies is due to electron antineutrinos produced at nuclear power plants, which are the strongest man-made antineutrino sources. With an average energy released per fission of approximately 200 MeV and 6 antineutrinos produced along the beta minus decay chains of the neutron-rich unstable fission products, $\sim 6 \cdot 10^{20}$ $\bar{\nu}$/s are emitted from a reactor having a thermal power of 3 GW. Evaluating the reactor antineutrino signal at a given location requires the knowledge of several ingredients, necessary for modeling the three reactor antineutrino life stages: production at reactor cores, propagation to the detector site and detection in liquid scintillation detectors via the IBD reaction.

In this calculation all the not movable operational reactors in the world used for commercial and research purposes have been taken into account. Hundreds of naval nuclear reactors with thermal power on the order of some hundreds of MW drive submarines, aircraft carriers and icebreakers cruising around the world (Hirdaris et al. 2014). A discussion of the potential effect due to nuclear propelled vessels on neutrino measurements is provided by Detwiler et al. 2002.

A comprehensive database containing the main features of each operational reactor core has been created and is available at `www.fe.infn.it/antineutrino`. The database of the operating com-

mercial reactors is compiled starting from 2003 on a yearly basis and updated using the operational information yearly published by the Power Reactor Information System (PRIS) of the International Atomic Energy Agency (IAEA) (`http://www.iaea.org/pris/home.aspx`). The nuclear power plant database contains 19 columns, structured as follows (for a given year of operation):

- core country acronym;
- core name;
- core location (latitude and longitude in decimal degrees);
- core type;
- use of MOX (1 for yes, 0 for no);
- thermal power P_{th} [MW];
- 12 columns listing the load factor for each month, expressed in percentage.

Latitude and longitude of core locations are taken from the World Nuclear Association Database (`http://world-nuclear.org/NuclearDatabase/Default.aspx?id=27232`). Core country acronyms, core name, core type, thermal and electrical power and load factors are defined and published in the PRIS annual publication entitled Operating Experience with Nuclear Power Stations in Member States.

1.2.1 Antineutrino production at reactor cores

The operating principle of nuclear power reactors lies in the generation of heat by the neutron-induced fissions of U and Pu isotopes and by the subsequent decays of unstable fission fragments. In a typical reactor, more than 99.9% of antineutrinos above the IBD energy threshold are emitted in large Q-value beta decays of unstable daughter fragments that originated in the fission process of just four isotopes: ^{235}U, ^{238}U, ^{239}Pu and ^{241}Pu (Djurcic et al. 2009). Therefore, the antineutrino spectrum produced by a given reactor can be expressed, in units of $\bar{\nu}$/MeV/fission, as:

$$\Lambda(E_{\bar{\nu}}) = \sum_{i=1}^{4} f_i \lambda_i(E_{\bar{\nu}}) \tag{1.2}$$

where $\lambda_i(E_{\bar{\nu}})$ and f_i are respectively the antineutrino emission spectrum normalized to one fission process and the fission fraction for the *i-th* isotope, where $i =^{235}$U, ^{238}U, ^{239}Pu and ^{241}Pu.

In literature, the different fuel isotope contributions to the generated thermal power are expressed as fission fractions or as power fractions, which have to be considered as different physical quantities. The fission fraction f_i is defined as a relative fission yield, i.e., as the fraction of fissions produced by the *i-th* isotope. This quantity is related to the reactor thermal power by the following energy

relation:

$$P_{th} = R\langle Q\rangle = R\sum_{i=1}^{4} f_i Q_i \tag{1.3}$$

where R is total fission rate (number of fissions per unit time) and $\langle Q\rangle$ is the average energy released per fission. The same energy relation can be expressed in terms of the power fractions p_i, corresponding to the fraction of the total thermal power produced by the fission of the $i\text{-}th$ isotope:

$$P_{th} = p_i P_i = p_i R f_i Q_i \tag{1.4}$$

where P_i is the thermal power generated by isotope i. Accordingly, the following relation between power fractions and fission fractions holds:

$$p_i = \frac{f_i Q_i}{\sum_{i=1}^{4} f_i Q_i} \tag{1.5}$$

During the power cycle of a nuclear reactor, the composition of the fuel changes as Pu isotopes are bred and U is consumed: thus, the power (fission) fractions are time-dependent quantities. Fuel isotope contributions also depend on the burn-up technology adopted in the given reactor core as different core types are characterized by different fuel compositions, which in turn give rise to different isotope contributions to the total thermal power.

The nuclear reactor operation relies on the use of cooling and moderating materials, which should be as safe and as cheap as possible. Typical coolants include materials such as water or gas which, due to their high thermal capacity, allow the collection and transfer of the energy released in the fission processes, while moderators are exploited to slow down the neutrons resulting from the fission processes to thermal energies in order to maintain the fission chain. Ordinary water is the most common moderator material: indeed, since hydrogen has a mass almost identical to that of the incident neutron, a single neutron-hydrogen collision can reduce the speed of the neutron substantially. However, due to the relatively high neutron capture cross section, reactors using light water as moderator (such as Pressurized Water Reactors (PWRs) and Boiling Water Reactors (BWRs)) require the adoption of enriched uranium as nuclear fuel, with a typical enrichment level of ^{235}U ranging from 2% to 5% (Bemporad et al. 2002). Pressurized Heavy Water Reactors (PHWRs) use heavy water as both moderator and coolant: due to the smaller neutron capture cross section with respect to ordinary water, PHWRs can burn natural uranium. However, as the reactor design is flexible and allows the use of advanced fuel cycles, using slightly enriched uranium, recovered uranium, Mixed OXide fuel (MOX), thorium fuels, and others (Rouben 1999) is possible. Gas Cooled Reactors (GCRs)[1] and Light Water Graphite Reactors (LWGRs) exploit graphite as moderator, which allows the adoption of

[1]Modern reactors using gas as cooling material and graphite moderated are also referred to as AGRs (Advanced Gas-cooled Reactors).

Table 1.1: ^{235}U, ^{238}U, ^{239}Pu, and ^{241}Pu fission/power fractions for PWRs, BWRs, GCRs, LWGRs, PHWRs and for reactors burning MOX, taken from literature references.

Reactor classes	Fractions	^{235}U	^{238}U	^{239}Pu	^{241}Pu	Reference
PWR BWR LWGR GCR	f_i	0.538	0.078	0.328	0.056	Mention et al. 2011
		0.614	0.074	0.274	0.038	
		0.620	0.074	0.274	0.042	
		0.584	0.068	0.298	0.050	
		0.543	0.070	0.329	0.058	
		0.607	0.074	0.277	0.042	
		0.603	0.076	0.276	0.045	
		0.606	0.074	0.277	0.043	
		0.557	0.076	0.313	0.054	
		0.606	0.074	0.274	0.046	
		0.488	0.087	0.359	0.067	Y. Abe et al. 2012
		0.580	0.074	0.292	0.054	
		0.544	0.075	0.318	0.063	
		0.577	0.074	0.292	0.057	
		0.590	0.070	0.290	0.050	Kopeikin et al. 2004
		0.570	0.078	0.295	0.057	S. Abe et al. 2008
		0.568	0.078	0.297	0.057	Eguchi et al. 2003
		0.563	0.079	0.301	0.057	Araki et al. 2005b
		0.650	0.070	0.240	0.040	Kopeikin 2012
		0.560	0.070	0.310	0.060	
		0.480	0.070	0.370	0.080	
	p_i	0.560	0.080	0.300	0.060	Bellini et al. 2010
MOX	p_i	0.000	0.081	0.708	0.212	Bellini et al. 2010
PHWR	p_i	0.543	0.024	0.411	0.022	Bellini et al. 2013

lower uranium enrichment levels, typically between 2.2% and 2.7% (Podvig 2011; Nonbøl 1996). Few tens of reactors (mainly located in Europe) use MOX, which is a mix of more than one oxide of fissile material and usually consists of plutonium recovered from spent nuclear fuel, blended with natural uranium, reprocessed uranium or depleted uranium. Generally, approximately 30% of the total power of these reactors comes from the MOX fuel, while the remaining 70% of the power is produced by standard fuel (Bellini et al. 2010).

In the calculation of the emitted reactor antineutrino spectrum $\Lambda(E_{\bar{\nu}})$ three reactor classes are distinguished according to the employed nuclear fuel. In Table 1.1 the typical fission/power fractions, together with the corresponding literature reference, are reported. PHWRs power fractions refer to reactors burning natural uranium (Cristoph et al. 1997); PWRs, BWRs, LWGRs and GCRs are assigned to the same class of enriched uranium burning reactors.

The contribution to the reactor thermal power given by each fuel isotope depends on its specific fission fraction as well as on the energy released per fission Q_i, which is obtained by:

$$Q_i = E^i_{tot} - \langle E_{\bar{\nu}} \rangle^i - \Delta E^i_{\beta\gamma} + E^i_{nc} \tag{1.6}$$

Table 1.2: Energy released per fission Q_i for ^{235}U, ^{238}U, ^{239}Pu, and ^{241}Pu taken from Ma et al. 2013.

Fissile isotope	Q_i(MeV)
^{235}U	202.36 ± 0.26
^{238}U	205.99 ± 0.52
^{239}Pu	211.12 ± 0.34
^{241}Pu	214.26 ± 0.33

where E_{tot}^{i} is the total energy produced in a fission process, starting from the moment the neutron that induces the process is absorbed until all of the unstable fission fragments have undergone beta decays; $\langle E_{\bar{\nu}} \rangle^{i}$ is the mean energy carried away by antineutrinos produced in the beta decays of fission fragments; $\Delta E_{\beta\gamma}^{i}$ is the energy of beta electrons and photons that, on average, does not contribute to the reactor energy during the operation of the core; E_{nc}^{i} is the energy released in neutron capture (without fission) by the reactor core materials (Ma et al. 2013). Table 1.2 lists the energies released per fission adopted in the calculation of the reactor antineutrino spectrum, which have been computed by Ma et al. 2013 following the approach described in Eq. 1.6.

The distribution of the fission products of uranium or plutonium involves hundreds of nuclei, each of them contributing to $\lambda_i(E_{\bar{\nu}})$ through various beta decay chains. Thus, the total antineutrino spectrum is the result of the sum of thousands of beta branches, weighted by the branching ratio of each transition and by the fission yield of the parent nucleus. The two traditional ways for predicting the total antineutrino spectrum are the summation and the conversion methods. The summation procedure reconstructs the beta spectra using available nuclear databases as the sum of the branch-level beta spectra of all the daughter isotopes and then converts the beta spectra in antineutrino spectra. The conversion technique relies on direct measurements of the beta spectra and exploits the energy conservation law between the two leptons involved in the beta minus decay:

$$E_e + E_{\bar{\nu}} = E_0 \tag{1.7}$$

where E_0 is the endpoint of the beta transition.

In the 1980s, measurements of the total beta spectra of fissile isotopes were performed at the Laue-Langevin Institute (ILL) in Grenoble where thin target foils of ^{235}U, ^{239}Pu and ^{241}Pu were exposed to an intense thermal neutron flux and the beta spectra of the unstable fragments were measured (Schreckenbach et al. 1985; Feilitzsch et al. 1982; Hahn et al. 1989). These spectra act as benchmarks for the summation calculations and are direct inputs for the conversion method. As ^{238}U undergoes fission when bombarded by fast neutrons, its beta spectrum could not be measured in the thermal flux of ILL. Recently, an experiment was performed at the neutron source FRM II in Garching to determine the cumulative antineutrino spectrum of the fission products of ^{238}U (Haag et al. 2014). The reference model adopted in the calculation is the one published by Mueller et al. 2011, where the spectra of all four contributing isotopes are consistently given in terms of the exponential of a

Table 1.3: Coefficients of the polynomial of order 5 used as argument of the exponential function for the analytical expression of the antineutrino spectra for ^{235}U, ^{238}U, ^{239}Pu, and ^{241}Pu, taken from Mueller et al. 2011.

Fissile isotope	a_1	a_2	a_3	a_4	a_5	a_6
^{235}U	3.217	-3.111	1.395	-3.690(10^{-1})	4.445(10^{-2})	-2.053(10^{-3})
^{238}U	4.833(10^{-1})	1.927(10^{-1})	-1.283(10^{-1})	-6.762(10^{-3})	2.233(10^{-3})	-1.536(10^{-4})
^{239}Pu	6.413	-7.432	3.535	-8.820(10^{-1})	1.025(10^{-1})	-4.550(10^{-3})
^{241}Pu	3.251	-3.204	1.428	-3.675(10^{-1})	4.254(10^{-2})	-1.896(10^{-3})

polynomial of order 5, as stated in Eq. 1.8. Mueller et al. 2011 derive the ^{235}U, ^{239}Pu and ^{241}Pu spectra based on a mixed approach that combines the accurate reference of the ILL electron spectra with the physical distribution of beta branches provided by the nuclear databases, and calculates the ^{238}U spectrum via a pure summation method.

$$\lambda_i(E_{\bar{\nu}}) = \exp\left(\sum_{p=1}^{6} a_p^i E_{\bar{\nu}}^{p-1}\right) \tag{1.8}$$

In Table 1.3, the coefficients of the polynomial function used in the parametrization of the reactor antineutrino spectrum generated by each fuel isotope are listed.

A reactor operational time profile is a required input for estimating the number of fissions occurring in a given time interval. The Load Factor (LF) is the percentage quantity expressing the effective working condition of a core in a specific period of the operating cycle and is defined as the ratio

$$LF = 100 \cdot \frac{EG}{REG} \tag{1.9}$$

where EG is the net electrical energy produced during the reference period as measured at the unit outlet terminals, i.e. after subtracting the electrical energy taken by auxiliary units, while REG is the net electrical energy that would have been supplied to the grid if the unit were operated continuously at the reference power unit during the whole reference period (J. Mandula, Nuclear Power Engeneering Section, International Atomic Energy Agency 2014). Load factor data are published by the IAEA, both on a monthly timeline and as an annual average. In the calculation the published values of electrical load factors are assumed to be equal to thermal load factors.

The spectrum of reactor antineutrinos emitted by a reactor core having a thermal power P_{th} and operating with a load factor LF can thus be evaluated according to Eq. 1.10.

$$S(E_{\bar{\nu}}) = P_{th} LF \sum_{i=1}^{4} \frac{p_i}{Q_i} \lambda_i(E_{\bar{\nu}}) \tag{1.10}$$

1.2.2 Antineutrino oscillation during propagation

The demonstration of the separate identity of muon and electron neutrinos (Danby et al. 1962), the discovery of the tauonic neutrino (Kodama et al. 2001) and the measurement of the decay width of the Z boson at LEP (Groom et al. 2000) endorsed the Standard Electroweak Model (SEM) as the most reasonable theory describing neutrino physics, according to which neutrinos exist in three light (with masses smaller than 1/2 M_Z) flavors and separate lepton numbers for electron, muon, and tau flavors are conserved. Nevertheless, an observed deficit in the solar neutrino flux with respect to the prediction of the Standard Solar Model started questioning the SEM, until the neutrino flavor change was definitely identified in 2001 by the SNO experiment (Ahmad et al. 2001) and subsequently the KL experiment provided clear evidence of the neutrino oscillatory nature (Gando et al. 2011).

At present, most experimental results on neutrino flavor oscillation agree with a three neutrino scenario, where weak neutrino eigenstates, i.e. flavor eigenstates $(\nu_e, \nu_\mu, \nu_\tau)$ mix with the mass eigenstates (ν_1, ν_2, ν_3) via three mixing angles $(\theta_{12}, \theta_{13}, \theta_{23})$ and a possible CP-violating phase δ. Therefore, to establish the reactor antineutrino flux at a given site, it is necessary to consider the survival probability of the electron antineutrino, which can be expressed (assuming that antineutrinos propagate in vacuum) in terms of the mass-mixing oscillation parameters $(\delta m^2, \theta_{12}, \theta_{13})$ as stated in G. Fiorentini et al. 2012:

$$P_{ee}(E_{\bar{\nu}}, L) = cos^4(\theta_{13}) \left(1 - sin^2(2\theta_{12}) sin^2 \left(\frac{\delta m^2 L}{4E_{\bar{\nu}}}\right)\right) + sin^4(\theta_{13}), \tag{1.11}$$

where L and $E_{\bar{\nu}}$ are the antineutrino path length and energy in natural units.[2]

The adopted values for the neutrino oscillation parameters are the ones obtained by Capozzi et al. 2014b from a global fit to data provided by different experiments.

The data combined analysis provides Nσ curves of the 3ν oscillation parameters, whose degree of linearity and symmetry is strictly related to the Gaussian nature of the probability distribution associated with that parameter. On the basis of Fig.3 of Capozzi et al. 2014b, $(\delta m^2, \theta_{12}, \theta_{13})$ are assumed to be described by Gaussian Probability Density Functions (PDF). The adopted central values and 1σ uncertainties are reported in Table 1.4, where, conservatively, the 1σ value has been selected as the maximum between σ^+ and σ^- for each parameter distribution.

The matter effect concerning the antineutrino propagation from the reactor to the experimental site has been investigated by adopting the Earth density profile as published in Dziewonski and Anderson 1981. The matter effect on the signal varies according to the investigated experimental site, giving a maximum contribution of 0.7% at Hawaii. In any case, it can be considered negligible at 1σ level with respect to the overall uncertainties reported in Table 1.7.

[2]The 3 flavor vacuum survival probability in principle depends on the difference between the squared masses $\Delta m^2 = m_3^2 - (m_1^2 + m_2^2)/2$, according to a relationship that is not invariant under a change of hierarchy (where $\Delta m^2 > 0$ and $\Delta m^2 < 0$ correspond respectively to the normal and inverted hierarchy scenarios). In any case, the Δm^2 dependence of the survival probability is negligible for $L >> 50$ km (Capozzi et al. 2014a). Considering the quality of the inputs used for the calculation, the differences on the expected signal due to the use of two survival probabilities (Δm^2 dependent and Δm^2 not dependent) are negligible, also in the case of JUNO and RENO-50.

Table 1.4: The 3ν mass-mixing parameters entering the electron antineutrino survival probability equation, adapted from Capozzi et al. 2014b

Oscillation parameter	Central value $\pm 1\sigma$ range
δm^2 (eV^2)	7.54 $\pm$0.26 (10^{-5})
$\sin^2(\theta_{12})$	3.08 $\pm$0.17 (10^{-1})
$\sin^2(\theta_{13})$	2.34 $\pm$0.20 (10^{-2})

With respect to the antineutrino pathlength, the distance L from the reactor to the experimental site has been evaluated using an ellipsoid as geometrical shape of the Earth. We use a= 6378136.6 m and b= 6356751.8 m as equatorial radius and polar radius, respectively (International Earth Rotation and Reference Systems Service (IERS) 2003).

1.2.3 Antineutrino detection at liquid scintillation detectors

The components presented in the last two sections allow the modeling of the expected (oscillated) reactor antineutrino flux at a given experimental site. To determine the predicted signal, it is necessary to account for the detection process via the IBD reaction on free protons. The IBD reaction effectiveness in antineutrino detection is the result of the relatively large reaction cross section (on the order of 10^{-42}cm^2), the feasibility of building large detectors (as materials rich in free protons, such as water and hydrocarbons, are relatively cheap) and the possibility of reducing backgrounds, which is possible due to the correlation between the prompt positron annihilation signal and the delayed neutron capture signal (Jocher et al. 2013). In this work, we use for the parametrization of the IBD reaction cross section the expression given by Strumia and Vissani 2003:

$$\begin{aligned}\sigma_{IBD}(E_{\bar{\nu}}) =& 10^{-43} cm^2 p_e E_e E_{\bar{\nu}}^{-0.07056+0.02018 ln E_{\bar{\nu}} - 0.001953 ln^3 E_{\bar{\nu}}},\\ & E_e = E_{\bar{\nu}} - \Delta,\\ & p_e = \sqrt{E_e^2 - m_e^2},\end{aligned} \tag{1.12}$$

where E_e is the positron energy, $\Delta = m_n - m_p \approx 1.293$ MeV, p_e is the positron momentum, $m_e = 0.511$ MeV is the positron mass. The final equation for the evaluation of the antineutrino signal from reactors is obtained considering the contribution at a given experimental site given by all operating reactors in the world, as stated in Eq. 1.13

$$N_{tot} = \varepsilon N_p \tau \sum_{i=1}^{N_{reactor}} \frac{P_{th}^i}{4\pi L_i^2} \langle LF_i \rangle \int dE_{\bar{\nu}} \sum_{k=1}^{4} \frac{p_k}{Q_k} \lambda_k(E_{\bar{\nu}}) P_{ee}(E_{\bar{\nu}}, L_i) \sigma_{IBD}(E_{\bar{\nu}}) \tag{1.13}$$

where ε is the detector efficiency, N_p is the number of free target protons, τ is the exposure time, $\langle LF_i \rangle$ is the average load factor of the *i-th* reactor over the given exposure time and L_i is the reactor-

detector distance. The reactor antineutrino signal is evaluated in TNU, i.e for a total number of free protons equal to $N_p = 10^{32}$, an acquisition time $\tau = 3.15 \cdot 10^7$ s (1 year) and a detector efficiency $\varepsilon = 1$.

1.3 Methods

1.3.1 Monte Carlo signal and uncertainty prediction

The calculation of the reactor antineutrino signal at a given site requires the knowledge of many factors related to reactor physics, in terms of reactor operations and of nuclear physics describing the fission process, and to antineutrino physics, which involves both the oscillation and the detection mechanisms. Uncertainties with respect to input data contribute with different weights and in different ways to the uncertainty on the reactor signal. Thus, given the complexity of the model, a Monte Carlo based approach has been used to estimate the global uncertainty on the reactor signal, together with the relative contributions associated with each component of the calculation.

According to Joint Committee for Guides in Metrology 2008, for the evaluation of the uncertainty on the signal due to a specific input quantity X_i all the components have been fixed to their central values and a Monte Carlo sampling of X_i pseudo random values has been conducted according to the specific PDF. With respect to the fission fractions, the adopted central values for the reactor class involving PWRs, BWRs, LWGRs and GCRs the set reported in Bellini et al. 2010. Table 1.6 shows a summary of the PDFs and the associated standard errors for the input quantities included in the propagation of the uncertainties, together with the reference from which each parameter has been extracted. Althought moderate correlations among some signal input quantities (e.g. thermal power and fission fractions) have been investigated by Djurcic et al. 2009, the analysis of their effects is out of the goal of this study as it would require punctual knowledge of input data (e.g. stage of burn up of the fuel, effective thermal power). In this framework we treat each parameter as uncorrelated with other input quantities.

The signal uncertainties associated with each single input for the KL, BX and SNO+ experiments (see Table 1.6) are obtained by performing 10^4 calculations of the global signal produced by all operating reactors in the world in 2013 and using the reactor antineutrino spectrum provided by Mueller et al. 2011.

With respect to the antineutrino oscillation parameters and the energy released per fission, the same X_i sampled value is used for all operating reactors for a given global signal calculation.

The fission fractions are extracted for the single cores for each of the 10^4 total reactor signal calculations at a given experimental site. The random sampling of the fission fractions allows to take into account the lack of knowledge concerning the detailed fuel composition of each reactor as well as the unknown stage of burn-up. The sampling is performed for PWRs, BWRs and GCRs and for the 70% contribution given by standard fuels for reactors using the MOX technology. This is carried out by extracting with equal probability one of the 22 sets of fission fractions listed in Table 1.1 (constant

Probability Mass Function (PMF)). For PHWRs and for the 30% MOX component the fixed values adopted are those presented in Bellini et al. 2010 and Bellini et al. 2013, listed in Table 1.1.

Although individual measurements of reactor thermal power can reach a sub-percent level accuracy (Djurcic et al. 2009; Bemporad et al. 2002), the regulatory specifications for safe reactor operations for Japan and United States require, at minimum, an accuracy of 2%. In this study, a conservative uncertainty value of 2% is adopted, including the error for thermal LF. The thermal power of each core has been sampled for every signal calculation.

The IBD cross section is extracted with a Monte Carlo sampling for each energy value at which the integrand of Eq. 1.12 is computed, where the adopted energy bin is equal to 1 keV.

The global uncertainty on the reactor signal is evaluated by extracting simultaneously all the ingredients entering the uncertainty propagation procedure. This analysis is performed for 14 peculiar locations in the world, corresponding to sites hosting experiments that are currently ongoing or entering operation, as well as candidate sites for future neutrino experiments. Results are reported in Table 1.7, where the central values correspond to the medians and the errors are expressed as 1σ uncertainties.

1.3.2 Effect of long-lived isotopes

During the operation of a nuclear reactor unstable fission fragments are constantly being produced, with half-lives in a wide range, from fractions of seconds up to 10^{18} years. The Long-Lived Isotopes (LLIs) accumulate during the running of the reactor and consequently there exist off-equilibrium effects in the antineutrino spectrum from an operating reactor. The ^{235}U, ^{239}Pu, and ^{241}Pu antineutrino reference spectra entering the calculation of the total reactor spectrum are determined from the beta spectra measured after an exposure time to thermal neutrons of 12 hours (^{235}U) (Schreckenbach et al. 1985), 1.5 days (^{239}Pu) (Feilitzsch et al. 1982) and 1.8 days (^{241}Pu) (Hahn et al. 1989), which implies that long-lived fission fragments have not yet reached equilibrium. Among unstable fission products of energy in the region $E_{\bar{\nu}}^{max} > 1.806$ MeV, the most important LLIs having half-lives longer than 10 hours contribute only in the LER (see Table 1.5), as the amplitude of the positive deviation from the reference spectra becomes negligible above 3.5 MeV (Mueller et al. 2011). The list of LLIs includes the Spent Nuclear Fuels (SNFs), i.e., ^{106}Ru, ^{144}Ce and ^{90}Sr, having $\tau_{1/2} \sim$ yr. As the off-equilibrium effects associated with the LLIs affect the antineutrino signal in the LER, understanding the LLIs contribution is a relevant issue in the geoneutrino framework.

The off-equilibrium corrections to the reference spectra reported in Table VII of Mueller et al. 2011 have been adopted in order to estimate the systematic uncertainty on the antineutrino signal due to the accumulation of LLIs during the running of the reactor. As the operational run of a reactor usually lasts 1 year, signal values reported in Table 1.7 include the 300 days off-equilibrium correction to the reference ^{235}U, ^{239}Pu and ^{241}Pu spectra published in Mueller et al. 2011.

After a time lapse on the order of one month with respect to the end of a reactor operating cycle, the SNF that has been pull out from the reactor contributes to approximately 0.6% of the IBD

Table 1.5: LLIs, responsible of the off-equilibrium contribution to the reactor antineutrino spectrum during the reactor operating period, together with the SNFs (in the last three rows), which contribute also after the shut down of the reactor. $\tau^P_{1/2}$, $\tau^D_{1/2}$, $E^{maxP}_{\bar{\nu}}$ and $E^{maxD}_{\bar{\nu}}$ are the half-lives and the maximum energy of the emitted antineutrino of the parent (P) and daughter (D) nucleus, respectively. Y_{235} and Y_{239} are respectively the daughter cumulative specific yields in percentage per fission event of ^{235}U and ^{239}Pu, except for the case of ^{93}Y and ^{97}Zr which refer to the parent nuclides (Kopeikin 2012).

P	$\tau^P_{1/2}$	$E^{max\ P}_{\bar{\nu}}$ [MeV]	D	$\tau^D_{1/2}$	$E^{max\ D}_{\bar{\nu}}$ [MeV]	Y_{235}(%)	Y_{239}(%)
^{93}Y	10.18 h	2.895	^{93}Zr	1.61 $\cdot 10^6$yr	0.091	6.35	3.79
^{97}Zr	16.75 h	1.916	^{97}Nb	72.1 m	1.277	5.92	5.27
^{112}Pd	21.03 h	0.27	^{112}Ag	3.13 h	3.956	0.013	0.13
^{131m}Te	33.25 h	/	^{131}Te	25.0 m	2.085	0.09	0.20
^{132}Te	3.204 d	0.24	^{132}I	2.295 h	2.141	4.31	5.39
^{140}Ba	12.753 d	1.02	^{140}La	1.679 d	3.762	6.22	5.36
^{144}Ce	284.9 d	0.319	^{144}Pr	17.28 m	2.998	4.58	3.11
^{106}Ru	371.8 d	0.039	^{106}Rh	30.07 s	3.541	0.30	3.24
^{90}Sr	28.79 yr	0.546	^{90}Y	64.0 h	2.280	0.27	0.10

unoscillated event rate in the Full Energy Region (FER) (see Fig.6 of Bin et al. 2012). Each reactor is generally subject to a scheduled preventive maintenance on a yearly basis during which one third of the burnt fuel is typically transferred to the water pool located near the reactor core for cooling and shielding. As the exhausted fuel storage time can be as long as 10 years, the presence of the SNFs in the water pools can affect the reactor signal predictions, especially in the LER. An average SNF half-life has been estimated by weighting the individual half-lives of the SNF species for the relative yields and fission fractions associated with each fissioning isotope, as stated in the following equation:

$$\tau^{SNF}_{1/2} = \sum_{i=^{144}\mathrm{Ce},^{106}\mathrm{Ru},^{90}\mathrm{Sr}} k_i \tau^i_{1/2}\ ,$$
$$k_i = \sum_{l=^{235}\mathrm{U},^{239}\mathrm{Pu}} f_l \overline{Y^i_l} \tag{1.14}$$

where $\tau^i_{1/2}$ is the half-life of the *i-th* SNF species, f_l is the fission fraction (normalized to unity) for the *l-th* fissioning isotope and $\overline{Y^i_l}$ is the production yield, with the normalization constraint $\sum_l \overline{Y^i_l} = 1$. Following this approach we estimate a SNF global half-life of

$$\tau^{SNF}_{1/2} = 1.9 \text{ yr} \tag{1.15}$$

The enhancement of the unoscillated IBD event rate due to the SNFs in the FER ΔN^{SNF}_{IBD} can be determined for a storage time T (expressed in units of years) according to Eq. 1.16:

$$\Delta N^{SNF}_{IBD} = \sum_{n=0}^{T} 0.2 \cdot \exp\left(-\frac{n}{\tau^{SNF}}\right) \tag{1.16}$$

where it is assumed that every year a SNF mass equal to 1/3 of the reactor mass, decaying with a mean lifetime $\tau^{SNF} = \tau_{1/2}^{SNF}/ln(2)$, is transferred to the cooling pools.

With the hypothesis of a 10 years storage time of SNFs, corresponding to the convergence of the series in Eq. 1.16, a 2.4% increase of the unoscillated IBD event rate in the LER has been estimated, in agreement with (Gando et al. 2013) and (Araki et al. 2005a). This potentially critical systematic uncertainty in geoneutrino measurements is not included in Table 1.7.

1.3.3 Research reactors

The research reactor (RR) class embraces a wide range of civil nuclear reactors that are generally not employed for power generation but they are mainly used as neutron sources, as well as for innovative nuclear energy researches and for teaching/training purposes. Among the major applications of the produced neutron beams are the non destructive tests of materials, neutron scattering experiments and the production of radioisotopes both for medical and industrial uses.

According to the 2013 IAEA data published in `http://nucleus.iaea.org/RRDB/RR/ReactorSearch.aspx?rf=1.`, there are 247 operational RRs in the world accounting for a total thermal power of 2.2 GW, to be compared with the 1160 GW global thermal power generated by the 441 operational commercial reactors.Half of the RR thermal power is generated by only 8 reactors having an individual thermal power between 100 and 250 MW.

The expected reactor signal has been calculated in the 14 experimental sites listed in Table 1.7, originating from the 40 RRs that account for the 90% of the thermal power considering an average 80% annual load factor. The effect of this contribution is in any case smaller than 0.2%, which can be considered as an upper limit enhancement of the commercial reactor signal.

1.4 Results and discussion

Table 1.6 reports the results regarding the uncertainties on the reactor signal due to the 1σ errors associated with single inputs. For the three operative long baseline experiments the major effect is attributed to $sin^2(\theta_{12})$, which generates an uncertainty on the signal of approximately 2.2% at 1σ level. The impact on the signal uncertainty due to the uncertainties on reactors thermal power and on the fission fractions is highly site dependent. It emerges as a combined effect of the different reactor distances from the experimental sites and of the number and class of close-by reactors.

In 2013, approximately 60% of the signal predicted at KL is almost equally shared between just two Japanese reactor cores (Ohi stations 3 and 4) which are located 180 km far away from the Kamioka mine. The same signal percentage is produced at BX by approximately 60 reactors located within a radius of 1000 km, where each core contributes to less than 3% of the signal. With respect to SNO+, 20 cores situated within a 500 km radius from the experimental site provide approximately 60% of the signal, each core contributing to 6% of the signal at maximum (see Fig. 1.5). As a consequence, the uncertainty on reactors thermal power generates at KL an uncertainty on the signal three times

Table 1.6: Uncertainty on the reactor signal in the FER for the long baseline experiments KL, BX and SNO+ due to the uncertainties on single inputs. Results are obtained by applying a Monte Carlo sampling of the input quantities according to the corresponding Probability Density Function (PDF).

Input quantity	Symbol	PDF	1σ unc on input[%]	Input reference	1σ unc on signal in the FER [%]		
					BX	KL	SNO+
$\bar{\nu}$ oscillation	δm^2	Gaussian	3.4	Capozzi et al. 2014b	< 0.1	0.9	< 0.1
	$sin^2(\theta_{12})$	Gaussian	5.5		+2.4/-2.2	+2.1/-2.0	+2.4/-2.2
	$sin^2(\theta_{13})$	Gaussian	8.5		0.4	0.4	0.4
Energy released per fission	$Q_{^{235}U}$	Gaussian	0.1	Ma et al. 2013	< 0.1	< 0.1	< 0.1
	$Q_{^{238}U}$		0.3				
	$Q_{^{239}Pu}$		0.2				
	$Q_{^{241}Pu}$		0.2				
Fuel composition	$f_{^{235}U}$	Constant PMF	/	Table 1.1	0.1	0.5	< 0.1
	$f_{^{238}U}$						
	$f_{^{239}Pu}$						
	$f_{^{241}Pu}$						
Thermal Power	P_{th}	Gaussian	2	Djurcic et al. 2009	0.2	0.9	0.3
IBD cross section	$\sigma_{IBD}(E_{\bar{\nu}})$	Gaussian	0.4	Strumia and Vissani 2003	< 0.1	< 0.1	< 0.1

higher than what estimated for BX and SNO+, on the order of 1%.

Fission fractions give rise to a few tenths of percent 1σ uncertainty on the reactor signal. The effect of fission fractions at KL is five times larger with respect to what estimated at BX: this behavoiur reproduces the one already observed for the thermal power, and is also related to the fact that reactors giving the highest contributions to the signal belong to the same reactor class. On the other hand, SNO+ is almost insensitive to fission fractions variability, since the signal is dominated by the Canadian PHWRs, for which a fixed single set of power fractions is currently available.

Fig. 1.2 shows a worldwide map (with a 1° x 1° spatial resolution) of expected reactor signals in the LER expressed in TNUs, produced using 2013 operational reactor data. This map provides evidence regarding the sites demonstrating the best discrimination power on geoneutrino measurements.

A particular focus is dedicated to sites hosting ongoing neutrino experiments (KL and BX), experiments entering operation (SNO+ and JUNO), and candidate sites for future experiments (RENO-50, Hanohano, LENA, Homestake, Baksan). For these specific locations we report in Table 1.7 the expected reactor signal both in the FER (R_{FER}) and in the LER (R_{LER}) according to 2013 reactor's operational data, together with the geoneutrino signal G estimated on the base of the reference Earth model published by Huang et al. 2013. In Appendix A the reactor signals evaluated for 2014 (Table A.1) and 2015 (Table A.2) reactor's operational data are also reported. The ratio R_{LER}/G is also evaluated, which can be considered as a figure of merit for assessing the sensitivity to geoneutrinos at

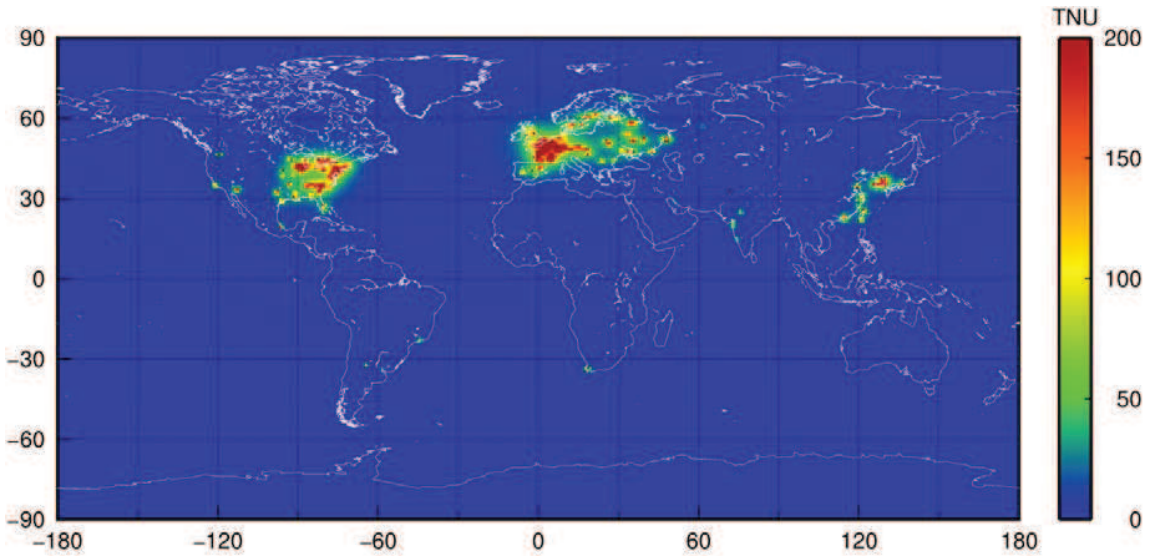

Figure 1.2: Map of the worldwide predicted antineutrino signals from nuclear power plants in the LER, expressed in TNUs. The map has a spatial resolution of 1° x 1° and it is produced with 2013 operational data on nuclear power plants.

a given site (see Table 1.7).

The reactor signals R_{FER} and R_{LER} are determined as median values of the signal distributions obtained from the Monte Carlo calculation. For each site the signals are computed 10^4 times using the Mueller et al. 2011 analytical parametrization of the reactor spectrum, including the 300 days off-equilibrium correction due to the LLIs, and simultaneously extracting, according to the corresponding PDF, all the inputs entering the uncertainty propagation procedure as described in Sec. 1.3.1. For the long baseline experiments, signal errors are evaluated as 1σ uncertainties and are estimated to be on the order of 3% and 4% for the signal in the FER and in the LER, respectively. Ratios R_{LER}/G between predicted geoneutrino and reactor signals in the LER (calculated using 2013 reactor operational features) show the high discrimination power on geoneutrinos achievable at Hawaii ($R_{LER}/G = 0.1$), Homestake and Baksan ($R_{LER}/G = 0.2$). In 2013 a relatively high sensitivity to geoneutrinos is attainable at Kamioka ($R_{LER}/G = 0.6$) thanks to the protracted shutdown of the Japanese reactors after the Fukushima accident, in comparison with the much lower geoneutrino discrimination power of 2006 ($R_{LER}/G = 5.4$) when the Japanese power industry was fully operational. In 2014 (Table A.1 and 2015 (Table A.2 KL sensitivity to geoneutrinos is even higher ($R_{LER}/G = 0.2$) as the Ohi3 and Ohi4 cores, which were fully operational till August 2013, were also temporarily shut down. Moreover, JUNO appears to be a good candidate site for geoneutrino measurements according to 2013 reactors operating status. Indeed, 105 days would be sufficient for the 20 kton detector to reach a 10% accuracy on geoneutrinos if one assumes a data taking period during which the Yangjiang (17.4 GW) and Taishan (18.4 GW) nuclear power plants are not operational (and assuming a $C_{17}H_{28}$ liquid

Table 1.7: Predicted antineutrino signals (in TNU) from nuclear power plants in the FER (R_{FER}) and in the LER (R_{LER}) obtained with 2013 reactor operational data, together with the expected geoneutrino signals (G) and R_{LER}/G ratios at current and proposed neutrino experimental sites. In Appendix A the reactor signals estimated with respect to the 2014 and 2015 reactor's operational data. Antineutrino signals in the FER and in the LER include the off-equilibrium contribution due to the accumulation of the LLIs during the running of the reactor. For the KL experiment we report also the values obtained using 2006 reactor operating records. For the JUNO experiment we predict the 2020 reactor signals, considering as operating with a 80% annual average load factor the Yangjiang (17.4 GW) and Taishan (18.4 GW) nuclear power stations which are actually under construction.

Site	Experiment	Coordinates	G [TNU]	R_{FER} [TNU]	R_{LER} [TNU]	R_{LER}/G
Gran Sasso (IT)[a]	Borexino	42.45 N, 13.57 E[b]	$40.3^{+7.3}_{-5.8}$	$83.6\ ^{+2.0}_{-1.9}$	$22.5^{+0.6}_{-0.6}$	0.6
Sudbury (CA)	SNO+	46.47 N, 81.20 W[b]	$45.4^{+7.5}_{-6.3}$	$191.5^{+4.6}_{-4.3}$	$48.3^{+1.8}_{-1.4}$	1.1
Kamioka (JP)	KamLAND	36.43 N, 137.31 E[b]	$31.5^{+4.9}_{-4.1}$	$65.7^{+1.7}_{-1.6}$	$18.7^{+0.6}_{-1.0}$	0.6
				$629.7^{+14.5c}_{-13.2}$	$171.3^{+5.7c}_{-6.3}$	5.3[c]
DongKeng (CH)	JUNO	22.12 N, 112.52 E[d]	$39.7^{+6.5}_{-5.2}$	$95.8^{+2.6}_{-2.5}$	$26.5^{+2.2}_{-2.2}$	0.7
				1566^{+111e}_{-100}	$354.5^{+44.5e}_{-40.6}$	8.9[e]
GuemSeong (SK)	RENO-50	35.05 N, 126.70 E[d]	$38.3^{+6.1}_{-4.9}$	1134^{+72}_{-70}	182^{+21}_{-20}	4.8
Hawaii (US)	Hanohano	19.72 N, 156.32 W[b]	$12.0^{+0.7}_{-0.6}$	$3.4^{+0.1}_{-0.1}$	$0.9^{+0.02}_{-0.02}$	0.1
Pyhäsalmi (FI)	LENA	63.66 N, 26.05 E[b]	$45.5^{+6.9}_{-5.9}$	$66.5^{+1.6}_{-1.5}$	$17.3^{+0.5}_{-0.4}$	0.4
Boulby (UK)	LENA	54.55 N, 0.82 W[b]	$39.2^{+6.3}_{-4.9}$	1239^{+35}_{-36}	245^{+12}_{-12}	6.2
Canfranc (SP)	LENA	42.70 N, 0.52 W[b]	$40.0^{+6.4}_{-5.1}$	$248.4^{+6.0}_{-5.7}$	$71.3^{+1.6}_{-1.7}$	1.8
Fréjus (FR)	LENA	45.13 N, 6.68 E[b]	$42.8^{+7.6}_{-6.4}$	549^{+12}_{-12}	$127.9^{+5.6}_{-5.2}$	3.0
Slănic (RO)	LENA	45.23 N, 25.94 E[b]	$45.1^{+7.8}_{-6.3}$	$109.7^{+2.7}_{-2.5}$	$29.9^{+0.7}_{-0.7}$	0.7
Sieroszowice (PL)	LENA	51.55 N, 16.03 E[b]	$43.4^{+7.0}_{-5.6}$	$153.9^{+3.7}_{-3.4}$	$42.0^{+1.1}_{-1.0}$	1.0
Homestake (US)	/	44.35 N, 103.75 W[b]	$48.7^{+8.3}_{-6.9}$	$30.6^{+0.7}_{-0.7}$	$8.2^{+0.2}_{-0.2}$	0.2
Baksan (RU)	/	43.20 N, 42.72 E[b]	$47.2^{+7.7}_{-6.4}$	$36.8^{+0.9}_{-0.8}$	$9.8^{+0.3}_{-0.3}$	0.2

[a] IT: Italy, JP: Japan, CA: Canada, CH: China, SK: South Korea, US: United States of America, FI: Finland, UK: United Kindom, SP: Spain, FR: France, RO: Romania, PL: Poland, RU: Russia.
[b] Huang et al. 2013
[c] 2006 reactor operational data.
[d] Ciuffoli et al. 2014
[e] 2013 reactor operational data plus Yangjiang (17.4 GW) and Taishan (18.4 GW) nuclear power stations operating with a 80% average annual load factor.

Table 1.8: Reactor signals (without the LLIs contribution) in the FER and in the LER obtained with the analytical parametrization of the reactor spectra from Huber 2011, Huber and Schwetz 2004, Vogel and Engel 1989 and Mueller et al. 2011 for the BX, KL and SNO+ experiments. Since in (Huber and Schwetz 2004) and (Huber 2011) there is no analytical expression for the ^{238}U antineutrino spectrum, the one reported in Mueller et al. 2011 is used in these two cases.

	R_{FER} [TNU]			R_{LER} [TNU]		
Reactor spectra model	BX	KL	SNO+	BX	KL	SNO+
Mueller et al. 2011	$83.2\ ^{+2.0}_{-1.8}$	$65.3\ ^{+1.7}_{-1.6}$	$190.2\ ^{+4.8}_{-4.3}$	$22.1^{+0.6}_{-0.5}$	$18.3^{+0.6}_{-1.0}$	$47.2\ ^{+1.7}_{-1.4}$
Huber 2011 + ^{238}U Mueller et al. 2011	$83.9\ ^{+2.0}_{-1.8}$	$65.9^{+1.7}_{-1.6}$	$192.0\ ^{+4.9}_{-4.3}$	$22.0^{+0.6}_{-0.5}$	$18.3^{+0.6}_{-1.0}$	$47.1\ ^{+1.7}_{-1.4}$
Huber and Schwetz 2004 + ^{238}U Mueller et al. 2011	$81.2\ ^{+2.0}_{-1.8}$	$63.7^{+1.6}_{-1.5}$	$185.5\ ^{+4.7}_{-4.1}$	$21.7^{+0.6}_{-0.5}$	$18.0^{+0.6}_{-1.0}$	$46.3\ ^{+1.7}_{-1.4}$
Vogel and Engel 1989	$81.6\ ^{+2.0}_{-1.8}$	$63.9^{+1.6}_{-1.6}$	$187.1\ ^{+4.7}_{-4.2}$	$21.6^{+0.5}_{-0.6}$	$17.9^{+0.6}_{-1.0}$	$46.0\ ^{+1.7}_{-1.4}$

scintillator composition, a 100% detection efficiency and that the geoneutrino background is due only to reactor antineutrinos). In contrast, the ratio R_{LER}/G dramatically increases from 0.7 to 8.9 if we consider both Chinese power stations to operate with an annual average load factor of 80%. In 2014 and 2015 the ratios R_{LER}/G for the JUNO experiment were equal to 1.4 and 2.0, corresponding respectively to the connection to the electrical grid of the core number 1 and core number 2 and 3 of the Yangjiang nuclear power plant.

To estimate the variability in the expected reactor signal due to different reactor spectra, the predicted signals at KL, BX and SNO+ have been calculated using three alternative parametrizations of the antineutrino spectra, i.e. the ones published by Huber 2011, Huber and Schwetz 2004 and Vogel and Engel 1989 (see Table 1.8). There is no expression for the ^{238}U spectrum in (Huber and Schwetz 2004) and (Huber 2011), as these parametrizations are based on the conversion of ILL beta spectra. Therefore, for these two sets of spectra, the adopted functional expression for the ^{238}U antineutrino spectrum is provided by Mueller et al. 2011. Median signal values are shown in Table 1.8, together with the 1σ uncertainties evaluated via Monte Carlo sampling. The maximum signal spread associated with the employment of different analytical functions as phenomenological parametrization of the reactor antineutrino spectrum is of the same order as the global uncertainty on the signal resulting from the combined effect of all the other input quantities. Therefore, the reactor antineutrino spectrum emerges as the most critical component in the signal calculation.

Fig. 1.3 shows a time profile of the expected reactor antineutrino signals at KL and BX over a period of 10 years on a monthly time-line, from 2003, when the KL detector entered operation, to 2013. The BX time profile exhibits a seasonal variation, suggesting that the periodic signal shape could be possibly implemented in the event analysis. The highest and lowest reactor signals occur respectively in correspondence with the cold and warm seasons, being the electricity demand typically higher during the winter. In connection to this, it can be noticed that refueling and maintenance for nuclear units are typically performed in the spring and fall seasons, when demand for electricity is generally

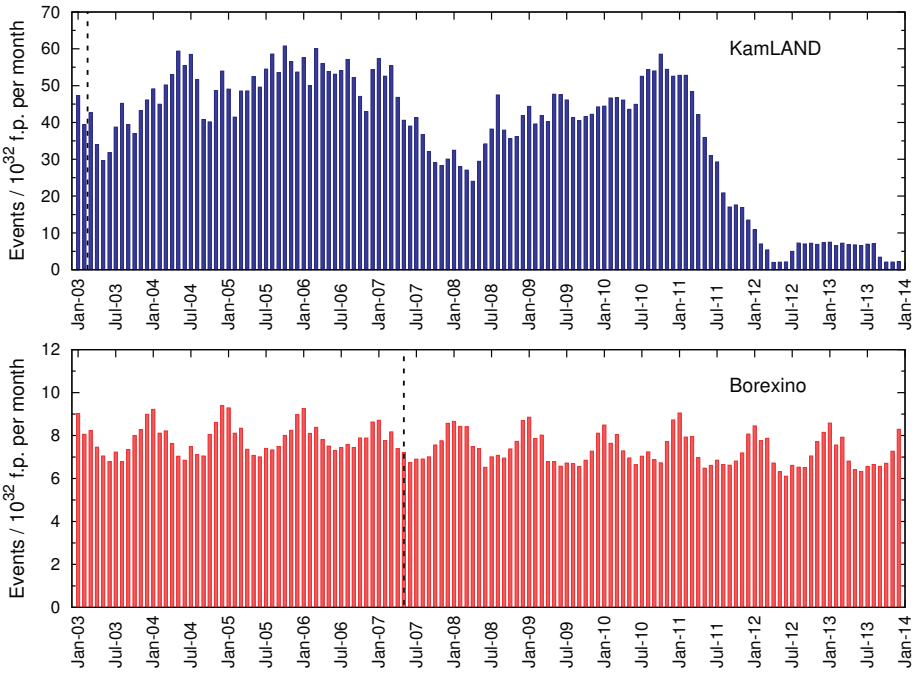

Figure 1.3: Reactor signals in the FER for the KL experiment (blue panel) and for the BX experiment (red panel), calculated from January 2003 to December 2013 on a monthly timeline. The vertical dashed lines indicate the data taking start of the experiments (March 2003 for KL and May 2007 for BX).

lower. In Agostini et al. 2015 the antineutrino event analysis on a 2056 days data taking period shows a good agreeement with this prediction, although the seasonal variation has been not studied. The KL signal time profile is instead highly affected by the operating conditions of the Japanese reactors. The shutdown of nuclear power plants concomitant to strong earthquakes in Japan is therefore manifestly visible as a pronounced decrease in the evaluated reactor signal. In particular, there is clear evidence of the protected shutdown of the Kashiwazaki-Kariwa and Hamaoka nuclear power plants subsequent to the Chuetsu earthquake in July 2007 and of the protected shutdown of the entire Japanese nuclear reactor industry following the Fukushima nuclear accident in March 2011.

The different signal time profiles for the two experiments reflect also in different reactor antineutrino spectra (see Fig. 1.4). As understood from the contribution on the signal uncertainty given by the reactor thermal power and fission fraction uncertainties (see Table 1.6), the antineutrino spectrum at BX is relatively insensitive to different operational conditions of individual nuclear power plants, as there are no close-by reactors dominating the antineutrino flux. Conversely, detailed information on the operating status of the near reactors emerges as a fundamental piece of knowledge for modelling the reactor spectrum at KL.

The distribution of the cumulative percentage contribution to the total reactor signal as a function

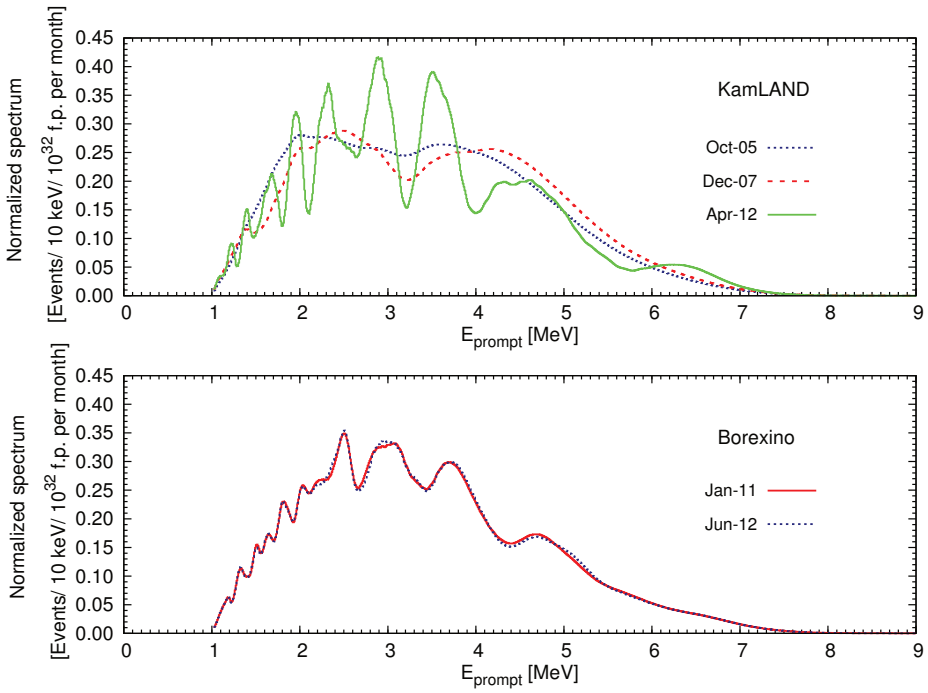

Figure 1.4: Reactor antineutrino spectra above IBD threshold for the KL experiment (upper panel) and for the BX experiment (lower panel) calculated over different data taking periods. KL spectra are evaluated over three peculiar time intervals, corresponding to a maximum, an average and a minimum expected reactor signal (October 2005, December 2007 and April 2012, respectively). BX spectra are calculated in correspondence to a winter and a summer seasonal signal variation (January 2011, June 2012). All the spectra are normalized to the signal corresponding to the specific month.

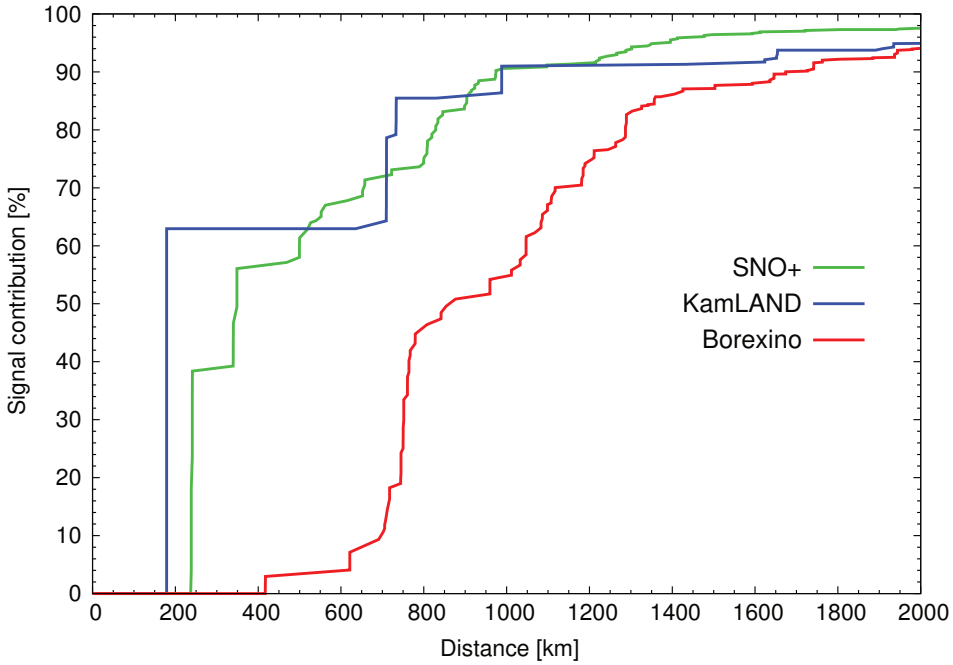

Figure 1.5: Cumulative percentage contribution to the total expected reactor signal as function of the distance of the reactors from the experimental site for KL, BX and SNO+. Data refer to 2013 reactor operational period.

of the distance of the reactors from the experimental site (see Fig. 1.5) yields a hint of the level of criticality associated with the knowledge of the operational parameters of reactors. The KL distance profile has a step-like function shape: the first discontinuity is observed at 180 km where the signals coming from units 3 and 4 of the Ohi nuclear power plant sum up and provide approximately 60% of the total reactor signal. The second and third discontinuities in the KL distribution (85% and 90% of the total signal, respectively) occur for a reactor-detector distance of 730 km (corresponding to the contribution given by all operating Japanese reactors and by the South Korean reactors located on the East coast) and 990 km (summing up the contribution of the Hanbit power plant, located in West South Korea). The BX distance profile is smoother compared to that of KL as the reactor signal is gradually spread out over the European countries. With respect to BX, the closest power station is at a distance of 415 km (Slovenia), which contributes the major fraction of the reactor signal, i.e., approximately 3%. With respect to the SNO+ experiment, the distribution is dominated at short distance by the Canadian Bruce power station, corresponding to the first step in the distance profile at 240 km (38% of the signal). The second step is associated with the Pickering and Darlington power plants and occurs at a site-reactor distance of 350 km (56% of the signal). For a site-reactor distance greater than 500 km the profile levels out due to the contributions given by the more distant power stations located in the United States.

The percentage contributions to the signal given by the relatively close reactors at long baseline experiments (KL, BX and SNO+) and at medium baseline experiments (JUNO and RENO-50) are displayed on a location map (see Fig. 1.6). In addition to the contributions of operating power plants in 2013, nuclear stations under construction are displayed.

1.5 Final remarks

One of the primary goals of the current and proposed reactor neutrino experiments is to investigate the neutrino properties at different wavelengths according to different reactor-detector baselines. While shedding light on the oscillatory neutrino nature, neutrino experiments also provide insight into the Earth's interior via the detection of geoneutrinos. In this framework, nuclear power plants emerge as the most severe background sources as approximately 27% of the reactor event rate is recorded in the geoneutrino energy window. The main results of this work are as follows.

- The expected antineutrino signal from not movable reactors has been evaluated for 14 peculiar locations in the world,estimating its uncertainties in view of reactors operational information yearly published by the Power Reactor Information System (PRIS) of the International Atomic Energy Agency (IAEA). A comprehensive database concering nuclear power plants operational status is published at `www.fe.infn.it/antineutrino` and we plan to update it every year. We evaluated the expected antineutrino signal from reactors and from the Earth for 14 peculiar locations in the world, corresponding to sites hosting experiments that are currently ongoing or entering operation, as well as candidate sites for future neutrino experiments.

- The Monte Carlo method applied for the propagation of (uncorrelated) uncertainties on reactor signals associated with the input quantities provided an overall uncertainty for the long baseline experiments of approximately 3% in the FER and of approximately 4% in the LER, for a fixed analytical expression of the reactor spectrum. The reactor signal uncertainty is dominated by $sin^2(\theta_{12})$, which solely provides an uncertainty of approximately 2.2% in the FER for KL, BX and SNO+.

- A comparison of the reactor signals obtained using different reactor spectra revealed that the uncertainty related to the antineutrino spectrum is as critical as the combined uncertainty of the other input quantities appearing in the signal calculation.

- A focus has been dedicated to the effect of systematic enhancement of the reactor antineutrino spectrum due both to the accumulation of the LLIs during the operation of a reactor and to the storage of the SNFs in the cooling pools. A 2.4% increase of the unoscillated IBD event rate in the LER due to the SNFs has been estimates, which potentially can be a critical systematic uncertainty in geoneutrino measurements.

- RRs, producing a total thermal power of 2.2 GW, contribute less than 0.2% to the commercial reactor signal in the investigated 14 sites.

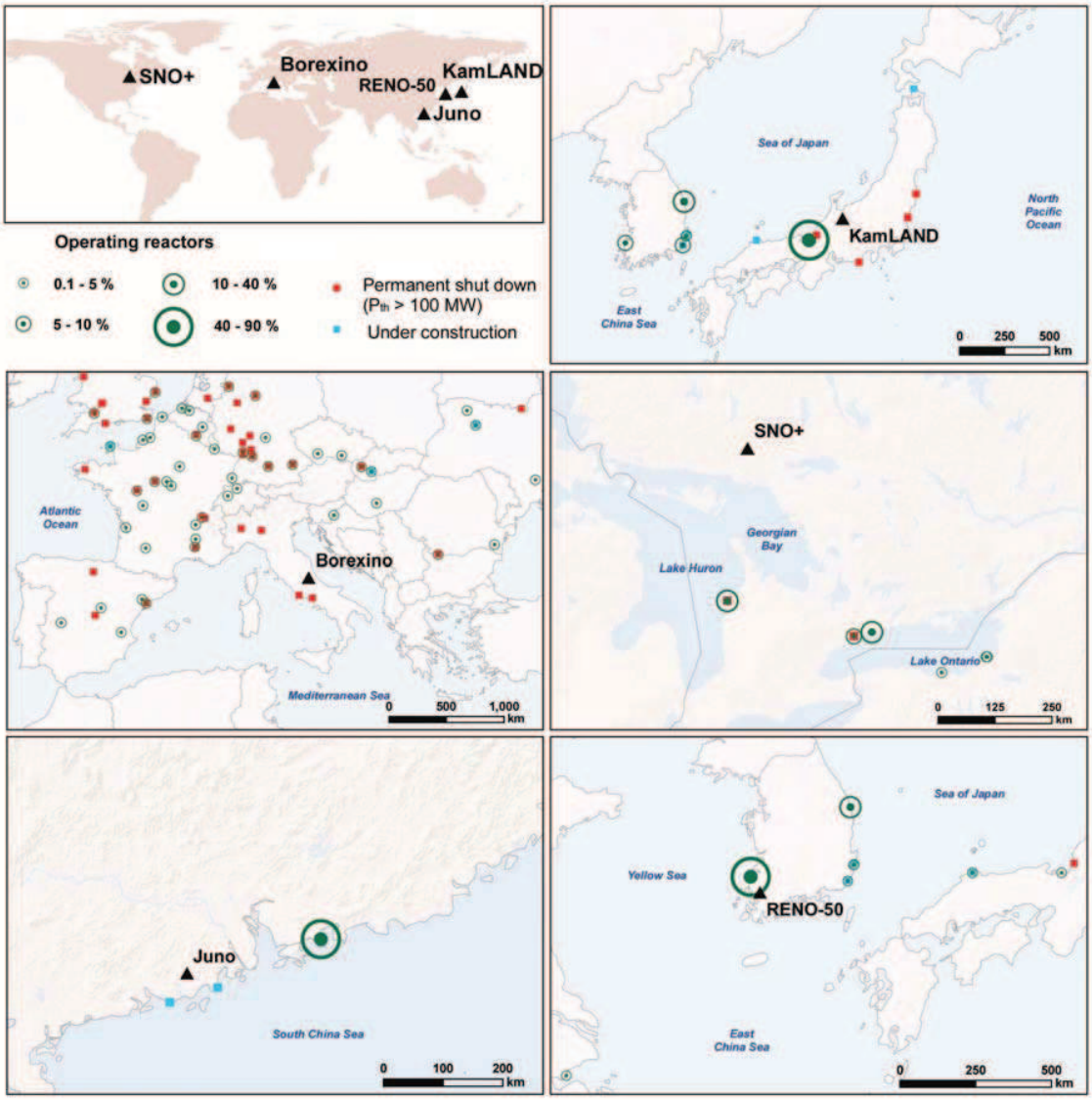

Figure 1.6: Location map of the percentage contributions to the reactor signal given by the close-by reactors for the three long baseline experiments KL, BX and SNO+ and for the medium baseline experiments JUNO and RENO-50. The map is produced with 2013 reactor operational data.

- A multitemporal analysis of the expected reactor signal at BX and KL over a time lapse of 10 years has been performed. With respect to BX, a periodic seasonal signal variation associated with the lower fall-spring electricity demand is recognized: expected reactor signals are relatively insensitive to the operational conditions of single cores, since there are no close-by reactors dominating the antineutrino flux. Conversely, the KL signal time profile is governed by the Japanese nuclear industry operational status, which make the shutdown of nuclear power plants concomitant to strong earthquakes manifestly visible.

The content of this chapter is based on the following publication:

Baldoncini M., Callegari I., Fiorentini G., Mantovani F., Ricci B., Strati V. and Xhixha G. "*Reference Worldwide Model for Antineutrinos from Reactors.*" Physical Review D 91, no. 6 (2015): 065002. doi:10.1103/PhysRevD.91.065002.

Bibliography

Abazajian, K. N. et al. (2012). "Light Sterile Neutrinos: A White Paper". *arXiv:1204.5379*.

Abe, S. et al. (2008). "Precision Measurement of Neutrino Oscillation Parameters with KamLAND". *Physical Review Letters* 100.22, p. 221803. DOI: 10.1103/PhysRevLett.100.221803.

Abe, Y. et al. (2012). *Physical Review Letters* 108.13, p. 131801. DOI: 10.1103/PhysRevLett.108.131801.

Agostini, M. et al. (2015). "Spectroscopy of geoneutrinos from 2056 days of Borexino data". *Physical Review D* 92.3, p. 031101. DOI: 10.1103/PhysRevD.92.031101.

Ahmad, Q. R. et al. (2001). *Physical Review Letters* 87.7, p. 071301. DOI: 10.1103/PhysRevLett.87.071301.

Ahn, J. K. et al. (2012). "Observation of Reactor Electron Antineutrinos Disappearance in the RENO Experiment". *Physical Review Letters* 108.19, p. 191802. DOI: 10.1103/PhysRevLett.108.191802.

An, F. P. et al. (2013). "Improved measurement of electron antineutrino disappearance at Daya Bay". *Chinese Physics C* 37.1, p. 011001. ISSN: 1674-1137. DOI: 10.1088/1674-1137/37/1/011001.

An, Fengpeng et al. (2016). "Neutrino physics with JUNO". *Journal of Physics G: Nuclear and Particle Physics* 43.3, p. 030401.

Araki, T. et al. (2005a). "Experimental investigation of geologically produced antineutrinos with KamLAND". *Nature* 436.7050, pp. 499–503. ISSN: 0028-0836. DOI: 10.1038/nature03980.

Araki, T. et al. (2005b). "Measurement of Neutrino Oscillation with KamLAND: Evidence of Spectral Distortion". *Physical Review Letters* 94.8, p. 081801. DOI: 10.1103/PhysRevLett.94.081801.

Bellini, G. et al. (2013). "Measurement of geo-neutrinos from 1353 days of Borexino". *Physics Letters B* 722.4–5, pp. 295–300. ISSN: 0370-2693. DOI: 10.1016/j.physletb.2013.04.030.

Bellini, G. et al. (2010). "Observation of geo-neutrinos". *Physics Letters B* 687.4, pp. 299–304. ISSN: 0370-2693. DOI: 10.1016/j.physletb.2010.03.051.

Bemporad, C. et al. (2002). "Reactor based Neutrino Oscillation Experiments". *Reviews of Modern Physics* 74.2, pp. 297–328. ISSN: 0034-6861, 1539-0756. DOI: 10.1103/RevModPhys.74.297.

Bin, Zhou et al. (2012). "A study of antineutrino spectra from spent nuclear fuel at Daya Bay". *Chinese Physics C* 36.1, p. 1. ISSN: 1674-1137. DOI: 10.1088/1674-1137/36/1/001.

Capozzi, F. et al. (2014a). "Neutrino mass hierarchy and electron neutrino oscillation parameters with one hundred thousand reactor events". *Physical Review D* 89.1, p. 013001. DOI: 10.1103/PhysRevD.89.013001.

Capozzi, F. et al. (2014b). "Status of three-neutrino oscillation parameters, circa 2013". *Physical Review D* 89.9, p. 093018. DOI: 10.1103/PhysRevD.89.093018.

Cicenas, Blake and Nickolas Solomey (2012). "The Hanohano Detector and Ongoing Research and Development". *Physics Procedia* 37, pp. 1324–1331. ISSN: 1875-3892. DOI: http://dx.doi.org/10.1016/j.phpro.2012.02.470.

Ciuffoli, Emilio et al. (2014). "Advantages of multiple detectors for the neutrino mass hierarchy determination at reactor experiments". *Physical Review D* 89.7, p. 073006. DOI: 10.1103/PhysRevD.89.073006.

Cowan, C. L. et al. (1956). "Detection of the free neutrino: A Confirmation". *Science* 124, pp. 103–104. DOI: 10.1126/science.124.3212.103.

Cristoph, E. et al. (1997). *Canada Enters the Nuclear Age: A Technical History of Atomic Energy of Canada Limited*. McGill-Queen's Press. ISBN: 9780773516014.

Danby, G. et al. (1962). "Observation of High-Energy Neutrino Reactions and the Existence of Two Kinds of Neutrinos". *Physical Review Letters* 9.1, pp. 36–44. DOI: 10.1103/PhysRevLett.9.36.

Detwiler, J. et al. (2002). "Nuclear Propelled Vessels and Neutrino Oscillation Experiments". *Physical Review Letters* 89.19, p. 191802. DOI: 10.1103/PhysRevLett.89.191802.

Djurcic, Z. et al. (2009). "Uncertainties in the anti-neutrino production at nuclear reactors". *Journal of Physics G: Nuclear and Particle Physics* 36.4, p. 045002. ISSN: 0954-3899. DOI: 10.1088/0954-3899/36/4/045002.

Domogatsky, G. V. et al. (2005). "Neutrino geophysics at Baksan I: Possible detection of georeactor antineutrinos". *Physics of Atomic Nuclei* 68.1, pp. 69–72. ISSN: 1063-7788, 1562-692X. DOI: 10.1134/1.1858559.

Dziewonski, A. M. and D. L. Anderson (1981). "Preliminary reference earth model". *Phys. Earth Planet. Interiors* 25, pp. 297–356.

Eguchi, K. et al. (2003). "First Results from KamLAND: Evidence for Reactor Antineutrino Disappearance". *Physical Review Letters* 90.2, p. 021802. DOI: 10.1103/PhysRevLett.90.021802.

Feilitzsch, F. von et al. (1982). "Experimental beta-spectra from 239Pu and 235U thermal neutron fission products and their correlated antineutrino spectra". *Physics Letters B* 118.1–3, pp. 162–166. ISSN: 0370-2693. DOI: 10.1016/0370-2693(82)90622-0.

Fiorentini, G. et al. (2007). "Geo-neutrinos and earth's interior". *Physics Reports* 453.5–6, pp. 117–172. ISSN: 0370-1573. DOI: 10.1016/j.physrep.2007.09.001.

Fiorentini, Gianni et al. (2010). "Nuclear physics for geo-neutrino studies". *Physical Review C* 81.3, p. 034602. DOI: 10.1103/PhysRevC.81.034602.

Fiorentini, G. et al. (2012). "Mantle geoneutrinos in KamLAND and Borexino". *Physical Review D* 86.3. ISSN: 1550-7998, 1550-2368. DOI: 10.1103/PhysRevD.86.033004.

Gando, A. et al. (2011). "Constraints on θ_{13} from a three-flavor oscillation analysis of reactor antineutrinos at KamLAND". *Physical Review D* 83.5, p. 052002. DOI: 10.1103/PhysRevD.83.052002.

Gando, A. et al. (2013). "Reactor on-off antineutrino measurement with KamLAND". *Physical Review D* 88.3, p. 033001. DOI: 10.1103/PhysRevD.88.033001.

Groom, D.E. et al. (2000). "Review of Particle Physics". *Eur. Phys. J. C, 15(1-4)*, pp. 1–878.

Haag, N. et al. (2014). "Experimental Determination of the Antineutrino Spectrum of the Fission Products of U238". *Physical Review Letters* 112.12, p. 122501. DOI: 10.1103/PhysRevLett.112.122501.

Hahn, A. A. et al. (1989). "Antineutrino spectra from 241Pu and 239Pu thermal neutron fission products". *Physics Letters B* 218.3, pp. 365–368. ISSN: 0370-2693. DOI: 10.1016/0370-2693(89)91598-0.

Hirdaris, S. E. et al. (2014). "Considerations on the potential use of Nuclear Small Modular Reactor (SMR) technology for merchant marine propulsion". *Ocean Engineering* 79, pp. 101–130. ISSN: 0029-8018. DOI: 10.1016/j.oceaneng.2013.10.015.

Huang, Yu et al. (2013). "A reference Earth model for the heat-producing elements and associated geoneutrino flux". *Geochemistry, Geophysics, Geosystems* 14.6, pp. 2003–2029. ISSN: 1525-2027. DOI: 10.1002/ggge.20129.

Huber, Patrick (2011). "Determination of antineutrino spectra from nuclear reactors". *Physical Review C* 84.2, p. 024617. DOI: 10.1103/PhysRevC.84.024617.

Huber, Patrick and Thomas Schwetz (2004). "Precision spectroscopy with reactor anti-neutrinos". *Phys.Rev.* D70, p. 053011. DOI: 10.1103/PhysRevD.70.053011,10.1103/PhysRevD.70.053011.

International Earth Rotation and Reference Systems Service (IERS) (2003). *IERS Technical Note No. 32*.

J. Mandula, Nuclear Power Engeneering Section, International Atomic Energy Agency (2014). "Operating Experience with Nuclear Power Stations in Member States in 2013-2014 Edition". *IAEA-PRIS database, IAEA-STI/PUB/1671*.

Jocher, Glenn R. et al. (2013). *Physics Reports* 527.3, pp. 131–204. ISSN: 0370-1573. DOI: 10.1016/j.physrep.2013.01.005.

Joint Committee for Guides in Metrology (2008). "JCGM 101: Evaluation of Measurement Data - Supplement 1 to the "Guide to the Expression of Uncertainty in Measurement" - Propagation of Distributions Using a Monte Carlo Method". *JCGM 101*.

Kim, S. B. (2013). *Proposal for RENO-50: Detector Design and Goals, International Workshop on RENO-50*.

Kodama, K. et al. (2001). "Observation of tau neutrino interactions". *Physics Letters B* 504.3, pp. 218–224. ISSN: 0370-2693. DOI: 10.1016/S0370-2693(01)00307-0.

Kopeikin, V. I. et al. (2004). "Reactor as a source of antineutrinos: Thermal fission energy". *Physics of Atomic Nuclei* 67.10, pp. 1892–1899. ISSN: 1063-7788, 1562-692X. DOI: 10.1134/1.1811196.

Kopeikin, V. I. (2012). "Flux and spectrum of reactor antineutrinos". *Physics of Atomic Nuclei* 75.2, pp. 143–152. ISSN: 1063-7788, 1562-692X. DOI: 10.1134/S1063778812020123.

Lasserre, Thierry et al. (2010). "SNIF: A Futuristic Neutrino Probe for Undeclared Nuclear Fission Reactors". *arXiv:1011.3850*.

Ma, X. B. et al. (2013). "Improved calculation of the energy release in neutron-induced fission". *Physical Review C* 88.1, p. 014605. DOI: 10.1103/PhysRevC.88.014605.

Maneira, José et al. (2013). "The SNO+ experiment: status and overview". *Journal of Physics: Conference Series* 447.1, p. 012065. ISSN: 1742-6596. DOI: 10.1088/1742-6596/447/1/012065.

Mention, G. et al. (2011). "Reactor antineutrino anomaly". *Physical Review D* 83.7, p. 073006. DOI: 10.1103/PhysRevD.83.073006.

Mueller, Th. A. et al. (2011). "Improved predictions of reactor antineutrino spectra". *Physical Review C* 83.5, p. 054615. DOI: 10.1103/PhysRevC.83.054615.

Nonbøl, E. (1996). "Description of the advanced gas cooled type of reactor (AGR)". NKS-RAK-2(96)TR-C2.

Podvig, Pavel (2011). "History of Highly Enriched Uranium Production in Russia". *Science & Global Security* 19.1, pp. 46–67. ISSN: 0892-9882.

Rouben, B. (1999). "CANDU Fuel-Management Course". *Atomic Energy of Canada Ltd.*

Schreckenbach, K. et al. (1985). "Determination of the antineutrino spectrum from 235U thermal neutron fission products up to 9.5 MeV". *Physics Letters B* 160.4–5, pp. 325–330. ISSN: 0370-2693. DOI: 10.1016/0370-2693(85)91337-1.

Šrámek, Ondřej et al. (2013). "Geophysical and geochemical constraints on geoneutrino fluxes from Earth's mantle". *Earth and Planetary Science Letters* 361, pp. 356–366. ISSN: 0012-821X. DOI: 10.1016/j.epsl.2012.11.001.

Strumia, Alessandro and Francesco Vissani (2003). "Precise quasielastic neutrino/nucleon cross-section". *Physics Letters B* 564.1–2, pp. 42–54. ISSN: 0370-2693. DOI: 10.1016/S0370-2693(03)00616-6.

Tolich, N. et al. (2006). "A Geoneutrino Experiment at Homestake". *Earth, Moon, and Planets* 99.1-4, pp. 229–240. ISSN: 0167-9295, 1573-0794. DOI: 10.1007/s11038-006-9112-8.

Vogel, P. and J. Engel (1989). "Neutrino electromagnetic form factors". *Physical Review D* 39.11, pp. 3378–3383. DOI: 10.1103/PhysRevD.39.3378.

Wurm, Michael et al. (2012). "The next-generation liquid-scintillator neutrino observatory LENA". *Astroparticle Physics* 35.11, pp. 685–732. ISSN: 0927-6505. DOI: 10.1016/j.astropartphys.2012.02.011.

Chapter 2

Predicting the reactor antineutrino and geoneutrino signals at SNO+

SNO+ is a multipurpose kiloton-scale liquid scintillation detector located at 2 km underground at SNOLAB, in the hearth of the Vale's Creighton mine close to Sudbury (Canada) (Andringa et al. 2015). It has been designed as a follow up of the precursor heavy water Sudbury Neutrino Observatory experiment, with the main goal of searching for the ^{130}Te neutrinoless double-beta decay, which is currently one of the most lively research fields in the low-energy neutrino sector. The observation of such a decay would reveal the Majorana nature of neutrinos and the measurement of the decay half-life would allow to estimate the effective Majorana neutrino mass, reaching a sensitivity lower than 70 meV in 5 years of data taking for a 2340 kg mass of natural tellurium loaded in the scintillator (Lozza 2016).

Thanks to the relatively large volume, the high radio purity and the $\sim$ 6 km of water equivalent rock shielding, SNO+ can afford a variety of physics goals, including the observation of electron antineutrinos produced by the Earth and by nuclear reactors via the Inverse Beta Decay (IBD) reaction (Chen 2006). Indeed, the SNO+ detector is foreseen to observe almost in equal proportion electron antineutrinos produced by U and Th in the Earth and by nuclear reactors and will be the first long baseline experiment to measure a reactor signal dominated by CANDU cores ($\sim$55% of the total reactor signal). Approximately 18% of the total geoneutrino signal is generated by the U and Th present in the rocks of the Huronian Supergroup-Sudbury Basin (HS-SB) (Huang et al. 2014). The 60% uncertainty on the signal produced by this lithologic unit plays a crucial role on the discrimination power on the mantle signal as well as on the geoneutrino spectral shape reconstruction, which can in principle provide a direct measurement of the Th/U ratio in the Earth.

The primary aim of this work is predicting the expected geoneutrino and reactor signals at SNO+ on the basis of existing reference Earth and reactor models. In this study I performed the reactor signal and spectra calculation, dedicating a special focus to the investigation of the signal and spectra variability associated with the temporal evolution of the reactor fissile inventory. I took part in the

discussions arisen from the interpretation of the geo and reactor antineutrino signal predictions and in particular of the degree and type of uncertainties that affect them, with the purpose of highlighting crucial points that need further investigation for future refinements.

This study made evident the need for a detailed geochemical characterization of the HS-SB in the light of improving the prediction of the local crust contribution to the geoneutrino signal. Moreover, the HS-SB signal profile as function of the distance from the detector location allowed to identify the areal scale of a new higher resolution regional model. Since ∼90% of the HS-SB signal comes from a radius of 25 km around the experimental site, the effort of improving the characterization of the geophysical and geochemical reservoirs has been concentrated in the region called CLose Crust (CLC), extending for 50 km × 50 km and centered at the SNO+ location. In this context, a systematic sampling of the main lithologies present in the CLC and in particular of the formations comprising the HS-SB reservoir has been performed. I took care of the laboratory gamma-ray spectroscopy measurements on the collected rock samples and I performed the study of the U and Th abundances in order to define the statistical distributions describing the geochemical attributes of the HS-SB reservoir. The refinement of the geochemical and geophysical model in the CLC is the object of a novel study which is going to be submitted to *Geochemistry, Geophysics, Geosystems*.

2.1 Background

Designed as a retrofit of the former Sudbury Neutrino Observatory (SNO) at SNOLAB, SNO+ is a large-scale liquid scintillation experiment aimed at performing low energy neutrino physics measurements, with the primary goal of investigating the Majorana nature of neutrinos (Andringa et al. 2015). The SNO+ detector is located inside a cavity excavated in the rock and consists of a 6 m radius spherical acrylic vessel which will be filled with ∼780 tonnes of ultra pure liquid scintillator, composed as a mixture of a linear alkylbenzene solvent and a 2 g/L of 2.5-diphenyloxazole (PPO) fluor. Scintillation light will be measured by around 9300 8-inch PMTs, anchored to a 8.9 m radius stainless steel structure. Both the cavity and the interstitial volumes will be filled with ultra pure water with the aim of shielding the inner detector from the radioactivity coming from the PMT array and the surrounding rock. As the liquid scintillator density (ρ = 0.86 g/cm^3 at 1°C) is lower than that of the water, a hold-down rope system is needed to keep the vessel fixed in its position.

Prior the deployment of natural tellurium for the search of $0\nu\beta\beta$ decay of ^{130}Te, the SNO+ data taking will be characterized by an initial water phase followed by a pure scintillation phase which will be dedicated to the assessment of the detector performances and to the calibration of the different detector components as well as to the exploration of secondary physics goals. The pure scintillation phase in particular will be devoted to the measurement of low energy solar neutrinos along with geo and reactor antineutrinos, which are the topics of this study.

Geoneutrinos produced in beta minus decays along the ^{238}U and ^{232}Th decay chains provide an exceptional insight into the Earth's interior, allowing for the determination of the heat-producing element abundances and hence of the total radiogenic heat power of the planet. The SNO+ detector

is located in the Superior Province (Ontario, Canada), one of the Earth's largest Archean's cratons, characterized by a thick ($\sim$ 42 km) continental crust, which gives rise to a sizable geoneutrino crustal signal rate (Huang et al. 2014). In this framework, nuclear reactors are the most severe source of background as there is a significant overlap between the reactor antineutrino energy spectrum and the geoneutrino one at low energies. The Bruce, Pickering and Darlington power stations host globally 18 operating cores for a total thermal power of approximately 43 GW (Baldoncini et al. 2015).

2.2 Reactor antineutrinos

The necessary pieces of information for evaluating the reactor signal and spectra cover three major data classes: (1) reactor physics (i.e. reactor thermal power, load factors and fission fractions), (2) nuclear physics (i.e. energy released per fission and individual fissile elements antineutrino spectra) and (3) antineutrino physics (i.e. antineutrino survival probability and IBD cross section). For modeling the production, propagation and detection of the reactor antineutrinos the adopted inputs are the ones described in Baldoncini et al. 2015, with the reactor database referred to the 2014 operational status, available at `www.fe.infn.it/antineutrino`.

In the reactor signal and spectra it is possible to identify a near component, corresponding to the contribution originating from the 8 CANDU cores of the Canadian Bruce power station, and a far component, generated by all the other 431 cores operating in the world.

CANDU reactors use heavy water as both coolant and neutron moderator material and, considering that heavy water has a lower neutron capture cross section compared to ordinary water, they can burn natural uranium since there is enough ^{235}U to sustain the criticality of the fission processes. Although the cost of heavy water is significantly higher than that of ordinary water, the pressurized heavy water reactor technology allows the core to operate without the employment of expensive fuel enrichment facilities. Moreover, in CANDU reactors most of the moderator is at lower temperatures than in other designs, reducing the spread of speeds and the overall speed of the moderator particles. As a consequence, most of the neutrons will reach lower energies increasing the probability of inducing fission processes, meaning that CANDU reactors not only burns natural uranium as fuel, but they do it more effectively. However, the reduced energy content of natural uranium as compared to enriched uranium necessitates more frequent replacement of fuel, which is generally accomplished by using an on-power refueling system.

The CANDU fission fractions f_i (with $i =^{235}$U, ^{239}Pu, ^{241}Pu and ^{238}U) have been determined on the base of the number of neutrons produced by the $i-th$ fissile isotope for a typical CANDU reactor (Table II.3 of (Bain et al. 1997)) and of the average number of neutrons produced in one fission of the $i-th$ isotope (Nichols et al. 2008). Applying the relation between fission fractions f_i and power fractions p_i (see e.g. Eq. 5 of (Baldoncini et al. 2015)) the resulting set of power fractions for a CANDU reactor is:

$$^{235}\text{U}:^{239}\text{Pu}:^{241}\text{Pu}:^{238}\text{U} = 0.543 : 0.411 : 0.022 : 0.024 \tag{2.1}$$

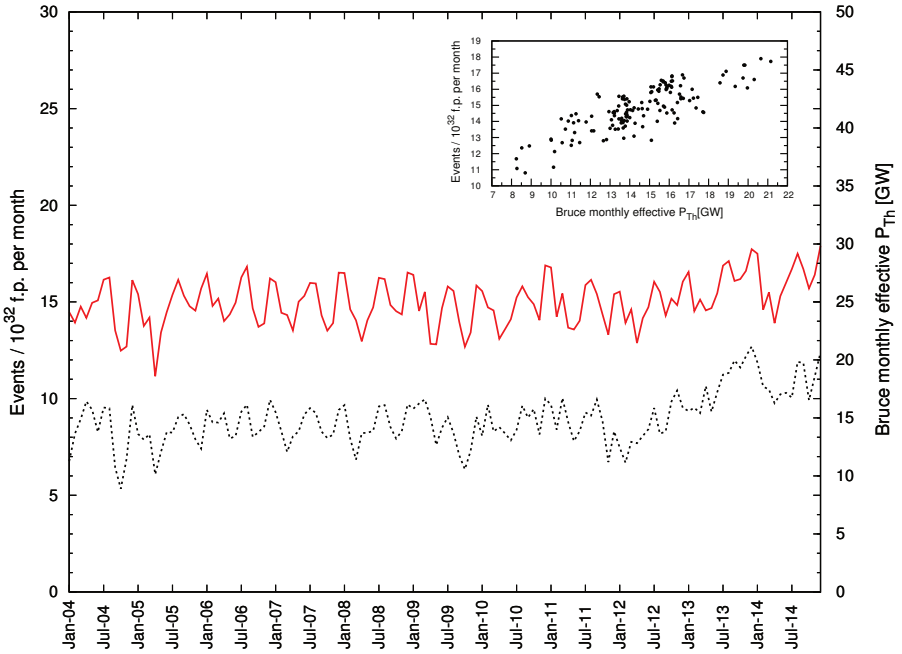

Figure 2.1: SNO+ reactor signal and Bruce power station's effective thermal power. The SNO+ signal in the FER (red solid line, left y axis) and the Bruce power station's effective thermal power (black dashed line, right y axis) are reported on a monthly time scale from January 2004 to December 2014. In the top-right box a scatter plot of the total reactor signal in the FER and the Bruce power station's effective thermal power is shown.

The investigated sources of uncertainties are the reactor thermal powers and fission fractions, the energy released per fission, the IBD cross section and the electron antineutrino survival probability (in terms of uncertainties on the oscillation parameters) from which an overall signal uncertainty has been estimated by following the Monte Carlo based approach of Baldoncini et al. 2015. The reactor signal is evaluated in Terrestrial Neutrino Units (TNU), corresponding to one IBD event per 10^{32} free protons per year.

In Table 2.3 the two components of the rector signal are given separately for the Low Energy Region (LER, 1.806 MeV – 3.272 MeV) and the Full Energy Region (FER, 1.806 MeV – 10.000 MeV), where the central values correspond to the medians and the errors are expressed as 1σ . It emerges that approximately 38% of the reactor signal in the FER at SNO+ is generated by the Bruce power station, which has a total thermal power of approximately 22 GW. As a consequence, the temporal profile of the signal at SNO+ resembles the temporal profile of the Bruce power station's effective thermal power, which is the sum of the 8 cores thermal powers, each one weighted by the corresponding monthly load factor. In Fig. 2.1 the SNO+ reactor signal in the FER and the Bruce power station's effective thermal power are reported on a monthly time scale, from January 2004 to December 2014. In

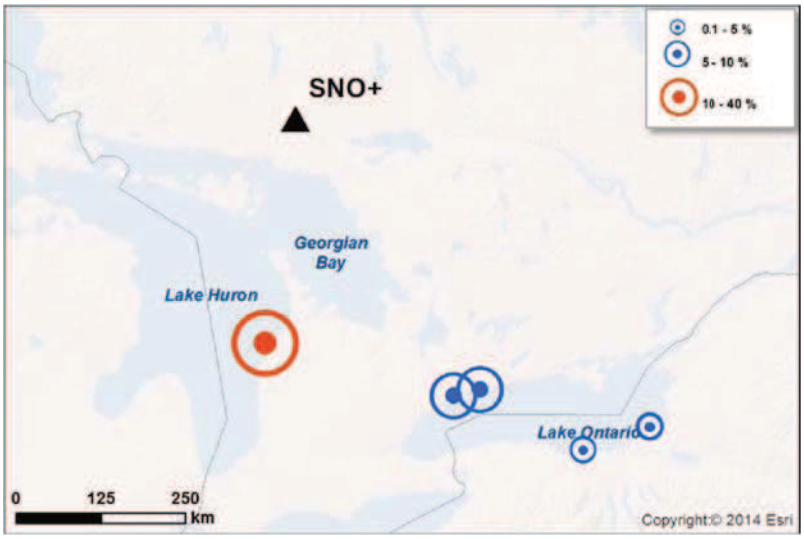

Figure 2.2: Location map of the percentage contributions to the reactor signal generated by the Canadian Bruce, Pickering and Darlington power stations at the SNO+ detector site.

these 10 years the average total reactor antineutrino signal in the FER is (14.8 ± 1.4) events per 10^{32} free protons per month, where the uncertainty corresponds to the standard deviation of the monthly signal values. According to Andringa et al. 2015, the signal fluctuations are expected to be reduced in the next future due to upgrades in the management of the turning off schedule of Canadian reactors. In the top-right box of Fig. 2.1 a scatter plot of the total reactor signal in the FER versus the Bruce power station's effective thermal power is also shown.

The 18 operating CANDU reactors belonging to the Bruce, Pickering and Darlington power stations, which are respectively 240 km, 340 km and 350 km far from the SNO+ site (Fig. 2.2), generate approximately 55% of the total reactor signal in the LER at SNO+. As a consequence the extrapolation of the geoneutrino spectrum, which critically provides information on the average Th/U ratio, can be affected by the reconstruction of the CANDU spectral shape. The general equation describing the reactor antineutrino spectrum generated by a single core operating with an average load factor $\langle LF(t) \rangle$ during the acquisition time t can be written as:

$$\frac{dS(E_{\bar{\nu}_e}, t)}{dE_{\bar{\nu}_e}} = \varepsilon N_p t \frac{P_{th}}{4\pi L^2} \langle LF(t) \rangle \sum_{k=1}^{4} \frac{\langle p_k(t) \rangle}{Q_k} \langle \lambda_k(E_{\bar{\nu}_e}, t) \rangle P_{ee}(E_{\bar{\nu}_e}, L) \sigma_{IBD}(E_{\bar{\nu}_e}) \tag{2.2}$$

where ε is the detector efficiency, N_p is the number of free target protons for the IBD reaction, P_{th} is the reactor nominal thermal power, L is the reactor-detector distance, $\langle p_k(t) \rangle$ and $\langle \lambda_k(E_{\bar{\nu}_e}, t) \rangle$ are the average power fraction and average individual antineutrino spectrum for the $k-th$ fissile isostope over the exposure time t, Q_k is the energy relase in one fission of the $k-th$ isotope, P_{ee} is the antineutrino survival probaility and σ_{IBD} the IBD cross section.

The crucial points for understanding the temporal evolution of the reactor antineutrino spectrum at a given site are related to the modeling of the time dependent quantities appearing in Eq. 2.2, i.e. the average over the time period t of the individual antineutrino spectra of the four fissile isotopes

Table 2.1: Relative contributions p_k of the fissile isotopes ^{235}U, ^{238}U, ^{239}Pu, and ^{241}Pu to the thermal power over a standard operating period of a PWR reactor.

	p_{235}	p_{239}	p_{241}	p_{238}
Beginning of the operating cycle	0.64	0.25	0.04	0.07
Middle of the operating cycle	0.55	0.32	0.06	0.07
End of the operating cycle	0.47	0.38	0.08	0.07

$\langle \lambda_k(E_{\bar{\nu}_e}, t) \rangle [\bar{\nu}_e/\text{MeV/fission}]$ and of the contribution that each one of the fissile isotopes provides to the total thermal power $\langle p_k(t) \rangle$. During a reactor burning cycle, even with the reactor operated with a constant load factor, the fuel composition and hence the power fractions of the four fissile isotopes change by several tens of percent as plutonium isotopes are bred and uranium is consumed. Indeed, assuming to switch on a core for the first time, in principle there is a null contribution to fissions from plutonium isotopes as ^{239}Pu and ^{241}Pu are produced respectively by neutron capture on ^{238}U and on ^{240}Pu:

$$
\begin{aligned}
{}^{238}_{92}U + n \longrightarrow {}^{239}_{92}U \longrightarrow^{\beta^-} {}^{239}_{93}Np \longrightarrow^{\beta^-} {}^{239}_{94}Pu \\
{}^{239}_{94}Pu + n \longrightarrow {}^{240}_{94}Pu + n \longrightarrow {}^{241}_{94}Pu
\end{aligned}
$$

Each isotope produces a unique antineutrino spectrum through the decay of its fission fragments and their daughters, meaning also that the average number of detectable antineutrinos produced per fission is different among the plutonium and uranium isotopes. According to the Mueller et al. 2011 parametrization of the antineutrino spectra, the average number of antineutrinos produced above the IBD threshold are:

$$^{235}\text{U}:^{239}\text{Pu}:^{241}\text{Pu}:^{238}\text{U} = 1.96 : 1.52 : 1.88 : 2.53$$

Hence, as the core evolves and the relative mass fractions and fission rates of uranium and plutonium isotopes vary, the number of detected antineutrinos will also change resulting in the so called burnup effect, which has been observed consistently in several neutrino physics experiments (Bemporad et al. 2002; Bowden et al. 2009). In principle there are also time dependent off-equilibrium corrections to the individual antineutrino spectra $\lambda_k(E_{\bar{\nu}_e})$ which are related both the accumulation of long lived isotopes during the running of the reactor and to the storage of spent nuclear fuels in water pools close to the reactor site (Baldoncini et al. 2015).

As illustrative example, Fig. 2.3 shows different scenarios for the reactor antineutrino spectrum generated by the sole Bruce power station at SNO+ where the detector efficiency ε, the number of free target protons N_p and the acquisition time t are taken respectively equal to 1, 10^{32} and 1 year (in order to obtain as integrated spectrum a signal in TNU).

In Fig. 2.3 the adopted value for the effective thermal power of each one of the 8 cores is 2.3

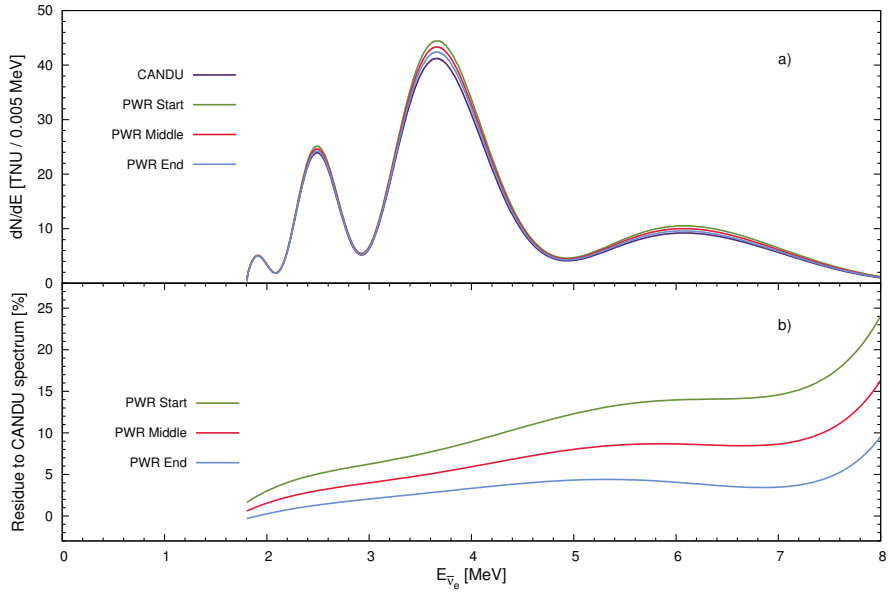

Figure 2.3: Panel a) shows the spectrum at SNO+ generated by the sole Bruce power station modeled using as individual antineutrino spectral shapes $\lambda_k(E_{\bar{\nu}_e})$ the one provided by Mueller et al. 2011 and as power fractions the one referred to CANDU reactors (violet line) (see Eq. 2.1) and the ones referred to PWR reactors at the start (green line), middle (red line) and end (blue line) of the operating cycle (see Table 2.1. Panel b) shows the percentage difference over the entire energy range between the three spectral shapes for PWR reactors at the start (green line), middle (red line) and end (blue line) of the operating cycle and the CANDU spectral shape.

GW, obtained from a 2.7 average nominal thermal power and a 85% annual load factor. The upper panel illustrates the Bruce reactor antineutrino spectra obtained by adopting a fixed parametrization of the individual reactor spectral shapes $\lambda_k(E_{\bar{\nu}_e})$ (Mueller et al. 2011) and four different sets of power fractions corresponding to a CANDU reactor that reached equilibrium (Eq. 2.1) and to a PWR reactor at the beginning, middle and end of the operating cycle (Table 2.1), which have been inferred from the fission fractions published by Kopeikin 2012. The lower panel shows the percentage difference between respectively the PWR spectrum referred to the beginning, middle and end of the operating cycle and the CANDU spectrum. As expected, the major discrepancy between the PWR and the CANDU spectral shape is observed for the PWR at the beginning of the operating cycle, as the ^{239}Pu reactor component is the lowest one compared to the other PWR reactor life stages.

Table 2.2 reports the calculated signals in the LER and in the FER in TNU for the Bruce power station assuming the above mentioned parameters for the construction of the spectral shapes. This theoretical exercise highlights that a poor knowledge of the power fractions (and their temporal evolution) can affect the estimation of the signal in the LER and in the FER up to 5% and 10% respectively.

Fig. 2.4 shows the near and far components of the reactor antinuetrino spectrum at SNO+,

Table 2.2: Reactor signal at SNO+ generated by the Bruce power station obtained by assuming the 8 cores working with typical CANDU power fractions and with PWR power fractions referred to the beginning, middle and end of the operating cycle.

Bruce reactor spectrum	LER [TNU]	FER [TNU]
CANDU	17.3	73.4
PWR at beginning of the operating cycle	18.2	80.2
PWR at middle of the operating cycle	17.8	77.7
PWR at end of the operating cycle	17.5	75.6

together with the geoneutrino spectra. The shape of the reactor spectrum produced by the Bruce power station has typical long baseline oscillation structures, modulated in frequency and amplitude by δm^2 and $\sin^2\theta_{12}$, respectively. The more muted oscillation structure of the spectrum produced by the rest of the reactors is a consequence of the averaging of the contributions of the residual cores globally distributed and reflects a wide range of reactor baselines and antineutrino luminosities.

2.3 Geoneutrinos

The prediction of the geoneutrino signal at SNO+ is based on the modeling of the distribution and amount of U and Th in the Earth's reservoirs. The continental crust, despite accounting for approximately 0.5% of the Earth's mass, is the main reservoir of U and Th and generates 75% of the total geoneutrino signal expected at SNO+ (Huang et al. 2013). For this reason a deep understanding of the continental crust, in particular the region immediately surrounding the detector, is mandatory to evaluate the geoneutrino signal and its uncertainties. These studies can be performed both via 3D geochemical and geophysical crustal models (Huang et al. 2014) and via heat balance models based on the combination of the Moho heat flux and of the crustal heat production (Phaneuf and Mareschal 2014).

The local crust of SNO+, i.e. six 2°×2° tiles centered at the detector location ($\sim$ 440 km $\times$ 460 km), is modeled in Huang et al. 2014 and is based on integrating regional geological, geophysical, and geochemical data. The geoneutrino signal from the local crust is predicted to be $15.6^{+5.3}_{-3.4}$ TNU. Fig. 2.4 shows the geoneutrino spectrum subdivided into two components, generated by the U and Th in the local crust and in the rest of the Earth. The antineutrino survival probability has been calculated by adopting the oscillation parameters reported in Huang et al. 2014. Table 2.3 reports a summary of the four main geoneutrino signal components at SNO+, corresponding to the local crust, rest of the crust, continental litospheric mantle and mantle contributions.

A detailed analysis of the geoneutrino signal contribution from the different lithologic units of the local crust reveals that the Huronian Supergroup-Sudbury Basin (HS-SB), with a signal of $7.3^{+5.0}_{-3.0}$ TNU, is the major source of signal as well as of uncertainty concerning the local contribution to the expected geoneutrino signal. The $\pm1\sigma$ range (4.3 - 12.3 TNU) of the geoneutrino signal produced by

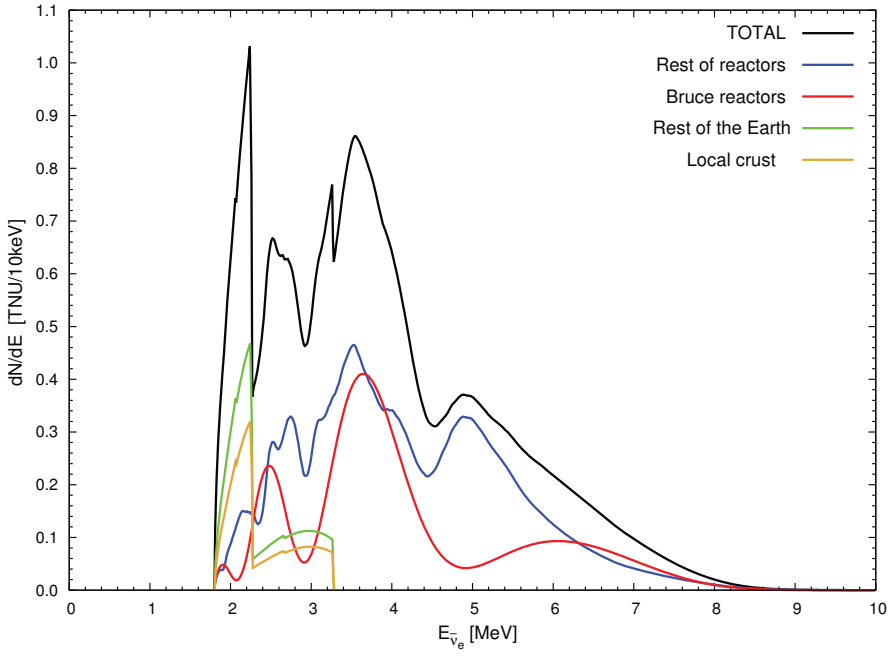

Figure 2.4: Geoneutrino and reactor antineutrino spectra at SNO+. The geoneutrino spectrum is subdivided into the local crust (brown line) and rest of the Earth (green line) components. The reactor spectrum is split into the contributions generated by the Bruce power station (red line) and by the rest of reactors (blue line). The overall antineutrino spectrum at SNO+ (black line) is also shown.

Table 2.3: Geoneutrino and reactor antineutrino signals at SNO+ reported in TNU. The total geoneutrino signal is the sum of the contributions from the local crust, the rest of the crust, the continental litospheric mantle and the mantle. The reactor signal is given separately for the LER and FER. The total reactor signal is the sum of the contributions generated by the Bruce power station and by the rest of the reactors.

Geoneutrinos		Reactor antineutrinos		
	LER [TNU]		LER [TNU]	FER [TNU]
Local crust	$15.6^{+5.3}_{-3.4}$	Bruce reactors	$17.3^{+1.0}_{-0.7}$	$73.7^{+2.0}_{-1.8}$
Rest of the crust	$15.1^{+2.8}_{-2.4}$	Rest of reactors	$31.2^{+0.9}_{-0.8}$	$118.9^{+2.8}_{-2.6}$
Continental litoshperic mantle	$2.1^{+2.9}_{-1.2}$			
Mantle	9			
TOTAL	40^{+6}_{-4}	TOTAL	$48.5^{+1.8}_{-1.5}$	$192.6^{+4.7}_{-4.4}$

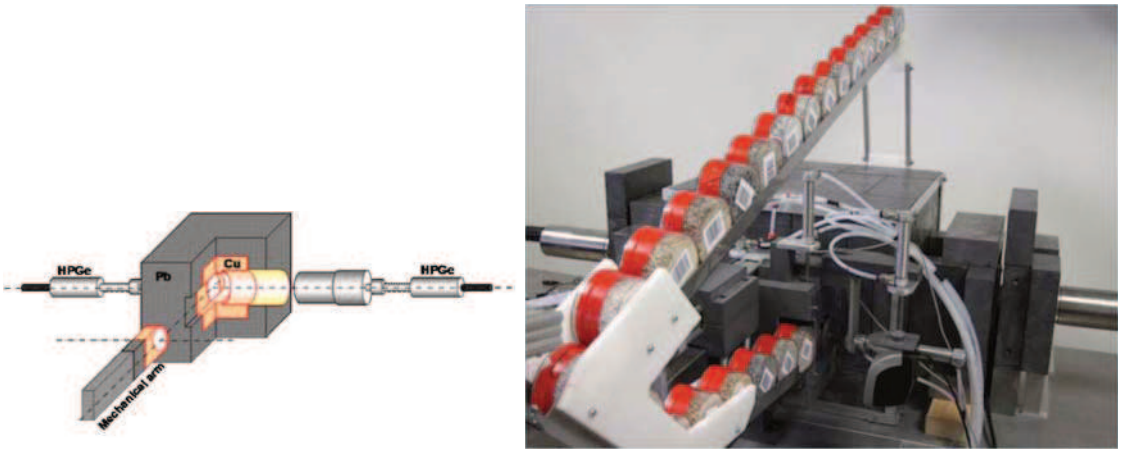

Figure 2.5: .The left panel shows a schematic design of the MCA_Rad system. The main lead shielding construction has dimensions 20 cm × 25 cm × 20 cm. The core copper shielding has dimensions 10 cm × 15 cm × 10 cm. The right panel is a view of the actual MCA_Rad system (Xhixha et al. 2013).

the HS-SB is comparable with the full range of the expected mantle signal (2 - 19 TNU) (Fiorentini et al. 2012; Šrámek et al. 2013). With the perspective of inferring the mantle geoneutrino signal by subtracting the estimated crustal contribution to the total (Fiorentini et al. 2012), improving the HS-SB modeling is mandatory. In the light of producing a new 3D higher resolution model describing the CLose Crust (CLC), corresponding to the 50 km x 50 km area around the detector, a detailed survey of the HS-SB ($\sim$ 32% of the CLC area) has been performed in 2016 throughout the collection of 51 rock samples (41 samples formally belonging to the Huronian Supergroup and 10 representative of the minor mafic and felsic intrusions).

The U and Th content of the 51 collected rock samples have been estimated via laboratory gamma-ray spectroscopy measurements performed with a High Pure Germanium detector (HPGe) called MCA_Rad (Xhixha et al. 2013). The MCA_Rad system is composed by two coaxial p-type HPGe detectors having a certified relative efficiency of 60% and 67% respectively and an energy resolution of about 1.9 keV at the ^{60}Co 1332.5 keV gamma emission line. The cooling technology employs mechanical coolers which allow to simplify the management of the system. The detectors are accurately shielded and positioned facing each other 5 cm apart (Fig. 2.5).

Gamma-ray spectroscopy measurements are affected by a background radiation which is mainly due to the combination of cosmic radiation, environmental gamma radiation and the radioactivity produced by radio-impurities both in the shielding materials and in the detector. In the MCA_Rad system a 10 cm thick lead house shields the detector assembly, leaving an inner volume around the detectors of about 10 dm^3. The lead used as shielding material adds some extra background due to the presence of ^{210}Pb, which has an half life of 22.3 years and which can be revealed by the detection of a 46.5 keV gamma photon and a bremsstrahlung continuum due to the beta decay of its daughter ^{210}Bi (extending from low energy up to 1162 keV). Furthermore, when a gamma-ray strikes the lead

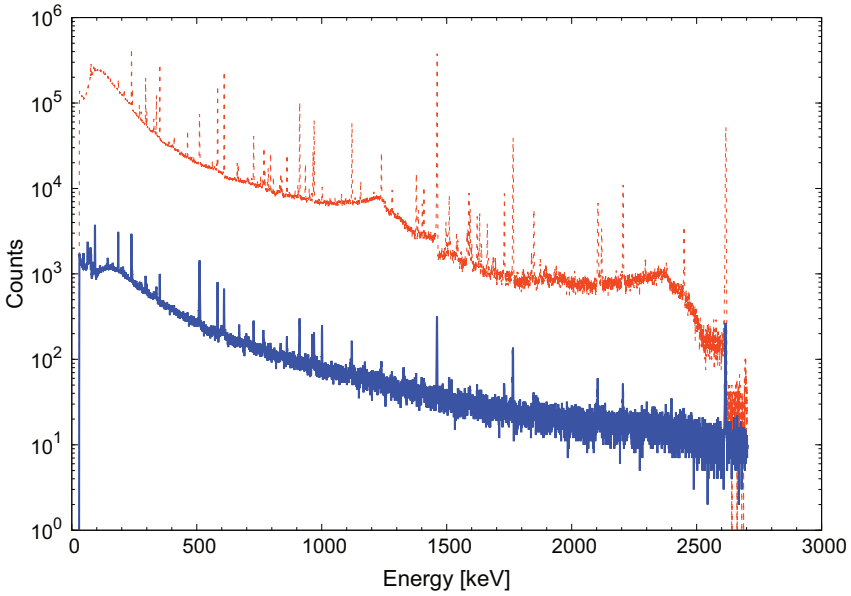

Figure 2.6: .The MCA_Rad system background spectra (acquisition live time 100 h) with (continuous green line) and without (dashed red line) shielding. Spectra are obtained by summing the single detector background after rebinning with 0.33 keV/channel.

surface, characteristic lead X-rays may escape and hit the detector. The inner volume is occupied by 10 cm thick oxygen free copper house, which allows to host the sample under investigation. In order to reduce the X-rays coming from the sample, the end-cup windows of the detectors are further shielded with a tungsten alloy sheet of 0.6 mm. A 10 mm thick bronze cylinder and walls of about 10 cm of lead are also shielding the rear part of the system. The final intrinsic background is reduced by two orders of magnitude compared to other unshielded detectors (Xhixha et al. 2013) (see Fig. 2.6).

For assessing and checking the stability of the background corrections a background measurement with acquisition time of several days is performed regularly. The final sensitivity of the measurements can be evaluated by using the detection limit (L_D) described in Currie 1968, assuming the Gaussian probability distribution of the number of counts in the background (B) and rejecting the data not included in a range of 1.645σ (95% confidence level):

$$L_D = 2.71 + 4.65\sqrt{B} \simeq 4.65\sqrt{B}$$

where the approximation is admitted for high number of counts. The minimum detectable activity (MDA) is calculated according to the formula:

$$MDA = \frac{L_D}{\varepsilon I_\gamma t}$$

where ε is the absolute efficiency, I_γ is the gamma line intensity and t is the acquisition live time. The full energy efficiency calibration was performed using certified reference materials traceable by the International Atomic Energy Agency at less than 5% accuracy in the energy range 200–2650 keV and will be discussed in the Chapter 3.

The 51 rock samples collected for the geochemical characterization of the HS-SB were crushed and sealed in a cylindrical polycarbonate box having a 75 mm diameter and 45 mm height, corresponding to a 180 cm^3 volume, labeled by a barcode. Up to 24 samples can be charged in a slider and further introduced at the inner chamber through an automatic "arm". The mechanical automation consists on a barcode scanner and a set of compressed air driven pistons. This mechanism not only makes the sample identification possible, but is also able to introduce/expel the samples. All operations, including measurements, are controlled by a PC by means of a dedicated software. The program receives by the operator an input file with the relevant informations about the slot of samples: acquisition live time, spectra file name, sample weight, sample description and barcode. The procedure is repeated until the barcode reader detects samples. A new batch command file is generated to be successively employed in the spectral analysis. For each measurement, the final spectrum is obtained by adding, after rebinning, the two simultaneously measured spectra: for this purpose an accurate energetic calibration of the system, along with a periodical check, is required. When a shift larger than 0.5 keV is observed, the energy calibration procedure is repeated.

Each sample is accurately sealed and left undisturbed for at least 4 weeks prior the measurement, with the objective of establishing radioactive equilibrium between ^{226}Ra and ^{222}Rn, as will be shown in Sec. 3.2. U and Th concentrations are both typically affected by overall relative uncertainties on the order of 10%, with MDA corresponding to about 0.2 μg/g and 0.7 μg/g, respectively. In the analyzed dataset one sample for U and one sample for Th have been found to have activities below the MDA (Fig. 2.8).

The geochemical characterization of the HS-SB requires the knowledge of the probability density function (pdf) describing the U and Th abundances of the reservoir, which can be inferred by a statistical analysis of the two datasets comprising the 51 values of U and Th content measured via laboratory gamma-ray spectroscopy. The Kolmogorov-Smirnov (KS) test appears to be a suitable statistical tool that can be used to compare the U and Th datasets with a reference continuous probability distribution. Generally speaking, given n independent and identically distributed random variables, if $X_1, ..., X_n$ indicates the ordered sample of the n random variables, the empirical cumulative distribution function (cdf) $F_n(x)$ is defined as:

$$F_n(x) = \begin{cases} 0 & \text{if } x \leq X_1 \\ \dfrac{k}{n} & \text{if } X_k \leq x < X_{k+1} \\ 1 & \text{if } x \geq X_n \end{cases} \tag{2.3}$$

The null and the alternative hypotheses are:

- H_0: the data follow the specified distribution;

- H_A: the data do not follow the specified distribution.

which can be translated in terms of empirical cdf $F_n(x)$ and theoretical cdf $F_0(x)$ as:

- $H_0 : F_n(x) = F_0(x), \forall x$
- $H_A : F_n(x) \neq F_0(x)$, for some x

The KS test uses as figure of merit for testing H_0 the test statistics D_n, which is a measure of the largest vertical difference between the theoretical and the empirical cdf:

$$\begin{aligned} D_n &= \max_{1\leq k\leq n} \left(F_0(X_k) - F_n(X_{k-1}), F_n(X_k) - F_0(X_k)\right) \\ &= \max_{1\leq k\leq n} \left(F_0(X_k) - \frac{k-1}{n}, \frac{k}{n} - F_0(X_k)\right) \end{aligned} \tag{2.4}$$

The hypothesis regarding the distributional form H_0 is rejected at the chosen significance level α if the test statistic D_n is greater than a critical value $D^*_{n,\alpha}$. The critical value depends both on α and on the dimension of the dataset n, but does not depend on the underlying cumulative distribution function being tested. The significance level α represents the probability of rejecting the null hypothesis H_0 when it is actually true. If

$$D_n \leq D^*_{n,\alpha} \tag{2.5}$$

then the sample data is a good fit with $F_0(x)$, i.e. H_0 can't be rejected at the α significance level. The p-value is instead calculated based on the test statistic D_n, and denotes the threshold value of the significance level: this means that the null hypothesis H_0 will be accepted for all values of α smaller than the p-value and rejected at all values of α greater than the p-value.

The KS test has been applied to the U and Th datasets adopting as theoretical distributions a normal and a lognormal distribution, where for each one the μ and σ values have been estimated from the dataset. The two pdfs describing the normal and lognormal distributions are the following:

$$f^{normal}(x) = \frac{exp\left(-\frac{1}{2}\left(\frac{x-\mu}{\sigma}\right)^2\right)}{\sigma\sqrt{2\pi}}$$

$$f^{lognormal}(x) = \frac{exp\left(-\frac{1}{2}\left(\frac{lnx-\mu}{\sigma}\right)^2\right)}{\sigma x\sqrt{2\pi}}$$

Fig. 2.7 shows the plots of the experimental cdf and of the theoretical normal and lognormal cdfs obtained in the analysis of the two datasets containing the U and Th abundances of the 51 samples collected to characterize the HS-SB reservoir. The D_n vertical distances between the experimental cdf and respectively the normal (black line) and lognormal (red line) theoretical cdfs are also shown.

Table 2.4 reports the results of the KS test, from which it is possible to evince that the vertical distance D_{51} obtained comparing the experimental cdf with the normal cdf is for both the U and Th datasets larger with respect to that obtained for a theoretical lognormal distribution ($D_{51}^{\text{normal}} >$

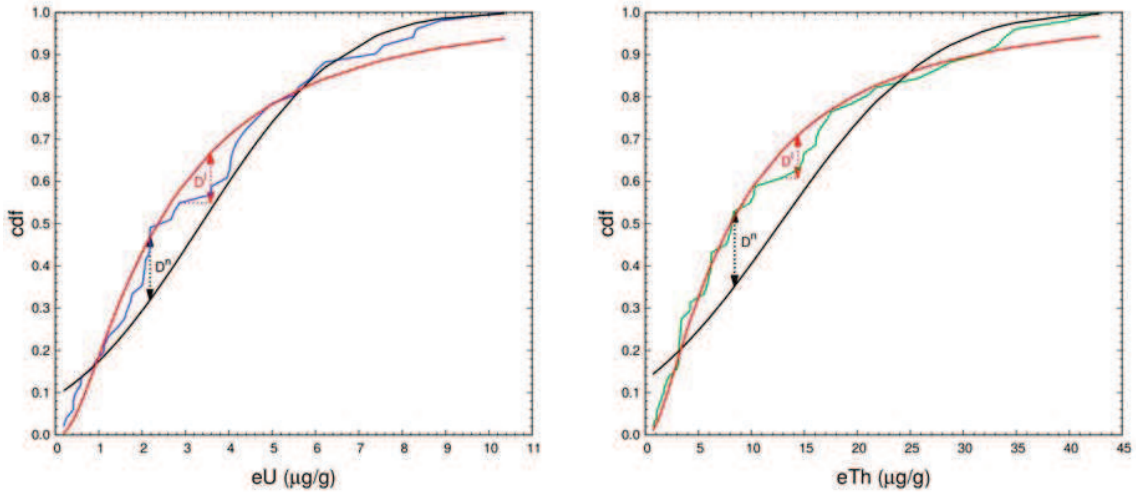

Figure 2.7: The left and right panels show the experimental and theoretical cumulative distribution functions (cdf) obtained respectively for the U and Th datasets. In the left panel the blue curve shows the experimental cdf for the U dataset and in the right panel the green curve shows the experimental cdf for the Th dataset. In both panels the black solid line and the red solid line represent respectively the cdf for a theoretical normal and lognormal distributions. The vertical distances associated to the KS test of a normal and a lognormal distribution D^n and D^l are also shown.

Table 2.4: The table reports the results of the KS test performed for comparing the datasets of U and Th abundances of the 51 collected samples with the normal and lognormal probability distributions. For both the normal and lognormal distributions the vertical distances D_{51} and the p-values are reported respectively in the third and fourth columns. In the last three columns there are the critical distances (independent on the underlying probability distribution) corresponding to a sample size equal to 51 and to a α level respectively equal to 0.1, 0.05 and 0.01.

	Theoretical pdf	D_{51}	p-value	$D^*_{51,0.1}$	$D^*_{51,0.05}$	$D^*_{51,0.01}$
U	Normal	0.172	0.09	0.168	0.187	0.224
	Lognormal	0.120	0.42			
Th	Normal	0.178	0.07			
	Lognormal	0.103	0.62			

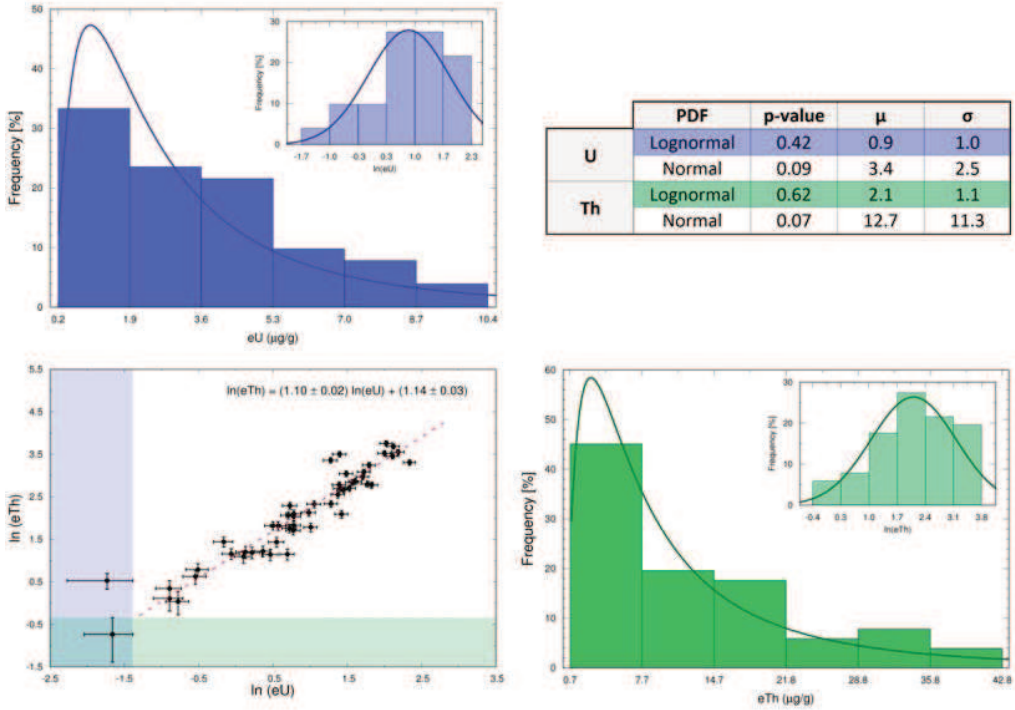

	PDF	p-value	μ	σ
U	Lognormal	0.42	0.9	1.0
	Normal	0.09	3.4	2.5
Th	Lognormal	0.62	2.1	1.1
	Normal	0.07	12.7	11.3

Figure 2.8: Frequency histograms for the measurements of U and Th abundances of the 51 rock samples collected for the characterization of the HS-SB reservoir at SNO+. The frequency distributions are fitted with a lognormal distribution and for the logarithm abundances a fit with a normal distribution is presented. The table reports the p-values of the Kolmogorov-Smirnov test and the parameters of the fit considering a lognormal or a normal distribution. The plot of the correlation of U and Th abundances and the result of the fit are reported, the colored bands defining the MDA values.

$D_{51}^{\text{lognormal}}$). This translates in a rejection of the normal null hypothesis at smaller α levels with respect to the case of lognormal null hypothesis: indeed, the normal null hypothesis can be rejected at 0.09 and 0.07 α level for U and Th respectively (corresponding by definition to the p-values), consistently with a vertical distance D_{51}^{normal} greater than the critical distance $D_{51,0.1}^{*}$, referred to a sample size of 51 and to a 0.1 α level.

Fig. 2.8 shows the frequency histograms of the U and Th concentrations in the HS-SB reservoir, which are positively skewed and as expected fit the lognormal distribution better than normal distribution.

The parameters, μ and σ, obtained from the lognormal distribution fitting (Fig. 2.8) are used to estimate the central tendency and the asymmetrical uncertainties of U and Th abundances (Table 2.5). In comparison with the U and Th abundances of the "Huronian Supergroup, Sudbury Basin" unit in Huang et al. 2014 (Table 2.5), the new results referred to the CLC show lower concentration values. From one side the 50% of the HS-SB area in the CLC is occupied by the Mississage Formation, characterized by relative lower U and Th concentrations, and from the other side Huang et al. 2014

Table 2.5: The table summarizes the HS-SB U and Th abundances for the Huang et al. 2014 model and Strati et al. 2017 model (to be submitted to G-cubed).

Model	U [μg/g]	Th [μg/g]
Huang et al. 2014	$4.2^{+2.9}_{-1.7}$	$11.1^{+8.2}_{-4.8}$
Strati et al. 2017 (to be submitted to G-cubed)	$2.3^{+3.8}_{-1.5}$	$8.0^{+15.1}_{-5.2}$

includes only samples located in the western area of the local crust, outside the CLC, which appear to be enriched in U and Th contents. Table 2.5 summarizes the U and Th abundances adopted in the reference model of Huang et al. 2014 and the new values obtained on the base of collected rock samples.

2.4 Final remarks

As the antineutrino signal in the LER at SNO+ is expected to be generated by nuclear reactors and by the Earth in a ratio of ∼1.2, a detailed characterization of both the geoneutrino and the reactor antineutrino sources is compulsory in terms of both absolute values and uncertainties.

A multitemporal analysis of the expected reactor signal at SNO+ over a time lapse of 10 years (January 2004 – December 2014) reveals that the monthly signal fluctuations associated to different reactors operational condition are on the order of 10% at 1σ level. The 18 operating CANDU reactors belonging to the Bruce, Pickering and Darlington power stations generate approximately 55% of the total reactor signal in the LER at SNO+. For this reason, an accurate profile of the CANDU fissile isotope inventory over the entire duty cycle is mandatory for the SNO+ experiment.

According to Huang et al. 2014 the HS-SB is the strongest geoneutrino source among the local crust (440 km × 460 km) reservoirs and it is predicted to produce $7.3^{+5.0}_{-3.0}$ TNU with respect to a total geoneutrino signal of 40^{+6}_{-4} TNU. The compositional heterogeneity of this lithologic unit, which is due to the presence of a mixture of Paleoproterozoic sedimentary, metasedimentary and igneous rocks of the Canadian Shield, affects the geoneutrino signal uncertainty on the order of 60%. A systematic sampling of the main lithologies of the HS-SB has been performed with the specific aim of improving the knowledge of the U and Th content of the unit and of putting more stringent constraints on the contribution to the geoneutrino signal at SNO+ coming from the close crust (50 km × 50 km area around the SNO+ detector).

The 51 collected samples have been characterized for their U and Th content by means of laboratory gamma-ray spectroscopy measurements, which have been perfomed with the MCA_Rad system, composed by a couple of high-efficiency HPGe detectors. The configuration of the lead and cooper shielding of the MCA_Rad system lead to a background reduction of two order of magnitude respect to laboratory radioactivity. Moreover, a fully automation of the MCA_Rad system allowed to lower the manpower cost and to measure up to 24 samples without any human attendance.

Considering the accessibility of the outcrops, the number of samples collected for each one of the main lithologies constituting the HS-SB reservoir was planned on the base of the exposure surface and the estimated volume, taking into account also the proximity to the detector. From this study it emerged that the HS-SB maintains its heterogeneity, which is reflected in relatively wide lognormal distributions describing the U and Th abundances of the reservoir. However, this refinement will lead to more robust results on the predicted geoneutrino signal as the statistical characterization of the HS-SB reservoir has been performed on the base of U and Th abundances datasets obtained after a dedicated sample collection survey.

The content of this chapter is based on the following publications:

Baldoncini M., Strati V., Wipperfurth S. A., Fiorentini G., Mantovani F., McDonough W. F. and Ricci B."*Geoneutrinos and Reactor Antineutrinos at SNO+.*"Journal of Physics: Conference Series 718, no. 6 (2016): 062003. doi:10.1088/1742-6596/718/6/062003.

Strati V., Wipperfurth S.A., **Baldoncini M.**, Mantovani F., McDonough W.F."*3D Geophysical and geochemical model of the close upper crust around Sudbury Neutrino Observatory for predicting geoneutrino flux.*". To be submitted to Geochemistry, Geophysics, Geosystems.

Bibliography

Andringa, S. et al. (2015). "Current Status and Future Prospects of the SNO+ Experiment". *arXiv:1508.05759*.

Bain, A.S. et al. (1997). "Canada enters the nuclear age: a technical history of Atomic Energy of Canada limited as seen from its research laboratories". *McGill-Queen's University Press*.

Baldoncini, M. et al. (2015). "Reference worldwide model for antineutrinos from reactors". *Phys. Rev. D* 91.6, p. 065002. DOI: 10.1103/PhysRevD.91.065002.

Bemporad, C. et al. (2002). "Reactor based Neutrino Oscillation Experiments". *Reviews of Modern Physics* 74.2, pp. 297–328. ISSN: 0034-6861, 1539-0756. DOI: 10.1103/RevModPhys.74.297.

Bowden, N. S. et al. (2009). "Observation of the Isotopic Evolution of Pressurized Water Reactor Fuel Using an Antineutrino Detector". *Journal of Applied Physics* 105.6, p. 064902. ISSN: 00218979. DOI: 10.1063/1.3080251. arXiv: 0808.0698[nucl-ex].

Chen, M. C. (2006). "Geo-neutrinos in SNO+". en. *Earth Moon Planet* 99.1-4, pp. 221–228. DOI: 10.1007/s11038-006-9116-4.

Currie, Lloyd A. (1968). "Limits for qualitative detection and quantitative determination. Application to radiochemistry". *Analytical Chemistry* 40.3, pp. 586–593. DOI: 10.1021/ac60259a007.

Fiorentini, G. et al. (2012). "Mantle geoneutrinos in KamLAND and Borexino". *Physical Review D* 86.3. DOI: 10.1103/PhysRevD.86.033004.

Huang, Y. et al. (2013). "A reference Earth model for the heat-producing elements and associated geoneutrino flux". en. *Geochem. Geophys. Geosyst.* 14.6, pp. 2003–2029. DOI: 10.1002/ggge.20129.

Huang, Y. et al. (2014). "Regional study of the Archean to Proterozoic crust at the Sudbury Neutrino Observatory (SNO), Ontario: Predicting the geoneutrino flux". *AGU Fall Meeting Abstracts* 15.10. ISSN: 1525-2027. DOI: 10.1002/2014GC005397.

Kopeikin, V. I. (2012). "Flux and spectrum of reactor antineutrinos". *Physics of Atomic Nuclei* 75.2, pp. 143–152. ISSN: 1063-7788, 1562-692X. DOI: 10.1134/S1063778812020123.

Lozza, V. (2016). "The SNO+ Experiment for Neutrinoless Double-Beta Decay". *Nuclear and Particle Physics Proceedings*. 37th International Conference on High Energy Physics (ICHEP) 273–275, pp. 1836–1841. ISSN: 2405-6014. DOI: 10.1016/j.nuclphysbps.2015.09.296.

Mueller, Th. A. et al. (2011). "Improved predictions of reactor antineutrino spectra". *Physical Review C* 83.5, p. 054615. DOI: 10.1103/PhysRevC.83.054615.

Nichols, AL. et al. (2008). "Handbook of nuclear data for safeguards: database extensions, August 2008". *IAEA INDC (NDS)-0534*.

Phaneuf, C. and J. Mareschal (2014). "Estimating concentrations of heat producing elements in the crust near the Sudbury Neutrino Observatory, Ontario, Canada". *Tectonophysics* 622, pp. 135–144. DOI: 10.1016/j.tecto.2014.03.001.

Šrámek, Ondřej et al. (2013). "Geophysical and geochemical constraints on geoneutrino fluxes from Earth's mantle". *Earth and Planetary Science Letters* 361, pp. 356–366. DOI: 10.1016/j.epsl.2012.11.001.

Xhixha, G. et al. (2013). "The worldwide NORM production and a fully automated gamma-ray spectrometer for their characterization". *Journal of Radioanalytical and Nuclear Chemistry* 295.1, pp. 445–457. ISSN: 0236-5731, 1588-2780. DOI: 10.1007/s10967-012-1791-1.

Chapter 3

Calibration of a HPGe detector by using certified reference materials

With the spread of nuclear technologies applied to energy, health and industrial production, the theme of environmental radioactivity monitoring is becoming increasingly important in policies dedicated to the safeguard of public health, both at national and international level. Gamma-ray spectroscopy is a valuable methodology for mapping environmental radioactivity due to the fact that gamma-rays have high penetration range and characteristic emission energies, which provide an unambiguous identification of the decayed isotope. During the last decades gamma-ray spectroscopy has been established as a well consolidated and widely used technique also thanks to its applicability in laboratory, in situ and in airborne measurements, which translates into the possibility of performing surveys at different spatial resolution scales. Large and restricted scale environmental surveys are relevant for monitoring natural radioactivity but also ground areas which can be potentially contaminated due to the fallout of artificial radionuclides as well as to the presence of Naturally Occurring Radioactive Materials (NORMs), which are typically wastes or by-products that industrial processes enriched with radioactive elements found in the environment (Xhixha et al. 2013a).

The potentialities of the gamma-ray spectroscopy method are not limited to the environmental monitoring but embrace also a variety of applications in the field of geosciences such as geological mapping, mineral exploration, heat-flow and geoneutrino studies. The common requirements in all the mentioned disciplines are a deep understanding and a reliable performance of the gamma-ray spectrometry method, achieved through dedicated instrumental calibrations and cross-validation tests.

This Chapter discusses the feasibility of using certified reference materials for the full energy efficiency calibration of p-type coaxial high-purity germanium detectors for the determination of radioactivity in environmental samples. The determination of the detector efficiency at a given energy strictly depends not only on the experimental counting statistics, but relies on the knowledge of a large number of correction factors related to the intrinsic features of the specific gamma decay as well as to the characteristics of the source material itself. Each correction factor and each source of uncertainty

entering the efficiency calibration procedure has been object of a dedicated study, implying also the adoption of distinct analysis strategies.

In particular I was assigned to evaluate the correction factor due to the self-absorption, which, for a given photon energy, allows to take into account variations in photon attenuation within the source material due to variations in sample chemical composition and density. While decay correction factors can be adequately treated according to a pure theoretical approach, in the case of self-absorption a Monte Carlo simulation was needed in order to investigate a wide phase space of sample materials and gamma photon energies. 1456 different configurations have been simulated, corresponding to 14 photon energies, 8 source matrix densities and 13 source matrix chemical compositions, the latter, as expected, affecting the variability of the self-absorption correction at a second order level compared to the other two parameters. In modeling the self-absorption correction I had to face the problem of integrating the results obtained for the investigated chemical compositions and of building a two dimensional fit curve describing simultaneously the behavior of the self-absorption correction factor for varying gamma energy and source density.

I also took part in the assessment of the uncertainty hierarchy and budget related to the efficiency calibration procedure. Indeed, the separate treatment of corrections and sources of uncertainty allowed to quantify for the most intense gamma lines the individual contribution each input quantity has on the total uncertainty. Finally, the calibration procedure has been validated for natural and artificial radionuclide determination in different matrices through an internal cross-validation and through the participation in a world-wide open proficiency test.

3.1 Background

High-resolution gamma-ray spectrometry is a widely used non-destructive measurement technique for the assessment of gamma-ray emitting radionuclides present in environmental samples. The process of the determination of the full energy calibration is of great importance for the accurate determination of natural and anthropogenic radionuclides in environmental samples such as soils, sediments, rocks, foodstuffs and surface and ground water. In cases when standard gamma-ray emitting point or volume sources are not accessible, certified reference materials (CRMs) have been demonstrated to be a suitable calibration source for the determination of the detection efficiency of hyper-pure germanium (HPGe) detectors (Ebaid 2009; Nir-El 1998; Iurian and Cosma 2014). CRMs of natural origin are an effective solution due to both the relatively low cost and to the presence of radionuclides with very long half-lives with respect to standard sources. Another important advantage of CRMs is that they can be easily managed by individual laboratories in order to reproduce specific counting geometries and density ranges. Using CRMs is an appropriate solution for the determination of the environmental radioactivity as they contain radionuclides which cover an energy range from 46.5 keV (^{210}Pb) up to 2614 keV (^{208}Tl). When using CRMs, however, particular attention must be paid to the presence of interfering radionuclides which should be accurately investigated (Oddone et al. 2008). Moreover, the self-attenuation due to sample matrix and density can give non negligible effects (Ebaid 2009; Oddone

et al. 2008; Miller and Voutchkov 2014). In this work, the CRMs RGK-1, RGU-1 and RGTh-1 traceable by the International Atomic Energy Agency (IAEA) (IAEA 1987) are used for the efficiency calibration of the MCA_Rad system entailing two p-type HPGe detectors (Xhixha et al. 2013a; Xhixha et al. 2013b). An analytical approach and a Monte Carlo simulation were used for the evaluation of the corrections due to self-absorption and true coincidence summing effects, respectively. A detailed study of the principal sources of uncertainty in order to assess the total uncertainty budget is performed. The description of the calibration process and the study of uncertainties presented in this work can be a useful guideline for a conscious use of CRMs for the determination of full energy efficiency of HPGe detectors. The efficiency calibration was internally cross-validated by using phopshogypsum IAEA 434 (IAEA 2010) and oilfield contaminated soil IAEA 448 (IAEA 2013) CRMs. Finally, an external cross-validation was performed by participating to the world-wide open proficiency test organized by IAEA (TEL2014-03).

3.2 Experimental setup and measurement procedure

The MCA_Rad system is made up two coaxial p-type HPGe detectors (certified by manufacturer with 60 and 67% of relative efficiency respectively) with a measured energy resolution of approximately 1.9 keV at 1332.5 keV (^{60}Co). The HPGe detectors are coupled with a self-designed automatic sample changer, which allows managing independently the measurement of up to 24 samples without any human intervention. The system is well shielded principally with 10 cm of lead and 10 cm of copper, which reduces the laboratory background by approximately two orders of magnitude. The fully automated HPGe gamma-ray spectrometer, called MCA_Rad system has been previously is described in detail in Xhixha et al. 2013a.

Gamma-ray spectrometry measurements are carried out simultaneously by the two HPGe detectors closely facing the opposite bases of a cylindrical polycarbonate sample container (7.5 cm in diameter and 4.5 cm in height). An a priori energy calibration procedure is performed by measuring the gamma radiation from a calibration source that covers the energy range from 186.2 keV (226Ra) to 2614.5 keV (208Tl). The energy and FWHM (Full Width at Half Maximum) determined for the most intense photopeaks are well fitted with a first order Eq. 3.1 and a second order Eq. 3.2 polynomial function, respectively, with a reduced $\chi^2 = 1.0$.

$$E(keV) = a_1 \cdot channel + a_2 \tag{3.1}$$

$$FWHM(keV) = b_1 E^2 + b_2 E + b_3 \tag{3.2}$$

where the fitting coefficients for Eq. 3.1 are 0.40, 0.91 for HPGe A and 0.40, 1.05 for HPGe B, while for Eq. 3.2 are -6.11 $\cdot 10^{-8}$, 7.25 $\cdot 10^{-4}$, 9.76 $\cdot 10^{-1}$ for HPGe A and -6.83 $\cdot 10^{-8}$, 8.34 $\cdot 10^{-4}$, 8.81 $\cdot 10^{-1}$ for HPGe B (Fig. 3.1).

After energy calibration, the spectra were rebinned by extracting pseudorandom numbers according to a Gaussian probability density function. The reference energy calibration function has a zero

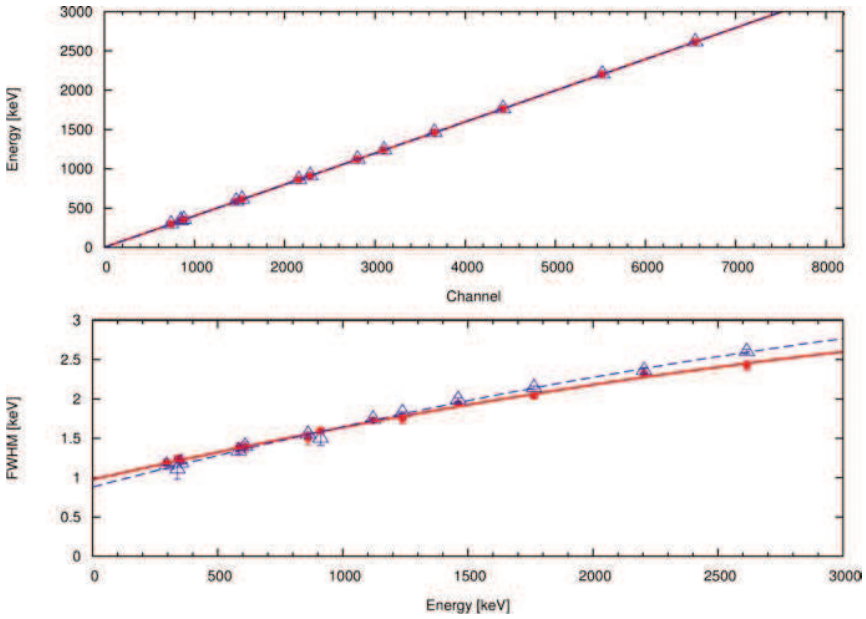

Figure 3.1: The energy and FWHM calibration of both HPGe detectors constituting the MCA_Rad system: continuous red line and red circles are referred to HPGe A, dashed blue line and blue triangles are referred to HPGe B.

offset and 0.35 keV per channel. The stability of the energy calibration is monitored periodically and the calibration is repeated if a shift larger than 0.5 keV is observed. A check on possible systematics introduced by the rebinning process was performed. Although the procedure was found to be dependent on the count rates, the amplitude of the fluctuations was always within the statistical counting uncertainty for this energy range and accordingly the net peak areas are not affected. Finally, the spectrum assigned to the single measurement is obtained by adding the two rebinned spectra.

The photopeak efficiency calibration was determined using three CRMs released by the IAEA and coded as RGU-1, RGTh-1 and RGK-1. The specific activities of the CRMs are certified at 95% confidence level and are equal to 4940 ± 30 Bq/kg for ^{238}U (RGU-1), 3250 ± 90 Bq/kg for ^{232}Th (RGTh-1) (both in secular equilibrium) and to 14000 ± 400 Bq/kg for ^{40}K (RGK-1) (IAEA 1987). The CRMs, already prepared in powder matrix (240 mesh) are dried at a temperature of 60 ˚C until a constant weight is achieved and transferred into the standard counting geometry. Each standard sample is accurately sealed using vinyl tape and then left undisturbed for at least 4 weeks in order to establish radioactive equilibrium between ^{226}Ra and ^{222}Rn prior to be measured. In the case of materials characterized by high radon exhalation, the sealing is very important in order to reduce the ^{222}Rn loss (Scholten et al. 2013; Mauring and Gäfvert 2013). The sealing effectiveness and consequently the ^{222}Rn growth within the container were successfully checked, as shown in Fig. 3.2 where the in-grow of count rates of radon progeny ^{214}Bi (at 609 keV) is displayed for a phosphogypsum sample. The in-growth counts were measured for six ^{222}Rn half-lives (corresponding to approximately

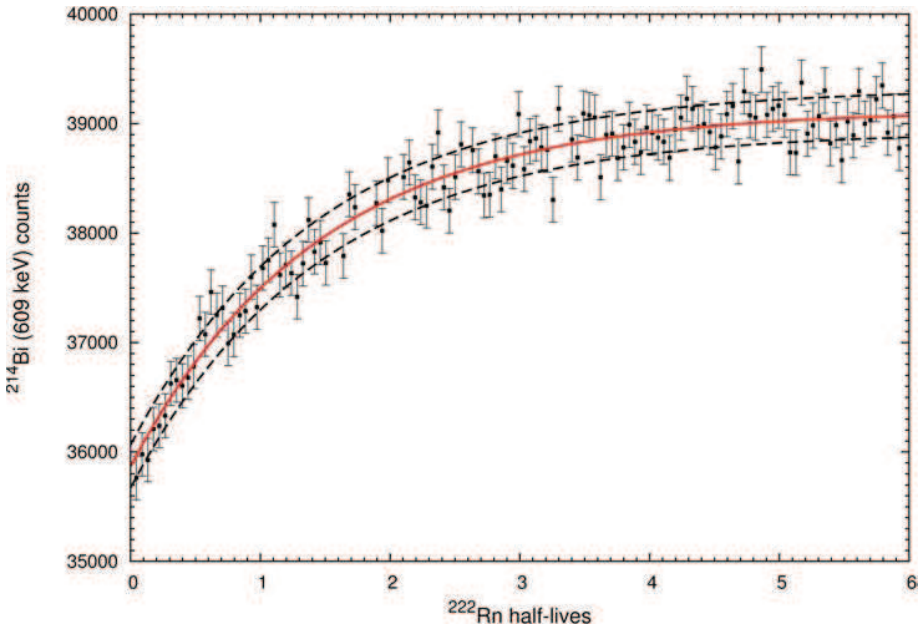

Figure 3.2: The radon daughter ^{214}Bi (at 609 keV) counts growth measured in standard counting geometry for six ^{222}Rn half-lives. Each data point corresponds to 4-hour measurements. The continuous red line represents the fitting curve and dashed black line represents the one sigma uncertainty.

99% of equilibrium). The experimental data points are well fitted (with a reduced $\chi^2 = 1.0$) taking the ^{222}Rn half-live (3.821 days (Bellotti et al. 2015) as a fixed parameter. The reproducibility of source positioning and instrument stability was checked by sequentially measuring the CRM for 1 h acquisition time for 12 h, first without removing the CRM from one measurement to the following one and secondly by removing the CRM at the end of each

measurement. In Table 3.1 and Table 3.2 are shown the statistical uncertainties and the standard deviation ($\pm 1\sigma$) for the count rates of the most intense gamma emissions, which are used for determining the photopeak efficiency curve. The corrected net peak area (N) for the background was obtained according to the expression ($N = N_{CRM} - (t_{L,CRM}/t_{L,bckg})/N_{bckg}$), where N_{CRM}, N_{bckg} are the net peak areas in the CRM spectrum and background spectrum, respectively, and $t_{L,CRM}$, $t_{L,bckg}$ are the respective acquisition live times. The combined uncertainty is derived by applying the uncertainty propagation law for the no-correlation case, as the CRM spectrum comes from the sum of the two HPGe uncorrelated spectra, which in turn are not correlated to the background spectrum. The standard deviation of the precision was found to be generally comparable with the counting uncertainty. In the case of measurements during repeated removing of the samples, the standard deviation of the precision slightly increased with respect to the previous case. As a result of these tests, the uncertainties due to the measurement repeatability (source positioning, homogeneity) and to instrument stability (background fluctuation) are found negligible with respect to the counting uncertainty.

Table 3.1: The precision with statistical uncertainty and 1σ standard deviation of 12 repeated measurements (1h live time) in counts per second (cps) without removing the sample.

	^{234m}Pa (1001 keV)	^{214}Pb (351 keV)	^{214}Bi (609 keV)	^{228}Ac (911 keV)	^{212}Pb (238 keV)	^{212}Bi (727 keV)	^{208}Tl (583 keV)	^{40}K (1460 keV)
Precision (stat.unc) ± st.dev.	0.33(2) ± 0.02	26.01(9) ± 0.07	19.95(8) ± 0.08	6.46(4) ± 0.08	25.32(29) ± 0.09	2.02(3) ± 0.03	8.83(5) ± 0.05	9.05(5) ± 0.04
Rel. unc. [%]	6.06	0.27	0.40	1.24	0.35	1.48	0.57	0.44

Table 3.2: The precision with statistical uncertainty and 1σ standard deviation of 12 repeated measurements (1h live time) in counts per second (cps) removing the sample at the end of each measurement.

	^{234m}Pa (1001 keV)	^{214}Pb (351 keV)	^{214}Bi (609 keV)	^{228}Ac (911 keV)	^{212}Pb (238 keV)	^{212}Bi (727 keV)	^{208}Tl (583 keV)	^{40}K (1460 keV)
Precision (stat.unc) ± st.dev.	0.33(2) ± 0.02	26.07(9) ± 0.14	19.96(8) ± 0.10	6.44(4) ± 0.03	25.30(27) ± 0.10	2.02(3) ± 0.04	8.80(5) ± 0.06	9.08(5) ± 0.05
Rel. unc. [%]	6.06	0.54	0.50	0.47	0.39	1.98	0.68	0.55

3.3 Absolute efficiency and uncertainty assessment

The photopeak efficiency ($\varepsilon_{CRM}(E_i)$) can be expressedgeneral by the following formula:

$$\varepsilon_{CRM}(E_i) = \frac{N}{A_{CRM} t_{L,CRM} I_\gamma(E_i) m_{CRM}} \frac{1}{C_{SA}} \frac{1}{C_{TCS}} \frac{1}{C_{D_1}} \frac{1}{C_{D_2}} \frac{1}{C_{D_3}} \frac{1}{C_{RS}} \frac{1}{C_G} \tag{3.3}$$

where A_{CRM} is the certified activity concentration (in Bq/kg) of the CRMs, $I_\gamma(E_i)$ is the gamma-ray energy emission probability corrected for the branching ratio, m_{CRM} is the mass (in kg) of the CRMs, C_{D_1}, C_{D_2} , C_{D_3} are respectively the decay correction factors for radionuclide decay during sampling period, during the end of sampling until the start of the measurement period and during the counting period, C_{RS} is the correction factor for random summing effect, C_G is the correction factor for different counting geometries, C_{SA} is the correction factor for mass density and atomic composition differences and C_{TCS} is the correction factor for the true coincidence summing effect. The decay data for natural radionuclides are taken from DDEP (Decay Data Evaluation Project) — LNHB Atomic and Nuclear Data (Bé et al. 2004; Bé et al. 2008; Bé et al. 2010; Bé et al. 2011; Bé et al. 2013).

3.3.1 Negligible corrections

The corrections for nuclide decay are negligible, since the half-lives of natural radionuclides are much longer compared to sampling (C_{D_1}), storage (C_{D_2}) and counting (C_{D_3}) periods: e.g. for experimental time periods of ¡1% of nuclide half-life the magnitude of the correction factor is ¡¡1% and therefore can be neglected. On the other hand, when all corrections are needed, attention must be paid to the correlation among the three correction factors (Makarewicz 2005). The correction on the random summing is considered negligible since the dead time is too low for low count rates which are of the order of few hundreds of cps. However, corrections for random summing effect (C_{RS}) has to be taken into account for high dead time. Moreover, in cases when the standard geometry is identical to the counting geometry, as in our case, the correction due to geometrical differences becomes virtually negligible. In different situations the geometrical corrections must be determined. An experimental approach for correcting for the geometrical factor when using standard point sources for absolute efficiency calibration has been previously shown by Xhixha et al. 2013a.

3.3.2 Self absorption correction

As the activity of the samples is determined based on the efficiency curve $\varepsilon(E)$ established for a calibration source, departures in sample chemical composition and density with respect to the standard have to be considered in order to account for different photon attenuation within the source material itself. In our approach the correction factor for the self-attenuation effect (C_{SA}) is determined considering that the mass attenuation coefficient is strongly dependent on the atomic composition below few hundred of keV, while for the energy range 200–3000 keV it can be well approximated with the average with a standard deviation of less than 2% (Xhixha et al. 2013a; Xhixha et al. 2013b;

Kaminski et al. 2014). Differently from the analytical approach discussed by Xhixha et al. 2013a, the C_{SA} was estimated by performing a Monte Carlo simulation in which the counting geometry was modeled as entirely composed by one major oxide at time. The Z-effective of the investigated minerals (SiO_2, Al_2O_3, CaO, MgO, FeO, K_2O, Fe_2O_3, $CaCO_3$, Na_2O, P_2O_5, MnO) range between 9.99 and 17.16 at 1 MeV (Taylor et al. 2012). For each chemical composition are considered homogeneous materials having densities from 0.75 to 2.25 g/cm^3 typical of environmental samples. The simulation was performed for each sample counting condition by isotropically generating some 10^5 gammas having energy from 200 up to 3000 keV. The C_{SA} was estimated as the ratio between the number of emitted and transmitted photons accordingly to the standard counting geometry.

However, particular attention must be paid to the case of Naturally Occurring Radioactive Materials (NORMs) generated in industrial processes, which can lead to the concentration of chemical elements other than radioelements. A typical example is the case of scales from oil and gas exploration (Landsberger et al. 2013) in which an accumulation of calcium, strontium and barium is generally observed, severely affecting the attenuation of gamma rays. Another case of study which involves titanium oxide production industry (Mantero et al. 2015) shows the importance of self-absorption correction, which can be studied with transmission method. In addition, the matrix composition can be determined using additional measurements by X-ray fluorescence spectrometry (XRF), neutron activation analysis (NAA) etc.

The C_{SA} exhibits a linear dependence on the sample density (Boshkova and Minev 2001), where the intercept and the slope are functions of the photon energy, as stated in the following relationship:

$$C_{SA}(\rho, E) = A(E) + B(E)\rho \tag{3.4}$$

The intercept was parametrized with respect to the photon energy E according to the following expression $A(E) = \sum_{i=0}^{3} a_i E^{-i}$ and the dependence of the slope on the photon energy E is equal to that of the mass attenuation coefficient, which is well approximated by a second order polynomial of the logarithm of the energy $B(E) = \sum_{i=0}^{2} b_i \ln(E)^i$. The C_{SA} surface shown in Fig. 3.3 was obtained by performing a two-dimensional fit according to Eq. 3.4 with a reduced $\chi^2 = 1.0$.

The input data points correspond to the C_{SA} determined for each sample density and for each photon energy as the uncertainty-weighted average among the values attained for the eleven different chemical compositions. The percentage uncertainties plotted in Fig. 3.4 correspond to the maximum variability with respect to the sample chemical composition of the C_{SA} (Fig. 3.3). The same procedure was followed separately for organic material and water obtaining the correction factor for self-absorption as function of density and energy.

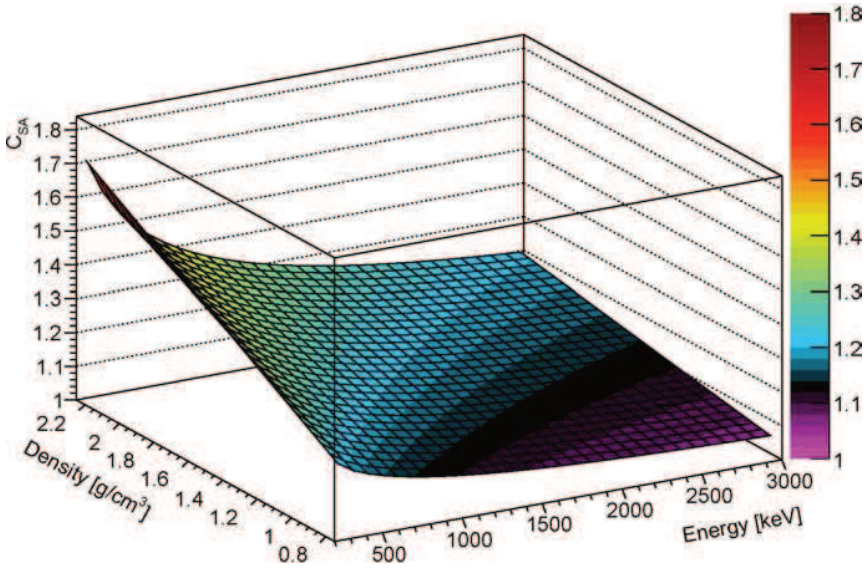

Figure 3.3: The correction factor for self-absorption effect (inorganic material matrix) for the MCA_Rad counting geometry determined via Monte Carlo simulation as a function of sample density and photon energy. The Eq. 3.4 is fitted with the following parameters $a_0 = 1.00$, $a_1 = -5.96$, $a_2 = -2.99 \cdot 10^3$, $a_3 = 5.66 \cdot 10^5$ and $b_0 = 1.77$, $b_1 = -0.37$, $b_2 = 0.02$ with a reduced $\chi^2 = 1.0$.

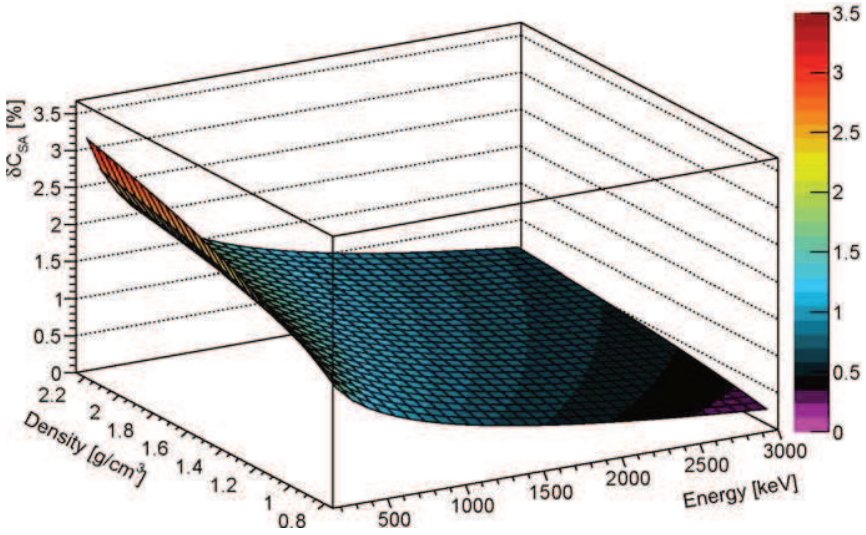

Figure 3.4: The percentage uncertainty on the C_{SA} estimated in as the maximum variability of the correction factor with respect to the sample chemical composition.

3.3.3 True coincidence summing correction

The correction factor for the true coincidence summing effect is determined using the mathematical formalism described by De Felice et al. 2000 and in particular, the coincidence summing (both summing-in and summing-out effects) of $\gamma - \gamma$ can be modeled as:

$$C_{TCS}(i) = \left(1 - \frac{\sum_j P_{t(i,j)} P_{(i)} P_{(j)} \varepsilon_{t(j)}}{I_{\gamma(i)}}\right)\left(1 + \frac{\sum_{k,m} P_{t(k,m)} P_{(k)} P_{(m)} \varepsilon_{p(k)} \varepsilon_{p(m)}}{I_{\gamma(i)} \varepsilon_{p(i)}}\right) \tag{3.5}$$

where $P_{(i)}$ is the probability of photon emission in the i transition, $P_{t(i,j)}$ is the probability of the coincident transition $i - j$, $\varepsilon_{p(i)}$ is the apparent full energy peak efficiency for the energy of the transition i, and $\varepsilon_{t(j)}$ is the total apparent efficiency for the energy of the transition j. Since the relative efficiencies of both HPGe detectors are checked to be similar, the true coincidence summing effect is reasonably treated as a unique correction factor and applied to the final spectrum.

In Table 3.3 are reported the correction equations for the true coincidence summing for the most intense gamma-rays as function of the "apparent" full energy peak efficiency ε_p and total efficiency ε_t calculated using decay data from Bé et al. 2004; Bé et al. 2008; Bé et al. 2010; Bé et al. 2011; Bé et al. 2013. The contribution of terms (coincident energies) having coefficients of less than five per thousand is not considered since their contribution in the correction factor is generally on the order of fractions of a percent. The correction equations are found to be comparable with those calculated in other studies (Tomarchio and Rizzo 2011; Dryák and Kovář 2009; Schima and Hoppes 1983), within few percent on the coefficients terms. The "apparent" full energy peak efficiency ε_p and total efficiency ε_t (Fig. 3.5) are determined as described in Xhixha et al. 2013a, by measuring peak-to-total ratio using Eq. 3.6.

Table 3.3: Expressions of coincidence-summing correction factors determined for the most intense gamma emissions of a selected set of nuclides.

Parent nuclide	Daughter nuclide	E (keV)	I_γ (%)	C_{TCS}	C_{TCS}
^{238}U	^{214}Pb	351.9	35.60	$\{1\text{-}0.0092\varepsilon_{t(478.1)}\}$	0.9983(2)
		295.2	18.41	$\{1+0.0284\varepsilon_{p(242.0)}\varepsilon_{p(53.2)}/\varepsilon_{p(295.2)}\}$	1.0007(1)
		242.0	7.27	$\{1\text{-}0.0720\varepsilon_{t(53.2)}\}$	0.9980(2)
	^{214}Bi	609.3	45.49	$\{1\text{-}0.3212\varepsilon_{t(1120.3)} - 0.1256\varepsilon_{t(1238.1)} - 0.1054\varepsilon_{t(768.4)} - 0.0668\varepsilon_{t(934.1)} - 0.0524\varepsilon_{t(1408.0)} - 0.0458\varepsilon_{t(1509.2)} - 0.0352\varepsilon_{t(1155.2)} - 0.0330\varepsilon_{t(665.4)} - -0.0309\varepsilon_{t(1281.0)} - 0.0287\varepsilon_{t(1401.5)} - 0.0272\varepsilon_{t(806.2)} - 0.0171\varepsilon_{t(1385.3)} - 0.0152\varepsilon_{t(1583.2)} - 0.0098\varepsilon_{t(1207.7)} - 0.0103\varepsilon_{t(703.1)} - 0.0085\varepsilon_{t(719.9)} - 0.0086\varepsilon_{t(1538.5)} - 0.0062\varepsilon_{t(454.8)} - 0.0074\varepsilon_{t(1838.4)} - 0.0070\varepsilon_{t(388.9)} - 0.0070\varepsilon_{t(1052.0)} - 0.0069\varepsilon_{t(1599.3)} - 0.0059\varepsilon_{t(1594.8)} - 0.0055\varepsilon_{t(1133.7)} - 0.0668\varepsilon_{t(934.1)} - 0.0126\varepsilon_{tXK(81.0)}\}$	0.844(46)
		1764.5	15.31	$\{1-0.0206\varepsilon_{t(964.1)}\}\{1+0.1047\varepsilon_{p(609.3)}\varepsilon_{p(1155.2)}/\varepsilon_{p(1754.5)} + 0.0091\varepsilon_{p(1377.7)}\varepsilon_{p(386.8)}/\varepsilon_{p(1764.5)}\}$	1.003(1)
		1120.3	14.91	$\{1 - 0.09800\varepsilon_{t(609.3)} - 0.0216\varepsilon_{t(388.9)} - 0.0069\varepsilon_{t(752.8)} - 0.0050\varepsilon_{t(474.5)} - 0.0191\varepsilon_{tXK(81.0)}\}\{1 + 0.0192\varepsilon_{p(454.8)}\varepsilon_{p(665.4)}/\varepsilon_{p(1120.3)}\}$	0.823(17)
		1238.1	5.83	$\{1-0.09800\varepsilon_{t(609.3)}\}\{1+0.0057\varepsilon_{p(832.4)}\varepsilon_{p(405.7)}/\varepsilon_{p(1238.1)} + 0.0121\varepsilon_{p(572.8)}\varepsilon_{p(665.5)}/\varepsilon_{p(1238.1)} + 0.0125\varepsilon_{p(469.8)}\varepsilon_{p(768.4)}/\varepsilon_{p(1238.1)}\}$	0.832(17)
		2204.2	4.91	$\{1 + 0.0136\varepsilon_{p(543.0)}\varepsilon_{p(1661.3)}/\varepsilon_{p(2204.2)} + 0.0116\varepsilon_{p(826.5)}\varepsilon_{p(1377.7)}/\varepsilon_{p(2204.2)} + 0.0547\varepsilon_{p(1594.8)}\varepsilon_{p(609.3)}/\varepsilon_{p(2204.2)}\}$	1.005(1)
^{232}Th	^{208}Tl	2614.5	99.76	$\{1 - 0.8500\varepsilon_{t(583.2)} - 0.2250\varepsilon_{t(510.7)} - 0.1240\varepsilon_{t(860.5)} - 0.0660\varepsilon_{t(277.4)} - 0.0180\varepsilon_{t(763.5)} - 0.0075\varepsilon_{t(252.7)} - 0.0.701\varepsilon_{tKX(76.6)}\}$	0.762(16)
		583.2	85.00	$\{1 - 0.9975\varepsilon_{t(2614.5)} - 0.2594\varepsilon_{t(510.7)} - 0.0761\varepsilon_{t(227.4)} - 0.0208\varepsilon_{t(763.5)} - 0.0087\varepsilon_{t(252.7)} - 0.0578\varepsilon_{tKX(76.6)}\}$	0.803(13)
		860.5	12.40	$\{1 - 0.9975\varepsilon_{t(2614.5)} - 0.0136\varepsilon_{t(233.4)}\}\{1 + 0.05216\varepsilon_{p(227.4)}\varepsilon_{p(583.2)}/\varepsilon_{p(860.5)}\}$	0.932(16)
	^{228}Ac	911.2	26.20	$\{1 - 0.0065\varepsilon_{t(57.8)} - 0.0175\varepsilon_{t(154.0)} - 0.0069\varepsilon_{t(199.4)} - 0.1033\varepsilon_{t(463.0)} - 0.0207\varepsilon_{t(562.5)} - 0.0239\varepsilon_{t(755.3)}\}\}$	0.966(2)
		338.3	11.40	$\{1 - 0.0327\varepsilon_{t(1247.0)} - 0.0069\varepsilon_{t(948.0)} - 0.0380\varepsilon_{t(830.5)} - 0.0948\varepsilon_{t(772.3)} - 0.0424\varepsilon_{t(726.9)} - 0.0052\varepsilon_{t(620.3)} - 0.0075\varepsilon_{t(583.4)} - 0.0140\varepsilon_{t(478.4)} - 0.0097\varepsilon_{t(572.3)} - 0.0065\varepsilon_{t(57.8)}\}\{1 + 0.0735\varepsilon_{p(209.3)}\varepsilon_{p(128.2)}/\varepsilon_{p(338.3)}\}\}$	0.955(3)

[a] Terms for $\gamma-$KX-ray coincidence summing are taken from bibliography (Tomarchio and Rizzo 2011; Dryák and Kovář 2009; Schima and Hoppes 1983).

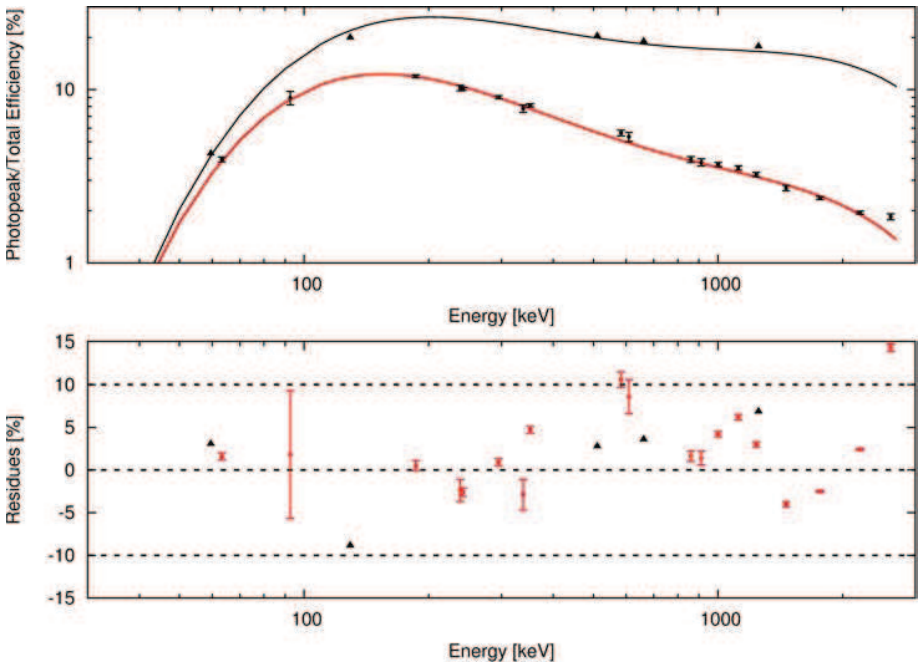

Figure 3.5: Apparent photopeak efficiency and total efficiency determined for the MCA_RAD system. Residues show the percentage differences with respect to the fitting curve (logarithmic polynomial of the fifth order). Black triangles show the total efficiency determined experimentally as a cross-check.

The peak-to-total ratio was determined by measuring the single gamma-ray emitting radionuclides ^{137}Cs (661.6 keV), ^{241}Am (59.4 keV) and close energy gamma-ray emitting radionuclides ^{60}Co (average energy 1252.5 keV), ^{57}Co (average energy 124 keV). In the case of ^{22}Na (511 keV corrected for 1274 keV) the peak-to-total ratio was instead interpolated from other energies as described in Debertin and Helmer 1988. Different approaches on calculation of total efficiency are described in De Felice et al. 2000.

$$\varepsilon_t(E) = \frac{\varepsilon_p(E)}{(P/T)} \tag{3.6}$$

3.3.4 Absolute efficiency curve modeling

The absolute efficiency is determined for the energy range from 160 to 2650 keV by using the function described in Tsoulfanidis and Landsberger 2015; Knoll 2010 Fig. 3.7:

$$\varepsilon = \left(\frac{a_0}{E/E_0}\right)^{a_1} + a_2 exp\left(-a_3\frac{E}{E_0}\right) + a_4 exp\left(-a_5\frac{E}{E_0}\right) \tag{3.7}$$

where a_i are the six fitting parameters (with fitting values equal to a_0 = 0.04, a_1 = -0.54, a_2 = -1.26, a_3 = 0.14, a_4 = -1.26 and a_5 = 0.14). This function fits the data with a reduced χ^2 = 0.9 with residues with respect to the fitting curve of generally less than 5%. The energy range of validity of the

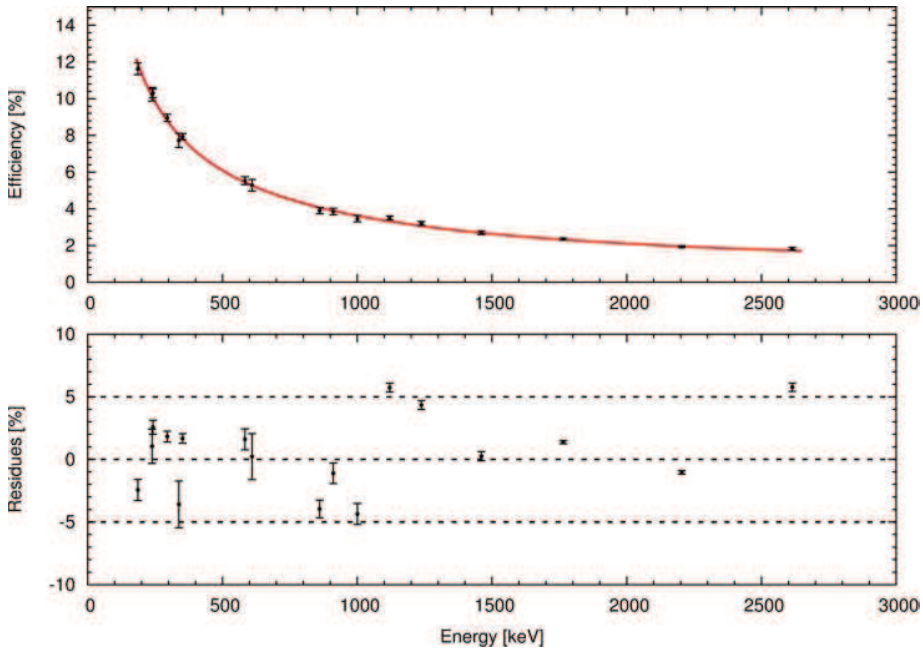

Figure 3.6: Full energy peak efficiency determined for the MCA_Rad system. Residues show the percentage differences with respect to the fitting curve.

fitting curve is not critical for the efficiency calibration of the MCA_Rad system since p-type HPGe gamma-ray spectrometers are not suitable for measuring low energy gamma-ray emitting radionuclides in environmental samples.

3.3.5 Total uncertainty budget and hierarchy

The combined standard uncertainty, $u_c(\varepsilon)$, of the full-energy peak efficiency ε was calculated from the relative standard uncertainties of its components x_i according to the Guides in Metrology (JCGM) 2008 as:

$$u_c(\varepsilon) = \varepsilon \sqrt{\sum_{i=1}^{n} \left(\frac{\partial \varepsilon}{\partial x_i} \frac{u(x_i)}{x_i} \right)^2} \tag{3.8}$$

The uncertainty propagation law of Eq. 3.8 assumes that the x_i parameters are not correlated. A way to simplify the calculation of the partial derivatives in calculating the combined uncertainties is to use a spreadsheet approach presented by Kragten 1994, which is based on a numerical calculation of the partial derivatives. The uncertainties of components are assessed either by Type A or by Type B evaluations. Type A evaluation is based on a statistical evaluation of measurement data, as in the case of the counting uncertainty which is normally evaluated according to the Poisson statistics. Type B evaluation is performed by any other method, e.g. in the case of data from certificates of reference materials or physical data from databases. The relative contribution of the major components is given

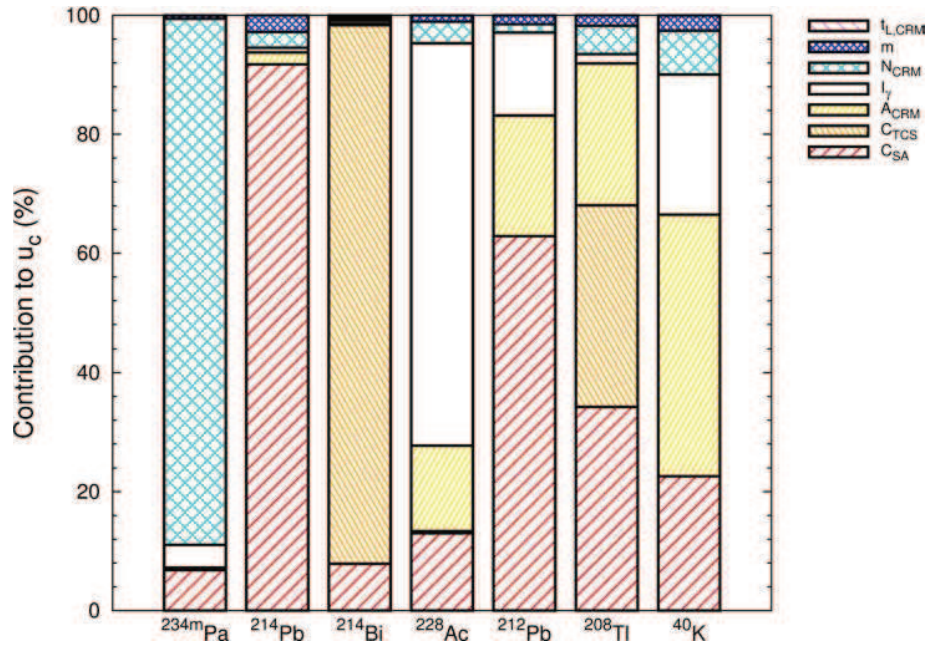

Figure 3.7: The percentage relative contributions to the uncertainty budget of the major components entering in the efficiency calibration Eq. 3.3 determination using CRMs.

Fig. 3.7 for the most intense gamma rays for all radionuclides present in the CRMs. The contribution to the combined uncertainty of the acquisition live time and of the sample mass is negligible for most gamma spectrometric applications.

In the case of efficiency calibration, the counting statistics contribute to the combined uncertainty with few percent, except for the case of the low yield gamma-ray emitter ^{234m}Pa, where the counting statistics contribution is approximately 80%. As it can be expected, the uncertainty on the CRM certified activity concentrations contribute to the uncertainty budget at the level of few percent for the RGU, while for the RGK and for the RGTh is the relative weight of this component is of about 20%. It is interesting to observe that a relatively high contribution to the combined uncertainty (about 60%) comes from the gamma yield data of 911 keV (^{228}Ac). Indeed, this gamma line has approximately a 3% relative uncertainty, which is relatively higher with respect to other gamma lines known with less than 1% relative uncertainty. Finally, the major contribution to the combined uncertainty appears to come from the correction factor for the self-absorption effect, except for the 609 keV (^{214}Bi) gamma line, where the contribution of the correction factor due to the coincidence summing effect is dominant due to the ^{214}Bi complex decay scheme.

Table 3.4: Cross-check control performed by measuring IAEA certified reference materials.

Reference material	Matrix	Radionuclide	Certified activity (Bq/kg)	Measured activity (Bq/kg)	Relative bias (%)	Within 1σ agreement
IAEA-434	Phosphogypsum	^{226}Ra[a]	780 ± 62	747 ± 45	-4.23	Yes
IAEA-448	Soil from oil field	^{226}Ra[a]	19050 ± 260	18376 ± 1060	-3.54	Yes
		^{208}Tl[b]	555 ± 26	521 ± 32	-6.13	Yes
		^{212}Pb[b]	1623 ± 69	1578 ± 97	-2.77	Yes
		^{228}Ac[b]	1166 ± 55	1020 ± 65	-12.52	No
		^{40}K[b]	234 ± 12	244 ± 32	4.27	Yes

[a] Certified values
[b] Informative values

3.3.6 Final remarks

The IAEA 434 (IAEA 2010) and IAEA 448 (IAEA 2013) certified reference materials were used to internally validate the efficiency calibration. The results Table 3.4 show relatively good agreement within the uncertainty determined for the efficiency calibration. The disequilibrium in the decay chains of uranium and thorium (Michalik, Brown, and Krajewski 2013) is taken into account for the IAEA 448 material by using the standard Bateman equation and by applying the appropriate decay correction factors to the results. Moreover, an external validation was performed participating in a worldwide proficiency test organizedIAEA (TEL 2014-03) on measuring environmental samples with different matrixes (water, hay, soil) which was organized by the IAEA. In Table 3.5 are reported the individual results for different matrices, evaluated by the IAEAterms both of accuracy and of relative precision with respect to the target values. Only in the case of ^{226}Ra in the water sample the relative bias was higher than the maximum acceptable value, although the internal quality control performed on sample 03-Water supplied by the IAEA (not shown) had satisfactory results. The relative bias was found to be -2.23% (^{226}Ra), -2.04% (^{137}Cs) and 0.76% (^{134}Cs). The higher relative difference for ^{226}Ra in 02-Water sample can possibly attributed to accidental loss of radon.

In this work, is described the procedure for the efficiency calibration of p-type HPGe detectors using certified reference materials (CRMs). The hierarchy of the main sources of uncertainties including the self-absorption and true coincidence summing corrections is discussed in detail. A calibration of HPGe detectors using certified reference materials has been performed for the determination of natural and artificial radioactivity in environmental samples of different matrices. An exhaustive and reproducible experimental method based on an analytical approach and Monte Carlo simulation for estimating individual sources of uncertainty in HPGe efficiency calibration was completed. The full energy efficiency calibration of the MCA_Rad system was performed at less than 5% accuracy for the energy range 200–2650 keV by using CRMs traceable by IAEA.

The self-absorption effect is evaluated by Monte Carlo method as the ratio between emitted and transmitted gammas as a function of energy (200–2650 keV) and sample density (0.75–2.25 g/cm^3) for homogeneous samples composed by the main minerals present in rock and soil. The $\gamma - \gamma$ true coincidence summing was analytically determined as a relationship among gamma emission probabilities

Table 3.5: Results from the IAEA evaluation in the framework of the world-wide open proficiency test IAEA-TEL-2014-03.

Sample code	Radionuclide	IAEA target value ± combined uncertainty (Bq/kg, dry weight)	Laboratory value ± combined uncertainty (Bq/kg, dry weight)	Relative bias (%)	Final score[a]
01-Water	^{134}Cs	21.4 ± 0.2	21.6 ± 1.3	0.93	A
	^{137}Cs	12.06 ± 0.1	11.6 ± 0.6	-3.81	A
02-Water	^{152}Eu	50.05 ± 0.41	53.0 ± 3.3	5.89	A
	^{226}Ra	14.21 ± 0.06	10.5 ± 0.8	-26.11	N
04-Seaweed	^{134}Cs	8.27 ± 0.2	8.0 ± 0.5	-3.26	A
	^{137}Cs	22.96 ± 0.45	21.4 ± 1.2	-6.79	A
	^{40}K	1780 ± 150	1672 ± 91.9	-6.07	A
05-Sediment	^{137}Cs	12.0 ± 0.4	12.2 ± 0.7	1.67	A
	^{228}Ac	12.1 ± 1.5	11.1 ± 0.9	-8.26	A
	^{40}K	270 ± 27	269.2 ± 14.9	-0.30	A
	^{212}Pb	12.2 ± 1.5	12.2 ± 0.7	0.00	A
	^{226}Ra	19.0 ± 4.8	17.8 ± 1.4	-6.32	A
	^{208}Tl	4.1 ± 0.7	4.8 ± 0.4	17.07	A

[a] A stands for accepted, N stands for Not Accepted.

and total and absolute photopeak efficiencies. The hierarchy of uncertainties that commonly affect an HPGe gamma ray spectrometry measurement were evaluated. The relative contributions to 1σ combined uncertainty for the most intense gamma emission of each radionuclide present in the CRMs were determined. The non-negligible uncertainty due to self-absorption correction become relevant (more than 70%) in particular for lower energy gamma lines of ^{214}Pb (351 keV) and ^{212}Pb (238 keV). The correction for true coincidence summing is negligible for all radionuclides, except in the case of ^{214}Bi and ^{208}Tl for which it is the most relevant contribution to the combined uncertainty. All radionuclides present in CRMs are suitable sources for accurate HPGe efficiency calibration, except for ^{234m}Pa that is not convenient due to its very low gamma yield. Finally, it is recommend a thoughtful choice of the nuclide datasheets because the gamma line intensity can be a dominant source of uncertainty as in the case of ^{228}Ac for the adopted DDEP (Decay Data Evaluation Project)-LNHB Atomic and Nuclear Data. The method was validated by measuring natural and artificial radionuclides in environmental samples of different matrices in the framework of an IAEA world-wide open proficiency test (IAEA-TEL-2014-03). An additional internal validation using certified reference material made up of NORM showed a 1σ level agreement, confirming the reliability of the efficiency calibration described.

The content of this chapter is based on the following publication:

Xhixha, G., Alberi M., **Baldoncini M.**, Bode K., Bylyku E., Cfarku F., Callegari I. Hasani F., Landsberger S., Mantovani F., Rodriguez E., Shala F., Strati V., Xhixha Kaçeli M. "*Calibration of HPGe Detectors Using Certified Reference Materials of Natural Origin.*" Journal of Radioanalytical and Nuclear Chemistry 307, no. 2 (2015): 1507–17. doi:10.1007/s10967-015-4360-6.

Bibliography

Bé, M. M. et al. (2004). "Monographie BIPM-5, Table of Radionuclides, Vol. 2". *Bureau International des Poids et Mesures (BIPM), Sèvres*.

Bé, M. M. et al. (2008). "Monographie BIPM-5, Table of Radionuclides, Vol. 4". *Bureau International des Poids et Mesures (BIPM), Sèvres*.

Bé, M. M. et al. (2010). "Monographie BIPM-5, Table of Radionuclides, Vol. 5". *Bureau International des Poids et Mesures (BIPM), Sèvres*.

Bé, M. M. et al. (2011). "Monographie BIPM-5, Table of Radionuclides, Vol. 6". *Bureau International des Poids et Mesures (BIPM), Sèvres*.

Bé, M. M. et al. (2013). "Monographie BIPM-5, Table of Radionuclides, Vol. 7". *Bureau International des Poids et Mesures (BIPM), Sèvres*.

Bellotti, E. et al. (2015). "Precise measurement of the 222Rn half-life: a probe to monitor the stability of radioactivity". *Physics Letters B* 743, pp. 526–530. ISSN: 03702693. DOI: 10.1016/j.physletb.2015.03.021. arXiv: 1501.07757.

Boshkova, T. and L. Minev (2001). "Corrections for self-attenuation in gamma-ray spectrometry of bulk samples". *Applied Radiation and Isotopes* 54.5, pp. 777–783. ISSN: 0969-8043. DOI: 10.1016/S0969-8043(00)00319-5.

De Felice, P. et al. (2000). "Fast procedures for coincidence-summing correction in γ-ray spectrometry". *Applied Radiation and Isotopes* 52.3, pp. 745–752. ISSN: 0969-8043. DOI: 10.1016/S0969-8043(99)00239-0.

Debertin, K. and R. G. Helmer (1988). "Gamma- and X-ray spectrometry with semiconductor detectors".

Dryák, P. and P. Kovář (2009). "Table for true summation effect in gamma-ray spectrometry". *Journal of Radioanalytical and Nuclear Chemistry* 279.2, pp. 385–394. ISSN: 0236-5731, 1588-2780. DOI: 10.1007/s10967-007-7208-x.

Ebaid, Y. Y. (2009). "On the use of reference materials in gamma-ray spectrometric efficiency calibration for environmental samples". *Journal of Radioanalytical and Nuclear Chemistry* 280.1, pp. 21–25. ISSN: 0236-5731, 1588-2780. DOI: 10.1007/s10967-008-7377-2.

Guides in Metrology (JCGM), Joint Committee for (2008). "Evaluation of measurement data Guide to the Expression of uncertainty in measurement". *JCGM 100:2008. ISO/IEC Guide 98-3*.

IAEA (1987). "Preparation and certification of IAEA gamma-ray spectrometry reference materials RGU-1, RGTh-1 and RGK-1".

IAEA (2010). "Reference Material IAEA 434: Naturally Occurring Radionuclides in Phosphogypsum".

IAEA (2013). "Certified Reference Material IAEA-448: Soil from Oil Field Contaminated with Technically Enhanced Radium-226".

Iurian, Andra-Rada and Constantin Cosma (2014). "A practical experimental approach for the determination of gamma-emitting radionuclides in environmental samples". *Nuclear Instruments and*

Methods in Physics Research Section A: Accelerators, Spectrometers, Detectors and Associated Equipment 763, pp. 132–136. ISSN: 0168-9002. DOI: 10.1016/j.nima.2014.06.032.

Kaminski, S. et al. (2014). "Uncertainty of gamma-ray spectrometry measurement of environmental samples due to uncertainties in matrix composition, density and sample geometry". *Applied Radiation and Isotopes* 94, pp. 306–313. ISSN: 0969-8043. DOI: 10.1016/j.apradiso.2014.08.008.

Knoll, G.F. (2010). "Radiation detection and measurement, 4th edn". *Wiley, USA*. ISSN: 978-0-470-13148-0.

Kragten, J. (1994). "Calculating standard deviations and confidence intervals with a universally applicable spreadsheet technique." *Analyst* 119. ISSN: 0003-2654. DOI: http://dx.doi.org/10.1039/an9941902161.

Landsberger, S. et al. (2013). "Determination of 226Ra, 228Ra and 210Pb in NORM products from oil and gas exploration: Problems in activity underestimation due to the presence of metals and self-absorption of photons". *Journal of Environmental Radioactivity*. 6th International Symposium on In Situ Nuclear Metrology as a Tool for Radioecology (INSINUME 2012) 125, pp. 23–26. ISSN: 0265-931X. DOI: 10.1016/j.jenvrad.2013.02.012.

Makarewicz, Marek (2005). "Estimation of the uncertainty components associated with the measurement of radionuclides in air filters using γ-ray spectrometry". *Accreditation and Quality Assurance* 10.6, pp. 269–276. ISSN: 0949-1775, 1432-0517. DOI: 10.1007/s00769-005-0931-5.

Mantero, J. et al. (2015). "Application of gamma-ray spectrometry in a NORM industry for its radiometrical characterization". *Radiation Physics and Chemistry*. Proceedings of the 9th International Topical Meeting on Industrial Radiation and Radioisotope Measurement Applications 116. ISSN: 0969-806X. DOI: 10.1016/j.radphyschem.2015.02.018.

Mauring, Alexander and Torbjörn Gäfvert (2013). "Radon tightness of different sample sealing methods for gamma spectrometric measurements of 226Ra". *Applied Radiation and Isotopes*. 6th International Conference on Radionuclide Metrology - Low Level Radioactivity Measurement Techniques 81, pp. 92–95. ISSN: 0969-8043. DOI: 10.1016/j.apradiso.2013.03.022.

Michalik, B., J. Brown, and P. Krajewski (2013). "The fate and behaviour of enhanced natural radioactivity with respect to environmental protection". *Environmental Impact Assessment Review* 38, pp. 163–171. ISSN: 0195-9255. DOI: 10.1016/j.eiar.2012.09.001.

Miller, Maurice and Mitko Voutchkov (2014). "The impact of uncertainty in the elemental composition of the certified reference material on gamma spectrometry". *Journal of Radioanalytical and Nuclear Chemistry* 299.1, pp. 551–558. ISSN: 0236-5731, 1588-2780. DOI: 10.1007/s10967-013-2781-7.

Nir-El, Y. (1998). "Application of reference materials in the accurate calibration of the detection efficiency of a low-level gamma-ray spectrometry assembly for environmental samples". *Journal of Radioanalytical and Nuclear Chemistry* 227.1, pp. 67–74. ISSN: 0236-5731, 1588-2780. DOI: 10.1007/BF02386433.

Oddone, M. et al. (2008). "Practical considerations regarding high resolution gamma-spectrometry measurements of naturally occurring radioactive samples". *Journal of Radioanalytical and Nuclear Chemistry* 277.3, pp. 579–585. ISSN: 0236-5731, 1588-2780. DOI: 10.1007/s10967-007-7113-3.

Schima, F. J. and D. D. Hoppes (1983). "Tables for cascade-summing corrections in gamma-ray spectrometry". *The International Journal of Applied Radiation and Isotopes* 34.8, pp. 1109–1114. ISSN: 0020-708X. DOI: 10.1016/0020-708X(83)90177-1.

Scholten, J. C. et al. (2013). "226Ra measurements through gamma spectrometric counting of radon progenies: How significant is the loss of radon?" *Marine Chemistry*. Radium and Radon Tracers in Aquatic Systems 156, pp. 146–152. ISSN: 0304-4203. DOI: 10.1016/j.marchem.2013.03.001.

Taylor, M. L. et al. (2012). "Robust calculation of effective atomic numbers: The Auto-Zeff software". *Medical Physics* 39.4. ISSN: 2473-4209. DOI: 10.1118/1.3689810.

Tomarchio, E. and S. Rizzo (2011). "Coincidence-summing correction equations in gamma-ray spectrometry with p-type HPGedetectors". *Radiation Physics and Chemistry* 80.3, pp. 318–323. ISSN: 0969-806X. DOI: 10.1016/j.radphyschem.2010.09.014.

Tsoulfanidis, N. and S. Landsberger (2015). "Measurement and detection of radiation, 4th edn". *CRC Press, Taylor and Francis Group,Boca Raton*. ISSN: 9781482215496.

Xhixha, G. et al. (2013a). "The worldwide NORM production and a fully automated gamma-ray spectrometer for their characterization". *Journal of Radioanalytical and Nuclear Chemistry* 295.1, pp. 445–457. ISSN: 0236-5731, 1588-2780. DOI: 10.1007/s10967-012-1791-1.

Xhixha, G. et al. (2013b). "First characterisation of natural radioactivity in building materials manufactured in Albania". *Radiation Protection Dosimetry* 155.2, pp. 217–223. ISSN: 0144-8420. DOI: 10.1093/rpd/ncs334.

Chapter 4

The FSA-NNLS method applied to gamma-ray spectroscopy

In the last decades gamma spectroscopy with sodium iodide scintillators has been proved to be an excellent method for in-situ and airborne quantitative assessment of gamma ray emitting radioisotopes, leading to a reduction of survey time and costs compared with soil sampling and laboratory-based analyses. Ground and airborne gamma ray measurements cover large areas of the Earth's surface, and many national and regional radiometric maps have been compiled and published (Minty et al. 2009; Matolín 2017; Bucher et al. 2009), with the perspective of adopting common strategies in data analysis and spatial interpolation required for realizing regionally unified cartographic products. Over the years gamma spectroscopy with sodium iodide scintillators has broadened its applications from the fields of geoscience (e.g. mineral prospecting, geochemical mapping and structural geology) to emergency situations in case of nuclear fallout and location of lost radioactive sources. Therefore, not only ^{40}K, ^{238}U, and ^{232}Th have to be measured, but there is also a growing interest to determine the abundances of anthropogenic radionuclides, like ^{137}Cs and ^{131}I. Improvements in technologies and data processing are increasing the reliability of the method in solving geological and environmental problems. In this context, the accurate and fast responses required from in-situ and airborne spectrometers renew the interest in sensitivity calibration approaches.

In this work the Full Spectrum Analysis (FSA) with Non Negative Least Square (NNLS) constraint has been applied to the sensitivity calibration of in-situ and airborne sodium iodide scintillators. With the FSA approach the gamma-ray spectrum is reconstructed as a linear combination of the spectral components generated by individual radionuclides, where the contribution given by each isotope is obtained weighting the detector response to a unitary isotope concentration (the so called fundamental spectrum) by the abundance of the specific isotope in the environment. The NNLS constraint allows to correct the intrinsic problem related with the χ^2 minimization which could lead to artifacts and non physical results in the analysis.

In order to perform the calibration procedure, having available sources of known radioactive content

is necessary. The International Atomic Energy Agency (IAEA 2003) suggests to use a set of three calibration pads having respectively anomalous concentrations of ^{40}K, ^{238}U and ^{232}Th and a fourth pad made up with a low radioactivity material to be used as background calibration source. These artificial pads are difficult to realize and their production, handling and storage costs are not negligible. Moreover, because of their finite size, a geometrical correction has to be applied in order to scale the limited geometry condition to the case of infinite calibration source.

In this work the calibration procedure has been performed by acquiring gamma spectra at natural calibration sites, which have been identified trying to match as much as possible the ideal characteristics of a calibration source, i.e. predominant abundance of one radionuclide with respect to the others, uniform radionuclides distribution and flat morphology. The radioactive content of the selected calibration sites have been determined carrying out independent laboratory measurements with the MCA_Rad system (see Chapter 3) on collected soil samples. The method has been applied to the ground sensitivity calibration of the ZaNaI, CavaRad and AGRS_16L detectors, which are respectively dedicated to static and dynamic in-situ measurements, in-situ measurements on restricted areas and airborne measurements.

This study gave me the opportunity to focus on the challenging task of the calibration of detectors dedicated to in-situ and airborne measurements. In particular I handled the application of the FSA-NNLS method to the sensitivity calibration, which emerged as a very effective tool in the treatment of gamma-ray spectroscopy measurements. Differently from the standard Window Analysis Method (IAEA 2003) which just looks to the spectral energy regions corresponding to the most intense ^{40}K, ^{238}U and ^{232}Th photopeaks, the FSA method relies on the reconstruction of the entire spectral shape, allowing to accommodate also for the presence of artificial radionuclides. Moreover, the implementation of the NNLS constraint avoids the potential presence of negative count rates in the fundamental spectra during the calibration procedure as well as of negative concentrations during the measurement analysis. Indeed, the application of the NNLS constraint does not modify the shape of the fundamental spectra but essentially acts forcing to zero the count rates in the spectral regions above the maximum decay energy of the specific radionuclide.

In dealing with the delicate issue of the FSA-NNLS sensitivity calibration I had to take into account that in-situ acquisitions are affected by a much higher degree of variability with respect to laboratory measurements and are characterized by a much wider field of view. This evidence stimulated the development of a method based on a Monte Carlo sampling for the investigation of the phase space of the possible solutions of the sensitivity calibration, i.e. Experimental Fundamental Spectra (EFS), that I implemented for the AGRS_16L detector calibration. If from one side the NNLS constraint heals the issue of negative counts, the χ^2 minimization can still give rise to non physical shapes in the fundamental spectra in terms of peaks or valleys not related to actual gamma emissions. At the same time, airborne surveys suffer from the non-feasibility of airborne calibration measurements and from the need for fundamental spectra at different altitudes above the terrain level.

I was stimulated by these issues to investigate the use of Monte Carlo simulations as an alternative way to face the problem of the sensitivity calibration of sodium iodide detectors. The power of

the Monte Carlo method relies into the possibility of investigating a variety of environmental and instrumental variables which can affect the shape and intensity of measured spectra, such as the source-detector geometrical configuration, the chemical composition and densities of attenuating and sensitive materials, the vertical migration of radionuclides in the soil.

I applied a Monte Carlo method based on two simulation steps in order to model the Monte Carlo Fundamental Spectra (MCFS) of the AGRS_16L detector. The reliability of the method has been tested by comparing simulated spectra with experimental spectra measured at natural calibration sites. The estimation of two independent sets of fundamental spectra (EFS and MCFS) for the AGRS_16L detector can open the way to the delicate point of the assessment of calibration uncertainties, which is currently a missing piece of information in the field of airborne gamma ray surveys.

4.1 Background

Gamma-ray spectrometry with sodium iodide scintillators is a well developed and consolidated method for radioactive survey (Nuccetelli 2008; Chiozzi et al. 2000; Tyler 2008) with a wide range of applications from mineral exploration to environmental radiation monitoring (IAEA 2003), providing quantitative information about the abundances of the main natural radioisotopes, ^{40}K, ^{238}U and ^{232}Th (International Atomic Energy Agency 1990). The experiences of nuclear power plant accidents and atmospheric nuclear weapon tests taught us that the fallout of man-made radioisotopes (^{137}Cs, ^{134}Cs and ^{131}I) can affect wide portions of the planet. In order to employ such powerful techniques in this context the sensitivity and the quickness have to be improved (Tyler 2004). The conventional approach for studying the specific activity concentration of the three principal natural radioisotopes is to monitor broad spectral windows during the analysis (Verdoya et al. 2009; Desbarats and Killeen 1990). Generally, these windows are chosen around the photopeaks of ^{40}K (1460 keV), of ^{214}Bi (1765 keV) and of ^{208}Tl (2614 keV). Since ^{238}U and the ^{232}Th are not gamma-rays emitters their concentrations are evaluated detecting the gamma-rays produced by ^{214}Bi and ^{208}Tl respectively. The assumption of secular equilibrium of the decay chains is required in order to use this approach. In addition to the above mentioned radionuclides, the three-windows method has been extended to the measurement of ^{137}Cs (Cresswell et al. 2006; Sanderson 1989).

The limit of this technique is that it becomes imprecise for short acquisition times and it suffers the poor intrinsic energetic resolution of NaI(Tl) detector. In particular, the Compton continuum around the ^{137}Cs photopeak is generally very intense compared to the intensity of 662 keV gamma-line. This translates into long acquisition times. Moreover, the intrinsic energetic resolution of sodium iodide detectors prevents to resolve the triplet at 583 keV (^{208}Tl), 609 keV (^{214}Bi), and 662 keV (^{137}Cs). This issue can be solved only by post processing the data.

In any case the window analysis method requires an a priori knowledge of the presence on site of such radioisotope. As a matter of fact, this method is blind to unexpected radionuclides. Significant improvements in gamma-ray spectrum analysis have been obtained by implementing the full spectrum analysis (FSA) method (Hendriks et al. 2001; Minty 1992; Guillot 2001; Gutierrez et al. 2002; Tyler

2004). Since the FSA uses the full extent of the spectrum, as opposed to the three windows method, it needs a much lesser statistic to reach the necessary accuracy. This, in turn, means a drastic reduction in acquisition times. The non-negative least square (NNLS) constraint has been implemented into the FSA algorithm. The efficiency calibration procedure was carried out by using, instead of calibration pads, the spectra acquired in sites selected specifically for calibration purposes as described later. A detailed characterization of each site was performed by measuring the radioisotopes concentrations of soil samples collected in the target area via laboratory gamma-ray spectroscopy performed with the MCA_Rad system (Xhixha et al. 2013). This new approach to the FSA was applied to the ZaNaI, CavaRad and AGRS_16L detection systems, NaI(Tl) based spectrometers that will be described in Sec. 4.3.1, Sec. 4.3.2 and Sec. 4.4.

4.2 Methods

Portable instruments are usually calibrated by means of standard spectra acquired at least using three concrete pads enriched in K, U and Th and a pad free of radioactivity representing the background (Hendriks et al. 2001; Engelbrecht and Schwaiger 2008; Loevborg et al. 1981). These pads are generally concrete constructions of cylindrical shape, having finite dimensions of 2-3 m in diameter and 0.3-0.5 m thick and for this reason a geometrical correction accommodating for the discrepancies with an infinite calibration sources is needed. The design of an ideal pad with one radionuclide inside and with a perfect homogeneous distribution of the radioisotope in its volume is impossible as impurities and non-homogeneities are always present. For example, a clear contamination of uranium in thorium pads has been often seen, as reported by Hendriks et al. 2001. In the case of in-situ gamma-ray spectrometry accuracies on the order of less than 15% are usually well accepted which legitimize the above assumptions. It is worth mentioning that the hypothesis of homogeneous distribution of the radionuclides in the pad mixture should be verified and that the cost of production, handling and storage of the pad is not negligible.

Instead of building pads, an alternative calibration procedure is based on the selection of sites characterized by a prevalent concentration of one of the natural radionuclides with respect to the others. Even if it is almost impossible to select one site which contains only one of the nuclides, the selection will be oriented towards sites with unbalanced contents. The number of gamma-rays reaching the top soil surface exponentially decreases with increasing depth of the emission point: as the photon flux originating below 40-50 cm of soil is almost negligible (IAEA 2003), the characterization of each site is performed by collecting samples at around 10 cm depth. All calibration sites were selected using geological and geomorphological considerations and further validated trough laboratory measurements (a list of all the sites and the concentration of each isotope for the calibration of the three detection systems are reported in Table 4.1, Table 4.2 and Table 4.5). In-situ measurements can be affected by the specificity of the place, like the soil non-homogeneity, the ground morphology, the non secular equilibrium in radioactive chains, the vertical distribution of ^{137}Cs, the presence of vegetation, moisture, etc. Thus, the calibration sites should be selected as far as possible according

to the following prescriptions:

- relatively uniform distribution of radionuclides in secular equilibrium with their products
- plane area without any steps and large enough to be approximated as an infinite source
- undisturbed areas (assuring relatively constant ^{137}Cs vertical distribution)
- uniform and relatively homogeneous soil moisture content and vegetable coverage.

Soil and rock samples collected for the sensitivity calibration procedure were dried, homogenized (less than 2 mm fine grain size) and sealed in measurement containers for at least four weeks in order to allow the ^{222}Rn growth up prior to be measured using the high-resolution gamma-ray spectrometry system MCA_Rad (see Chapter 2 and Chapter 3) (Xhixha et al. 2013).

The choice of a number of calibration sites greater than the number of analyzed elements is mandatory to avoid artifacts in the sensitive spectra. One advantage of this calibration approach is the possibility to take into account radionuclides other than ^{40}K, ^{232}Th, and ^{238}U, like ^{137}Cs whose presence cannot be considered a priori negligible after the Chernobyl accident (in general a minimum of k+1 sites are needed, where k is the number of investigated nuclides).

The full spectrum analysis method has been developed in different approaches (Minty 1992; Maučec et al. 2009; Hendriks et al. 2001; Crossley and Reid 1982) and was found to be a successful spectrum analysis tool. The FSA encompasses almost the full energy spectrum, reducing the required statistic of a single measurement and therefore its duration in time. The spectra acquired in-situ are fitted by a linear combination of the fundamental spectra derived for each isotope from the calibration analysis. The events registered in each channel in the measured spectrum, N, can be expressed as:

$$N(i) = \sum_{k=1}^{4} C_k S_k(i) + B(i) \tag{4.1}$$

where

- $N(i)$ are the counts in the $i-th$ channel
- C_k is the concentration of the $k-th$ radionuclide
- $S_k(i)$ are the associated counts to the fundamental spectrum of the $k-th$ element in the $i-th$ channel
- $B(i)$ are the counts in the $i-th$ channel due to the intrinsic background.

and the index k stays for ^{40}K, ^{232}Th, ^{238}U, and ^{137}Cs.

The activity concentrations are deduced from the measured spectrum by applying the least square algorithm to rectangular matrix and minimizing the χ^2 as in the following equation:

$$\chi^2 = \frac{1}{n-5} \sum_{i=1}^{n} \frac{\left[N(i) - \sum_{k=1}^{4} C_k S_k(i) - B(i)\right]^2}{N(i)} \tag{4.2}$$

where $N(i)$ is considered Poisson distributed and n is the number of channels in the spectrum used in the analysis.

Using a matrix notation, Eq. 4.1 can be written also as:

$$N = CS \tag{4.3}$$

where

- n_{ij} is the background corrected count rate recorded in channel j at the i site;
- c_{ik} is the concentration of radioelement k at the i site;
- s_{kj} is the count rate recorded in channel j due to the presence of a unitary concentration of the k element.

During the calibration of the ZaNaI, CavaRad and AGRS_16L detectors the fundamental spectra (the S matrix) are obtained by solving Eq. 4.1 with the radionuclide concentrations (the C_k coefficients) determined after the characterization of the area with laboratory gamma-ray spectroscopy measurements on collected samples, which in matrix notation means solving the following equation:

$$S = C^+ N = \left(C^T C\right)^{-1} C^T N \tag{4.4}$$

where C^+ is the so called pseudo-inverse matrix, which is a generalization of the inverse matrix in the case of rectangular matrices having the property of being left-inverse ($C^+C = I$) but not right-inverse ($C^+C \neq I$) .

Only a sub energy range (typically from 300 keV up to 2900 keV) is considered in the FSA. At energies lower than few hundreds keV there is a strong presence of the back-scattering events which depend on the atomic number and density of the surrounding materials. Above 2900 keV only the cosmic ray contribution is present.

The χ^2 minimization without any further conditions, which is the base of the FSA method, can bring to sensitive spectra having energy regions of negative counts. The presence of these non physical results introduces crosstalk effects in the analysis, leading to systematic errors. In the sensitivity calibration of the three detectors, the NNLS (Non Negative Least Square) constraint (Lawson and Hanson 1995; Désesquelles et al. 2009; Boutsidis and Drineas 2009), which forces the counts on each bin to be zero or positive, has been implemented in the FSA algorithm in order to avoid this problem.

Figure 4.1: Field measurement using the ZaNaI detector.

Figure 4.2: Field measurement using the CavaRad detector.

4.3 Application of the FSA-NNLS to in-situ gamma-ray spectroscopy

The FSA-NNLS method has been applied to the sensitivity calibration of two NaI(Tl) detectors dedicated to in-situ gamma-ray spectroscopy measurements, the ZaNaI and the CavaRad detector (see Fig. 4.1 and Fig. 4.2. For each detector a measurement campaign has been dedicated to the experimental validation of the calibration procedure, reported in Sec. 4.3.1 and Sec. 4.3.2.

4.3.1 Calibration of the ZaNaI detector

The ZaNaI detector is a 10.16 cm cubic shaped NaI(Tl) crystal housed inside a backpack and it is dedicated to static and dynamic in-situ gamma-ray measurements. The NaI(Tl) detector is coupled with a photomultiplier (PMT) base with integrated high-voltage supply, preamplifier and digital multichannel analyzer (MCA). The PMT base is connected via USB to a notebook which is intended both for powering the electronics and for storing the data. The ZaNaI is equipped also with auxiliary sensors like a GPS antenna and a pressure and temperature sensor which can be used to record the measurement location as well as the main environmental parameters.

In performing the efficiency calibration procedure of the ZaNaI detector, 9 natural calibration sites have been selected (see Table 4.1).

A variable number of samples from 5 to 12 was collected in random positions within 10 m radius in order to assess the degree of homogeneity of the site around the detector since more than 90% of gamma-rays detected by the sodium iodide are produced by the 7 m radius and 0.5 m deep area around (Grasty and others. 1979). The heterogeneity of each site is properly implemented by the errors which are dominated by the spread in the results of the collected samples in each calibration site. Only the CA1 site is not an outdoor site, but it is made by a pad of KCl fertilizer, used as

Table 4.1: The activity concentrations ($\pm$ 1σ uncertainty) of radionuclides measured in 9 sites selected for the sensitivity calibration of the ZaNaI detector. The errors correspond to the standard deviation of the average abundances. Data indicated as less than are the minimum detectable activities.

Site	K [10^{-2}g/g]	eU [μg/g]	eTh [μ/g]	Cs [Bq/kg]
CA1	53.9 $\pm$ 0.7	< 1.0	6.0 $\pm$ 0.5	< 1
CC2	0.06 $\pm$ 0.02	0.7 $\pm$ 0.3	0.6 $\pm$ 0.7	8 $\pm$ 4
GC1	0.07 $\pm$ 0.04	0.27 $\pm$ 0.08	1.14 $\pm$ 0.13	0.87 $\pm$ 0.04
GV1	4.9 $\pm$ 0.6	7.5 $\pm$ 1.1	7 $\pm$ 1	31 $\pm$ 18
PM2	2.26 $\pm$ 0.05	2.27 $\pm$ 0.18	10.7 $\pm$ 0.8	18 $\pm$ 9
RT1	0.10 $\pm$ 0.01	6.8 $\pm$ 1.1	1.74 $\pm$ 0.16	6 $\pm$ 5
SM1	1.54 $\pm$ 0.14	1.6 $\pm$ 0.3	8.6 $\pm$ 0.6	$26\ ^{+37}_{-26}$
SP2	2.92 $\pm$ 0.08	7.5 $\pm$ 0.4	39 $\pm$ 2	23 $\pm$ 2
ST2	7.8 $\pm$ 0.9	36 $\pm$ 5	124 $\pm$ 16	$61\ ^{+100}_{-61}$

potassium calibration site.

Spectra measured by placing the ZaNaI on the ground at the different calibration sites have been energetically calibrated and rebinned in order to have spectra with zero energy offset and 3 keV/channel. The sensitive spectra calculated with the new algorithm in the energy range [300-2900] keV are shown in Fig. 4.3. The sensitive spectra resolution can be severely affected by gain mismatch between the different site spectra, which has to be always calibrate properly. Finally, residual correlations between isotopes are still present in the sensitive spectra shape, due to the presence of all the radionuclides in most of the selected sites.

The NaI(Tl) detector was used within a larger project devoted to the investigation of the soil characteristics in the Ombrone basin (located in Tuscany Region) in morphologic, pedologic, and lithostratigraphic way. About 80 different sites have been measured, providing a large dataset for the validation of the calibration method. The results of the FSA-NNLS analysis are compared to the characterization performed by measurements on sample in laboratory with the MCA_Rad system.

For each site the 10.16 cm $\times$ 10.16 cm NaI(Tl) detector was used to perform 5 minutes ground measurements in-situ. In each site one sample was collected in the position where the detector was grounded and four samples were collected on the side bisectors of a 2 m side square centered at the grounded position of the detector. Each sample is treated in the same way as the one collected for the efficiency calibration of the system. The averages of the results obtained from measurements in laboratory for each site were used as reference to be compared with the outputs of the FSA-NNLS methods. The correlation factor, Ω, which minimizes the relative dispersion is obtained by using the following equation:

$$y = \sum_{i=1}^{80} \frac{(NaI_i - \Omega MCA_i)^2}{MCA_i^2} \tag{4.5}$$

where, MCA and NaI are referred to the radioisotopes concentrations obtained from laboratory

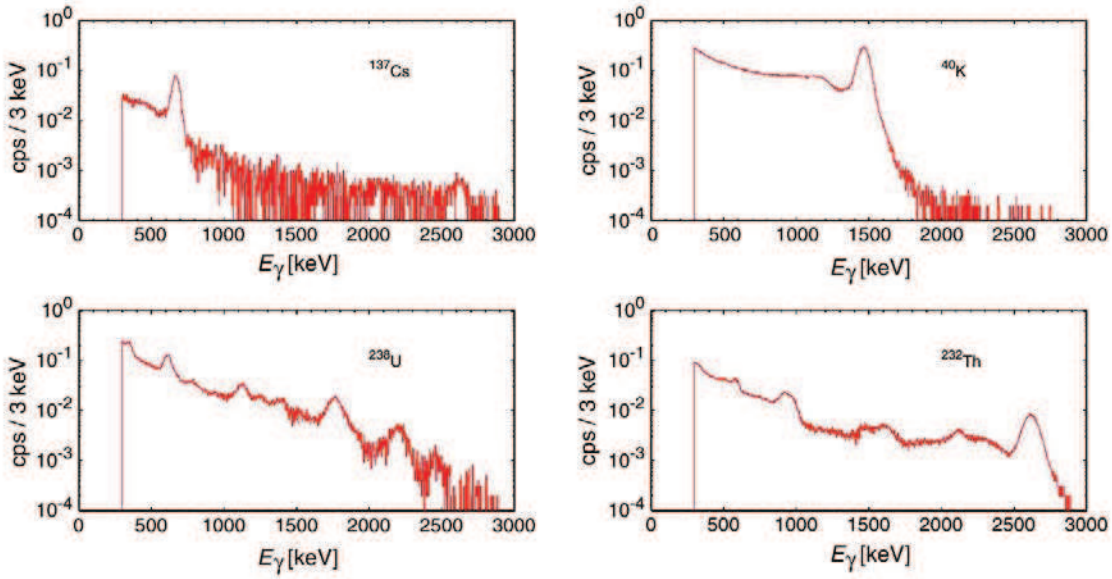

Figure 4.3: The sensitive spectra obtained for the ZaNaI detector through the FSA with NNLS constraint.

and in-situ measurements. Results reported in panel d) of Fig. 4.4 agree with a factor $\Omega = 1$, which guaranties the reliability of the method for all elements.

The correlation for the uranium element is affected by the atmospheric radon concentration at the time of the in-situ measurement, although this discrepancy is within the uncertainties. The correlation between the in-situ measurements, analyzed by the FSA-NNLS, and the MCA_Rad measurements for all 80 sites are for K, U and Th respectively in panel a), panel b) and panel c) of Fig. 4.4. The uncertainty reported on the MCA_Rad measurements is the standard deviation of the average calculated over the five collected samples. The uncertainties on the Ω factors are used as systematic uncertainties on the concentration measurements with the sodium iodide, since they contain both the contribution from the non homogeneity of soil ground and the systematics due to the analysis algorithm. The uncertainties found in this way are: 5% for the potassium, 14% for the uranium and 7% for thorium, which are smaller than the ones requested for outdoor in situ studies, for civil and also geological purposes.

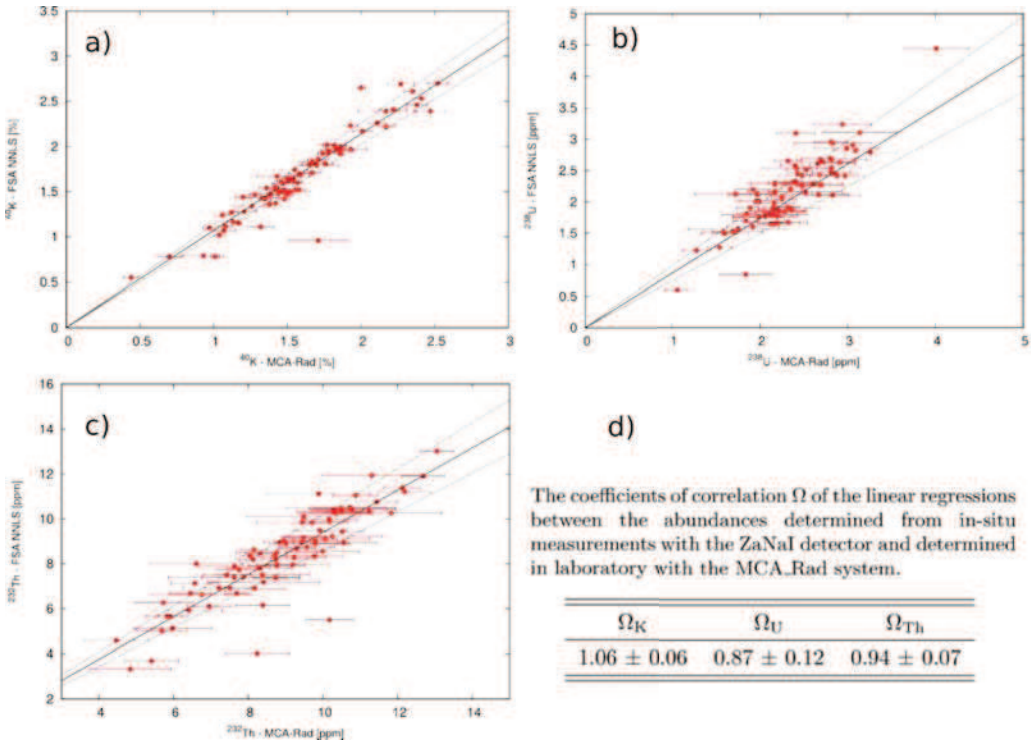

Figure 4.4: Correlations for K (panel a), U (panel b) and Th (panel c) between measurements performed by ZaNaI and MCA_Rad in 80 test sites. The coefficients of linear correlation obtained weighting the experimental uncertainties are reported in the table of panel d). Error bars show the 1σ statistical uncertainty.

4.3.2 Calibration of the CavaRad detector

The CavaRad detector is a portable collimated gamma-ray spectrometer whose functioning is based on the lead-plate method. The design of the CavaRad detector has been thought to attenuate the environmental noise without compromising the portability and without significantly extending the counting time, which are the major drawbacks of reducing the detector field of view by folding the spectrometer with lead. The CavaRad detector is essentially made up of a lead plate of 9.0 cm × 9.0 cm × 3.0 cm dimensions, which is fully automated to shield on/off a 7.6 cm cubic shaped NaI(Tl) crystal having an energy resolution of 7.3% at 662 keV (^{137}Cs), 5.2 % at 1172 and 1332 keV (^{60}Co). The lead plate is used to partially shield a target area of approximately 100 cm^2 that is defined as the Field Of View (FOV) of the detector. Subtracting from the spectrum acquired with shielding off (PbOut of the FOV) the spectrum obtained with the shielding on (PbIn the FOV), the Difference Spectrum (DS) is obtained which is estimated to have about 20% of the total counts collected with PbOut. The dimension of the lead plate and in particular the shielding thickness (34 g/cm^2) is crucial since it determines the quality of the DS and therefore the accuracy of the measurement. The obtained DS reproduces the collimation effect by filtering the surrounding background. The system is mounted

Table 4.2: The activity concentrations (± 1σ statistical uncertainty) of radionuclides measured in 10 natural sites selected for the sensitivity calibration of the CavaRad detector. The errors correspond to one standard deviation. The n/a annotation stay for non-available data, while data indicated as less than are the minimum detectable activities.

Site	K [10^{-2}g/g]	eU [μ/g]	eTh [μ/g]	Cs [Bq/kg]
K2	6.0 ± 0.1	4.9 ± 0.2	27.9 ± 1.1	10.2 ± 1.1
K4	2.8 ± 0.1	2.5 ± 0.3	13.4 ± 0.8	6.5 ± 0.8
U1	< 0.04	7.4 ± 0.2	< 1.0	2.0 ± 0.6
U3	0.05 ± 0.01	7.5 ± 0.2	< 1.0	< 1.4
Th1	2.1 ± 0.1	0.9 ± 0.1	4.2 ± 0.6	< 1.6
Th	2.3 ± 0.1	25.6 ± 0.5	360.7 ± 3.3	< 3.2
Cs1	0.5 ± 0.1	1.2 ± 0.2	< 3.9	1496 ± 13
H1	4.2 ± 0.1	12.3 ± 0.3	55.9 ± 1.5	< 2.8
H2	4.1 ± 0.1	8.0 ± 0.2	36.8 ± 1.3	< 2.6
Bckg1	n/a	n/a	n/a	n/a

on a rugged case in PVC where the NaI(Tl) detector is rigidly arranged in order to prevent possible damages on the field (Fig. 4.2). The NaI(Tl) detector is coupled with a photomultiplier (PMT) base with integrated bias supply, preamplifier and digital multichannel analyzer (MCA). It is powered through a universal serial bus (USB) communication connector by a notebook which is also used for data storage. The movement of the lead shield upon a conveyor belt is driven by an electric motor powered by a 9 V battery. The lead plate movement is automatically governed by an electronic set-up together with a JAVA program. The user can set also some data taking parameters (e.g. live time).

The CavaRad system is designed for in situ gamma spectroscopy for quantifying the abundances of radionuclides (i.e. ^{40}K, ^{238}U, ^{232}Th and ^{137}Cs) in a restricted area underneath the scintillation detector (NaI(Tl)). Its calibration is based on the selection of 10 calibration sites which have been characterized for the abundances of ^{40}K, ^{238}U, ^{232}Th and ^{137}Cs by collecting a sample underneath the target area of the CavaRad. A bulk sample is also collected around the target position within a radius of 1 meter, with the aim to check the homogeneity with respect to the target area. Collected samples were measured via laboratory gamma-ray spectroscopy measurements by using the MCA_Rad system (see Chapter2). Table 4.2 reports the abundances with their experimental uncertainties of radionuclides in the target area measured with the MCA_Rad system. From measurements on the bulk samples surrounding the target area we infer that the variability in the calibration sites is generally $< 30\%$ for ^{40}K and ^{238}U and $< 20\%$ for ^{232}Th. The calibration spectra of ^{137}Cs allows us to better reconstruct the measured spectra in the case of the presence of this radionuclide.

In each calibration site two measurements (PbOut and PbIn measurements) of 20 minutes each are performed placing the CavaRad system on the target location. A blank site, i.e. the site assumed to have negligible level of terrestrial radioactivity, is chosen 0.5 km offshore in the Adriatic Sea (Lido di Spina). The CavaRad system is mounted on an inflatable boat over approximately 3 m of water, which is enough to shield more than 99% of the seabed radioactivity. The main sources of background

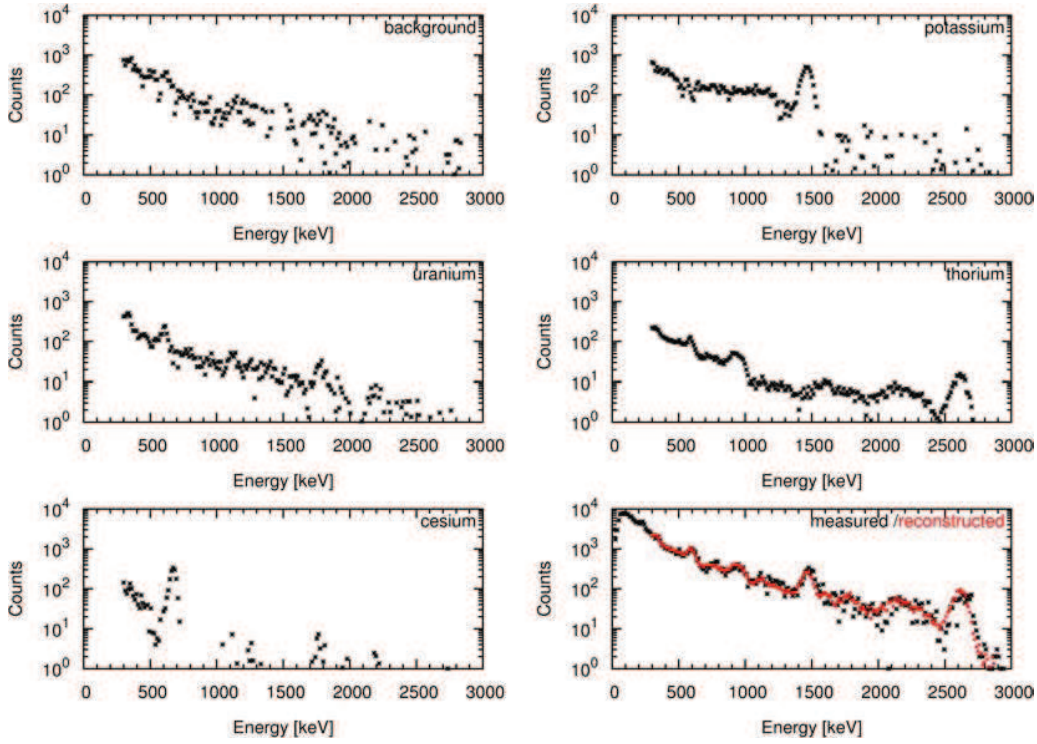

Figure 4.5: Fundamental standard spectra of background, ^{40}K, ^{238}U, ^{232}Th and ^{137}Cs obtained with the FSA-NNLS method applied to CavaRad system. In the last panel we report a typical measured/reconstructed spectrum having a reduced χ^2 of 1.2.

events are cosmic radiation, atmospheric radon (^{222}Rn) and the lead shield activity. The contribution from inflatable boat is considered negligible. Taking into account the low counting rate the acquisition time of this acquisition is extended to 1 hour. Each measured spectra is energetically calibrated and rebinned in order to have a spectrum with zero offset and 12 keV/channel. The FSA-NNLS method is applied to the calibration of the CavaRad detector in the [300 - 2900 keV] energy range, therefore the contamination by the lead plate (X-rays and backscattered events) on the spectrum quality is negligible. For each acquisition the DS is calculated, and then the FSA-NNLS algorithm described in Sec. 4.2 is applied using as know concentrations of the target areas the ones measured with MCA_Rad. The obtained standard spectra are shown in Fig. 4.5.

The performances of the CavaRad system and the robustness of the calibration method are cross-validated comparing the results obtained in-situ with those from MCA_Rad for 35 test sites: 20 sites belong to the Mt. Vulsini-Latera complex, a volcanic area of the Tuscan Magmatic Province, 8 sites correspond to acid effusive outcrops in the Euganean Hills region, 4 sites belong to the Ordovician terrigenous succession in Sardinia, the rest are chosen in random deposits of soil and sand. In each site a representative sample is collected from the target location investigated by the CavaRad system and measured in laboratory with the MCA_Rad system.

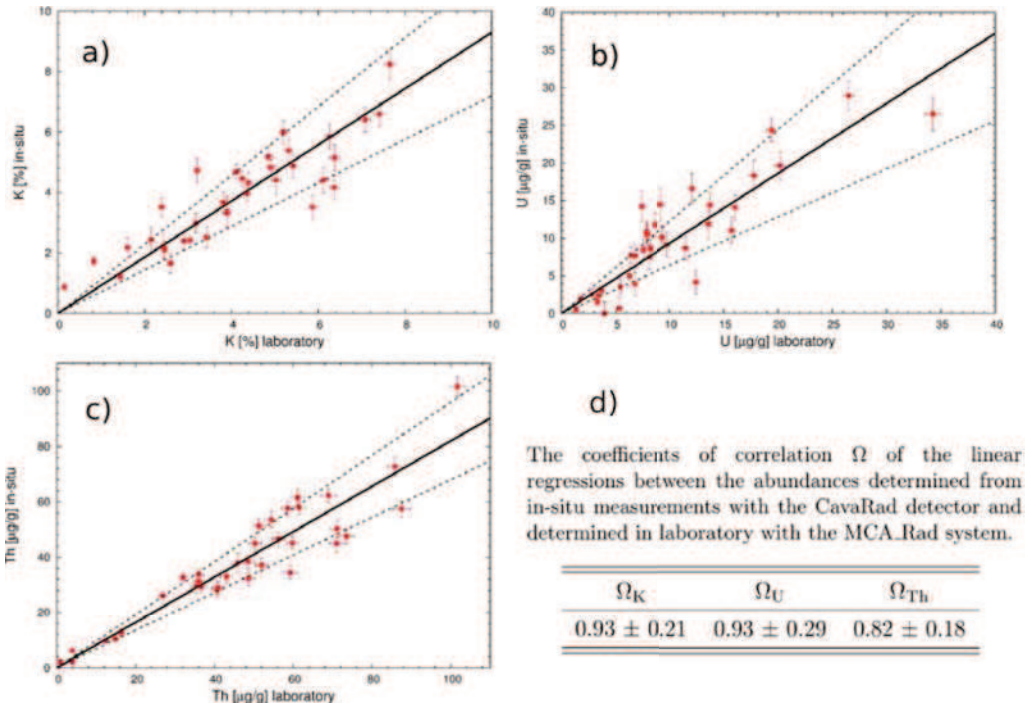

The coefficients of correlation Ω of the linear regressions between the abundances determined from in-situ measurements with the CavaRad detector and determined in laboratory with the MCA_Rad system.

Ω_K	Ω_U	Ω_{Th}
0.93 ± 0.21	0.93 ± 0.29	0.82 ± 0.18

Figure 4.6: Correlations for K (panel a), U (panel b) and Th (panel c) between measurements performed by CavaRad and MCA_Rad in 35 test sites. The coefficients of linear correlation obtained weighting the experimental uncertainties are reported in the table of panel d). Error bars show the 1σ statistical uncertainty.

On the base of measurements in laboratory the test sites are characterized by ranges of abundances $0.2 \div 7.7\ 10^{-2}$g/g, $1.3 \div 34.3\ \mu$g/g and $1.0 \div 101.7\ \mu$g/g for ^{40}K, ^{238}U and ^{232}Th respectively. The activity concentration of ^{137}Cs is found to be below the minimum detectable activity and therefore it has been neglected for this comparison. The average relative uncertainties affecting the in situ measurement are approximately 8% for ^{232}Th, 10% for ^{40}K and 20% for ^{238}U. Globally there is a good agreement between the results obtained in-situ and those measured in laboratory (see Fig. 4.6): the coefficients of the linear correlation Ω (see Eq. 4.5) obtained weighting the experimental uncertainties are compatible to unity at 1 sigma level. The CavaRad system seems to underestimate weakly the abundances measured with the MCA_Rad, which could be a consequence of the transparency of lead for photons with highest energy (i.e. 2614 keV of ^{208}Tl in the ^{232}Th decay chain). The relative percentage uncertainties of the Ω coefficients are used as systematic uncertainties on the concentration measurements obtained with CavaRad.

4.4 Monte Carlo simulation and FSA-NNLS ground calibration of the AGRS_16L detector

Monte Carlo methods refer to a broad class of computational techniques that use random sampling to address the study of stochastic processes, i.e. processes involving a sequence of states whose evolution is determined by random events. What a Monte Carlo simulation does is attempting to generate a sample of representative scenarios for a model in which a complete enumeration of all possible states would be prohibitive or impossible. Photon emission, transport and detection are examples of physical processes for which Monte Carlo simulations can be an ideal investigation tool. In this context, the power of Monte Carlo methods relies in the possibility of simulating the behavior of each single photon, by simulating both the emission and propagation of photons one-by-one. Monte Carlo simulations generate the random distances each photon travels before undergoing interactions in a specific medium, testing the interaction most likely to occur and determining full or partial energy deposition. Simulations allow to study the behavior of the system by investigating a variety of conditions that affect a gamma-ray spectroscopy measurement, such as the types and abundances of radionuclides, the characteristics of the traversed media and of the detection devices and the geometrical source-detector configuration. Here a GEANT4 based Monte Carlo code characterized by two independent simulation steps is used to reconstruct the fundamental spectra of the AGRS_16L system described in the Sec. 4.4.1.

4.4.1 Monte Carlo simulation strategy

The three major tasks of the Monte Carlo code consist in:

- generating random radioactive decays from a source having specific physical features;
- chasing photons propagation in different media, simulating random interactions;
- reconstructing the gamma-ray spectrum recorded by a specific detection system.

In principle, the photon flux that a detector intercepts comes from all the radioactive sources present in the environment, therefore the signal produced by a soil of infinite lateral dimension and infinite thickness should be reproduced. However, if the photon emission points are spread throughout a soil of infinite dimensions and if they radiate photons isotropically, the probability for a photon to reach the detector position is extremely low; as a consequence, the time needed for the simulation to attain enough statistics is dramatically high. Here a simulation structured in two independent steps is adopted whose strategy is based on a geometrical invariance.

From the symmetry of the problem a geometrical reversed modeling as the one illustrated in Fig. 4.7 produces the same photon flux as the one coming from a direct simulation of the real infinite source geometry. The idea behind the geometrical reversed model is that, for a homogeneous radioactive source and homogeneous traversed materials, a photon emitted from a given point inside a volume

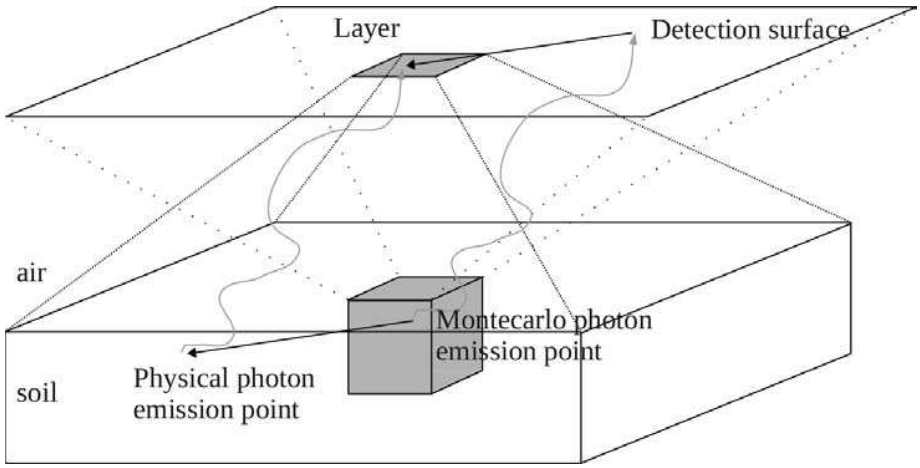

Figure 4.7: scheme of the photon emission and transport simulation strategy. After the simulation of photon emission from a cubic volume source and of photon transport through the air and soil materials, a geometrical transformation is applied in order to shift the photons arrival positions on the detection surface in a smaller layer centered above the cube position. The shift applied to the photons positions is equivalent to a shift applied to the photons emission points, without any change in photons path and interactions.

source travels a distance in soil and air equal to the distance traveled by a photon emitted from a laterally shifted point at the same depth. The Monte Carlo simulation of photon transport does not vary by shifting the emission point; indeed, the distance traveled in both soil and air remains the same, implying also that there is no difference in the interactions photons underwent. Using a cubic volume source and an infinite plane detection surface, which in principle can be placed at a desired height above the ground level, ensures to obtain the photon flux theoretically expected: this increases the Monte Carlo calculation efficiency reducing the simulation time. Once photons have been generated one-by-one from the emission point and tracked till they reach the detection surface (or till they lose all their energy or escape the global simulation volume), the first step is completed (see Fig. 4.8(a). The original theoretical geometry is then restored by shifting a posteriori the photons arrival positions on the plane surface in order to create a layer having the same areal dimension of the base of the cubic volume source. The areal dimension of the cubic volume source has to be chosen according to the dimensions of the detection systems which has to be simulated.

At this point a homogeneous layer is obtained, which contains the photon flux originating from an infinite volume source that the detection system intercepts for a specific height above the air-ground interface where the detection surface is located (see Fig. 4.8(b)). The expected radial and homogeneous patterns of the original and the transformed photons areal distributions shown respectively in Fig. 4.8(a) and Fig. 4.8(b) are observed also for the areal distributions of photons energies.

Some of the variables that can be set in the first step of the Monte Carlo simulation are: the geometry of the system, the materials used (in terms both of chemical composition and of density), the source configuration, the type of radionuclide emitting gamma radiation, the radionuclide distribution

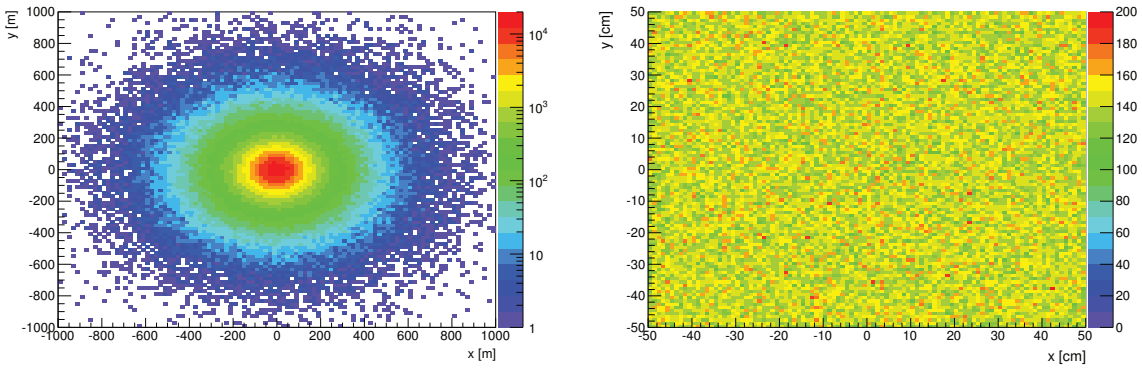

(a) Areal distribution of photons traveling upwards for a detection surface placed 100 m above the ground level. The colored scale corresponds to #photons/400 m^2.

(b) Areal distribution of photons traveling upwards on a layer of $1m^2$, obtained after the application of the photons positions shift. The colored scale corresponds to #photons/$1cm^2$.

Figure 4.8: The left and right panels are both obtained with a cubic source volume of 1 m linear dimension, located at the center of the soil volume and whose upper surface coincides with the air-ground interface. The photon emission points are homogeneously distributed inside the source volume and the events simulated are 20 million 1460.5 keV photons, isotropically radiated in the 4π solid angle. The soil and air material properties are the ones reported in Table 4.6.

in the source. The user can also decide the number and position of the detection surfaces, which do not act as physical media in which photons propagate (so they do not correspond to photons physical interactions) but they simply allow to record photons flow at a given height, along with all the useful informations regarding photon states.

The radioactive content of the source is defined setting the total number of photons generated inside the source volume and their energy according to the emission spectrum of the parent nuclide. The number of emitted photons is strictly related to the radionuclides concentrations and to the spectra acquisition time, as well as to the radionuclide species. Once the intensity of each emission line is known, the number of photons emitted per disintegration can be computed for each decay series (see Table 4.3). If the half-life and the isotopic abundance of each radionuclide are known, conversion factors from radioelement concentrations to specific activity a_i can be derived (see Table 4.3).

The photon emission rate can be computed knowing the number of photons emitted per decay, the conversion factors from unitary radioelement abundances to specific activity and the soil density (hence the mass of the source volume). The number of photons emitted per second by a unitary concentration of the i-th atomic species n_i can be determined as stated by Eq. 4.6:

$$n_i = N_i a_i \rho_{soil} V \tag{4.6}$$

where N_i is the number of photons emitted per decay by the i-th atomic species (photons/decay), a_i is the specific activity associated to a unitary concentration of the i-th atomic species (Bq/kg), ρ_{soil}

Table 4.3: The second column reports the number of photons emitted per decay for the ^{40}K, ^{238}U, ^{232}Th and ^{Cs} decay chains, assuming that the condition of secular equilibrium holds. The third columns reports the multiplication factors that allow to convert radionuclide concentrations into specific activity (IAEA 2003). K, U and Th are expressed as mass ratios respectively in 10^{-2}g/g, μ/g and μ/g units. For Cs the standard abundance unit of measurement is Bq/kg.

Radioelement	N [photons/decay]	Activity [Bq/kg]
^{40}K	0.107	1 10^{-2}g/g = 313
^{238}U	2.022	1 μ/g = 12.35
^{232}Th	2.437	1 μ/g =4.06
^{137}Cs	0.944	/

is the soil density (kg/m^3) and V is the source volume. The total number of photons γ_i, emitted on the average by a soil having radioelement concentration c_i during a time interval t, can be evaluated using Eq. 4.7.

$$\gamma_i = n_i c_i t \tag{4.7}$$

where n_i is the number of photons radiated per second by the i-th atomic species (photons/sec), c_i is the i-th radioelement abundance and t is the acquisition time (sec).

The output file obtained after the first simulation step is made up of a list of the "histories" of each single photon. There is one block of informations for each photon and each photon is characterized by its own identity number. The stored data are the position of the photon emission point inside the volume source, the energy the photon had at the emission time and the direction cosines indicating the initial photon direction of flight. The informations regarding photon energy, position and direction cosines are also separately recorded for each detection surface the photon traverses during the flight. When the photon escapes the global simulation volume or photon energy degrades below a given threshold, photon tracking stops.

The homogeneous layers for photons moving upwards and downwards obtained after the photons positions shift are used in the second stage as source of the photon flux impinging on the detector. The user can define the detector geometry and the materials the detector is made of. Furthermore, the detector can be designed as a system made up of different and separated sensitive devices. The number of energy channels and the detector gain can also be chosen. In the simulation of the spectra acquisition the detector is treated has a device having ideal energy resolution. This means essentially that the deposited energy inside the detector material is exactly equal to the detected energy and that the photopeak corresponding to a given gamma emission is reproduced in the spectrum as a delta function. The output of this second simulation stage is a file containing the spectra separately acquired by each sensitive volume constituting the total detection system. After the simulation of the detection process, a smoothing to the acquired spectra has to be applied, in order to take into account the finite energy resolution of the real detector. Fig. 4.9 illustrates the different processes involved in the second simulation step.

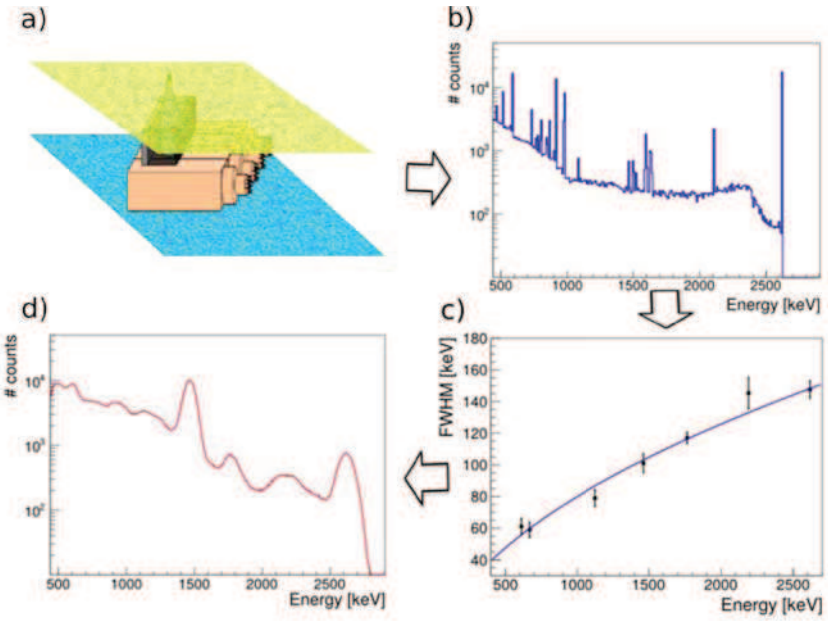

Figure 4.9: Diagram of the different processes involved in the second simulation step. In panel a) the Monte Carlo detector is placed in between the layers of photons moving downwards and photons moving upwards. The energy deposition inside the 4 4L crystals is recorded, producing a gamma-ray spectrum of an ideal detector having infinite energy resolution. Panel b) shows an example of Th spectrum recorded by the Monte Carlo detector. In order to simulate a real measurement, a smearing is applied to the recorded spectrum according to the experimental energy resolution charactering each detector. Panel c) shows the energy resolution curve in terms of FWHM as function of the gamma energy, as stated in Eq. 4.8. Finally, panel d) illustrates an example of Monte Carlo spectrum referred to the 16L acquisition volume and simulated for K, U and Th abundances respectively equal to 1.5 10^{-2}g/g, 1.4 μ/g and 4.1 μ/g.

4.4.2 Monte Carlo modeling of the AGRS_16L detector

The modeled detector is the AGRS_16L system, a modular instrument composed of four NaI(Tl) detectors (102 mm $\times$ 102 mm $\times$ 406 mm each) with a total volume of about 16 liters. Each crystal has a 1mm thick stainless steel housing and is coupled through a quartz glass window to a 89 mm diameter PMT with blue-green sensitive bialkali photocathode. The four crystals are lengthwise put one next to the other, with all the PMTs oriented in the same direction, aiming at reducing wiring issues. The signals are processed by a CAEN DT5740 module, a 32 channel 12 bit 62.5 MS/s waveform digitizer. The system is further equipped with a 1 liter "upward-looking" NaI(Tl) detector located on the upper plane, surrounded by 3 batteries, which is partially shielded from the ground radiation and which can be used to account for atmospheric radon (see Fig. 4.10(a) and Fig. 4.10(b)). During airborne surveys the AGRS_16L detector is mounted on a ultra-light vehicle called Radgyro, a prototype aircraft dedicated to multispectral airborne measurements (see Chapter 5). A power unit located on the upper plane and shared among all the sensors mounted on the aircraft supplies a 12V

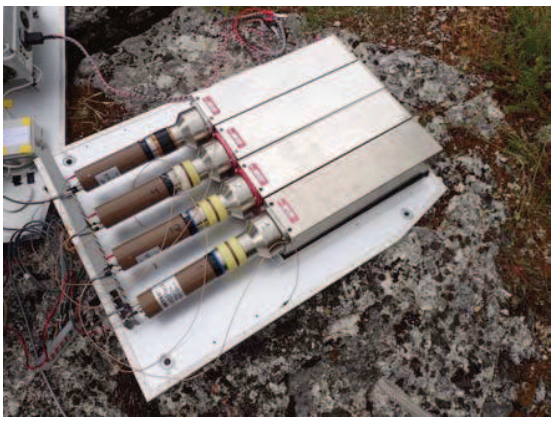

(a) Picture of the lower plane where the four 4L NaI(Tl) crystals of the AGRS_16L system are accomodated.

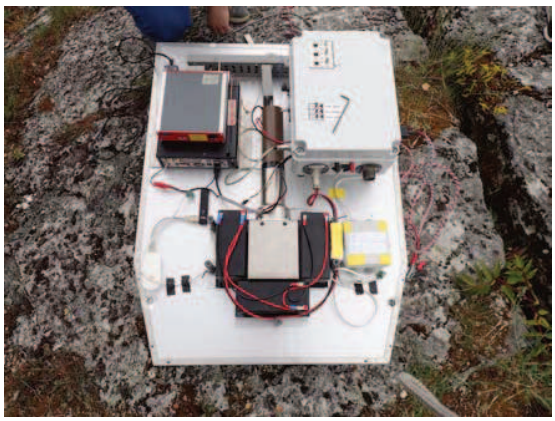

(b) Picture of the upper plane where the 1L NaI(Tl) crystal is housed, together with the power unit, the 3 batteries and the computer.

Figure 4.10: Picture of the AGRS_16L system, together with the two planes housing structure used to mount the detector on the aircraft.

bias voltage to the PMT bases of the spectrometers.

In order to simulate gamma-ray spectra measured by the AGRS_16L, a GEANT4 model of the detector has been developed: this set up is called MC_AGRS_16L: Table 4.4 reports the geometrical dimensions together with the physical and chemical characteristics of each constituent element of the Monte Carlo detector. Each detector component acts as a gamma-ray absorbing medium: the 4L crystals are the only sensitive elements of the model detector and behave as detectors having ideal energy resolution. For each crystal the acquired spectrum is made up of 2048 energy bins and the gain is equal to 8 keV per bin.

The smoothing of the infinite resolution spectra is done detector by detector by applying the individual energy resolution empirically determined on the base of the shapes of prominent photopeaks observed in the measured spectra, associated with the most intense gamma lines of the ^{238}U and ^{232}Th decay chains (basically the gamma emissions ^{214}Bi and ^{208}Tl) and the single gamma emissions of ^{40}K and ^{137}Cs. Individual photopeaks have been fitted according to the expected Gaussian shape, providing a mean value and a FWHM value. For each detector, the FWHM values have subsequently been fitted according to the Eq. 4.8, providing a FWHM energy resolution curve as the one shown in panel c) of Fig. 4.9.

$$FWHM = a \cdot \sqrt{E} + b \tag{4.8}$$

The smearing of the infinite energy resolution spectra has been performed distributing the number of counts recorded in each energy bin according to a Gaussian probability distribution function, whose parameters vary from bin to bin. The mean value of a specific Gaussian corresponds to the energy associated to the bin center, while the FWHM is determined for the same energy using the analytical resolution function obtained from the fit. For each radioelement, the total spectrum has been created

Table 4.4: Geometrical dimensions, physical and chemical features of the components of the MC_AGRS_16L model.

MC_AGRS_16L component	Dimensions [mm]	% by weight	Density [g/cm^3]
4L crystal	width = 101.6	100 NaI	3.67
	height = 101.6		
	length = 406.4		
Crystal housing	thickness = 1	69 Fe	7.93
	top plate = 11	19 Cr	
	bottom plate = 4.75	9 Ni	
		2 Mn	
		1 Si	
PMT	radius = 45	96 Air	0.34
	length = 146	4 Cu	
1L crystal	width = 101.6	100 NaI	3.67
	height = 65		
	length = 101.6		
Battery	width = 75	79 Air	2.41
	height = 69	21 Pb	
	length = 148		
PC	width = 185	93 Air	0.6
	height = 60	7 Cu	
	length = 235		
Power Unit	width = 235	70 $C_4H_6O_3$	0.84
	height = 129	30 Air	
	length = 315		
Plane	width = 656	75 $C_4H_6O_3$	0.30
	height = 20	25 Air	
	length = 851		

Table 4.5: Activity concentrations of radionuclides measured in 10 natural sites and 1 artificial pad made up with KCl, selected for the sensitivity calibration of the AGRS_16L detector. Reported values are given as average abundances ± 1 standard deviation.

Site	K [10^{-2}g/g]	eU [μg/g]	eTh [μg/g]	Cs [Bq/kg]
KCl	54 ± 3	2 ± 1	6.0 ± 0.5	1 ± 1
ASIAGO	0.82 ± 0.18	3.2 ± 1.4	6.1 ± 1.0	231 ± 39
LOCALITA' OSTERIA	1.01 ± 0.10	10.2 ± 0.8	10.1 ± 1.2	285 ± 106
BAONE	2.65 ± 0.09	2.77 ± 0.02	28.9 ± 1.3	3.5 ± 1.3
MONSELICE	2.80 ± 0.11	25.1 ± 1.3	20.2 ± 1.7	7.1 ± 1.0
RAPOLANO	0.04 ± 0.01	8.0 ± 0.2	1.0 ± 0.2	4.0 ± 2.3
SAN CASCIANO	1.76 ± 0.05	4.9 ± 0.5	63.7 ± 1.3	5.0 ± 1.3
SCHIO	1.80 ± 0.06	23.0 ± 1.7	17.0 ± 0.8	39.9 ± 3.4
SORANO	2.79 ± 0.07	7.0 ± 0.4	38.7 ± 1.5	13.4 ± 1.8
SORDINO	2.02 ± 0.08	3.1 ± 0.2	13.8 ± 0.7	7.2 ± 0.8
PORTO GARIBALDI	1.44 ± 0.08	1.1 ± 0.3	3.7 ± 0.4	1 ± 1

as the sum of the two smoothed spectra associated to photons moving upwards and downwards.

4.4.3 Monte Carlo and experimental ground fundamental spectra of the AGRS_16L detector

The Monte Carlo method described in Sec. 4.4.1 and Sec. 4.4.2 and the FSA-NNLS method based on the χ^2 minimization of experimental measurements have been applied to the ground calibration of the AGRS_16L detector, providing respectively the Experimental Fundamental Spectra (EFS) and the Monte Carlo Fundamental Spectra (MCFS). The ideal characteristic features of a calibration measurement are suitable for the employment of the Monte Carlo method since natural calibration sites are chosen for their flat morphology and for their radionuclide distribution (which should be as uniform as possible), which are the same underlying assumptions at the base of the Monte Carlo simulation strategy. For the calibration of the AGRS_16L detector 10 natural calibration sites have been selected and characterized via laboratory gamma-ray spectroscopy measurement on collected soil samples (see Table 4.5 and Fig. 4.11). For calibrating for K, an artificial mattress made up with KCl fertilizer was used (KCl site in Table 4.5) as shown in Fig. 4.12(a). For the assessment of the background spectrum a measurement over sea water has been performed by placing the AGRS_16L detector on a boat (Fig. 4.13). The measurement has been performed for about 8 hours 15 km offshore where the water depth was approximately 30 m.

The FSA-NNLS method has been applied to the ground calibration of the AGRS_16L according to the procedure illustrated in the flow-chart of Fig. 4.14, which is subdivided into 5 steps. The first step involves the determination of the C, σ_C and N matrices, where C contains the K, U, Th and Cs abundances of the calibration sites, σ_C the uncertainties on the abundances and N the background

Figure 4.11: Soil samples collected at a natural calibration site to be characterized via laboratory gamma-ray spectroscopy measurements.

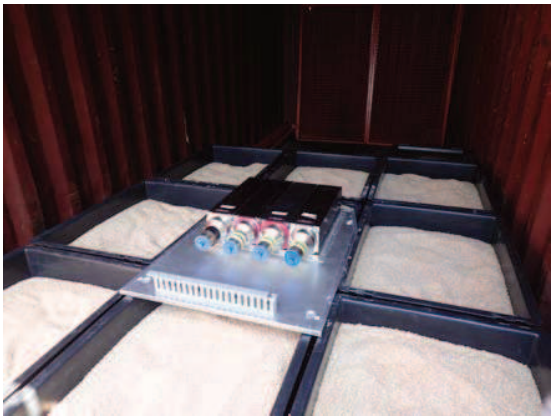

(a) Acquisition of a ground calibration measurement with the AGRS_16L detector using the KCl pad.

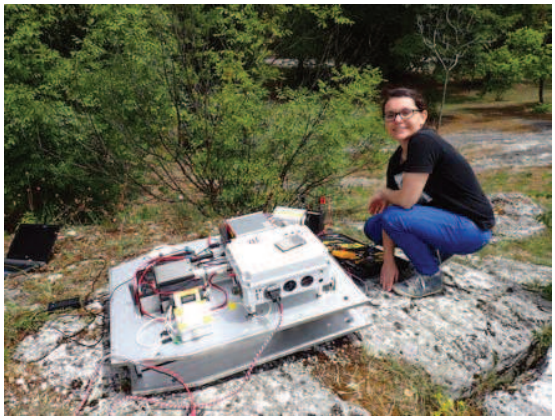

(b) Acquisition of a ground calibration measurement with the AGRS_16L detector.

Figure 4.12: Ground calibration of the AGRS_16L detector.

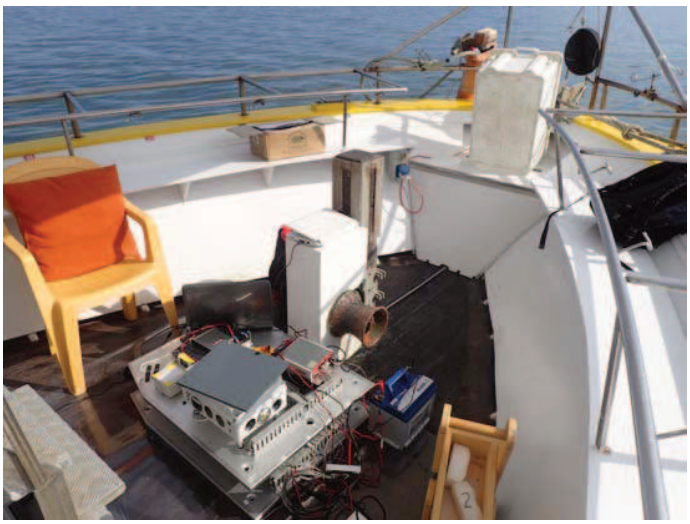

Figure 4.13: Background measurement over sea water performed for the ground sensitivity calibration of the AGRS_16L detector.

corrected energy calibrated spectra in the energy range 450 ÷ 2900 keV, corresponding to 307 energy channels having 8 keV width.

In the second step, for each calibration site and for each radionuclide, a random sampling of the specific element concentration is performed according to a Gaussian probability density function. The obtained C^{random} matrix is employed in the FSA-NNLS algorithm applied to the AGRS_16L calibration, which is aimed at determining the sensitivity matrix S containing the K, U, Th and Cs EFSs.

Once the matrix S has been determined, it is employed in the Inverse Analysis step in order to reconstruct the AGRS_16L spectra acquired at calibration sites, obtaining the matrix of back-estimated concentrations $\widetilde{C}$. If the S matrix determined at the end of the Calibration step is a good representation of the AGRS_16L response function, then the $\widetilde{C}$ matrix should "resemble" the C matrix, i.e. the concentrations evaluated by analyzing the experimentally measured spectra with the AGRS_16L sensitivity matrix S are comparable with the abundances independently measured in laboratory on collected soil samples.

The last statement is verified in the Validation step where for K, U and Th a linear regression among $\widetilde{C}$ and C abundances is performed, taking into account the uncertainties on the abundances populating the C matrix contained in the σ_C matrix. If a good linear regression is obtained simultaneously for K, U and Th (in terms of allowed intervals of the slope and intercept parameters), then the S matrix is stored in the database of good EFSs candidates, otherwise the entire procedure is started again from the beginning of the Calibration phase.

Fig. 4.15 shows the EFSs determined after the selection of the best candidate matrices S and determined also according to the shape of each vector matrix, i.e. of the ^{40}K, ^{238}U, ^{232}Th and ^{137}Cs

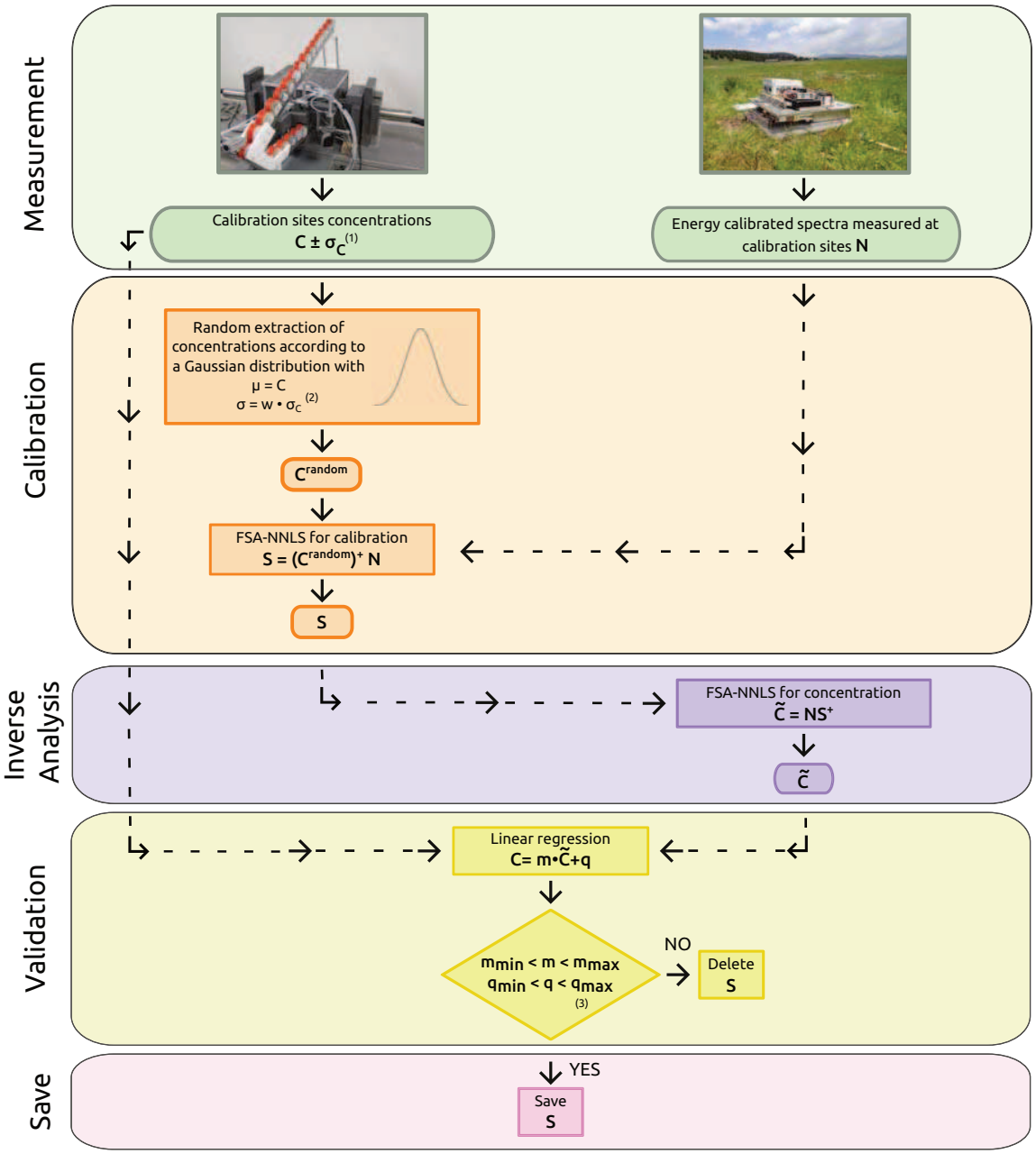

Figure 4.14: Flow chart illustrating the 5 steps performed in the determination of the AGRS_16L experimental fundamental spectra, corresponding to the Measurement, Calibration, Inverse Analysis, Validation and Save steps. (1) For the construction of the σ_C matrix, the standard deviations reported in Table 4.5 are adopted for K, U and Th if they are greater than 10%, otherwise 10% is chosen. (2) In order to investigate a wider concentration phase space, each value of the σ_{ij} used in the Gaussian random sampling of the $\widetilde{c}_{ij}$ matrix element is obtained scaling the $\sigma_{C_{ij}}$ by w equal to 4. (3) S matrix candidates are saved if $0.9 < m_{K,U,Th} < 1.1$, $-0.1 < q_K < 0.1$ and $-0.2 < q_{U,Th} < 0.2$.

fundamental spectral shapes.

The linear regression selection cuts have been applied to the K, U and Th species: for what concerns Cs the picture is more complex as it can have a high spatial variability in the environment. This variability emerges from the laboratory measurements, as the typical standard deviation of Cs abundances on collected samples is on the order of 20%. Moreover, Cs generally has a not uniform vertical distribution, showing normally in undisturbed soils an activity concentration that exponentially decreases with increasing depth (Perrin et al. 2006). For this reason it has been decided to apply selection cuts only on K, U and Th reconstructed abundances, as these species are generally more homogeneously distributed in the environment.

The NNLS algorithm applied to the FSA assures in the calibration stage that the fundamental spectra do not have negative counts in each energy bin. On the other hand, even if the non-negative constraint is applied to the solution of the χ^2 minimization, a pure least square method accommodates for the minimum discrepancy between observed and expected quantities but is not aware of the physics of the event under investigation. In other words, the NNLS method is not informed about the intensities and energies of the gamma emission lines as well as about the existence of a Compton continuum associated to each photopeak. As a consequence, the χ^2 minimization can produce artifacts and cross-talk effects in the spectral shapes: for instance it is not unusual to obtain a Cs EFS comprising the sole photopeak where the Cs Compton spectral shape is inherited by the EFS of another radionuclide. It can also happen that interferences appear in the spectral shape of a given EFS in correspondence of a photopeak of a different nuclear species, e.g. in the case of the Cs and U EFSs around the Cs gamma emission line at 662 keV, which is close in energy to the 609 keV emission of ^{214}Bi, belonging to the ^{238}U decay chain (Fig. 4.15). This is a delicate point of the sensitivity calibration procedure which is strictly connected also with the characteristics of the natural calibration sites. Indeed, in addition to Cs intrinsic variability in the environment and to its typically not uniform distribution with soil depth, laboratory measurements showed that natural sites characterized by sizable amounts of Cs have also relatively high content of U and in some cases also of Th, which also has a gamma line close to the Cs one, corresponding to the 583 keV emission of ^{208}Tl. This aspect makes even harder the disentanglement mainly between Cs and U, but at some degree also Th.

The Monte Carlo method for the AGRS_16L calibration on the other side does not suffer from residual correlations since each radionuclide fundamental spectrum is obtained independently of all the other radionuclides. The $i-th$ fundamental spectrum is the result of the detection of gamma-rays originating from the $i-th$ decay series by the AGRS_16L model detector. No chi square minimization process is involved, which can give rise to spectral structures that are unrelated to the actual emission lines of the investigated nuclear species.

The Monte Carlo simulation has been performed by using the soil and air materials having density and compositions reported in Table 4.6. A uniform spatial distribution of the photon emission points inside the source volume (1m $\times$ 1m $\times$ 1m) has been adopted, together with an isotropic photon emission from the decaying radionuclide. The simulation of emission and propagation of photons

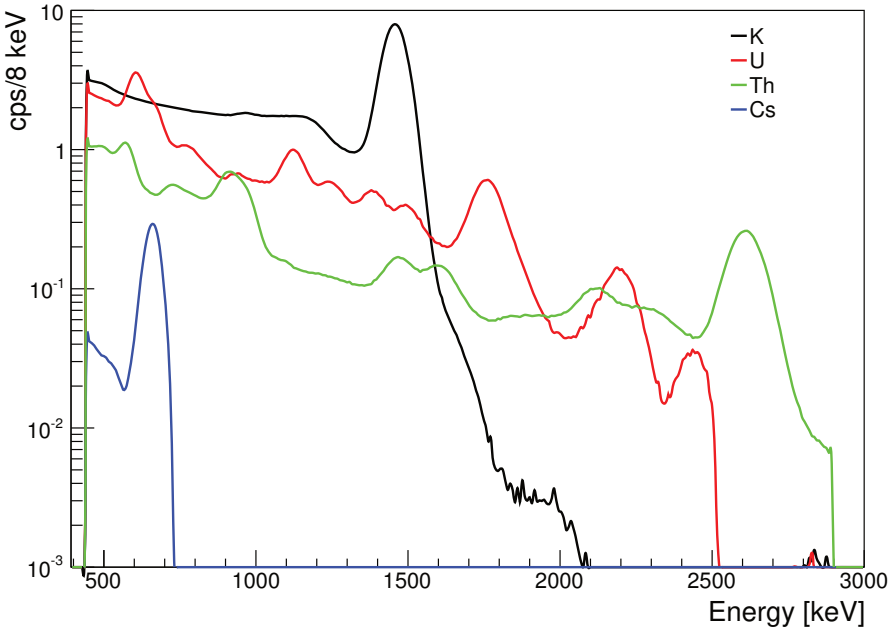

Figure 4.15: K, U, Th and Cs Experimental Fundamental Spectra (EFS) obtained with the application of the FSA-NNLS method to the sensitivity calibration of the AGRS_16L detector.

coming from the decay of K, U, Th and Cs has been separately performed according to their specific gamma emission spectra. Considering that the Monte Carlo simulation of the photon emission process takes into account the intensities of the individual gamma lines, according to Eq. 4.6 and Eq. 4.7 the Monte Carlo simulated statistics can be scaled in order to compare Monte Carlo simulated spectra with experimental spectra referred to a given acquisition time and acquired at a calibration site characterized by given abundances. Fig. 4.16 shows an example of Monte Carlo reconstruction of the experimental spectrum acquired at the Porto Garibaldi natural calibration site. The Monte Carlo reconstructed spectra, referred to 10 minutes acquisition time, are displayed for mean, mean $+1\sigma$ and mean -1σ abundances of the calibration site (see Table 4.5). With the same strategy, appropriate scaling factors can be computed to reconstruct the Monte Carlo Fundamental Spectra (MCFS) (see Fig. 4.17) which by definition correspond to the spectra measured by the AGRS_16L system for a 1 second acquisition time and a unitary radionuclide concentration.

The MCFSs, together with the experimentally measured background spectrum, have been used to analyze with the FSA-NNLS method the spectra acquired by the AGRS_16L detector at calibration sites. A linear regression between the concentration values C of calibration sites obtained from HPGe measurements and the ones obtained with the application of the FSA-NNLS method with the MCFSs ($\widetilde{C}_{MC}$) has been performed. The $\widetilde{C}_{MC}$ values have been also compared with the concentration values obtained with the application of the FSA-NNLS method with the EFSs ($\widetilde{C}$). Fig. 4.18, Fig. 4.19 and

Table 4.6: Chemical composition and density of the soil and air materials adopted in the Monte Carlo simulation of the AGRS_16L fundamental spectra at ground level. Soil chemical composition and density are the ones published respectively by Beck et al. 1972 and Telford et al. 1990, while air chemical composition and density are the ones referred to standard air at sea level at 15°C.

Material	Density [g/cm^3]	Composition	% by weight
Air	$1.225 \cdot 10^{-3}$	N_2	75.5
		O_2	23.2
		Ar	1.3
Soil	1.9	SiO_2	67.5
		Al_2O_3	13.5
		Fe_2O_3	4.5
		H_2O	10.0
		CO_2	4.5

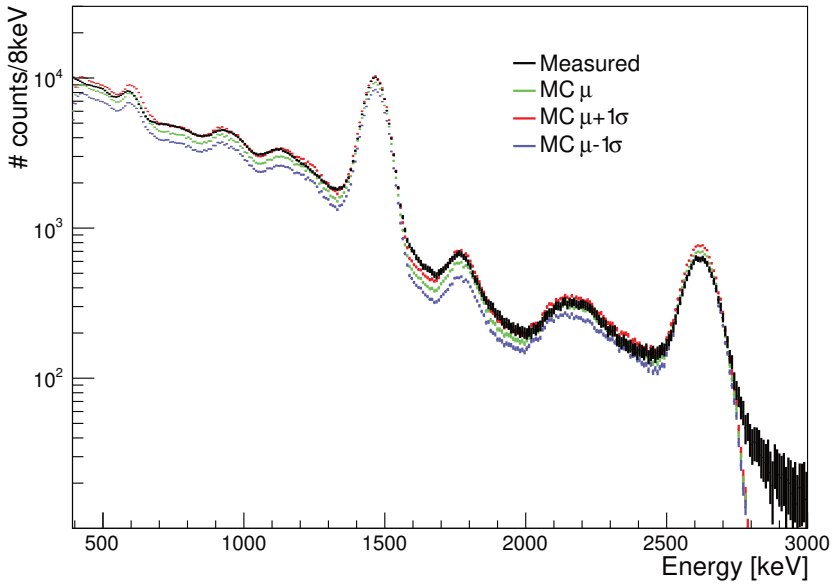

Figure 4.16: In black the 10 minutes spectrum (after background subtraction) measured at the Porto Garibaldi site and in green the simulated spectrum with average radionuclide abundances, respectively equal to a(K)= (1.44 ± 0.14) 10^{-2}g/g, a(U) = (1.12 ± 0.26) μg/g and a(Th) = (3.75 ± 0.38) μg/g. The spectra MC $\mu + 1\sigma$ (red) and MC $\mu - 1\sigma$ (blue) are obtained rescaling with $\pm\sigma$ abundances for each radioisotope.

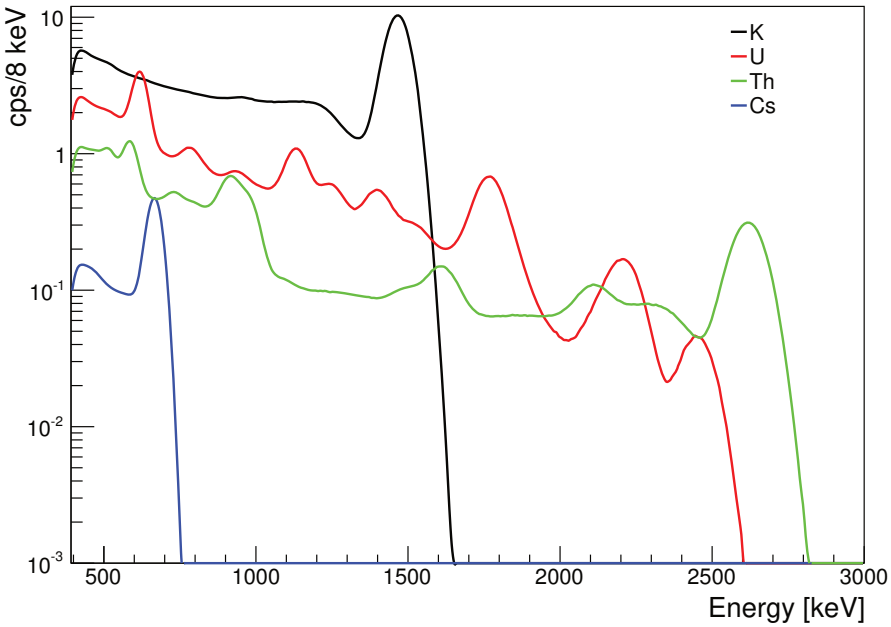

Figure 4.17: K, U, Th and Cs Monte Carlo Fundamental Spectra (MCFS) simulated at ground level for the AGRS_16L detector.

Fig. 4.20 shows the results attained for K, U and Th respectively. In panel d) of each figure a table listing the linear regression parameters is reported.

For what concerns the determination of the Th fundamental spectrum there is a good agreement between the three datasets corresponding to the C, $\widetilde{C}$ and $\widetilde{C}_{MC}$ abundances. The agreement emerges not only in terms of parameters of the linear regression lines but also in terms of r^2 coefficient of determination. Moreover, the concentration values belonging to the $\widetilde{C}$ and $\widetilde{C}_{MC}$ matrices, although being globally in agreement with the laboratory measurements C, display the same kind of deviation from the regression lines (see panel a) and b) of Fig. 4.20). This translates in an excellent linear correlation among $\widetilde{C}$ and $\widetilde{C}_{MC}$ values, denoted by a coefficient of determination equal to 0.996 and by a slope and intercept linear curve parameters compatible with a bisection line. This is a remarkable result as the two sensitivity calibration procedures that lead to the determination of the EFSs and the MCFSs are completely independent one from the other, one relying on the FSA-NNLS algorithm and the characterization with HPGe measurements of the calibration sites, the other resulting from a pure Monte Carlo modeling of radionuclide sources, photon propagation and interaction with the detector materials.

For what concerns U, a much higher variability is observed between reconstructed concentration values ($\widetilde{C}$ and $\widetilde{C}_{MC}$) and laboratory measurements (C), which is manifested in terms of relatively poor r^2 coefficients of determination. Although globally the parameters of the linear regression lines are

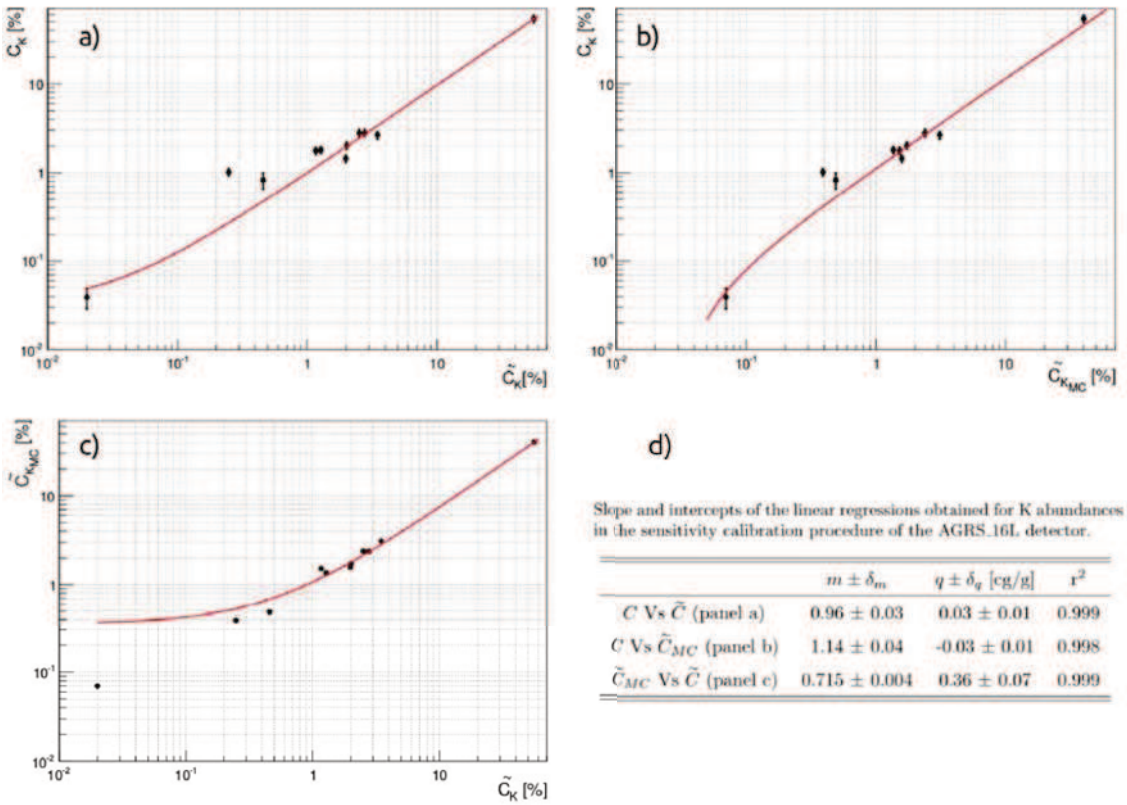

Slope and intercepts of the linear regressions obtained for K abundances in the sensitivity calibration procedure of the AGRS_16L detector.

	$m \pm \delta_m$	$q \pm \delta_q$ [cg/g]	r^2
C Vs $\widetilde{C}$ (panel a)	0.96 ± 0.03	0.03 ± 0.01	0.999
C Vs $\widetilde{C}_{MC}$ (panel b)	1.14 ± 0.04	-0.03 ± 0.01	0.998
$\widetilde{C}_{MC}$ Vs $\widetilde{C}$ (panel c)	0.715 ± 0.004	0.36 ± 0.07	0.999

Figure 4.18: Linear regressions for K between C and $\widetilde{C}$ (panel a), C and $\widetilde{C}_{MC}$ (panel b) and $\widetilde{C}_{MC}$ and $\widetilde{C}$ (panel c), where C are the concentration values obtained by measuring samples collected at calibration sites with the MCA_Rad system (Table 4.5), $\widetilde{C}$ and $\widetilde{C}_{MC}$ are the concentration values obtained by reconstructing measured spectra at calibration sites with EFSs and MCFSs respectively. The table in panel d) reports the values of the linear regression coefficients together with the r^2 coefficient.

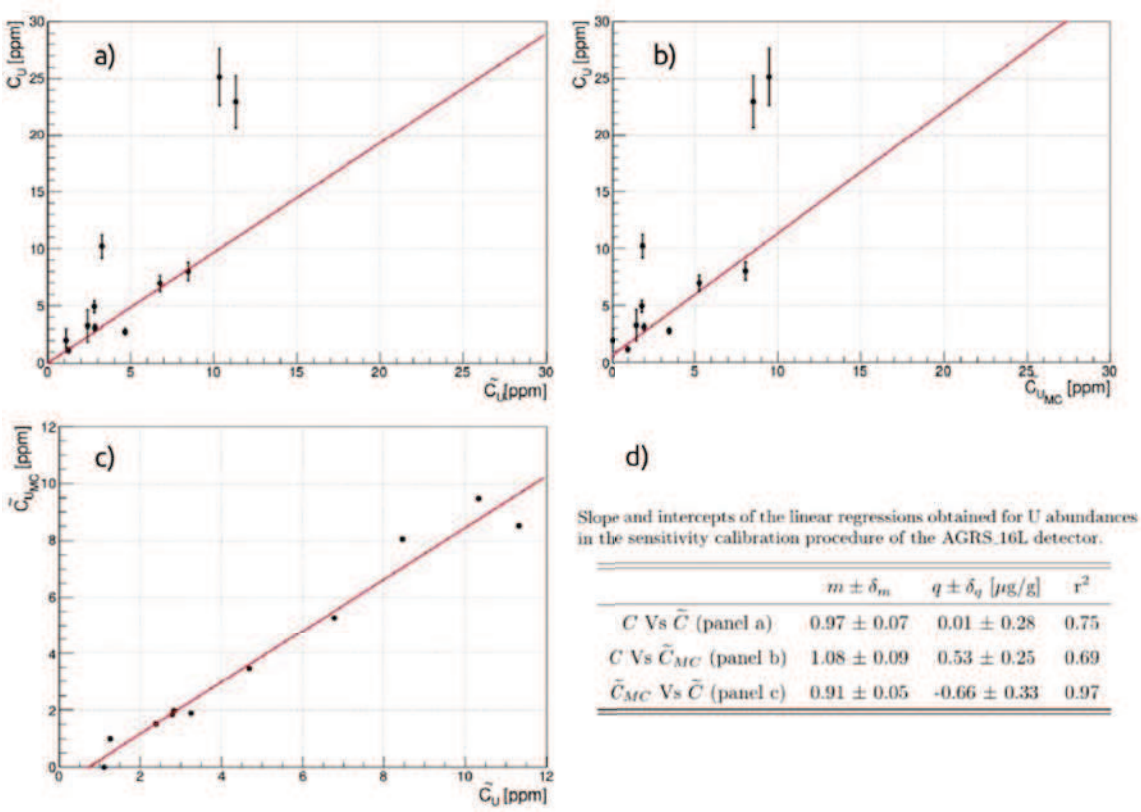

Slope and intercepts of the linear regressions obtained for U abundances in the sensitivity calibration procedure of the AGRS_16L detector.

	$m \pm \delta_m$	$q \pm \delta_q$ [μg/g]	r^2
C Vs $\widetilde{C}$ (panel a)	0.97 ± 0.07	0.01 ± 0.28	0.75
C Vs $\widetilde{C}_{MC}$ (panel b)	1.08 ± 0.09	0.53 ± 0.25	0.69
$\widetilde{C}_{MC}$ Vs $\widetilde{C}$ (panel c)	0.91 ± 0.05	-0.66 ± 0.33	0.97

Figure 4.19: Linear regressions for U between C and $\widetilde{C}$ (panel a), C and $\widetilde{C}_{MC}$ (panel b) and $\widetilde{C}_{MC}$ and $\widetilde{C}$ (panel c), where C are the concentration values obtained by measuring samples collected at calibration sites with the MCA_Rad system (Table 4.5), $\widetilde{C}$ and $\widetilde{C}_{MC}$ are the concentration values obtained by reconstructing measured spectra at calibration sites with EFSs and MCFSs respectively. The table in panel d) reports the values of the linear regression coefficients together with the r^2 coefficient.

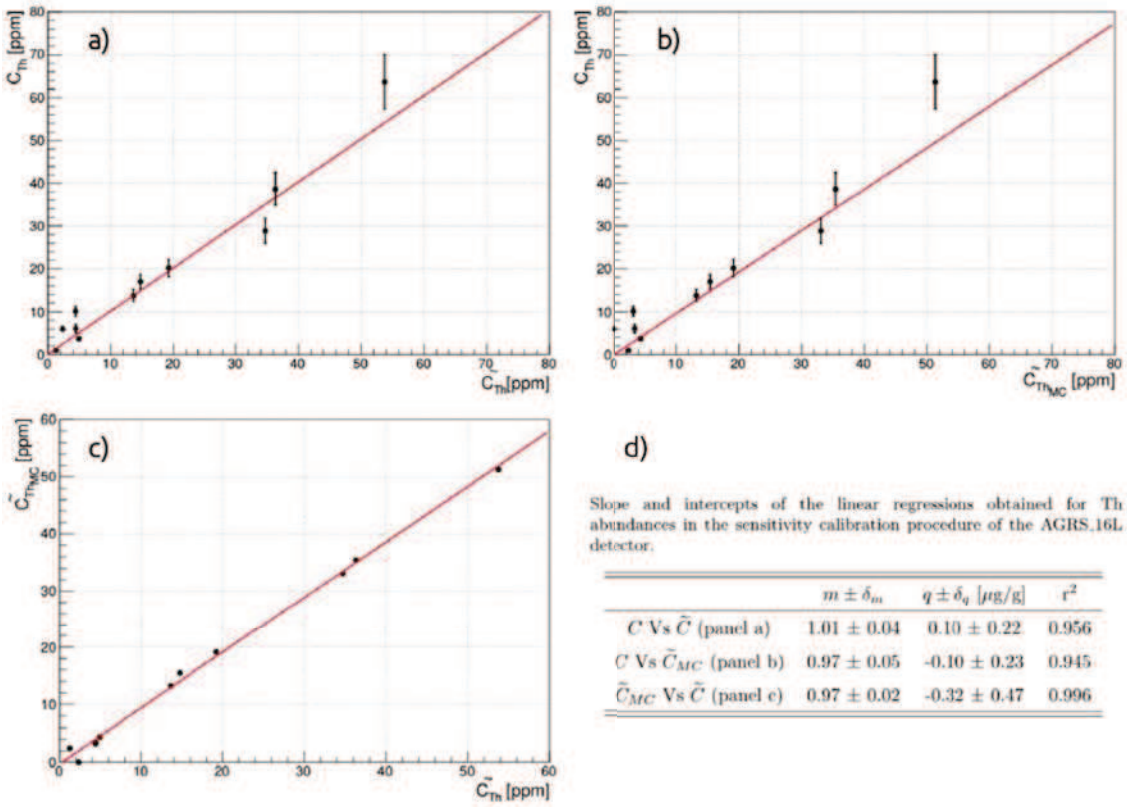

Slope and intercepts of the linear regressions obtained for Th abundances in the sensitivity calibration procedure of the AGRS_16L detector.

	$m \pm \delta_m$	$q \pm \delta_q$ [μg/g]	r^2
C Vs $\widetilde{C}$ (panel a)	1.01 ± 0.04	0.10 ± 0.22	0.956
C Vs $\widetilde{C}_{MC}$ (panel b)	0.97 ± 0.05	-0.10 ± 0.23	0.945
$\widetilde{C}_{MC}$ Vs $\widetilde{C}$ (panel c)	0.97 ± 0.02	-0.32 ± 0.47	0.996

Figure 4.20: Linear regressions for Th between C and $\widetilde{C}$ (panel a), C and $\widetilde{C}_{MC}$ (panel b) and $\widetilde{C}_{MC}$ and $\widetilde{C}$ (panel c), where C are the concentration values obtained by measuring samples collected at calibration sites with the MCA_Rad system (Table 4.5), $\widetilde{C}$ and $\widetilde{C}_{MC}$ are the concentration values obtained by reconstructing measured spectra at calibration sites with EFSs and MCFSs respectively. The table in panel d) reports the values of the linear regression coefficients together with the r^2 coefficient.

quite satisfactory, reconstructed abundances are sparsely distributed with respect to MCA_Rad average abundances. This kind of result highlights the intrinsic vulnerability related to the experimental sensitivity calibration procedure: the determination of EFSs vitally depends on the the abundances (and uncertainties) assigned to natural calibration sites on the base of laboratory measurements on collected samples, which are characterized by different sources of uncertainty and especially by different fields of view. In order to keep this susceptibility as much as possible under control, using a relatively high number of calibration sites can be a strategy: this aspect can give an aid to better constraint the modeling of the overall scintillation detector response function on the base of a relatively high number of experimental measurements. This insidious issue vaguely seems to emerge as reconstructed abundances $\widetilde{C}$ and $\widetilde{C}_{MC}$ show similar deviations with respect to C abundances and consequently the r^2 coefficient of determination substantially improves in the $\widetilde{C}_{MC}$ Vs $\widetilde{C}$ linear regression.

Concerning K, in addition to the potential issues just specified, there is a further delicate point as there are among the calibration sites two particular cases corresponding to Rapolano and KCl (se Table 4.5). The peculiarity of the Rapolano site resides in its very low K activity concentration, which is almost equal to the minimum detectable activity of the MCA_Rad system. On the opposite side of the K abundances axis there is the KCl site, which is not really a natural calibration site but a sort of artificial pad made up with potassium fertilizer having limited dimensions, therefore not properly reproducing the geometrical characteristics of a calibration site. The linear regression between C and $\widetilde{C}$ gives good results by construction: however, it is important to keep in mind that the extreme points constraining the linear regression curve can be affected by the mentioned problematic aspects. The agreement between C and $\widetilde{C}_{MC}$ is less satisfactory. The reason for this disagreement at the level of $\sim$15% can be indeed searched, among other factors, in the poor reconstruction of the KCl site abundance which can suffer both for geometrical effects (as the Monte Carlo simulation strategy is based on the hypothesis of infinite and homogeneous volume source) and for different density and chemical composition of the source material. Considering the central range of K abundance values characterizing the calibration sites ($0.5\ 10^{-2}$g/g $<$ K $<$ $3.5\ 10^{-2}$g/g, which is not far from the typical environmental range of variability) the discrepancy between $\widetilde{C}$ and $\widetilde{C}_{MC}$ is at the level of 10%, however a deeper investigation of the issues encountered in the determination of the K EFS and K MCFS is highly desirable.

4.5 Final Remarks

In-situ and airborne gamma-ray spectroscopy with sodium iodide scintillators is one of the most powerful techniques for the measurement of radionuclides concentration in the environment. The main advantages are the relatively high efficiency, the modest time consumption, the portability, and the reasonable cost of the detector with respect to competing systems. The Full Spectrum Analysis (FSA) with Non Negative Least Square (NNLS) constraint has been applied to the ground sensitivity calibration of the ZaNaI, CavaRad and AGRS_16L detectors, which are instrumental setup designed for static and dynamic in-situ measurements, in-situ measurements on restricted areas and airborne

measurements. In order to address this challenge natural calibration sites have been identified and characterized by means of laboratory gamma-ray spectroscopy measurements performed with the MCA_Rad system on collected soil samples (see Chapter 3). This calibration procedure, which is based on the redundancy of calibration measurements, has been investigated as a supplementary and integrative calibration strategy with respect to the use of calibration pads.

With the FSA approach the gamma-ray spectrum is modeled as a linear combination of the spectral components generated by individual radionuclides, where the contribution given by each isotope is obtained weighting the fundamental spectrum (i.e. the detector response to a unitary isotope concentration) by the abundance of the specific isotope in the environment. The FSA is a powerful tool for gamma spectra analysis thanks to its reduction in required statistic and its increase in analyzable radionuclides. For the ZaNaI, CavaRad and AGRS 16L detectors the ^{40}K, ^{238}U, ^{232}Th and ^{137}Cs fundamental spectra have been determined, which are the essential components required for the reconstruction of environmental gamma-ray spectra. The NNLS constraint solves the intrinsic limits of the χ^2 minimization founding the FSA analysis, which can provide numerical results not positively defined, both as negative count rates in the fundamental spectral components and as negative abundances in the reconstruction of measured spectra.

The new algorithm has been validated in the calibration of the ZaNaI detector, a 10.16 cm cubic shaped NaI(Tl) crystal housed inside a backpack, with measurements performed in 80 sites in Tuscany. The coefficients of linear correlation ($\Omega_K = 1.06 \pm 0.06$, $\Omega_U = 0.87 \pm 0.12$ and $\Omega_{Th} = 0.94 \pm 0.07$) between the in-situ measurements performed with the ZaNaI detector and the laboratory measurements carried out with the MCA_Rad system are comparable to the unity at 1 sigma level.

The CavaRad system is a portable (8 kg) collimated gamma-ray detector in which the employment of the lead-plate method is improved in order to filter the background noise, reducing the instrument weights and the counting response time. Subtracting two spectra obtained with shielding on/off, one can calculate the DS which contain approximately 20% of the unattenuated gamma-rays from the target area. The reliability of the ^{40}K, ^{238}U, ^{232}Th and ^{137}Cs DS fundamental spectra determined with the FSA-NNLS method has been tested by measuring in-situ the radionuclide abundances in 35 different sites characterized with HPGe independent measurements on samples. The coefficients of linear correlation ($\Omega_K = 0.93 \pm 0.21$, $\Omega_U = 0.93 \pm 0.29$ and $\Omega_{Th} = 0.82 \pm 0.18$) between CavaRad and laboratory results are comparable to the unity at 1 sigma level. The CavaRad system seems to underestimate weakly the radioactive contents measured with the MCA_Rad detector, which could be a consequence of the transparency of lead for photons with highest energy (i.e. 2614 keV of ^{208}Tl in the Th decay chain).

The AGRS_16L detector, a modular instrument dedicated to airborne surveys made up of 4 NaI scintillators having each one the volume of 4L, has undergone a double sensitivity calibration procedure: an experimental one based on the FSA-NNLS algorithm applied to in-situ measurements performed at natural calibration sites, and a second procedure based on Monte Carlo simulation. The first strategy is based on the selection of the S best solutions coming out from the FSA-NNLS sensitivity calibration, where the criterion for selecting a set of fundamental spectra is based on the

goodness of the reconstruction of input concentrations derived from HPGe measurements on collected samples.

The Monte Carlo simulation is based on a first step devoted to the simulation of photon propagation in matter and on a second step dedicated to the simulation of the detection process: this scheme allows for distinguishing the features related to the photon flux generation, such as the radioactive content of a given source and the characteristics of the traversed media, from what concerns the detection process, i.e. from the specific properties of a given gamma detection device. In principle the separation of the two physical processes can be a key point for discriminating the different effects resulting in the formation of the final gamma spectrum, but also for reducing the simulation time in testing the response of various gamma detectors to the same photon flux source. In this approach no arbitrary scaling factors are adopted, but counts simulated as detected by a Monte Carlo designed instrumental setup are only proportionally scaled with respect to the acquisition times and the radioactive contents of the experimental measurement used as basis for comparison.

The distinct calibration strategies lead to the determination of two sets of AGRS_16L fundamental spectra, the Experimental Fundamental Spectra (EFS) and the Monte Carlo Fundamental Spectra (MCFS). Both sets of fundamental spectra have been used in an internal cross validation test, aimed at assessing the quality of the reconstruction of the calibration sites average concentrations (C).

The experimental calibration procedure provides solutions to the sensitivity calibration problem that by construction well reproduce the HPGe average abundances. The FSA-NNLS method assures in the calibration stage that the fundamental spectra do not have negative counts in each energy bin: however, even if the non-negative constraint is applied to the solution of the $\chi 2$ minimization, there is no guarantee about the reconstruction of physically meaningful solutions. Indeed, the least square method accommodates for the minimum discrepancy between observed and expected quantities but is not informed about the intensities and energies of the gamma emission lines as well as about the existence of a Compton continuum associated to each photopeak. As a consequence, the $\chi 2$ minimization can produce artifacts and cross-talk effects in the spectral shapes, which has been taken into account in the selection of the best EFSs. On the other side, Monte Carlo simulation produces the fundamental spectrum for each isotope independently on all the others.

For Th an excellent result has been obtained comparing the performances of the EFS and the MCFS: a linear regression between Th concentrations reconstructed with EFS ($\widetilde{C}$) and MCFS ($\widetilde{C}_{MC}$) produces slope and intercept linear curve parameters compatible with a bisection line. The same is true for the linear regression between C and $\widetilde{C}$ abundances and C and $\widetilde{C}_{MC}$ abundances.

For what concerns U some variability is observed between reconstructed concentration values ($\widetilde{C}$ and $\widetilde{C}_{MC}$) and laboratory measurements C, which is manifested in terms of relatively poor r^2 (~ 0.7) coefficients of determination. This evidence highlights the susceptibility of the experimental sensitivity calibration procedure, as the determination of EFSs strongly depends on the the abundances (and uncertainties) assigned to natural calibration sites, which come from laboratory measurements that are characterized by different sources of uncertainty and different fields of view, providing information on the radioactive content of $\sim$cm scale samples.

Although the linear regression between C and $\widetilde{C}$ is satisfactory by construction, for the case of K it has to be considered that the low and high extreme abundances values constraining the linear regression curve are related respectively to HPGe MDA values and to a pad-like site whose features (mainly geometrical) deviate from that of a natural calibration site. This could be one clue for understanding the ∼30% discrepancy among $\widetilde{C}$ and $\widetilde{C}_{MC}$ K abundances.

These studies highlighted the importance of performing dedicated instrumental calibrations and cross-validation tests, which often involve dealing with experimental measurements characterized by different sources of uncertainty and different fields of view. Issues related to spectral fitting can affect gamma-ray spectroscopy measurements as the reliability of the estimated radioactive contents is strictly correlated with the reliability of the templates used in the reconstruction of experimental gamma-ray spectra. This point allowed me to focus on problematic aspects related to detector calibrations and background radiation assessment which can easily introduce systematic biases in the estimation of radionuclide abundances and which will be the subject of a future publication.

The content of this chapter is based on the following publications:

Caciolli, A., **Baldoncini M.**, Bezzon G.P., Broggini C., Buso G.P., Callegari I., Colonna T., Fiorentini G., Guastaldi E., Mantovani F., Massa G., Menegazzo R., Mou L., Rossi Alvarez C., Shyti M., Zanon A., Xhixha G. " *New FSA Approach for in Situ γ Ray Spectroscopy.*" The Science of the Total Environment 414, (2012): 639–45. doi:10.1016/j.scitotenv.2011.10.071.

Xhixha G., **Baldoncini M.**, Bezzon G.P., Buso G.P., Carmignani L., Callegari I., Colonna T., Guastaldi E., Fiorentini G., Mantovani F., Mou L., Robustini C., Rossi Alvarez C., Strati V., Kaçeli Xhixha M., Zanon A. "*Performances of a lightweight collimated γ-ray spectrometer for in-situ surveys.*" EUNORM 2 Symposium (2014), Prague, Czech Republic.

Bibliography

Beck et al. (1972). *In situ Ge (Li) and NaI (Tl) gamma-ray spectrometry.* Tech. rep. Health and Safety Lab.,(AEC), New York.

Boutsidis, Christos and Petros Drineas (2009). "Random projections for the nonnegative least-squares problem". *Linear Algebra and its Applications* 431.5, pp. 760–771. ISSN: 0024-3795. DOI: 10.1016/j.laa.2009.03.026.

Bucher, G. et al. (2009). "International Intercomparison Exercise of Airborne Gammaspectrometric Systems of Germany, France and Switzerland in the Framework of the Swiss Exercise ARM07." *IAEA Technical Report*. ISSN: PSI-Bericht Nr. 09-07, ISSN 1019-0643.

Chiozzi, P. et al. (2000). "Laboratory application of NaI(Tl) gamma-ray spectrometry to studies of natural radioactivity in geophysics". *Applied Radiation and Isotopes* 53.1, pp. 127–132. ISSN: 0969-8043. DOI: 10.1016/S0969-8043(00)00123-8.

Cresswell, A. J. et al. (2006). "137Cs measurement uncertainties and detection limits for airborne gamma spectrometry (AGS) data analysed using a spectral windows method". *Applied Radiation and Isotopes* 64.2, pp. 247–253. ISSN: 0969-8043. DOI: 10.1016/j.apradiso.2005.07.013.

Crossley, D. and A. Reid (1982). "Inversion of gamma-ray data for element abundances". *GEOPHYSICS* 47.1, pp. 117–126. ISSN: 0016-8033. DOI: 10.1190/1.1441273.

Desbarats, A. J. and P. G. Killeen (1990). "A least-squares inversion approach to stripping in gamma-ray spectral logging". *Nuclear Geophysics* 4.3, pp. 343–352. ISSN: ISSN 0886-0130.

Désesquelles, P et al. (2009). "NNLC: non-negative least chi-square minimization and application to HPGe detectors". *Journal of Physics G: Nuclear and Particle Physics* 36.3, p. 037001.

Engelbrecht, Rudolf and Martina Schwaiger (2008). "State of the art of standard methods used for environmental radioactivity monitoring". *Applied Radiation and Isotopes*. Environmental Radioactivity Environmental Radioactivity: From Measurements and Assessments to Regulation 66.11, pp. 1604–1610. ISSN: 0969-8043. DOI: 10.1016/j.apradiso.2008.01.021.

Grasty, R. and others. (1979). "Fields of view of airborne gamma-ray detectors". *GEOPHYSICS* 44.8, pp. 1447–1457. ISSN: 0016-8033. DOI: 10.1190/1.1441017.

Guillot, L. (2001). "Extraction of full absorption peaks in airborne gamma-spectrometry by filtering techniques coupled with a study of the derivatives. Comparison with the window method". *Journal of Environmental Radioactivity* 53.3, pp. 381–398. ISSN: 0265-931X.

Gutierrez, S et al. (2002). "Contribution of a germanium detector in mobile gamma-ray spectrometry. Spectral analysis and performance". *Nuclear Instruments and Methods in Physics Research Section A: Accelerators, Spectrometers, Detectors and Associated Equipment* 482.1, pp. 425–433. ISSN: 0168-9002. DOI: 10.1016/S0168-9002(01)01521-2.

Hendriks, P. H. et al. (2001). "Full-spectrum analysis of natural gamma-ray spectra". *Journal of Environmental Radioactivity* 53.3, pp. 365–380. ISSN: 0265-931X.

IAEA (2003). *Guidelines for Radioelement Mapping Using Gamma Ray Spectrometry Data*. IAEA-TECDOC-1363. Vienna: International Atomic Energy Agency.

International Atomic Energy Agency (1990). *The Use of Gamma Ray Data to Define the Natural Radiation Environment*. IAEA-TECDOC-566. Vienna: INTERNATIONAL ATOMIC ENERGY AGENCY.

Lawson, C.L. and R.J. Hanson (1995). *Solving Least Squares Problems*. Classics in Applied Mathematics. Society for Industrial and Applied Mathematics. ISBN: 9780898713565.

Loevborg, L. et al. (1981). *Pad facility for the calibration of gamma-ray measurements on rocks*. RISO-R–454. Risoe National Lab.

Matolín, Milan (2017). "Verification of the radiometric map of the Czech Republic". *Journal of Environmental Radioactivity* 166 (Pt 2), pp. 289–295. ISSN: 1879-1700. DOI: 10.1016/j.jenvrad.2016.04.013.

Maučec, M. et al. (2009). "Determination of correction factors for borehole natural gamma-ray measurements by Monte Carlo simulations". *Nuclear Instruments and Methods in Physics Research Section A: Accelerators, Spectrometers, Detectors and Associated Equipment* 609.2, pp. 194–204. ISSN: 0168-9002. DOI: 10.1016/j.nima.2009.08.054.

Minty, B. (1992). "Airborne gamma-ray spectrometric background estimation using full spectrum analysis". *GEOPHYSICS* 57.2, pp. 279–287. ISSN: 0016-8033. DOI: 10.1190/1.1443241.

Minty, B. et al. (2009). "The Radiometric Map of Australia*". *Exploration Geophysics* 40.4, pp. 325–333.

Nuccetelli, Cristina (2008). "In situ gamma spectroscopy in environmental research and monitoring." *Applied radiation and isotopes : including data, instrumentation and methods for use in agriculture, industry and medicine* 66.11, pp. 1615–1618. ISSN: 0969-8043. DOI: 10.1016/j.apradiso.2007.10.019.

Perrin, J. et al. (2006). "Determination of the vertical distribution of radioelements (K, U, Th, Cs) in soils from portable HP-Ge spectrometer measurements: A tool for soil erosion studies". *Applied Radiation and Isotopes* 64.7, pp. 830–843. ISSN: 0969-8043. DOI: http://dx.doi.org/10.1016/j.apradiso.2006.01.003.

Sanderson, D.C.W. (1989). "The use and potential of radiometrics for monitoring environmental radioactivity". *COGER, Conferences at the University of Lancaster, UK*.

Telford, W. M. et al. (1990). *Applied geophysics*. Vol. 1. Cambridge university press.

Tyler, Andrew N. (2004). "High accuracy in situ radiometric mapping". *Journal of Environmental Radioactivity* 72.1, pp. 195–202. ISSN: 0265-931X. DOI: 10.1016/S0265-931X(03)00202-9.

Tyler, Andrew N. (2008). "In situ and airborne gamma-ray spectrometry". *Radioactivity in the Environment*. Ed. by Pavel P. Povinec. Vol. 11. Analysis of Environmental Radionuclides. Elsevier, pp. 407–448.

Verdoya, M. et al. (2009). "Natural gamma-ray spectrometry as a tool for radiation dose and radon hazard modelling". *Applied Radiation and Isotopes: Including Data, Instrumentation and Methods for Use in Agriculture, Industry and Medicine* 67.5, pp. 964–968. ISSN: 1872-9800. DOI: 10.1016/j.apradiso.2009.01.066.

Xhixha, G. et al. (2013). "The worldwide NORM production and a fully automated gamma-ray spectrometer for their characterization". *Journal of Radioanalytical and Nuclear Chemistry* 295.1, pp. 445–457. ISSN: 0236-5731, 1588-2780. DOI: 10.1007/s10967-012-1791-1.

Chapter 5

Airborne gamma ray spectroscopy for modeling cosmic radiation and effective dose in the lower atmosphere

Although far from being a novel technique, the frontiers of airborne gamma-ray spectrometry (AGRS) and its applications are continuously pushed forward thanks to advances in multichannel processing, statistical methods for spatial resolution enhancement and data analysis procedures (B. Minty and R. Brodie 2016; Iza et al. 2016; Varley et al. 2016; Beamish 2016). New challenges come also from the employment of novel acquisition technologies, such as the unmanned aerial vehicle (UAV) devices, characterized by different detection performances compared to standard acquisition systems, which are reawakening the effort in estimating detectors efficiencies and minimum detectable activities (MDA) (Gong et al. 2014; Cao et al. 2015; Tang et al. 2016). In order to address the AGRS new demands, an adequate understanding and knowledge of the background spectral components is mandatory for processing airborne gamma-ray spectrometric data.

This study reports the results of a ∼5 hours AGRS survey over the sea dedicated to the measurement of the gamma radiation originating from the aircraft materials and cosmic rays, which constitute a background source for the estimation of the gamma radiation of terrestrial origin coming from ^{40}K, ^{214}Bi (eU) and ^{208}Tl (eTh). In performing this study I participated to the airborne measurement campaign, which allowed to investigate the AGRS non-geological background radiation with high statistics measurements in a wide range of elevations (77 – 3066 m). I took the lead in the data analysis, both in the treatment of raw list mode data for the conversion to airborne energy calibrated spectra and in the statistical analysis of measured count rates for the background components estimation. The acquisition of spectra over water at a number of different heights allowed me to split the constant contribution coming from the radioactivity of the aircraft from the height dependent contributions associated with cosmic radiation. I applied a statistical analysis based on the minimization of a χ^2 function separately to the ^{208}Tl background estimation with respect to ^{214}Bi (eU) and ^{40}K, as the

latter can be potentially affected by the presence of atmospheric radon (B. R. S. Minty, Luyendyk, and R. C. Brodie 1997). Finally, the use of a monitoring cosmic energy window allowed to model the height dependence of the count rate purely cosmic in nature which, on the base of a semi-empirical calibration curve, can be converted to the cosmic effective dose to the human population.

5.1 Background

During the last years, the interest in the airborne gamma-ray spectrometry method has been renewed thanks to the exploration of multidisciplinary fields (e.g. landslide monitoring (Baroň et al. 2013), peat thickness estimation (Keaney et al. 2013), prediction models for trees' growth (Mohamedou, Tokola, and Eerikäinen 2014) and precision agriculture (Söderström et al. 2016)), the opening scenario of real time surveys (Detwiler et al. 2015; Kock, Lanke, and Samuelsson 2012; Cardarelli et al. 2015; Kulisek et al. 2015), the spreading of intercomparison exercises related to multi-regional AGRS campaigns dedicated to the homeland security (Bucher et al. 2009), which are a driver for going beyond standard acquisition practices. The widening of AGRS applications is reflecting in a heterogeneous interpretation of survey methodologies, detector calibration strategies and background radiation sources (Kock, Rääf, and Samuelsson 2014; Sanderson, Cresswell, and White 2008; R. Grasty, P. Bates, and Smetny-Sowa 2015; Sandness et al. 2009).

Airborne gamma-ray spectra are indeed affected by many variables: in surveys intended for lithological mapping multiple data processing are necessary to correct the data for those influences which are not related to actual gamma emissions from geological sources, with the aim of transforming observed spectra into equivalent concentrations of radionuclides. In this scenario, a crucial step is related to the removal of background radiation, which is intended as radiation not originating from the ground and which corresponds to the cosmic background, the aircraft background and, if present, the atmospheric radon background.

The use of a high energy window that records all the counts having energies in the range 3 – 7 MeV allows to identify signals of pure cosmic origin, as the end point of gamma-rays of terrestrial origin corresponds to the ^{208}Tl emission at 2.614 MeV. This information can be used not only for predicting the cosmic background in the ^{40}K, ^{214}Bi and ^{208}Tl photopeak energy windows, but also for assessing the cosmic radiation dose to the human population which can account up to 50% of the average annual whole-body outdoor effective dose from natural sources of radiation. The annual effective dose due to cosmic ray exposure averaged over the world's population has been estimated to be 0.38 μSv/y by the UNSCEAR 2008, although recent efforts have been done in order to give more accurate estimates on the base of advanced cosmic-ray fluxes calculation and refined grid databases of population and terrain elevation models (Sato 2016). These estimations take into account the amount of time people spend indoor (80% of the day) and the mean thickness of the walls acting as a shield for the cosmic radiation. Cosmic dosimetric measurements are generally focused on the assessment of air crew members exposure, but there are also regional measurement campaigns addressing the question of outdoor population dose exposure (Cavalcante et al. 2011; Tsui, Wong, and Lee 1991). In

this context, the calibration of an airborne gamma-ray detector for the assessment of dose rates can provide a supplementary technique for the cosmic exposure assessment.

In this work we estimate the AGRS cosmic and aircraft background on the basis of a ∼5 hours AGRS survey over the sea, which is needed for the determination of gamma radiation from ^{40}K, ^{214}Bi (eU) and ^{208}Tl (eTh) deployed in the ground. The broad range of elevations covered during the survey (77 – 3066 m) plays a decisive role in separating the constant contribution due to the aircraft radioactivity from the cosmic radiation component, which is expected to exponentially increase with increasing height. Moreover, the cosmic effective dose to human population has been estimated on the base of the statistics recorded in the monitoring cosmic energy window and of a semi-empirical calibration curve.

5.2 Instruments and methods

5.2.1 Experimental setup, survey and data

Airborne gamma ray surveys over the sea were carried out with the Radgyro (Fig. 5.1), a prototype aircraft dedicated to multispectral airborne measurements. The Radgyro is an autogyro specifically designed to host a large network of sensors which are able to investigate simultaneously and independently the electromagnetic spectrum in a variety of spectral ranges, from thermal infrared (13000 - 7500 nm) to gamma radiation ($3{\cdot}10^{-3}$ - $4{\cdot}10^{-4}$ nm) (Tufarolo et al. 2014). The high autonomy and payload (3 hours for a 120 kg equipment weight), the modularity of the acquisition system, together with the possibility of time correlating the information coming from the different sensors, make the Radgyro a unique aircraft in the field of proximal remote sensing.

During the surveys the Radgyro position is recorded every second by a GPS system composed of 2 u-blox EVK-6T antennas. Gamma radiation is measured with the AGRS_16L system, which has been already described in Sec. 4.4.2. AGRS raw data are acquired event by event separately for each of the four NaI(Tl) detectors: each list mode file contains the time stamp of a given energy deposition (in units of digitizer clock) together with the corresponding acquisition channel. The list mode files are cut offline for each detector in order to produce 1 second acquisition spectra which subsequently undergo an energy calibration procedure. The latter is performed by determining with a Gaussian fit the positions of the prominent ^{40}K and ^{208}Tl photopeaks in 600 seconds spectra acquired on the ground before the take off. A linear function is then fitted to the photopeaks' positions for estimating the energy corresponding to the first acquisition channel (keV) and the gain (keV/channel). Summing up the four calibrated spectra it is possible to obtain the gamma-ray 1 second spectrum acquired by the entire 16L detection volume, which has an energy end point of 7 MeV. For what concerns the Radgyro positioning, each GPS antenna produces two separate ASCII files, one containing the temporal information in terms of PC and GPS acquisition times, the second storing the information on position in the standard of NMEA GGA sentence. The mean 1 second position and altitude above sea level of the Radgyro is computed as the average of the coordinates obtained from the single GPS

Figure 5.1: Picture of the Radgyro, the autogyro dedicated to multi-spectral airborne acquisitions, used for the AGRS surveys over the sea.

antennas. As both the radiometric and positioning data are acquired with the same PC, the computer time stamp is used for the synchronization of the different devices. Airborne gamma-ray background calibration surveys were performed in a series of 4 flights over the Tyrrhenian Sea close to Viareggio (Tuscany, Italy). In order to avoid taking into account gamma-ray signals potentially spoiled by ground radiation, gamma-ray measurements acquired at a distance from the coast less than 300 m have been excluded from the analysis. In Fig. 5.2 the effective paths of the different flights are shown, which correspond to a total acquisition time of 17612 seconds and an explored range of altitudes going from 77 to 3066 m. In Table 5.1 a summary of the main parameters related to each of the 4 flights are shown.

According to the purpose of the experiment, the flight paths have been planned with the aim of investigating the entire reported range of heights with enough statistics for well constraining the analysis of the altitude dependent gamma-ray cosmic component. This strategy, together with the flight conditions and the non feasibility for the Radgyro to hover at a given elevation, allowed us to collect the elevation flight statistics shown in Fig. 5.3.

5.2.2 Theoretical modeling and data analysis

Airborne gamma-ray spectroscopy measurements are affected by background radiation, which is intended generally as radiation not originating from the Earth's surface and which has to be removed during data processing. The three major sources of background radiation are cosmic background,

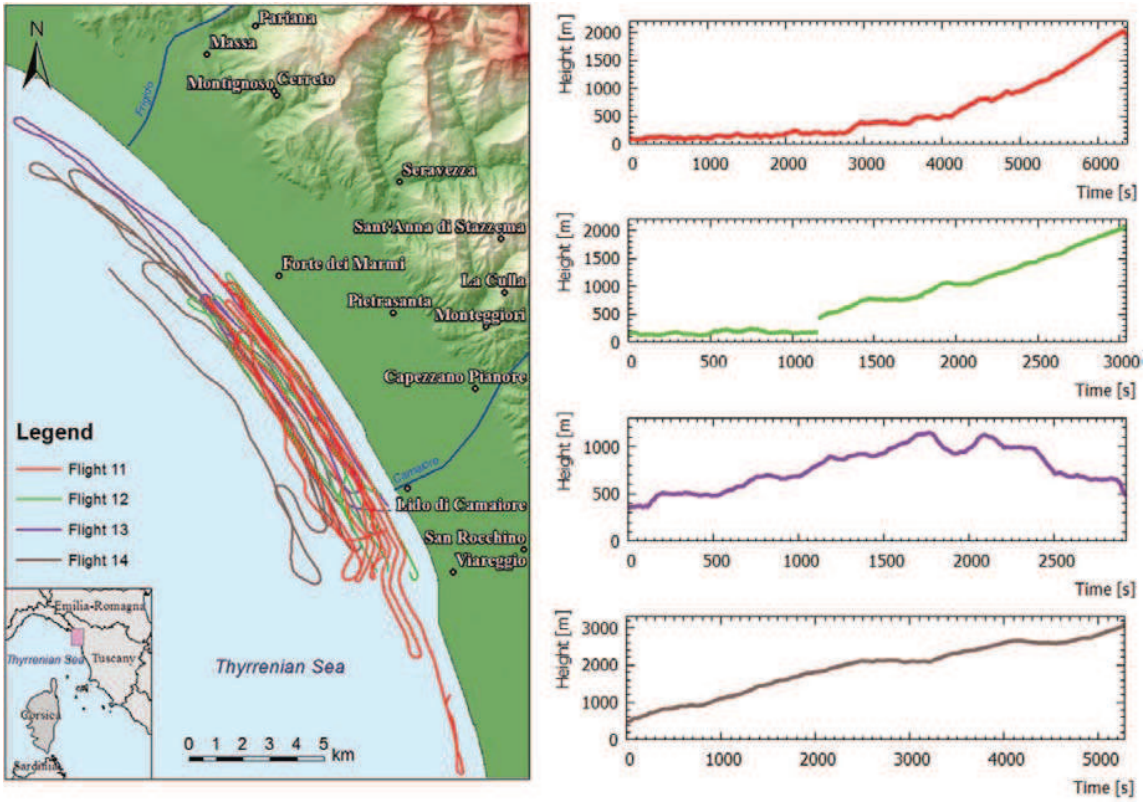

Figure 5.2: The left panel shows a map of the effective flight lines of the surveys over the sea performed near Viareggio (Tuscany, Italy). The acquisition tracks are the ones corresponding to data points acquired at a minimum distance from the coast of 300 m. The four panels on the right show the altitude profiles for the different flights.

Table 5.1: Summary of the main parameters for each of the 4 surveys over the sea. For each flight the ID, date, time, minimum and maximum altitude and acquisition time are reported, respectively. In the case of flights 11 and 14, 83 seconds and 30 seconds have been cut due to some radiofrequency interference between the PMT and the aircraft transponder. The long interruption of the data taking of flight 12 (2531 seconds) has been imposed by civil traffic of the Pisa airport.

Flight ID	Date	Time	z min [m]	z max [m]	Acquisition time [s]
11	30/03/2016	17:42:10 19:29:43	77	2019	6370
12	31/03/2016	18:13:55 19:46:47	126	2070	3041
13	05/04/2016	11:39:53 12:28:36	348	1144	2924
14	05/04/2016	16:37:16 18:05:43	461	3066	5277
Global			77	3066	17612

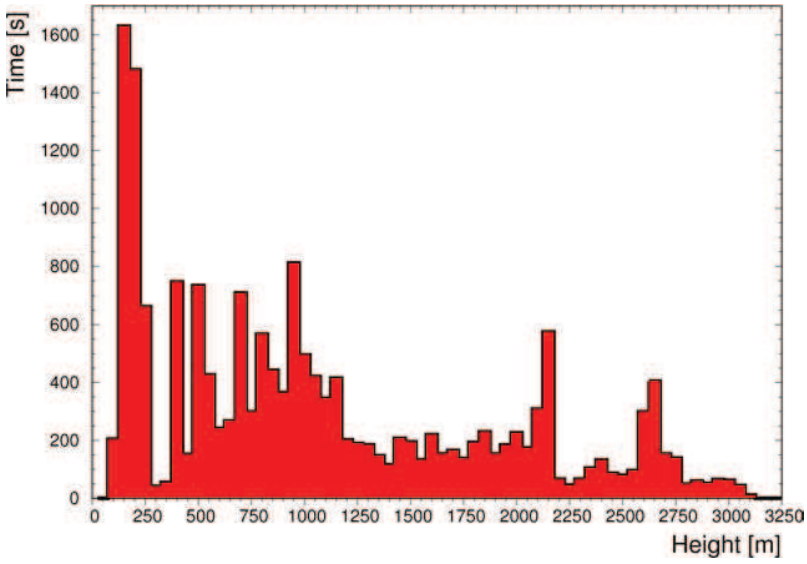

Figure 5.3: Histogram describing the effective overall temporal statistics: the data taking time at a given survey altitude is shown, with an altitude binning of 50 m.

instrumental plus aircraft background and atmospheric radon (^{222}Rn).

Galactic cosmic ray particles, with energies extending up to few 10^{20} eV (Abraham et al. 2010; Bird et al. 1993), are produced outside the Solar System and are constituted by a nucleonic component (98%) and electrons (2%). The nucleonic component is primarily made up by protons (∼85% of the flux) and alpha particles (∼12%), with a remaining fraction comprising heavier nuclei (UNSCEAR 2008). In entering the Earth's atmosphere, these particles collide with atoms of air constituents, giving rise to cascades of secondaries, including neutrons, pions, muons and gamma radiation. In the investigated range of altitudes, the gamma component of the secondary cosmic radiation contributes to about 15% of the mean cosmic effective dose rate (CED) (Friedberg and Copeland 2011). The cosmic gamma background resulting from this cosmic secondary radiation interaction with the air, the aircraft and the detector materials is foreseen to monotonically increase with increasing altitude.

Concerning the energy dependence, the cosmic-induced gamma-ray energy spectrum is expected to have a polynomial dependence with respect to gamma-ray energy (Sandness et al. 2009). The count rate energy dependence of the cosmic component is reconstructed according to a polynomial function having the following expression:

$$cps(E) = aE^b + c \tag{5.1}$$

where E is the gamma-energy in MeV and a, b and c are constants for a spectrum measured at a given altitude. The energy dependence of the count rate has been estimated by fitting the measured spectrum with the above model function both in the 0.8 – 7 MeV energy range and in the 3 – 7 MeV energy range, called respectively the Full Energy Window (FEW) and the Cosmic Energy Window (CEW). A third fit has been performed using as input data points the measured count rates in the CEW, plus the three points corresponding to the estimated count rates due to cosmic radiation in the ^{40}K, ^{214}Bi and ^{208}Tl photopeak energy windows (see Table 5.3), which have been determined on the base of the linear regression parameters reported in Table 5.5. In Table 5.2 the same analysis in two different ranges of altitudes is reported. Fig. 5.4 shows an example of background airborne gamma-ray spectrum measured with the AGRS_16L in the elevation range 2050 – 2150 m and normalized with respect to an 870 seconds acquisition time, together with the three curves resulting from the different fitting procedures.

From this exercise it is possible to evince that the fitting of the measured spectrum is dependent on the energy range chosen, as the spectral shape under reconstruction contains different pieces of information in the CEW and in the FEW. Using only the CEW for constraining the cosmic spectral shape from one side assures the pure cosmic nature of the counting statistics, but on the other side the sole reconstruction of the spectral high energy tail prevents a correct estimation of the curve slope in the low energy range as emphasized by the large uncertainties on the best fit parameters. By fitting in the FEW the steep behavior at low energies is reproduced: however in this case the measurement under reconstruction contains not only the cosmic contribution to the signal, but also the signal coming from the equipment radioactivity and in particular from the ^{40}K, ^{238}U and ^{232}Tl decay series. On the

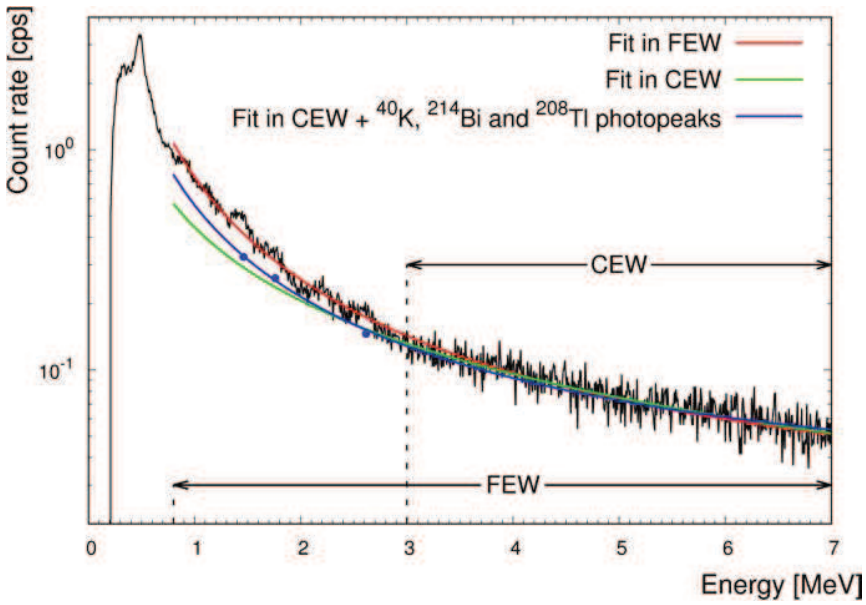

Figure 5.4: Gamma-ray spectrum acquired by the AGRS_16L for 870 seconds at the altitude range 2050 – 2150 m (black solid line). The red solid line shows the fitting curve obtained using as model function Eq. 5.1 and as energy fitting range the FEW, the green solid line shows the curve obtained by fitting the measured spectrum in the CEW. The blue points correspond to the count rates in the KEW, BEW and TEW associated with the cosmic induced background and obtained on the base of the linear relation having as parameters the ones reported in Table 5. The blue solid line is the result of the fit of the measured spectrum in the CEW and of the blue points.

Table 5.2: Fit parameters of the count rate energy dependence modeled with Eq. 5.1 for two spectra measured at 2100 m and 2650 m for respectively 870 seconds and 550 seconds. For each measured spectrum the fit has been performed in the FEW, in the CEW and in the CEW plus the ^{40}K, ^{214}Bi and ^{208}Tl photopeaks.

z range [m]	Fit energy range	(a $\pm\delta$ a) [cps]	b $\pm\delta$b	(c $\pm\delta$ c) [cps]
2050 - 2150	FEW	0.73 ± 0.10	-1.62 ± 0.40	0.02 ± 0.03
	CEW	0.44 ± 0.42	-1.11 ± 1.60	0.00 ± 1.40
	CEW + ^{40}K, ^{214}Bi and ^{208}Tl photopeaks	0.54 ± 0.04	-1.49 ± 0.05	0.02 ± 0.01
2600 - 2700	FEW	0.90 ± 0.11	-1.53 ± 0.33	0.02 ± 0.04
	CEW	0.62 ± 0.61	-1.14 ± 1.66	0.00 ± 1.87
	CEW + ^{40}K, ^{214}Bi and ^{208}Tl photopeaks	0.71 ± 0.05	-1.45 ± 0.03	0.02 ± 0.01

Table 5.3: Energy windows for natural and cosmic radiation used for the background calibration of the AGRS_16L system. The last two columns report for each energy window the measured counting statistics for gamma-ray spectra acquired at the altitude range 2050 – 2150 m and 2600 – 2700 m, respectively.

Energy Window	Emission line [keV]	Energy range [keV]	Measured cps (2050 - 2150) m	Measured cps (2600 - 2700) m
KEW	1460	1370 - 1570	12.2	15.0
BEW	1765	1660 - 1860	8.7	11.1
TEW	2614	2410 - 2810	8.8	11.9
CEW	/	3000 - 7000	41.9	54.8

other hand, the idea behind the third fitting approach is to reinforce the fit performed by using the sole count rates in the CEW with the addition of three relatively well separated points corresponding to the cosmic count rates in the ^{40}K, ^{214}Bi and ^{208}Tl photopeak energy windows. Among the above mentioned three strategies this is the one providing the most reliable estimation of the cosmic spectral shape in the FEW.

Instrumental and aircraft background corresponds to the constant gamma signal generated by trace amounts of K, U and Th contained in the detector materials and ancillary equipment, together with the aircraft material itself. ^{222}Rn, the only gaseous daughter product of the ^{238}U decay chain, can escape from rocks and soils and, considering its 3.8 days half-life, can accumulate in the lower atmosphere. Its gamma-emitting daughter nuclei ^{214}Bi and ^{214}Pb can attach to airborne aerosols and dust particles, giving rise to the atmospheric radon background gamma signal (R. Grasty and B. Minty 1995).

The determination of the K, U and Th ground concentrations during an airborne gamma-ray survey relies on the estimation of the background corrected count rates recorded in the ^{40}K, ^{214}Bi (eU) and ^{208}Tl (eTh) photopeak energy windows, called KEW, BEW and TEW, respectively (see Table 6.3).

Aircraft and cosmic background calibration flights are usually performed offshore for altitudes greater than 1500 m above the ground level in order to avoid the contamination from terrestrial radiation and radon decay products. In this scenario, as the instrumental background is supposed to be constant and the cosmic background is expected to exponentially increase with increasing height, the measured count rates in the i-th energy window during a calibration flight over the sea is predicted to follow the subsequent equation:

$$n^i(z) = A^i e^{\mu^i z} + B^i \tag{5.2}$$

where n^i is the count rate in the $i'th$ energy window (with i = KEW, BEW, TEW and CEW) A^i, μ^i and B^i are constants (International Atomic Energy Agency 1991; R. Grasty and B. Minty 1995).

The count rate in the CEW is also expected to be linearly related to the count rates in the natural radionuclides energy windows, as stated in the following equation:

$$n^i = a^i + b^i n^{CEW} \tag{5.3}$$

where n^i is the count rate in the $i'th$ energy window (with i = KEW, BEW, TEW), a^i is the aircraft background count rate in the $i'th$ energy window, b^i is the cosmic stripping ratio (i.e. the cosmic background count rate in the $i'th$ energy window normalized to unit counts in the CEW) and n^{CEW} is the count rate in the CEW. The parameter a^i is the expected count rate for null cosmic count rate and therefore represents the constant background component generated by the Radgyro and by the detectors materials. Determining these linear functions for the natural radionuclides energy windows allows to correct the count rates measured at a given height during regional AGRS surveys for the aircraft and height dependent cosmic ray backgrounds, provided the monitoring of the count rate in the CEW.

Eq. 5.2, as well as Eq. 5.3 holds in the absence of any terrestrial and atmospheric radon radiation component. A potential radon contamination in any case would act on the count rates in the KEW and BEW but not on the count rates in the TEW and CEW as they are not affected by the lower energy gamma emissions of radon daughter nuclei. The presence of a radon background component in the measured count rates can be generally identified as a breakdown of the linear relationship between the cosmic and the ^{214}Bi count rates at low elevations (R. Grasty and B. Minty 1995). The estimated count rates in the energy windows of interest have been clustered according to an altitude binning of 15 m, which is conservative with respect to the estimated accuracy on the vertical position resulting from the combination of all the altimeters present on board of the Radgyro (Albéri et al. 2016). The count rates used as input for the background modeling are therefore estimated summing all the input count rates acquired in the same elevation bin and dividing by the number of 1 second spectra entering the summation.

The parameters of the exponential curves A^i, μ^i and B^i have been determined via the minimization of the χ^2 function:

$$\chi^2_{exp} = \sum_{j=1}^{nbin} \left[\frac{n_j^i - \left(A^i e^{\mu^i z_j} + B^i \right)}{\sigma_{n_j^i}} \right]^2 \tag{5.4}$$

where $nbin$ is equal to the number of elevation bins entering the χ^2 minimization, n_j^i is the average count rate obtained for the $j'th$ elevation bin in the $i'th$ energy window, z_j is the average elevation obtained for the $j'th$ elevation bin and $\sigma_{n_j^i}$ is the 1 sigma uncertainty associated to the counting statistics, corresponding to the square root of the total counts recorded at z_j in the $i'th$ energy window divided by the acquisition time at z_j.

The objective χ^2 function to be minimized for determining the linear curve parameters has instead to be built taking into account not only the statistical error associated to the quantity n^i but also the uncertainty on the "independent variable" n^{CEW}. Therefore, the adopted definition for the χ^2 function is:

$$\chi^2_{lin} = \sum_{j=1}^{nbin} \frac{\left[n_j^i - \left(a^i + b^i n_j^{CEW} \right) \right]^2}{\left(\sigma_{n_j^i} \right)^2 + \left(b^i \sigma_{n_j^{CEW}} \right)^2} \tag{5.5}$$

Monitoring the CEW allows to estimate the variation of the counting statistics of pure cosmic origin with respect to the altitude, which in principle can be used for estimating the CED to human population. The cosmic dose component corresponds on average to about 16% of the total effective dose from natural sources (UNSCEAR 2008), which is defined as the total sex-averaged whole-body absorbed dose, obtained summing the doses absorbed by individual tissues (due both to radiations incident on the body and/or to internal radiation emitters), weighted by a radiation weighting factor and by a tissue weighting factor. The radiation weighting factor accounts for the relative biological effectiveness associated to the type and energy of the radiation, while the tissue weighting factor takes into account where the radiation energy is deposited.

Gamma-ray spectrometers for dosimetric measurements are generally calibrated by exposing them to certified radiation fields, which can be collimated beams at irradiation facilities, calibrated radioactive point sources with known activities covering both high and low energy ranges or calibration pads generally made of concrete and doped with radionuclides of known gamma dose-rates (R. L. Grasty et al. 2001; Tuan et al. 2013; Mercier and Falguères 2007). Multiple publications on calibration of dosimetric equipments report also validation tests in which the measured dose rates are compared with values obtained from various codes, typically used for assessing radiation exposure of aircraft crew due to cosmic radiation (Spurný and Daschev 2002; Dachev et al. 2002; Bilski, Olko, and Horwacik 2004; Kleinschmidt and Watson 2016). Some of these codes are based on Monte Carlo simulations of the radiation field (e.g. EPCARD), while others rely on analytic calculations of particle transport through the atmosphere (e.g. CARI-6) (Bottollier-Depois et al. 2009).

The popular program CARI-6, developed by the Civil Aerospace Medical Institute (CAMI) of the Federal Aviation Administration (FAA), allows to calculate the effective dose of galactic cosmic

radiation received by an individual (based on an anthropomorphic phantom) for altitudes up to ∼18.3 km (FAA 2014). This code requires information on the altitude, the geographic location and the time period, the latter related to changes in the Earth's magnetic field and in solar activity. By establishing a relation between the measured n^{CEW} and the dose rate values predicted by the CARI-6 code it is possible to determine a semi-empirical calibration curve to estimate the CED on the base of the count rates recorded in the CEW of airborne gamma-ray spectra. The CED values as function of altitude in the range 77 – 3066 m have been determined by running the CARI-6 code using the geographic location and the acquisition time corresponding to the performed airborne surveys, which are 43° 56' North 10° 09' East and March 2016. The semi-empirical calibration curve allowing to convert the count rates in the CEW n^{CEW} to the CED has been estimated via a linear fit of the type (see Appendix):

$$CED = a_{CED} + b_{CED} n^{CEW} \tag{5.6}$$

5.3 Results and discussion

In this section we report the results regarding the background calibration of the AGRS_16L spectrometer performed via the analysis of 1 second gamma ray spectra acquired during a 17612 seconds airborne survey over the sea. For ^{40}K and ^{214}Bi the relation between n^i and the altitude above the sea level is not guaranteed to be purely exponential down to low elevations, as the count rates in the ^{40}K and ^{214}Bi photopeaks may be contaminated by the presence of atmospheric radon. As already mentioned, this potential contamination also translates in a deviation from a purely linear relation between n^i and n^{CEW} at low elevations. The concentration of ^{222}Rn in the atmosphere can change considerably according to the different diffusion conditions. Nevertheless, above 1000-1500 m, mean ^{222}Rn concentrations of the daytime atmosphere drop sharply to values compatible with zero (around 2 ± 2 Bq/m^3) and then slowly reduce further with height until they reach 0.3 ± 0.4 Bq/m^3 above 3000 m (Williams et al. 2010). In our analysis the count rates in the KEW and in the BEW is conservatively studied only for altitudes greater than 2000 m. Fig. 5.5a shows the experimental count rates in the CEW, distinguished by colour according to the different flight IDs: the homogeneity of this partial datasets assures that there are no systematic effects related to the different acquisition times. Fig. 5.5b shows the experimental data for the count rates in the CEW obtained from the entire dataset, with the superimposed curve resulting from the minimization of the χ^2 function described by Eq. 5.4. The values of the fitting curve parameters are reported in Table 5.4.

The 1.12 reduced chi-square value denotes a good agreement between the model function and the experimental data. Although the parameters A and B in the CEW (Table 5.4) are affected by uncertainties having different order of magnitudes, at the nominal 100 m survey height of an airborne survey the two uncertainties separately produce approximately the same variation on the estimated count rates, which is below 3%. Thanks to the high acquisition statistics and to the wide range of investigated altitudes, the fit well constraints the value of the μ parameter entering the exponential

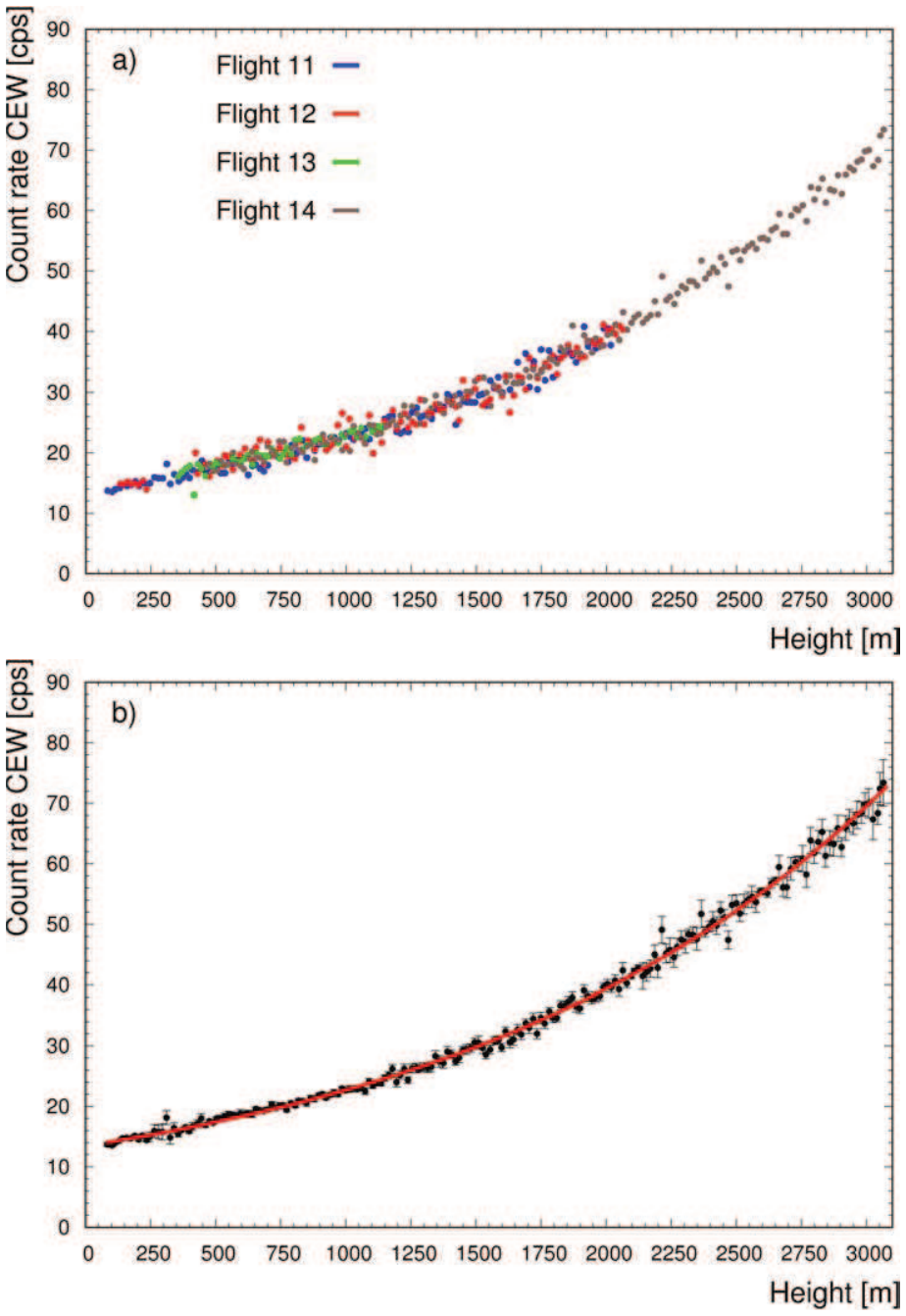

Figure 5.5: Panel a) displays the count rate in the CEW as function of the altitude for the four different flights carried out during the background calibration survey over the sea. Data from different flights sit on top of each other, excluding systematic effects associated to the different acquisition times. Panel b) shows the count rate in the CEW obtained from the entire dataset (black points) as function of the altitude with the superimposed exponential fit function (red solid line). Each point populating the global dataset has been obtained by clustering with an altitude binning of 15 m the spectra measured in that specific height range, disregarding any flight ID classification.

Table 5.4: Fit parameters of the model curve formulated by Eq. 5.2 describing the count rate dependence with respect to the elevation for the count rates measured in the TEW and in the CEW. The last column reports the value of the reduced χ^2 obtained at the end of the minimization procedure.

Energy Window	(A $\pm\delta$ A) [cps]	($\mu \pm \delta\mu$) [m^{-1}]	(B $\pm\delta$B) [cps]	Reduced χ^2
TEW	2.4 ± 0.2	(5.5 ± 0.2) $\cdot 10^{-4}$	1.6 ± 0.2	0.94
CEW	11.4 ± 0.3	(5.9 ± 0.1) $\cdot 10^{-4}$	2.0 ± 0.4	1.12

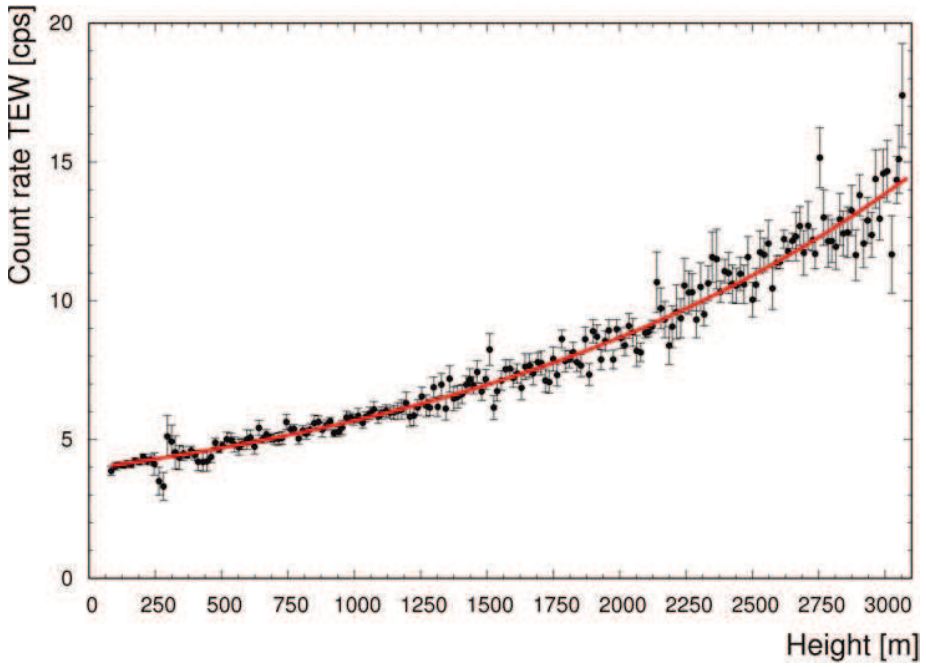

Figure 5.6: Plot of the experimental count rate in the TEW as function of the altitude (black points) together with the corresponding fitting curve (solid red line).

dependency, which is estimated with an uncertainty of 2%.

Fig. 5.6 shows the experimental count rates in the TEW evaluated on the entire dataset, together with the best fit exponential curve, whose parameters values are listed in Table 5.4. Also in this case the reduced chi-square value reflects the high data quality as well as the goodness of the model function in interpreting the measured count rates. The impact of the fitting parameter uncertainties on the estimated count rate is negligible for what concernsμ while the uncertainties on A and B in the TEW individually give rise to a 5% variation of the predicted count rate at 100 m.

For both the CEW and the TEW, the minimization of the χ^2 functions defined by Eq. 5.4 has been performed over the whole altitude range, corresponding to 200 height bins having a 15 m width. In both cases it is possible to recognize the presence of high statistics experimental points for height values below 200 m and around approximately 900, 2100 and 2650 m, which reflect the time flight statistics

Table 5.5: Fit parameters of the model curve formulated by Eq. 5.3 describing the dependence of the count rates in the KEW, BEW and TEW with respect to the count rate in the CEW. The last column reports the value of the reduced χ^2 obtained at the end of the minimization procedure.

Energy Window	(a $\pm\delta$ a) [cps]	(b $\pm\delta$b) [cps/cps in CEW]	Reduced χ^2
KEW	3.7 ± 0.4	0.20 ± 0.01	1.00
BEW	2.0 ± 0.4	0.16 ± 0.01	1.02
TEW	1.58 ± 0.04	0.179 ± 0.002	1.02

illustrated in Fig. 5.3. As a result of the definition of the objective χ^2 function, the discrepancy between the fitting function and the data is minimum in correspondence of the experimental points having the smallest statistical uncertainty.

In International Atomic Energy Agency 1991 and R. Grasty and B. Minty 1995 an analogous study of the count rate in the TEW as function of altitude is shown: this kind of reconstruction is carried out in both cases with a NaI spectrometer having 33.6 L volume, which precludes the possibility of a direct comparison with the results of this study. However, from a qualitative point of view, it emerges that the μ coefficient entering the exponential dependence (and essentially quantifying the rate of increase of the counting statistics) is for the three cases in the range $(4 - 6) \cdot 10^{-4}$ m^{-1}. Previous studies focused on a different altitude range, from around 1500 m to 4500 m: in this framework, this work demonstrates that the count rate both in the CEW and in the TEW maintains its exponential behavior down to tens of meters above sea level. The analysis of the exponential trend of the count rates with respect to the altitude could have been done in principle also for the count rates in the KEW and in the BEW, restricting the fitting domain to the range of altitudes greater than 2000 m. However, as the velocity of increase of the count rate with respect to the altitude is very slow, fitting in the 2000 – 3000 m height domain would suffer the lack of the low altitude tail, producing incorrect extrapolations down to sea level. This point can be a trigger for a deeper investigation, as it can potentially be a way for exploring the content of ^{222}Rn in the lower atmosphere.

Fig. 5.7 shows the experimental data with the superimposed linear curve resulting from the minimization of the χ^2 function described by Eq. 5.5, where the number of bins is equal to 200 for the TEW and is equal to 72 for the KEW and the BEW. Table 5.5 lists the fitting parameters together with the associated uncertainties and the reduced χ^2 value, which is almost 1 for all the three energy windows. In the perspective of using these linear relations for applying the Window Analysis Method (International Atomic Energy Agency 2003) to airborne gamma-ray spectra, the uncertainties estimated in Table 5.5 are relevant for attempting an evaluation of systematics associated with aircraft and cosmic background corrections. With the hypothesis of flying at 100 m height, the mentioned background count rate is (6.5 ± 0.5) cps in the KEW, (4.3 ± 0.6) cps in the BEW and (4.1 ± 0.1) cps in the TEW.

For the count rate in the TEW, as both the exponential and linear curve reconstructions have been performed, it is possible to check the consistency of the obtained results according to the existing

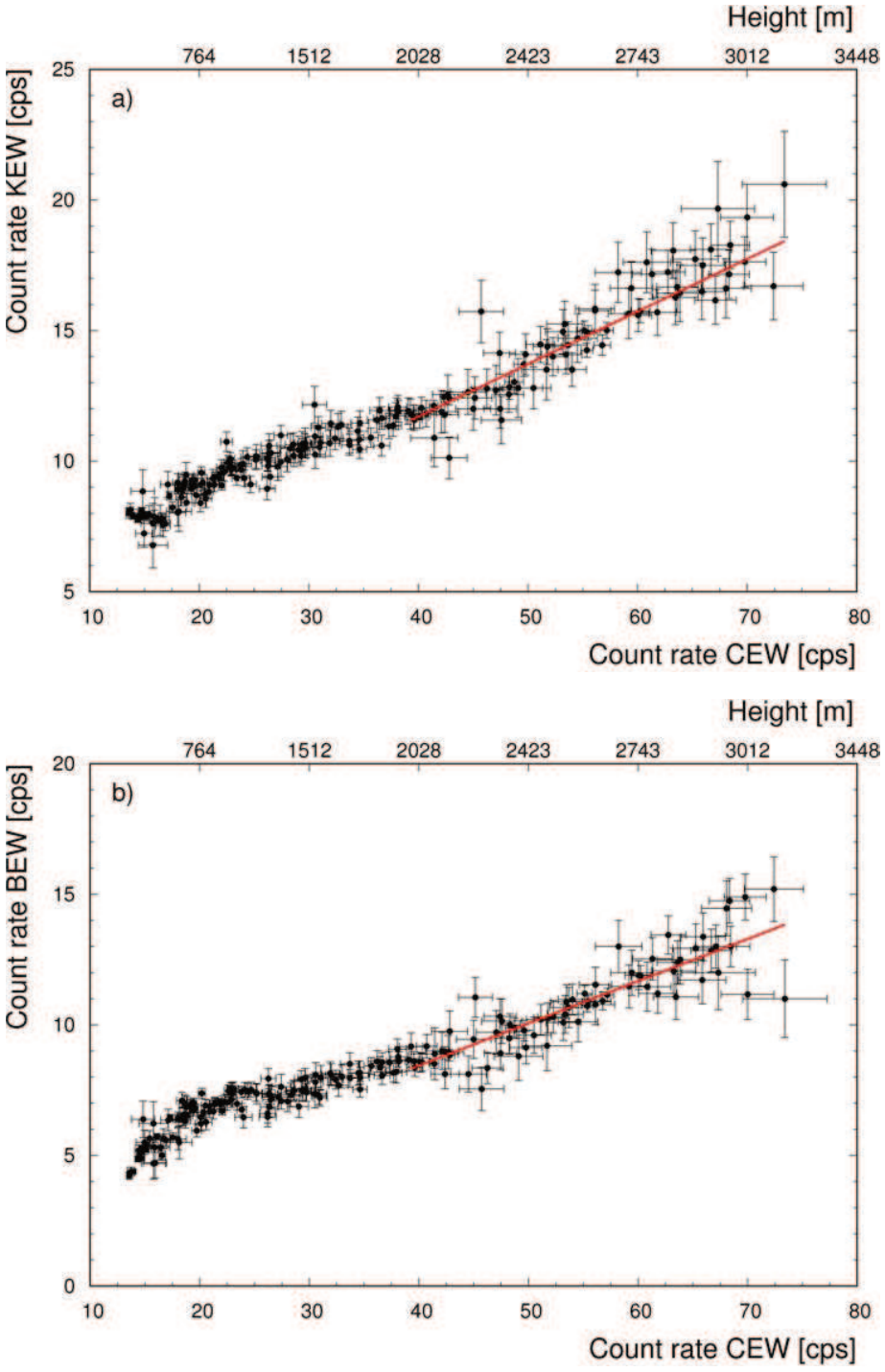
Height [m]
764
1512
2028
2423
2743
3012
3448
a)
Count rate KEW [cps]
25
20
15
10
5
10
20
30
40
50
60
70
80
Count rate CEW [cps]
Height [m]
764
1512
2028
2423
2743
3012
3448
b)
Count rate BEW [cps]
20
15
10
5
0
10
20
30
40
50
60
70
80
Count rate CEW [cps]

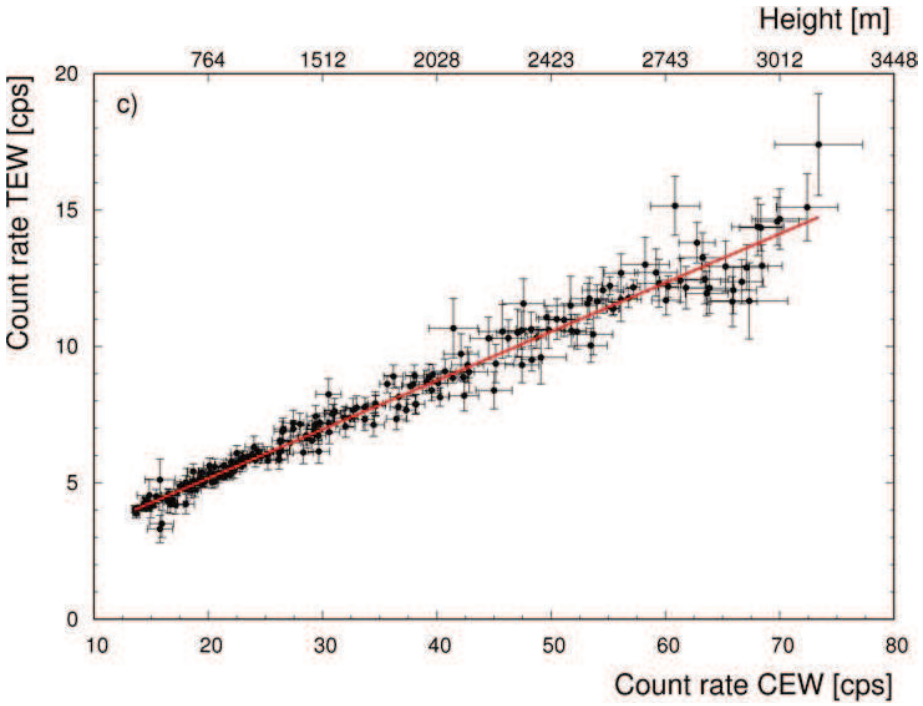

Figure 5.7: Panels a), b) and c) report respectively the experimental count rates (black points) in the KEW, in the BEW and in the TEW as function of the count rate in the CEW, together with the corresponding fitting curve (solid red line).

relations among the fit parameters. On the base of the expected value of the count rates in the CEW and in the TEW at zero altitude, it is also possible to establish the following relationship among fit parameters:

$$A^{TEW} + B^{TEW} = a^{TEW} + b^{TEW} \left(A^{CEW} + B^{CEW} \right) \tag{5.7}$$

Adopting the parameters reported in Table 5.4 one can calculate the left hand side of Eq. 5.7, which corresponds to (4.0 ± 0.4) cps.The right hand side of the equation can be estimated using the parameters listed in Table 5.4 and in Table 5.5, which provide a count rate of (4.0 ± 0.2) cps. The perfect agreement gathered from this analysis is an important internal consistency check of the goodness of both the exponential and linear model function in interpreting the experimental data.

Eq. 5.7 describes the minimum detectable count rate of the AGRS_16L detector: indeed, it provides the sum of the constant aircraft count rate plus the minimum cosmic count rate component, corresponding to the one determined at zero altitude. As the right hand side of Eq. 5.7 can be calculated not only for the TEW, but also for the KEW and for the BEW, it is possible to estimate the minimum detectable count rates for the three energy windows of interest. These counting statistics can be naively converted to equivalent K, U and Th abundances homogeneously distributed across an infinite flat earth by means of sensitivity coefficients obtained from a dedicated ground calibration campaign on natural sites. According to this approach it is possible to estimate that the AGRS_16L detector can not measure K, U and Th concentrations lower than $0.05 \cdot 10^{-2}$ g/g, 0.4 μg/g, 0.8 μg/g, respectively.

The CED profile has been reproduced by multiple runs of the CARI-6 code for different elevations, from which an exponential trend of the CED with respect to the altitude has been determined (see Appendix). In the Appendix a comparison between CED values obtained from CARI-6 runs and estimated according to different analytical models is shows. Fig. 5.8 shows a scatter plot of the CARI-6 CED versus n^{CEW} values, which has been fitted according to the model linear relation of Eq. 5.6, depicted with the solid blue line. The best linear relation has been determined with a r^2 coefficient of determination equal to 0.99 and with linear regression parameters respectively equal to a_{CED} = (58.5 ± 3.2) μSv/y and b_{CED} = (20.6 ± 0.1) μSv/(ycps).

The results obtained on the cosmic effective does rate (CED) from the CARI-6 code have been compared with the analytical models providing the CED as function of altitude, published by Bouville and Lowder 1988; Biirgi and Hisch 1991; Rybach, Medici, and Schwarz 1997; Sztanyik and Nikl 1982. Except for the model published by Bouville and Lowder 1988, these effective dose models don't take into account the neutron component of the cosmic rays. In order to compare the values obtained from these analytical models to the CARI-6 results, the neutron component of Bouville and Lowder 1988 has been added to each one of the other models. The percentage variation among the different analytical models is on the order of 20% in the altitude range of 0 – 3000 m and the values obtained with the CARI-6 code are always within the range of variability. Fig. 5.9 shows the altitude profiles of the CED obtained with the CARI-6 code and with the different analytical models. The data points estimated with the CARI-6 code have been fitted according to the following exponential model

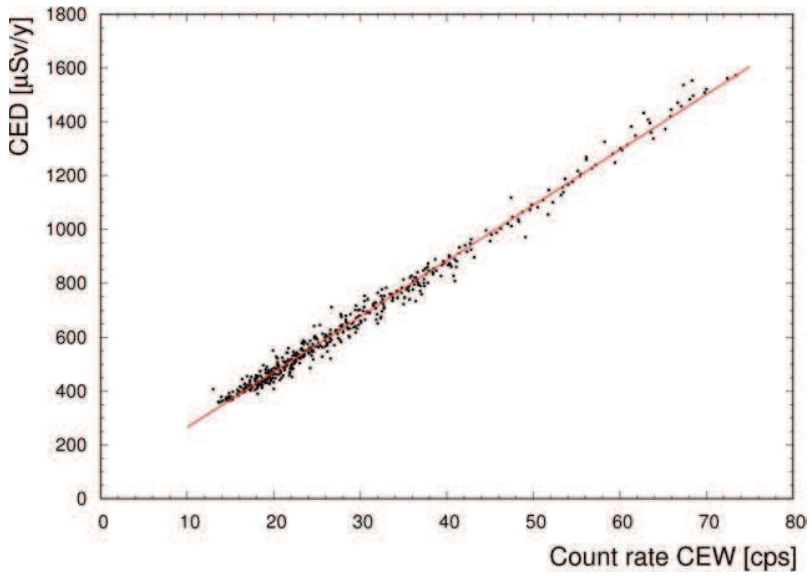

Figure 5.8: CED versus the experimental count rate in the CEW (black points), together with the corresponding fitting curve (red solid line) having best fit parameters equal to $a_{CED} = (58.5 \pm 3.2)$ μSv/y and $b_{CED} = (20.6 \pm 0.1)$ μSv/(y·cps).

function:

$$CED(z) = A^{CED} e^{\mu^{CED} z} + B^{CED} \tag{5.8}$$

Both the CED and the n^{CEW} dependence on the elevation are exponentials: as a consequence it is possible to establish a relation between CED and n^{CEW} of the type:

$$CED = A^{CED} \left(\frac{n^{CEW} - B^{CEW}}{A^{CEW}} \right)^{\frac{\mu^{CED}}{\mu^{CEW}}} + B^{CED} \tag{5.9}$$

which, in the hypothesis of $\frac{\mu^{CED}}{\mu^{CEW}} \sim 1$ translates in an approximately linear relation between CED and n^{CEW}:

$$CED \approx \frac{A^{CED}}{A^{CEW}} n^{CEW} - \frac{A^{CED} B^{CEW}}{A^{CEW}} + B^{CED} \tag{5.10}$$

As the relation $\frac{\mu^{CED}}{\mu^{CEW}} \sim 1$ holds, this justifies the use of a linear relation as stated by Eq. 5.6 in modeling the dependence of CED on n^{CEW} .

The CARI-6 program has different available variants: the CARI-6P version in particular estimates the effective dose and dose rate for single locations providing separate information for the principal contributing particle groups, which are muons, electromagnetic showers (electrons, positrons and

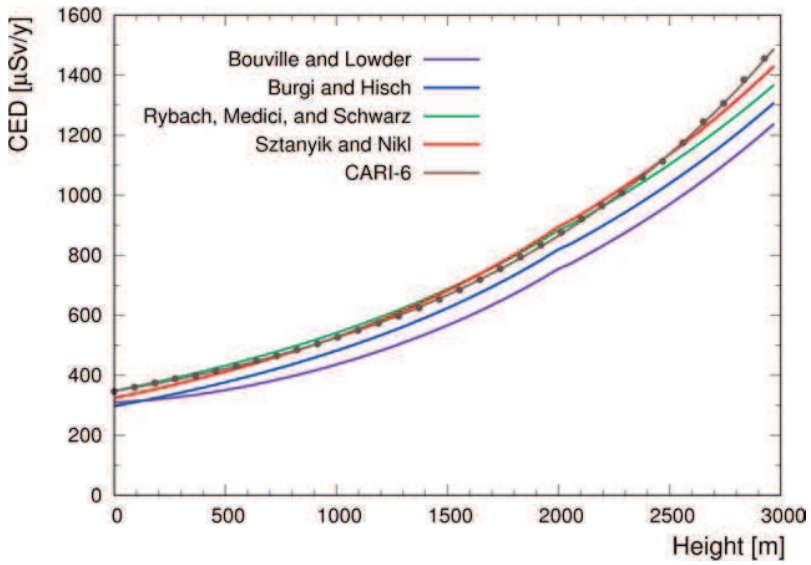

Figure 5.9: CED profiled with respect to the altitude obtained with the CARI-6 code and with the analytical models provided by Bouville and Lowder 1988; Biirgi and Hisch 1991; Rybach, Medici, and Schwarz 1997; Sztanyik and Nikl 1982. The slight kink in the analytical models at 2000 m is due to the change in the neutron component. The data points determined with the CARI-6 software have been fitted with the model function given by Eq. 5.8 which has best fit parameters equal to A^{CED}= (195.71 ± 3.29) μSv/y, μ^{CED}= (6.47 ± 0.05) $\cdot 10^{-4}$ m−1 and B^{CED}= (151.27 ± 4.25) μSv/y.

photons), charged pions, protons and neutrons. By running the CARI-6P version with the same approach described for the CARI-6 program, it is possible to produce a scatter plot of the cosmic effective dose rate due to electromagnetic showers (CED^{EMS}) versus the CED, which is due to all the particle groups (see Fig. 5.10). The relation between CED^{EMS} and CED remains is well reproduced by a polynomial of order 3, which reflects the change with respect to the altitude of the contribution given by the electromagnetic showers to the total cosmic dose (FAA 2014).

As the CED^{EMS} also has an exponential behavior with respect to the altitude $\frac{\mu^{CED^{EMS}}}{\mu^{CEW}} \sim 1$, it is possible estimate a linear relation which converts the count rates in the CEW n^{CEW} to the CED^{EMS}

$$CED^{EMS} = a_{CED^{EMS}} + b_{CED^{EMS}} \cdot n^{CEW} \tag{5.11}$$

Fig. 5.11 shows a scatter plot of the CED^{EMS} obtained by running the CARI-6PM version versus n^{CEW} values, fitted according to Eq. 5.11. The best linear relation has been determined with a r^2 coefficient of determination equal to 0.99 and with linear regression parameters respectively equal to $a_{CED^{EMS}}$= (1.1 ± 0.5) μSv/y and $b_{CED^{EMS}}$= (3.08 ± 0.01) μSv/(y·cps).

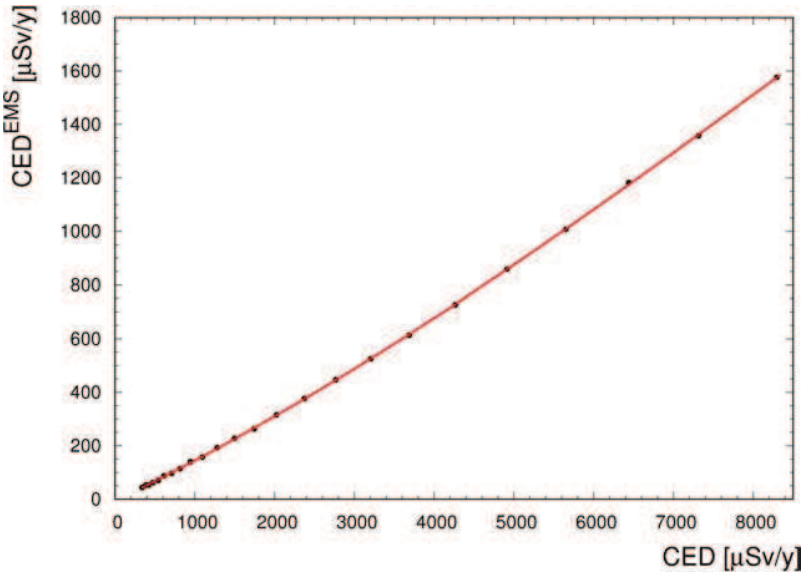

Figure 5.10: Plot of the electromagnetic shower component of the cosmic effective dose rate CED^{EMS} versus the total cosmic effective dose rate CED.

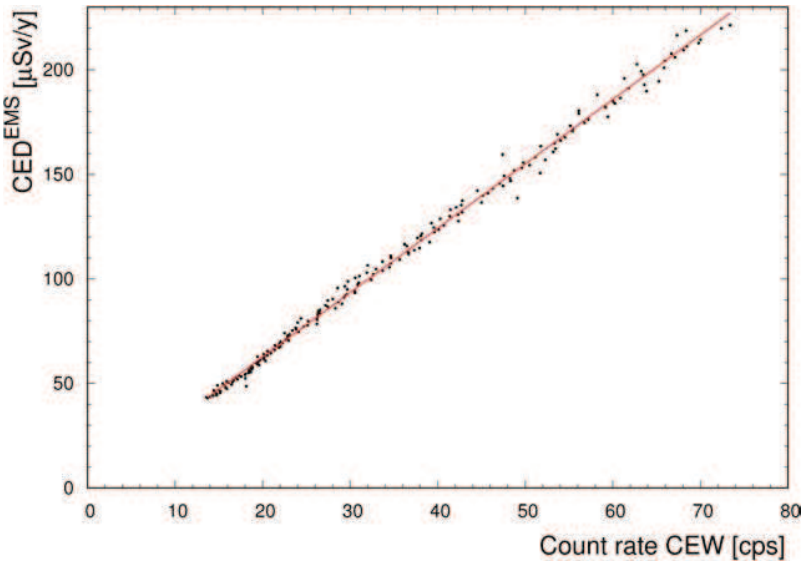

Figure 5.11: Cosmic effective dose rate due to electromagnetic showers (CED^{EMS}) versus the experimental count rate in the CEW (black points), together with the corresponding fitting curve (red solid line) having best fit parameters equal to $a_{CED^{EMS}}$= (1.1 ± 0.5) μSv/y and $b_{CED^{EMS}}$= (3.08 ± 0.01) μSv/(y·cps).

5.4 Final remarks

This work illustrates the results of a ∼5 hour airborne offshore survey dedicated to the AGRS_16L detector calibration for the gamma background signal originating from cosmic radiation and equipment radioactivity and for the assessment of cosmic effective dose to human population. This airborne campaign has been conducted with the Radgyro, an ultra-light aircraft dedicated to multispectral airborne surveys, and has the peculiarity of having investigated a wide range of altitudes above sea level (77 – 3066 m). The acquisition of high-statistics spectra over the sea at different altitudes allowed to separate the background count rate into a constant aircraft component and a cosmic component exponentially increasing with increasing height.

A statistical analysis has been performed to determine the parameters that linearly relate the count rates in the energy windows associated to the K, U and Th photopeaks and the counting statistics recorded in the cosmic energy window (CEW) in which no event coming from terrestrial radioactivity is expected. By monitoring the count rate in the CEW and by applying the obtained linear relations it is possible to calculate for every airborne gamma-ray spectrum the background count rates in the photopeaks of interest that need to be subtracted prior the implementation of the height and stripping corrections before finally convert corrected elemental count rates to ground abundances. Minimum detectable K, U and Th abundances have been inferred from the minimum detectable count rates in the KEW, BEW and TEW, which correspond to the overall background count rates at zero altitude. On the basis of ground sensitivity coefficients, it is possible to assess that the AGRS_16L detector can not measure K, U and Th concentrations lower than 0.05 $\cdot 10^{-2}$ g/g, 0.4 μg/g, 0.8 μg/g, respectively.

For the count rates in the CEW and in the TEW the exponential increase of counting statistics with respect to the altitude has been reconstructed, providing as argument for the exponential function a μ coefficient of 6 $\cdot 10^{-4}$ m^{-1} which is comparable with the value published in International Atomic Energy Agency 1991 and R. Grasty and B. Minty 1995. Moreover, the analysis of the count rates in the TEW highlighted a perfect internal consistency among linear fit and exponential fit parameters. The exponential analysis for the count rates in the KEW and in the BEW was unfeasible due to the application of a low altitude cut to the dataset (z>2000 m), which allowed to exclude potential contamination caused by atmospheric ^{222}Rn. This point, however, deserves a deeper investigation as deviations from purely exponential/linear behaviors could in principle be used to quantify the atmospheric ^{222}Rn abundance at different elevations.

The AGRS_16L has also been calibrated for assessing the annual cosmic effective dose to human population by using as calibrating reference the dose rate values obtained with the program CARI-6, developed by the Federal Aviation Administration (FAA 2014). The relation between the count rate in the CEW and the annual cosmic effective dose has been found to be linear with a r^2 coefficient of determination equal to 0.99, and linear regression parameters respectively equal to a_{CED} = (58.5 ± 3.2) μSv/y and b_{CED} = (20.6 ± 0.1) μSv/(y·cps).

The content of this chapter is based on the following publication:

Baldoncini M., Alberi M., Bottardi C., Mantovani F., Minty B., Raptis K.G.C., Strati V."*Airborne gamma-ray spectroscopy for modeling radiation and effective dose in the lower atmosphere.*" To be submitted to Remote Sensing of Environment.

Bibliography

Abraham, J. et al. (2010). "Measurement of the energy spectrum of cosmic rays above 1018 eV using the Pierre Auger Observatory". *Physics Letters B* 685.4, pp. 239–246. ISSN: 0370-2693. DOI: 10.1016/j.physletb.2010.02.013.

Albéri, M. et al. (2016). "Studio della quota di volo mediante GNSS, altimetro radar e barometro per rilievi di spettroscopia gamma da velivolo". *Atti della 20° Conferenza Nazionale ASITA 2016 di Cagliari - Federazione ASITA*.

Baroň, I. et al. (2013). "Airborne geophysical survey of the catastrophic landslide at Stože, Log pod Mangrtom, as a test of an innovative approach for landslide mapping in steep alpine terrains". *Natural Hazards and Earth System Science* 13.10, pp. 2543–2550. ISSN: 1684-9981. DOI: 10.5194/nhess-13-2543-2013.

Beamish, David (2016). "Enhancing the resolution of airborne gamma-ray data using horizontal gradients". *Journal of Applied Geophysics* 132, pp. 75–86. ISSN: 0926-9851. DOI: 10.1016/j.jappgeo.2016.07.006.

Biirgi, Andreas and Markus Hisch (1991). "Cosmic ray dose rate determination using a portable gamma-ray spectrometer". *Ancient TL vol. 9 n. 1*, pp. 1–5.

Bilski, P., P. Olko, and T. Horwacik (2004). "Air-crew exposure to cosmic radiation on board of Polish passenger aircraft". *Nukleonika* 49.2, pp. 77–83. ISSN: ISSN 0029-5922.

Bird, D. J. et al. (1993). "Evidence for correlated changes in the spectrum and composition of cosmic rays at extremely high energies". *Physical Review Letters* 71.21, pp. 3401–3404. DOI: 10.1103/PhysRevLett.71.3401.

Bottollier-Depois, J. F. et al. (2009). "Comparison of codes assessing galactic cosmic radiation exposure of aircraft crew". *Radiation Protection Dosimetry* 136.4, pp. 317–323. ISSN: 1742-3406. DOI: 10.1093/rpd/ncp159.

Bouville, A. and W. M. Lowder (1988). "Human population exposure to cosmic radiation". *ResearchGate* 24.1, pp. 293–299. ISSN: 0144-8420.

Bucher, G. et al. (2009). "International Intercomparison Exercise of Airborne Gammaspectrometric Systems of Germany, France and Switzerland in the Framework of the Swiss Exercise ARM07." *IAEA Technical Report*. ISSN: PSI-Bericht Nr. 09-07, ISSN 1019-0643.

Cao, Ye et al. (2015). "Spectrum correction algorithm for detectors in airborne radioactivity monitoring equipment NH-UAV based on a ratio processing method". *Nuclear Instruments and Methods in Physics Research Section A: Accelerators, Spectrometers, Detectors and Associated Equipment* 797, pp. 290–296. ISSN: 0168-9002. DOI: 10.1016/j.nima.2015.07.012.

Cardarelli, John et al. (2015). "Real-Time Radionuclide Identification and Mapping Capabilities of the U.S. Environmental Protection Agency's Airborne Spectral Photometric Environmental Collection Technology". *Nuclear Terrorism and National Preparedness*. Ed. by Samuel Apikyan and David Diamond. NATO Science for Peace and Security Series B: Physics and Biophysics. Springer Netherlands, pp. 105–116. ISBN: 978-94-017-9890-7 978-94-017-9891-4.

Cavalcante, F. et al. (2011). "Effective dose rate evaluation from natural gamma radiation in the region of Ribeirao Preto, SP-Brazil". *Radioprotection* 46.6, S145–S150. ISSN: 0033-8451, 1769-700X. DOI: 10.1051/radiopro/20116921s.

Dachev, Ts et al. (2002). "Calibration results obtained with Liulin-4 type dosimeters". *Advances in space research: the official journal of the Committee on Space Research (COSPAR)* 30.4, pp. 917–925. ISSN: 0273-1177.

Detwiler, R. S. et al. (2015). "Spectral anomaly methods for aerial detection using KUT nuisance rejection". *Nuclear Instruments and Methods in Physics Research Section A: Accelerators, Spectrometers, Detectors and Associated Equipment*. Symposium on Radiation Measurements and Applications 2014 (SORMA XV) 784, pp. 339–345. ISSN: 0168-9002. DOI: 10.1016/j.nima.2015.01.040.

FAA (2014). "CARI-6 Program to Calculate Galactic Cosmic Radiation". *http://www.faa.gov/data_research/research/med_humanfacs/aeromedical/radiobiology/cari6/*.

Friedberg, Wallace and Kyle Copeland (2011). "Ionizing Radiation in Earth's Atmosphere and in Space Near Earth". *Final Report*.

Gong, ChunHui et al. (2014). "Minimum detectable activity for NaI(Tl) airborne gamma-ray spectrometry based on Monte Carlo simulation". *Science China Technological Sciences* 57.9, pp. 1840–1845. ISSN: 1674-7321, 1869-1900. DOI: 10.1007/s11431-014-5553-x.

Grasty, R. L. et al. (2001). "Calibration of a 7.6 cm x 7.6 cm (3 inch x 3 inch) sodium iodide gamma ray spectrometer for air kerma rate". *Radiation Protection Dosimetry* 94.4, pp. 309–316. ISSN: 0144-8420.

Grasty, R.L. and Brian Minty (1995). *A guide to the technical specifications for airborne gamma-ray surveys*. Geoscience Australia.

Grasty, R.L., M. P. Bates, and A. Smetny-Sowa (2015). "Monitoring airborne gamma ray spectrometer sensitivities using the natural background." *ASEG Extended Abstracts* 2015.1, p. 1. ISSN: 2202-0586. DOI: 10.1071/ASEG2015ab116.

International Atomic Energy Agency (1991). *Airborne Gamma Ray Spectrometer Surveying*. Technical Reports Series 323. Vienna: International Atomic Energy Agency.

International Atomic Energy Agency (2003). *Guidelines for Radioelement Mapping Using Gamma Ray Spectrometry Data*. IAEA-TECDOC-1363. Vienna: International Atomic Energy Agency.

Iza, Edgar Romeo Herrera de Figueiredo et al. (2016). "Boolean and fuzzy methods for identifying lateritic regoliths in the Brazilian Amazon using gamma-ray spectrometric and topographic data". *Geoderma* 269, pp. 27–38. ISSN: 0016-7061. DOI: 10.1016/j.geoderma.2016.01.037.

Keaney, A. et al. (2013). "Spatial statistics to estimate peat thickness using airborne radiometric data". *Spatial Statistics*. GeoENV2012: Geostatistics for Environmental Applications 5, pp. 3–24. ISSN: 2211-6753. DOI: 10.1016/j.spasta.2013.05.003.

Kleinschmidt, R. and D. Watson (2016). "Terrestrial gamma radiation baseline mapping using ultra low density sampling methods". *Journal of Environmental Radioactivity* 151 Pt 3, pp. 609–622. ISSN: 1879-1700. DOI: 10.1016/j.jenvrad.2015.05.008.

Kock, Peder, Jan Lanke, and Christer Samuelsson (2012). "A real-time statistical alarm method for mobile gamma spectrometry—Combining counts of pulses with spectral distribution of pulses". *Nuclear Instruments and Methods in Physics Research Section A: Accelerators, Spectrometers, Detectors and Associated Equipment* 681, pp. 55–60. ISSN: 0168-9002. DOI: 10.1016/j.nima.2012.04.038.

Kock, Peder, Christopher Rääf, and Christer Samuelsson (2014). "On background radiation gradients-the use of airborne surveys when searching for orphan sources using mobile gamma-ray spectrometry". *Journal of Environmental Radioactivity* 128, pp. 84–90. ISSN: 0265-931X. DOI: 10.1016/j.jenvrad.2013.10.022.

Kulisek, J. A. et al. (2015). "Real-time airborne gamma-ray background estimation using NASVD with MLE and radiation transport for calibration". *Nuclear Instruments and Methods in Physics Research Section A: Accelerators, Spectrometers, Detectors and Associated Equipment*. Symposium on Radiation Measurements and Applications 2014 (SORMA XV) 784, pp. 287–292. ISSN: 0168-9002. DOI: 10.1016/j.nima.2014.11.110.

Mercier, N and C Falguères (2007). "Field gamma dose-rate measurement with a NaI (Tl) detector: re-evaluation of the "threshold" technique". *Ancient TL 25.1*, pp. 1–4.

Minty, B. R. S., A. P. J. Luyendyk, and R. C. Brodie (1997). "Calibration and data processing for airborne gamma-ray spectrometry". *ResearchGate* 17.2, pp. 51–62. ISSN: 1320-1271.

Minty, Brian and Ross Brodie (2016). "The 3D inversion of airborne gamma-ray spectrometric data". *Exploration Geophysics* 47.2, pp. 150–157. ISSN: 1834-7533. DOI: 10.1071/EG14110.

Mohamedou, Cheikh, Timo Tokola, and Kalle Eerikäinen (2014). "Applying airborne gamma-ray and DEM-derived attributes to the local improvement of the existing individual tree growth model for diameter increment". *Remote Sensing of Environment* 155, pp. 248–256. ISSN: 0034-4257. DOI: 10.1016/j.rse.2014.08.033.

Rybach, L., F. Medici, and G. F. Schwarz (1997). "Construction of radioelement and dose rate baseline maps by combining ground and airborne radiometric data".

Sanderson, D. C. W., A. J. Cresswell, and D. C. White (2008). "The effect of flight line spacing on radioactivity inventory and spatial feature characteristics of airborne gamma-ray spectrometry data". *International Journal of Remote Sensing* 29.1, pp. 31–46. ISSN: 0143-1161. DOI: 10.1080/01431160701268970.

Sandness, G. A. et al. (2009). "Accurate modeling of the terrestrial gamma-ray background for homeland security applications". *2009 IEEE Nuclear Science Symposium Conference Record (NSS/MIC)*. 2009 IEEE Nuclear Science Symposium Conference Record (NSS/MIC), pp. 126–133. DOI: 10.1109/NSSMIC.2009.5401843.

Sato, Tatsuhiko (2016). "Evaluation of World Population-Weighted Effective Dose due to Cosmic Ray Exposure". *Scientific Reports* 6, p. 33932. ISSN: 2045-2322. DOI: 10.1038/srep33932.

Söderström, Mats et al. (2016). "Adaptation of regional digital soil mapping for precision agriculture". *Precision Agriculture* 17.5, pp. 588–607. ISSN: 1385-2256, 1573-1618. DOI: 10.1007/s11119-016-9439-8.

Spurný, F. and T. Daschev (2002). "On Board Aircrew Dosimetry with a Semiconductor Spectrometer". *Radiation Protection Dosimetry* 100.1, pp. 525–528. ISSN: 0144-8420, 1742-3406.

Sztanyik, L. B. and I. Nikl (1982). "Contribution of cosmic rays to radiation exposure of the population". *Acta Physica Academiae Scientiarum Hungaricae* 53.1, pp. 189–200. ISSN: 0001-6705. DOI: 10.1007/BF03156189.

Tang, Xiao-Bin et al. (2016). "Efficiency calibration and minimum detectable activity concentration of a real-time UAV airborne sensor system with two gamma spectrometers". *Applied Radiation and Isotopes* 110, pp. 100–108. ISSN: 0969-8043. DOI: 10.1016/j.apradiso.2016.01.008.

Tsui, K.C., M.C. Wong, and B.Y. Lee (1991). "Field estimation of cosmic contribution to total external gamma radiation in Hong Kong". *Royal Observatory Hong Kong*.

Tuan, Nguyen Duc et al. (2013). "Design And Construction Of The Portable Gamma-Ray Spectrometer For Environmental Dose Rate Measurement And Radioisotope Identification".

Tufarolo, E. et al. (2014). "Il Radgyro: un autogiro dedicato ad acquisizioni airborne multiparametriche". *Atti della 18° Conferenza Nazionale ASITA 2014 di Firenze - Federazione ASITA*.

UNSCEAR (2008). "Sources and efffects of ionizing radiation - Annex B".

Varley, Adam et al. (2016). "Mapping the spatial distribution and activity of 226Ra at legacy sites through Machine Learning interpretation of gamma-ray spectrometry data". *Science of The Total Environment* 545–546, pp. 654–661. ISSN: 0048-9697. DOI: 10.1016/j.scitotenv.2015.10.112.

Williams, Alastair G. et al. (2010). "The Vertical Distribution of Radon in Clear and Cloudy Daytime Terrestrial Boundary Layers". *Journal of the Atmospheric Sciences* 68.1, pp. 155–174. ISSN: 0022-4928. DOI: 10.1175/2010JAS3576.1.

Chapter 6

Exploring atmospheric radon with airborne gamma ray spectroscopy

^{222}Rn is a naturally occurring noble gas produced via alpha decay of ^{226}Ra and it is the only gaseous daughter product of the decay chain of ^{238}U, which is present in the majority of soils and rocks and which has a half-life of $\sim 4.5 \cdot 10^9$ yr, comparable to the Earth's age. As ^{222}Rn is inert and hardly soluble in water, it exhales from soil and rocks into the atmosphere and migrates by diffusion and convection almost without being subject to atmospheric removal processes, therefore running out mainly through radioactive decay (Jacobi and André 1963). ^{222}Rn half-life is of 3.82 days, which is relatively long for being connotative of events related to turbulence (having a typical 1 hour time scale), but also short enough to have a high concentration gradient through the lower troposphere, thanks to which it is possible to gather insights into air vertical mixing mechanisms and help in tracing air transport processes. Generally, the vertical distribution of radon in the atmosphere is studied by performing counting experiments of alpha or beta particles emitted in the decay of radon daughter products, which is commonly a time demanding process relying on the collection and filtering of air mass samples.

In the light of airborne gamma-ray spectroscopy (AGRS), ^{222}Rn is typically treated as a source of background as it affects the indirect estimate of the equivalent ^{238}U concentration. Indeed, the observed gamma-ray spectrum associated to the presence of ^{238}U in the environment results mainly from the gamma emissions associated to the decays of ^{214}Pb and ^{214}Bi, which occur far down in the ^{238}U radioactive decay chain, and in particular after the ^{222}Rn alpha decay .

In this work the AGRS method is applied in order to test the feasibility of distinguishing and quantifying the presence of radon in the atmosphere. This study is performed by monitoring the expected count rate in the ^{214}Bi photopeak at 1765 keV, which is sufficiently well separated from other natural radionuclides photopeaks and which is intense enough to have a statistically significant signal during typical airborne survey acquisition times. I was personally involved in the data acquisition during a $\sim$4 hours airborne gamma-ray survey over the sea, covering an altitude range of 77 - 3066 m

above sea level. Flying offshore assures that no gamma rays from geological origin are detected and that the observed spectra originate from the superposition of an aircraft, a cosmic and an atmospheric radon component. I took care of the raw data processing and of the statistical analysis founded on a χ^2 minimization procedure, according to which two analytical models respectively excluding and accounting for the presence of atmospheric radon have been tested. The model accounting for the presence of radon in the atmosphere provided a better fit to data, along with values of atmospheric radon abundance and vertical extent of radon distribution comparable with literature references.

6.1 Background

^{222}Rn, a noble gas produced along the ^{238}U decay chain, asserted its effectiveness as atmospheric tracer thanks to its poor chemical reactivity and to its half-life, which is comparable with chemical lifetimes of short-lived air pollutants and with resident times of atmospheric constituents like water and aerosols. Monitoring atmospheric ^{222}Rn has a variety of applications in climate, air quality and pollution studies, including tracing air mass transport, tracing diurnal mixing in the lower atmosphere, calibrating seasonal regional emissions of climatically sensitive tracers including CO_2, CH_4, N_2O, and validating transport and mixing schemes in climate/weather models (International Atomic Energy Agency 2012). ^{222}Rn atmospheric abundance is strictly connected with its exhalation rate from soils, which is typically on the order of 0.8-1.2 atoms /(cm$^2\cdot$ s) and which is in turn affected by soil type, granulometry and moisture content, as well as by porosity and permeability (Turekian, Nozaki, and Benninger 1977). In the past a great effort has been dedicated in modeling the radon flux and air transport in the atmospheric boundary layer over land disregarding the contribution coming from the ocean, but recently it has been found that radon from the ocean can dominate that from land for specific wind conditions (Schery and Huang 2004).

Measurements of the vertical distribution of ^{222}Rn can be conducted as tower-based studies, which generally have high vertical resolution but altitude limited to 5 – 40 m, as well as via airborne ^{222}Rn or ^{222}Rn progeny measurements, which can span a larger height range (from hundreds of m to more than 10 km) but typically resolve few altitudes (Williams et al. 2010). Direct ^{222}Rn measurements are generally carried out by laboratory extraction of ^{222}Rn absorbed by activated charcoal after the exposure to sampled air, while indirect measurements are generally made by alpha counting of ^{222}Rn progeny. The former provides direct radon concentrations, even if having an extracting and counting apparatus at short distance is necessary in order to reduce the time available for ^{222}Rn to decay as much as possible. On the other hand, ^{222}Rn progeny measurements rely on the assumption of secular equilibrium between ^{222}Rn and its daughter products (Williams et al. 2010). Variations in the vertical radon concentration profiles produce changes in the natural background gamma-ray flux which, in turn, can be responsible for perturbations and contaminations in aerial monitoring results (Beck 1974). ^{214}Pb, having a half-life of 26.8 minutes, and ^{214}Bi, having a half-life of 19.8 minutes, are the two principal gamma-emitting daughters of ^{222}Rn, which, thanks to their short decay time, are usually in equilibrium with each other (i.e., their activities are about the same at all elevations).

When the vertical mixing conditions are not characterized by quick variations (as instead happens close to sunrise and sunset), the steady state is generally reached which means that the concentration profiles of radon and its daughters tend to be near secular equilibrium, except near ground (h $<$ 25 m) (Gogolak 1977).

In this work we present the results of a $\sim$4 hours airborne gamma-ray survey over the sea: when flying offshore no geological gamma signal is detected and the measured spectra result from the superposition of a constant contribution coming from the radioactivity of the equipment and of the height dependent contributions associated with the cosmic radiation and with atmospheric radon. The airborne gamma-ray spectrometry campaign has been conducted over a wide range of altitudes, from 77 m up to 3066 m. Thanks to this large elevation extent, it has been possible to explore the presence of radon in the atmosphere via the modeling of the expected count rate in the ^{214}Bi photopeak energy window according to two analytical models which respectively exclude and account for the presence of atmospheric radon.

6.2 Experimental setup, survey and data

Airborne gamma-ray surveys were carried out in a series of 3 flights over the Tyrrhenian Sea close to Viareggio (Tuscany, Italy), accounting for a total acquisition time of 14688 seconds. The surveys were performed by acquiring gamma-ray signals with the AGRS_16L detector mounted on the Radgyro aircraft (see Fig. 6.1) described in Sec. 4.4.2 and Sec. 5.2.1. The Radgyro spatial coordinates are determined as mean 1 second position and altitude above sea level starting from the NMEA GGA sentences recorded by the two GPS antennas mounted on the aircraft (see Sec. 5.2.1). Table 6.1 reports a summary of the main parameters related to each of the 3 flights, where it is important to remark that measurements acquired at a distance from the coast less than 300 m have been excluded from the analysis in order to avoid potential degradation of the data quality due to gamma-rays of geological origin.

The estimated count rates in the energy windows of interest (see Table 6.2) have been clustered according to an altitude binning of 15 m, which is conservative with respect to the estimated accuracy on the vertical position resulting from the combination of all the altimeters present on board of the Radgyro (Albéri et al. 2016). The count rates are estimated summing all the input count rates acquired in the same elevation bin and dividing by the number of 1 second spectra entering the summation. Fig. 6.2 shows the count rates measured respectively in the ^{40}K Energy Window (KEW), ^{214}Bi Energy Window (BEW), ^{208}Tl Energy Window (TEW) and Cosmic Energy Window (CEW) as function of the altitude above sea level, distinguished according to the different flights. In the TEW and CEW the variation of the count rates in different flights is compatible with the statistical fluctuation of the count rates: there is no systematic effect related to the different flight times and the exponential behavior is maintained down to low elevations. With respect to the count rates in the KEW and BEW there is some evidence of data clustering for different flights, in particular at low elevations, which could be a hint of the presence of radon gas in the atmosphere.

Figure 6.1: Picture of the Radgyro taken during the airborne gamma-ray survey over the sea.

Table 6.1: Summary of the main parameters for each of the 3 surveys over the sea. For each flight the ID, date, time, minimum and maximum altitude and acquisition time are reported, respectively. In the case of flights 11 and 14, 83 seconds and 30 seconds have been cut due to some radiofrequency interference between the PMT and the aircraft transponder. The long interruption in the data taking of flight 12 (2531 seconds) has been imposed by civil traffic of the Pisa airport.

Flight ID	Date	Time	z min [m]	z max [m]	Acquisition time [s]
11	30/03/2016	17:42:10 19:29:43	77	2019	6370
12	31/03/2016	18:13:55 19:46:47	126	2070	3041
14	05/04/2016	16:37:16 18:05:43	461	3066	5277
Global			77	3066	14688

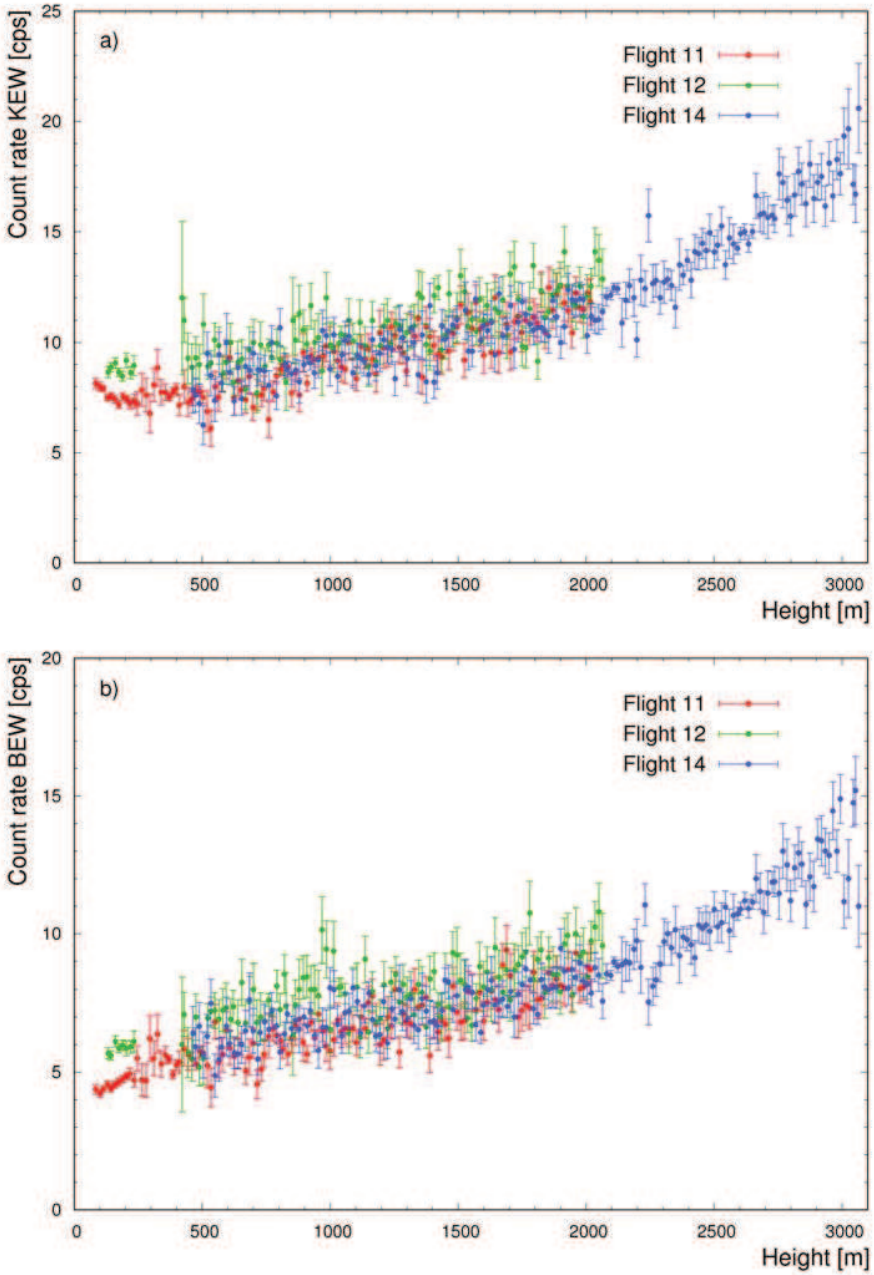
a)
Count rate KEW [cps]
Height [m]
Flight 11
Flight 12
Flight 14
0
5
10
15
20
25
0
500
1000
1500
2000
2500
3000
b)
Count rate BEW [cps]
Height [m]
Flight 11
Flight 12
Flight 14
0
5
10
15
20
0
500
1000
1500
2000
2500
3000

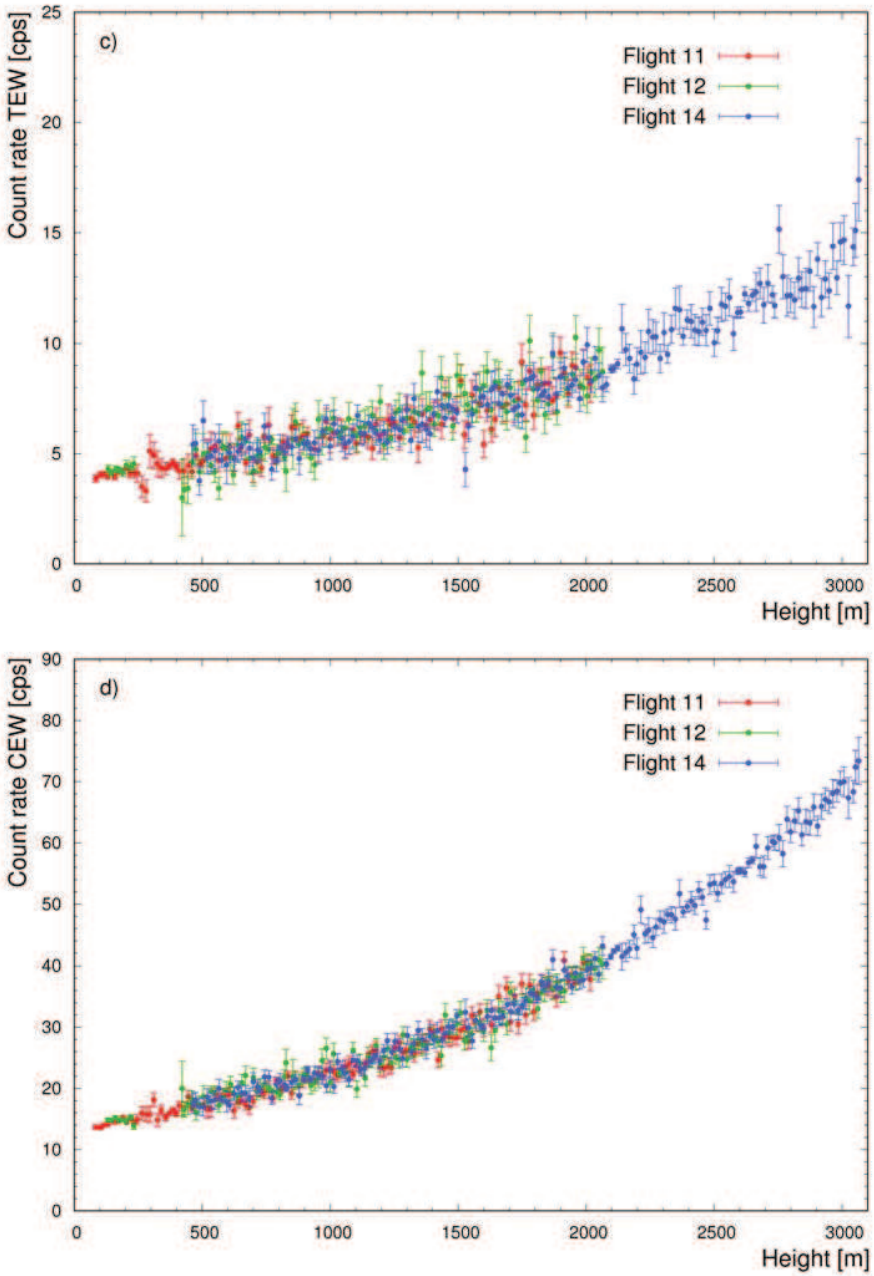

Figure 6.2: Panels a), b), c) and d) show the count rate respectively in the KEW, BEW, TEW and CEW as function of the altitude for the 3 different flights carried out during the survey over the sea. In the TEW and CEW experimental data from different flights sit on top of each other, excluding systematic effects associated to the different acquisition times. In the KEW and BEW it is possible to recognize the effect of atmospheric radon contamination for the 3 different flights.

Table 6.2: Energy windows for natural and cosmic radiation used for the background calibration of the AGRS_16L system. The last two columns report for each energy window the measured counting statistics for gamma-ray spectra acquired at the altitude range 2050 – 2150 m and 2600 – 2700 m, respectively.

Energy Window	Emission line [keV]	Energy range [keV]	Measured cps (2050 - 2150) m	Measured cps (2600 - 2700) m
KEW	1460	1370 - 1570	12.2	15.0
BEW	1765	1660 - 1860	8.7	11.1
TEW	2614	2410 - 2810	8.8	11.9
CEW	/	3000 - 7000	41.9	54.8

6.3 Theoretical model

^{222}Rn gas is the only gaseous daughter product of the ^{238}U decay series and constitutes a large component of background radiation in airborne gamma-ray spectroscopy measurements. Indeed, its daughter products ^{214}Pb and ^{214}Bi are the main gamma-emitters in the ^{238}U decay chain and since they bind to airborne aerosols they are responsible of the measured radon background. Estimates of the uranium content via airborne gamma-ray spectroscopy measurements rely on the evaluation of background subtracted count rates in the ^{214}Bi photopeak energy window (BEW), which corresponds to the (1660 – 1860) keV energy range centered on the 1765 keV ^{214}Bi gamma emission line. Background correction involves the removal of gamma signal of non-geologic nature, which consists of three components resulting respectively from the decay of ^{214}Bi in the atmosphere, the radioactivity of the aircraft and its equipment, and the interaction of secondary cosmic radiation with the air, the aircraft and the detector (B. Minty 1998). Airborne gamma-ray detectors are generally calibrated for the aircraft and cosmic background by performing high-altitude offshore flights in an area where atmospheric radon is at minimum. Spectra are measured in a range of heights, typically from 1.0-1.5 km up to 3.0-3.5 km above the water with a 300-500 m step, for generally 10-15 minutes accumulation time at each height (International Atomic Energy Agency 2003). In the absence of radon gas in the atmosphere, experimental data can be described on the base of a radon free model according to which the counting statistics in the BEW results from the superposition of an aircraft and a cosmic component. The contribution associated to the radioactivity of the aircraft corresponds to the count rates originated mainly by the 1765 keV ^{214}Bi gamma emission, plus a tiny Compton signal associated to higher energy gamma lines emitted by daughter nuclei of trace amounts of ^{238}U and ^{232}Th present in the detector and aircraft materials. The cosmic component is instead the result of cosmic secondary radiation interaction with the air, the aircraft and the detector materials. The sum of the constant aircraft count rate and the count rate of cosmic origin $n_{BEW}^{aircraft+cosmic}(z)$ is expected to increase exponentially with height above sea level according to the following equation:

$$n_{BEW}^{aircraft+cosmic}(z) = A_{BEW} e^{\mu_{BEW} z} + B_{BEW} \tag{6.1}$$

where $n_{BEW}^{aircraft+cosmic}(z)$ is the count rate in the BEW and A_{BEW}, μ_{BEW} and B_{BEW} are constants (Grasty and Brian Minty 1995; International Atomic Energy Agency 1991). This radon free model is expected to accommodate experimental measurements, generally at altitudes greater than 2000 m. Indeed, although the atmospheric concentration of ^{222}Rn and of its daughter products can vary significantly with different diffusion conditions, mean ^{222}Rn concentrations are (4 ± 3) Bq/m^3 in the lowest 30-1000 m, while above 1000-1500 m mean ^{222}Rn concentrations generally show a steep decrease to values compatible with zero (around (2 ± 2) Bq/m^3), dropping even further to (0.3 ± 0.4) Bq/m^3 above 3000 m (Williams et al. 2010). When looking to experimental data acquired at low altitudes, a deviation from the mentioned exponential behavior can be observed due to radon accumulation in the atmosphere. Traditionally, the presence of atmospheric radon is identified as a breakdown of the linear relation that is supposed to hold between the count rates in the BEW and the count rates measured in the CEW, the latter having exclusively cosmic origin since the maximum terrestrial gamma energy corresponds to the 2614 keV ^{208}Tl emission (Grasty and Brian Minty 1995).

An alternative model can be developed with the aim of covering the entire altitude range and of recognizing and possibly quantifying the presence of the gas radon in the atmosphere via the detection of the gamma-signal generated by the decay of ^{214}Bi. In presence of atmospheric radon, the overall count rate recorded in the BEW $n_{BEW}(z)$ can be decomposed into the sum of two terms as follows:

$$n_{BEW}(z) = n_{BEW}^{aircraft+cosmic}(z) + n_{BEW}^{Rn}(z) \tag{6.2}$$

where $n_{BEW}^{aircraft+cosmic}(z)$ is the aircraft plus cosmic component and $n_{BEW}^{Rn}(z)$ is the altitude dependent component arising from the atmospheric ^{214}Bi. With respect to the modeling of the $n_{BEW}^{Rn}(z)$ component, an altitude profile of radon concentration in the atmosphere is theoretically required, which is directly connected with the dynamics of the atmospheric boundary layer.

The diurnal evolution of the atmospheric boundary layer, i.e. the ∼1-2 km thick layer where the atmosphere feels the contact with the ground surface, is governed by the mechanical and thermal surface-air interactions which are respectively driven by wind and solar radiation. Under clear skies, the night generally ends with a shallow nocturnal boundary layer in which mixing is caused by wind. After sunrise the warmed ground heats the air touching the ground, creating thermals that rise and cause intense convective motions which gradually erode the stratified layer created during the night replacing it by the convective boundary layer (or mixed layer), generally characterized by high homogeneity. As time passes, the growing convective region eventually reaches as high as it did on the previous day; at sunset thermals cease and convection terminates, leading to the formation of a residual layer containing near zero turbulence and the residual moisture, heat, and pollutants that were mixed during the day. The cold surface cools the air near the ground, transforming the bottom of the residual layer into a new nocturnal boundary layer. As long as the weather remains fair the cycle repeats on a daily timescale. The efficiency of erosion during the day depends in part on the amount of cloud cover as a cloud layer can intercept portions of the sunlight and reduce the amount of heat delivered to ground level (Stull 2012).

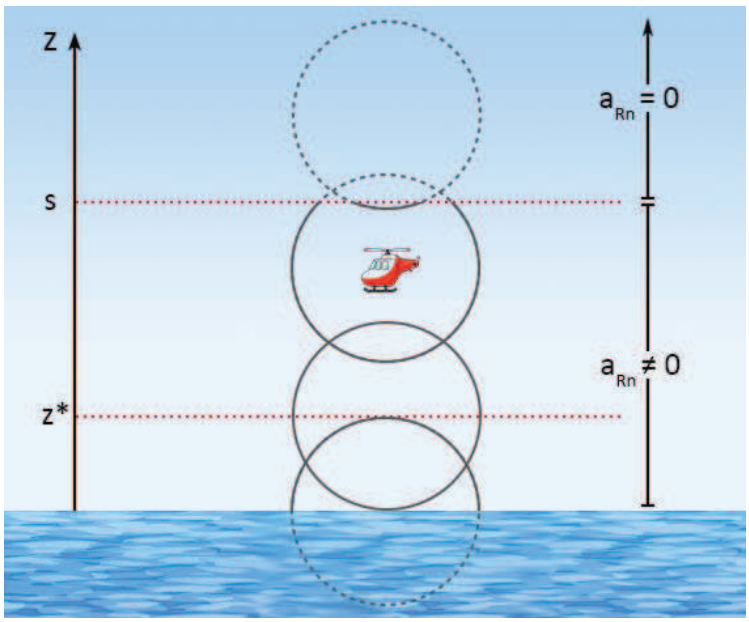

Figure 6.3: Schematic illustration of the variation of the detector field of view to the atmospheric ^{214}Bi gamma signal with respect to the height. When the detector is at sea level, the field of view will be that of a half-sphere. With increasing height the detector starts seeing the upward photon flux till the field of view reaches saturation at the altitude z*, corresponding to the full-sphere case. Approaching the separation altitude s between the two radon layers the field of view starts shrinking and finally vanishes when the detector is completely immersed in the radon free layer.

In cases of fair weather, for convective boundary layers a very marked drop in radon concentrations is generally observed in crossing the separation between the mixed layer and the free troposphere, where radon abundances reach typically near-zero values (Williams et al. 2010). In the case of mixed layers topped with residual layers radon exhibits a fairly constant profile in the mixed layer and tends to reduce linearly with height in the residual layers.

As the airborne campaign was conducted under clear sky conditions in a narrow range of days and always in the late afternoon, the simplified radon vertical profile adopted in this study is a discrete model according to which the radon concentration is uniform up to a cutoff altitude s, basically corresponding to the depth of the mixed layer, and null above the cutoff height. Fig. 6.3 shows a schematic example of the behavior of the field of view of the gamma-ray detector to ^{214}Bi gamma signal as it moves to increasing altitude, starting from sea level up to the separation height between the two radon gas layers, till it reaches the radon free zone.

In the lower layer where the radon activity is uniform, the contribution to the count rate in the BEW originated by the atmospheric ^{214}Bi will have a monotonic increase with increasing altitude. Indeed, at altitude zero the detector field of view can be approximated by a half-sphere as the gamma photon flux has only a downward incoming direction; when the detector starts lifting from sea level an upward incoming photon flux will start being visible enhancing the detected gamma signal. At an

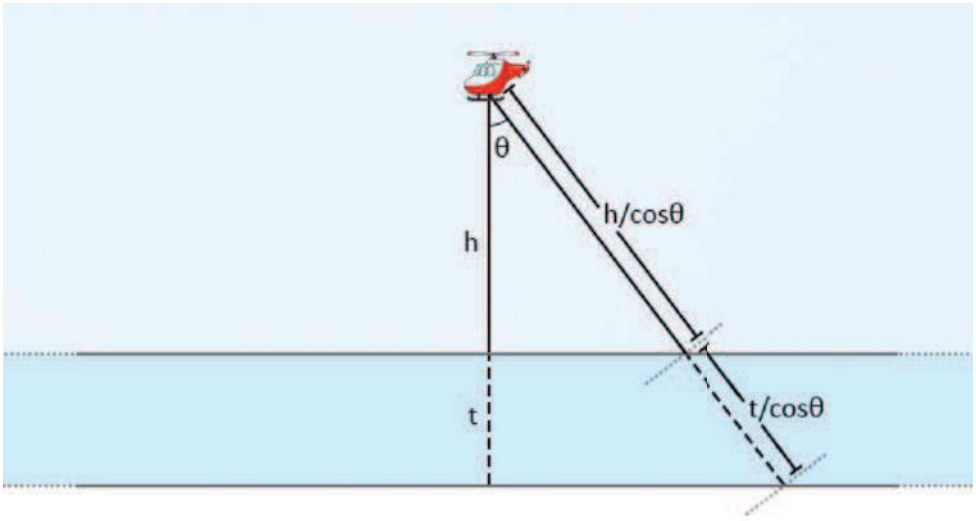

Figure 6.4: Schematic diagram of the geometrical model adopted for estimating the unscattered photon flux reaching a detector situated at a vertical distance h from a source having infinite lateral extension and thickness t. In this context the source of thickness t corresponds to an air layer in which a homogeneous radon concentration is present.

altitude equal to half the separation height $n^{Rn}_{BEW}(z)$ will reach its maximum. If the cutoff altitude s is high enough (for s > 400 m, corresponding to ∼2.3 photon mean free paths, the count rate gradient will be < 0.01%), the maximum count rate will reach a saturation value almost equal to double the count rate recorded at sea level, corresponding to the full-sphere field of view. Approaching the separation height s, the

$n^{Rn}_{BEW}(z)$ count rate will start monotonically decreasing till it vanishes when the detector is far enough from the lower radon layer.

From the theoretical point of view it is necessary to model the propagation of unscattered photons from the source to the detector position: this modeling is simplified by the fact that air corresponds to both the source material and the material photons traverse after having exited the source. Fig. 6.4 shows the geometrical model for the theoretical calculation of the unscattered photon flux.

The flux of unscattered 1765 keV photons emitted by atmospheric ^{214}Bi is given by the following equation:

$$\Phi = \frac{A_t}{2\mu_a} \int_0^1 dcos\theta e^{\frac{-\mu_a h}{cos\theta}} \left[1 - e^{\frac{-\mu_a t}{cos\theta}} \right] \tag{6.3}$$

where A_t is the volumetric gamma activity [γ/m^3] of the uniformly distributed ^{214}Bi, μ_a is the air linear attenuation coefficient referred to 1765 keV photons, t is the thickness of the air layer in which gamma photons are homogeneously and isotropically emitted, h is the vertical distance of the detector from the source layer. Assuming the detector's effective cross sectional area to be a constant,

the expression for the photon flux directly translates into the expression describing the variation of the count rate as function of altitude, as stated by the following equation:

$$n = C \int_0^1 dcos\theta e^{\frac{-\mu_a h}{cos\theta}} \left[1 - e^{\frac{-\mu_a t}{cos\theta}} \right] \tag{6.4}$$

where C represents the count rate in cps measured at zero distance from a semi-infinite homogeneous air volume source, i.e. the count rate obtained for $h = 0$ and $t \to \infty$.

The dependence of $n_{BEW}^{Rn}(z)$ with respect to the altitude can be modeled by distinguishing the case in which the detector vertical position z is below or above the cutoff altitude s. In both scenarios the air layer at an altitude greater than s does not give any contribution to the signal as it has zero activity volume concentration. As illustrated in Fig. 6.5a, when the detector position z is below the cutoff altitude s, two air source layers can be identified having respectively thickness equal to z and $s - z$. Considering that the detector is at zero vertical distance from both layers, the $n_{BEW}^{Rn}(z)$ count rate can be written as the sum of $n_1(z)$ and $n_2(z)$, corresponding respectively to the contribution coming from the layer 1 and the layer 2, as stated by the following equation:

$$n_{BEW}^{Rn}(z) = n_1(z) + n_2(z) = C \int_0^1 dcos\theta \left[1 - e^{\frac{-\mu_a z}{cos\theta}} \right] + C \int_0^1 dcos\theta \left[1 - e^{\frac{-\mu_a (s-z)}{cos\theta}} \right] \quad (z < s) \tag{6.5}$$

If the detector position is above the cutoff altitude ($z > s$), the detected count rate arises only from layer number 3 (see Fig. 6.5b), where the air source layer thickness is s and the detector vertical distance from the source is z, corresponding to:

$$n_{BEW}^{Rn}(z) = n_3(z) = C \int_0^1 dcos\theta e^{\frac{-\mu_a (z-s)}{cos\theta}} \left[1 - e^{\frac{-\mu_a s}{cos\theta}} \right] \tag{6.6}$$

Therefore, the theoretical expression for the count rate in the BEW $n_{BEW}^{Rn}(z)$ can be summarized according to the following equation:

$$n_{BEW}^{Rn}(z) = \Theta(s - z) \left[n_1(z) + n_2(z) \right] + \Theta(z - s) n_3(z) \tag{6.7}$$

where $\Theta(x)$ represents the Heaviside step function.

In Fig. 6.6 the $n_{BEW}^{Rn}(z)$ curve is plotted for a cutoff altitude s equal to 1500 m and count rate value C equal to 1.5 cps which, on the base of sensitivity values obtained from a dedicated calibration campaign on natural calibration sites, corresponds to a radon concentration of 2 Bq/m^3. The adopted value for the gamma linear attenuation coefficient μ_a for 1765 keV photons propagating in air is equal to 0.005829 m^{-1}. This value has been estimated using an air density of 1.225 kg/m3 and a

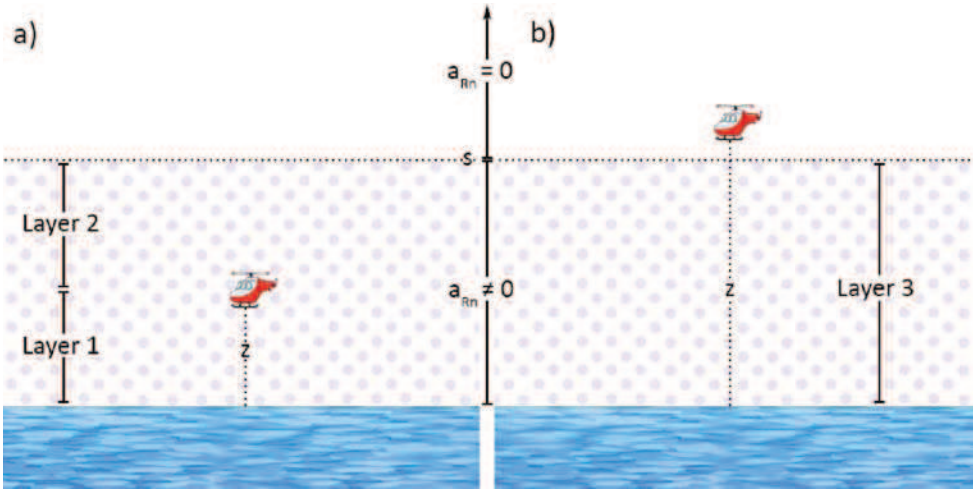

Figure 6.5: . Schematic illustration of the air layers generating the radon contribution to the count rate in the BEW. When the detector vertical position z is below the cutoff altitude s (which separates the lower atmospheric portion having uniform radon concentration from the upper one which has null radon abundance), there are two layers generating the ^{214}Bi gamma signal (a). When the detector vertical position z is above the cutoff altitude s, there is only one layer generating the ^{214}Bi gamma signal (b).

gamma mass attenuation coefficient of 0.04758 cm^2/g, taken from the National Institute of Standard and Technology website (http://physics.nist.gov/PhysRefData/Xcom/html/xcom1.html), where an air composition of 78% N_2, 21% O_2 and 1% Ar by weight has been given for the description of the composite traversed material. As expected, the curve is symmetrical with respect to an altitude value equal to half the separation height. The separation altitude s corresponds to ∼8.7 photon mean free paths, which is a long enough distance for the count rate at sea level $n^{Rn}_{BEW}(0)$ to reach the C value, corresponding to the count rate associated to a semi-infinite volume source. Similarly, $n^{Rn}_{BEW}(z)$ gets to reach and maintain the saturation value equal to $2C$ before starting to decrease when the altitude approaches s.

On the base of the modelling of the gas radon contribution, the overall count rate in the BEW can be expressed according to the following equation:

$$n_{BEW}(z) = A_{BEW}e^{\mu_{BEW}z} + B_{BEW} + \Theta(s-z)\left[n_1(z) + n_2(z)\right] + \Theta(z-s)n_3(z) \tag{6.8}$$

Fig. 6.7 shows the global behavior of $n_{BEW}(z)$, together with the separate components associated with the aircraft plus cosmic background and with the radon background. The aircraft plus cosmic background (red dashed line) represents the count rate that would have been observed in absence of atmospheric radon. The black solid line displays the overall count rate obtained by adding the radon component (blue dashed line) on top of the aircraft plus cosmic count rate. The radon contribution produces a curvature in the model function which is evident in the low altitude range ($z < 200$ m) where the initial half-spherical field of view approaches a full-spherical field of view. After the radon

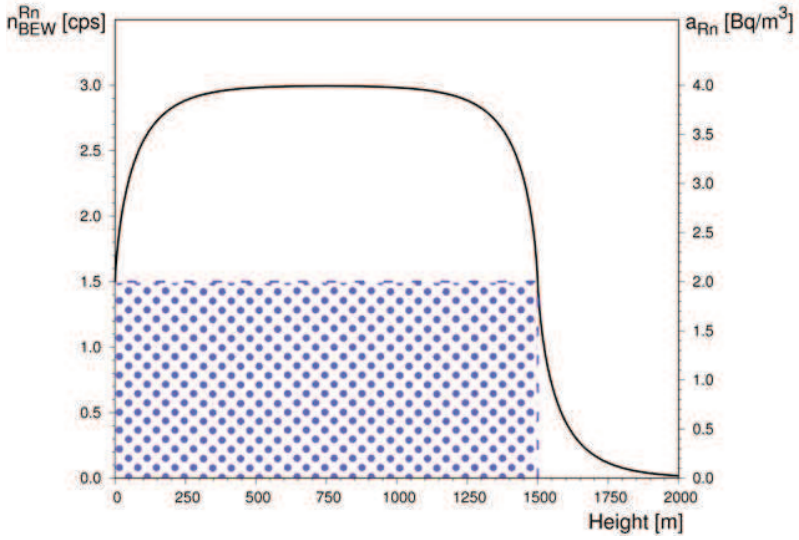

Figure 6.6: . The black solid line illustrates the $n^{Rn}_{BEW}(z)$ count rate (left y axis) as function of the altitude for a C count rate value equal to 1.5 cps and a cutoff altitude s equal to 1500 m (see Eq. 6.7). The blue polka-dotted pattern represents the 2 Bq/m^3 homogenous radon concentration (right y axis) in the atmospheric layer below 1500 m. In the air layer at altitude larger than 1500 m the radon concentration vanishes.

component has reached the plateau, the model curve grows in parallel to the radon free curve just shifted upward by the radon saturation count rate. In approaching the separation altitude between the two radon layers the model curve exhibits a kink, whose vertical extent depends on the values of the exponential function parameters and of the radon concentration gradient between the two layers. This kink translates into a local count rate decrease till the model curve matches the curve obtained in the radon free scenario at an altitude which is ∼400 m (∼2.3 photon mean free paths) higher than the cutoff altitude.

6.4 Data analysis and results

The two theoretical models described in the previous section have been used in order to reconstruct the observed count rate in the BEW as function of altitude. The parameters of the theoretical curves have been determined via the minimization of a χ^2 function. For the radon free model the χ^2 minimization has been performed for the count rates measured at elevations greater than 2000 m, where the condition of absence of radon is supposed to hold. On the base of Eq. 6.1, the following definition of the χ^2 function has been used:

$$\chi^2 = \sum_{j=1}^{N} \left[\frac{n^j_{BEW} - (A_{BEW} e^{\mu_{BEW} z_j} + B_{BEW})}{\sigma_{n^j_{BEW}}} \right]^2 \tag{6.9}$$

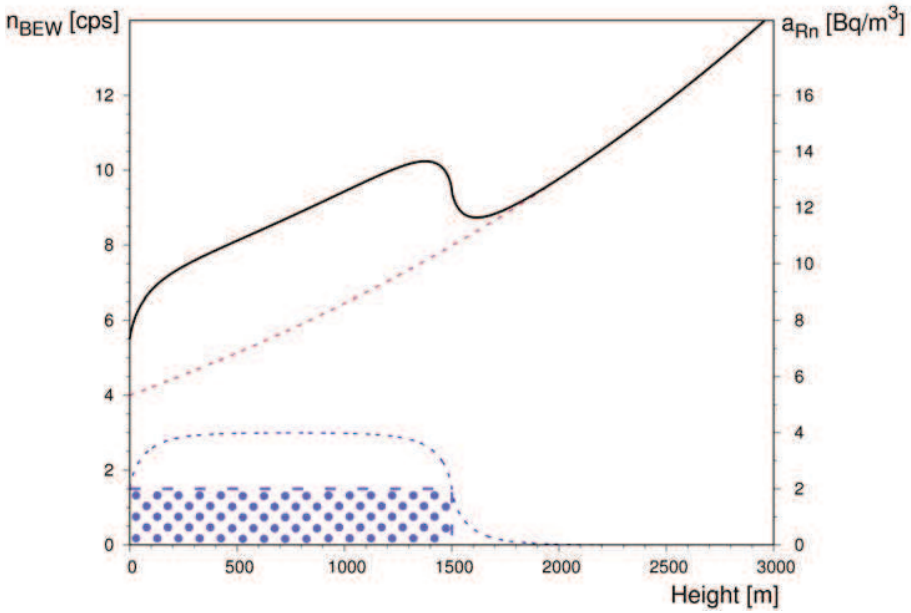

Figure 6.7: . The blue dashed line shows the curve for the count rate in the BEW (left y axis) due to the presence of atmospheric radon $n_{BEW}^{Rn}(z)$ obtained for a cutoff altitude s equal to 1500 m and a C value of 1.5 cps (see Eq. 6.7). The blue polka-dotted pattern represents the 2 Bq/m^3 homogenous radon concentration (right y axis) in the atmospheric layer below 1500 m. In the air layer at altitude larger than 1500 m the radon concentration vanishes. The red dashed line shows the aircraft plus cosmic contribution obtained with A_{BEW} = 7 cps, $\mu_{BEW} = 3 \cdot 10^{-4}$ m^{-1} and B_{BEW} = -3 cps (see Eq. 6.1). The black solid line represents the overall count rate in the BEW, determined as the sum of the aircraft plus cosmic contribution and the atmospheric radon contribution (see Eq. 6.8).

Table 6.3: Fit parameters of the model curves defined by Eq. 6.1 and by Eq. 6.8 describing the dependence with the altitude of the count rate in the BEW respectively in the absence or presence of atmospheric radon. The last column reports the value of the reduced χ^2 referred to the entire range of investigated altitudes.

Theoretical model	$A_{BEW} \pm \delta A_{BEW}$ [cps]	$\mu_{BEW} \pm \delta\mu_{BEW}$ [m^{-1}]	$B_{BEW} \pm \delta B_{BEW}$ [cps]	s [m]	C$\pm\delta$C [cps]	Reduced χ^2
without Rn (Eq. 6.1)	0.39 ± 0.07	$(1.0 \pm 0.1)\cdot 10^{-3}$	5.5 ± 0.3	/	/	5.0
with Rn (Eq. 6.8)	8.2 ± 0.2	$(2.5 \pm 0.1)\cdot 10^{-4}$	-4.9 ± 0.2	1318 ± 22	0.68 ± 0.05	2.1

where N is 79, equal to the number of experimental data measured at z_j >2000 m, n^j_{BEW} is the count rate in the BEW measured at z_j, z_j is the average elevation obtained for the $j-th$ elevation bin and $\sigma_{n^j_{BEW}}$ is the 1 sigma uncertainty associated to the counting statistics, corresponding to the square root of the total counts recorded at z_j in the BEW divided by the acquisition time. For the model containing the radon contribution, the χ^2 minimization has been performed over the entire altitude range corresponding to the 14688 seconds of data taking. On the base of Eq. 6.8, the following definition of the χ^2 function has been used:

$$\chi^2 = \sum_{j=1}^{N} \left[\frac{n^j_{BEW} - (A_{BEW} e^{\mu_{BEW} z_j} + B_{BEW} + \Theta(s - z_j)\,[n_1(z_j) + n_2(z_j)] + \Theta(z_j - s) n_3(z_j))}{\sigma_{n^j_{BEW}}} \right]^2 \tag{6.10}$$

where N is 423, equal to the number of experimental data measured in the entire altitude range, and n^j_{BEW}, z_j, $\sigma_{n^j_{BEW}}$ defined as previously described. The best fit solutions have been found using a fixed value for the 1765 keV gamma linear attenuation coefficient μ_a equal to 0.005829 m^{-1}.

Fig. 6.8 shows the results of the χ^2 minimization procedure: panel a) illustrates the experimental data with the superimposed model curve (extrapolated at low elevations) obtained by fitting the count rates measured at an altitude greater than 2000 m with a theoretical function that accommodates for the aircraft plus cosmic components (see Eq. 6.1). Panel b) shows instead the curve resulting from the fitting of the entire dataset with the theoretical model that accounts also for a signal contribution generated by ^{214}Bi in the atmosphere (see Eq. 6.8). In Table 6.3 the parameters obtained at the end of the fitting procedure are reported.

From Fig. 6.8 it appears that a theoretical model which accounts only for the cosmic and aircraft component is not satisfactory in describing the data distribution, especially at low elevations. Indeed, the model allowing for the presence of radon in the atmosphere provides a better fit to the data, as proved by the reduction of the reduced χ^2 value from 5.0 for the radon free model to 2.1 for the model accounting for radon in the atmosphere. The model that includes the atmospheric radon component produces a better fit to data, not only in terms of reduced χ^2, but also in terms of fit parameters values. Indeed, the goodness of the A_{BEW} and B_{BEW} fit parameters can be checked according to

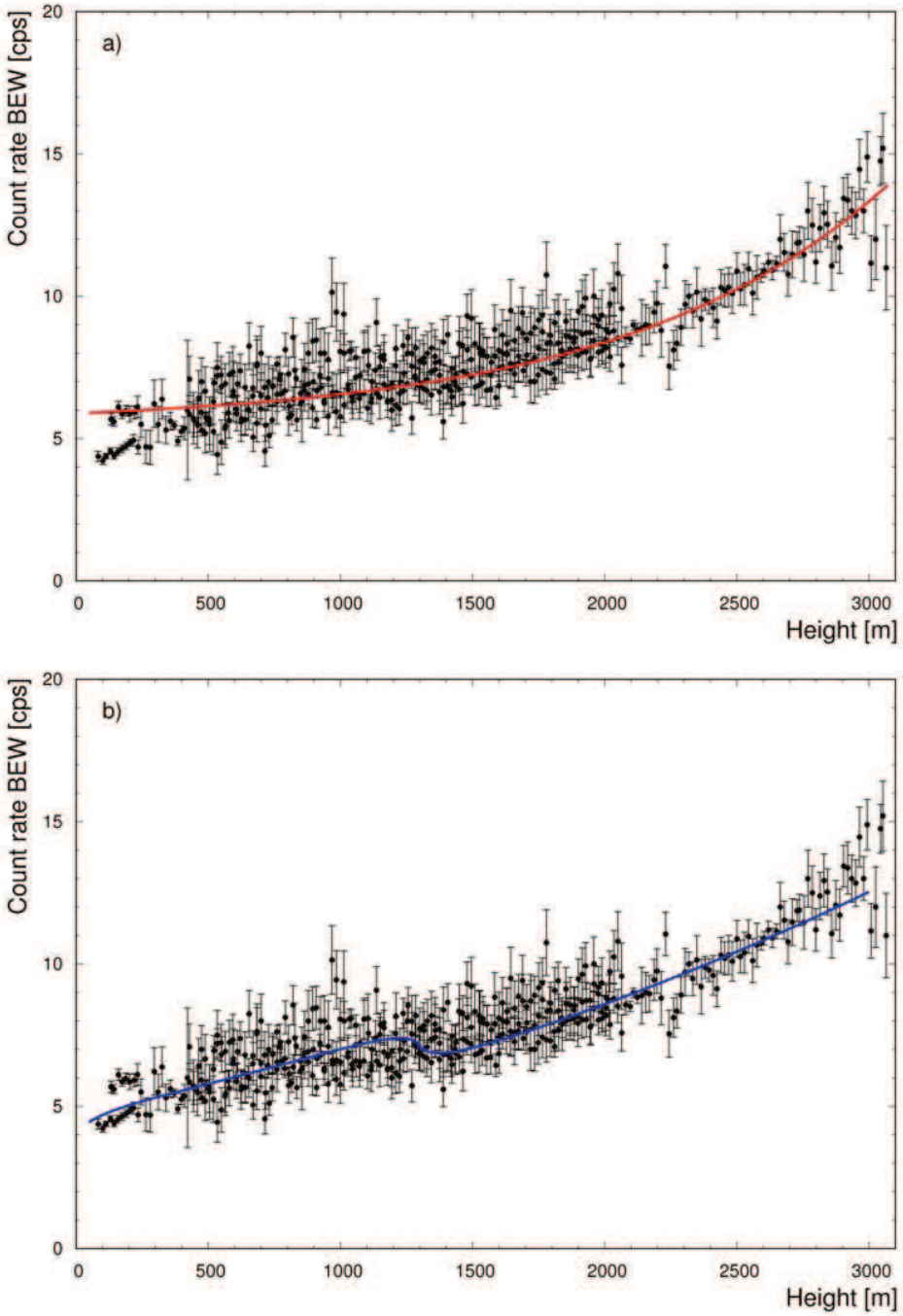

Figure 6.8: . Panel a) shows the count rate recorded in the BEW during the entire survey (black points) together with the curve (red solid line) obtained by fitting the data acquired at $z > 2000$ m with a theoretical model that includes only the aircraft and cosmic components of the gamma signal (see Eq. 6.1). Panel b) shows the same dataset (black points) with the model curve (blue solid line) obtained by fitting the data acquired in the entire elevation range with the theoretical model that accounts also for the presence of radon in the atmosphere (see Eq. 6.8).

their relation with the parameters of the linear function describing the relation between the count rates in the BEW and the count rates in the CEW (see Chapter 5):

$$A_{BEW} + B_{BEW} = a_{BEW} + b_{BEW}\,(A_{CEW} + B_{CEW}) \tag{6.11}$$

On the base of the values obtained in Chapter 5 ($a_{BEW} = (2.0 \pm 0.4)$ cps, $b_{BEW} = (0.16 \pm 0.01)$ cps in BEW/cps in CEW, $A_{CEW} = (11.4 \pm 0.3)$ cps and $B_{CEW} = (2.0 \pm 0.4)$ cps) the right hand side of Eq. 6.11 is estimated to be (4.1 ± 0.7) cps. The value obtained for the left hand side of Eq. 6.11 according to the radon free model is (5.9 ± 0.4) cps, while the model accounting for atmospheric radon provides (3.2 ± 0.5) cps, which are respectively incompatible and compatible at 1σ level with the right hand side value. The fit value for the s parameter is equal to 1300 m, comparable with atmospheric radon ranges reported in Williams et al. 2010. The fit value for the C parameter corresponds to the sea level count rate associated to the presence of radon (and its gamma emitting daughter nuclei) in the atmosphere, which can be converted into radon abundance, provided a sensitivity calibration factor. From an independent ground calibration campaign, the sensitivity matrix necessary for the estimation of the natural radionuclide concentrations via the Window Analysis Method has been determined (International Atomic Energy Agency 1991). The $S_{UU} = 0.71$ cps/(Bq/m^3) element of the sensitivity matrix, corresponding to the count rate in cps in the BEW for unitary concentration of eU in ppm, has been adopted for having a crude estimate of a (1.1 ± 0.1) Bq/m^3 mean radon concentration in the atmospheric (mixed) layer having 1300 m depth. The obtained values for the mean radon abundance and for the mixed layer height are comparable with data published by Williams et al. 2010 and Chen et al. 2016. In Figure 6 of Chen et al. 2016 it is shown that radon concentration is inversely related to the mixing layer height, corresponding typically to about 1 Bq/m^3 for a mixing layer height of 1500 m. Moreover, the diurnal variations of radon abundance and mixing layer height in different season (Figure 5 of Chen et al. 2016) show that typical values of radon abundance in the spring late afternoon are about 1.2 Bq/m^3 for a mixing layer height of ∼1000 m.

6.5 Final remarks

This work presents the results of a ∼4 hour airborne survey over the sea in which the potentialities of the airborne gamma-ray spectrometry method in revealing the presence of radon in the atmosphere have been explored. Typically, indirect radon measurements are performed by counting experiments of alpha-particles or beta-particles emitted in the decay of radon progeny, requiring the collection and filtering of air mass samples which can be a time consuming procedure. Airborne gamma-ray spectroscopy on the other hand could provide a direct measurement of the gamma emissions of ^{214}Bi, although the discrimination of the atmospheric ^{214}Bi component from other sources of radiation is far from being trivial. Airborne gamma-ray spectra acquired over the sea contain no gamma signal produced by the decay of natural radionuclides of geological origin, but they result from the superposition of a cosmic radiation component, a component arising from the equipment radioactivity

and an atmospheric radon component. Offshore detector calibration surveys are generally conducted at altitudes larger than 1500 m in order to avoid taking into account the negligible radon contribution: in this study an attempt of applying a three component model to the analysis of airborne gamma-ray spectra acquired in fair weather conditions in the altitude range 77-3066 m has been carried out. In particular, a model reproducing the altitude dependence of the count rate in the ^{214}Bi photopeak energy window due to the presence of atmospheric radon has been developed. It is based on the theoretical description of photon transport in matter and on a simplified radon vertical profile typically observed in clear sky conditions, according to which radon concentration is uniform up to the mixed layer height and vanishes above. The analysis of the 14688 one second gamma spectra acquired during the campaign showed a statistical evidence of a better fit to data with the model accounting for the presence of radon in the atmosphere with respect to the radon free model, providing respectively a reduced chi-square equal to 2.1 and 5.0. The best fit parameters obtained by allowing for the presence of atmospheric radon are in agreement at 1σ level with parameters obtained by a separate detector calibration procedure for the estimation of the gamma-ray background (see Chapter 5). Finally, the mixed layer depth of 1300 m and of the radon concentration of (1.1 $\pm$0.1) Bq/m^3 are comparable with typical values reported in literature (Williams et al. 2010; Chen et al. 2016).

The content of this chapter is based on the following publication:

Baldoncini M., Alberi M., Bottardi C., Mantovani F., Minty B., Raptis K.G.C., Strati V."*Exploring atmospheric radon with airborne gamma-ray spectroscopy.*" To be submitted to Journal of Advances in Modeling Earth Systems.

Bibliography

Albéri, M. et al. (2016). "Studio della quota di volo mediante GNSS, altimetro radar e barometro per rilievi di spettroscopia gamma da velivolo". *Atti della 20° Conferenza Nazionale ASITA 2016 di Cagliari - Federazione ASITA*.

Beck, Harold L. (1974). "Gamma radiation from radon daughters in the atmosphere". *Journal of Geophysical Research* 79.15, pp. 2215–2221. ISSN: 2156-2202. DOI: 10.1029/JC079i015p02215.

Chen, Xuemeng et al. (2016). "Responses of the atmospheric concentration of radon-222 to the vertical mixing and spatial transportation". *Boreal Environment Research*. ISSN: 1239-6095.

Gogolak, C. V. (1977). "Variation of radon and radon daughter concentrations with height above ground". *HASL–325*.

Grasty, R.L. and Brian Minty (1995). *A guide to the technical specifications for airborne gamma-ray surveys*. Geoscience Australia.

International Atomic Energy Agency (1991). *Airborne Gamma Ray Spectrometer Surveying*. Technical Reports Series 323. Vienna: International Atomic Energy Agency.

International Atomic Energy Agency (2003). *Guidelines for Radioelement Mapping Using Gamma Ray Spectrometry Data*. IAEA-TECDOC-1363. Vienna: International Atomic Energy Agency.

International Atomic Energy Agency (2012). *Sources and Measurements of Radon and Radon Progeny Applied to Climate and Air Quality Studies*. STI/PUB/1541. Vienna: International Atomic Energy Agency. ISBN: 978-92-0-123610-4.

Jacobi, W. and K. André (1963). "The vertical distribution of radon 222, radon 220 and their decay products in the atmosphere". *Journal of Geophysical Research* 68.13, pp. 3799–3814. ISSN: 2156-2202. DOI: 10.1029/JZ068i013p03799.

Minty, B. (1998). "Multichannel models for the estimation of radon background in airborne gamma-ray spectrometry". *Geophysics* 63.6, pp. 1986–1996. ISSN: 0016-8033. DOI: 10.1190/1.1444492.

Schery, S. D. and S. Huang (2004). "An estimate of the global distribution of radon emissions from the ocean". *Geophysical Research Letters* 31.19, p. L19104. ISSN: 1944-8007. DOI: 10.1029/2004GL021051.

Stull, Roland B. (2012). *An Introduction to Boundary Layer Meteorology*. Springer Science & Business Media. 671 pp. ISBN: 978-94-009-3027-8.

Turekian, K K, Y Nozaki, and {and} L. K. Benninger (1977). "Geochemistry of Atmospheric Radon and Radon Products". *Annual Review of Earth and Planetary Sciences* 5.1, pp. 227–255. DOI: 10.1146/annurev.ea.05.050177.001303.

Williams, Alastair G. et al. (2010). "The Vertical Distribution of Radon in Clear and Cloudy Daytime Terrestrial Boundary Layers". *Journal of the Atmospheric Sciences* 68.1, pp. 155–174. ISSN: 0022-4928. DOI: 10.1175/2010JAS3576.1.

Conclusions and future perspectives

The path I walked during my PhD is the natural continuation of a journey started in 2010 when I came in contact with the topics of environmental radioactivity monitoring in the framework of my Bachelor and Master degree thesis. Since then I was fascinated by the multifaceted nature characterizing the field of geophysics where particle physics, earth sciences, statistics, computer science coexist and cooperate in order to address fundamental questions concerning the evolution and structure of our planet as well as to propose operative solutions related to applications.

The challenges I faced allowed me to take an active part in a lively and stimulating scientific environment, giving me the chance to improve technical as well as communication skills. During these years I found the support of a wide community of scientists and of national and international institutions. Spending a formation period at the University of Maryland and at the Barcelona Supercomputing Center had a strong positive impact in my professional and personal growth. The support I received from the University of Ferrara and from the INFN stimulated and helped me to push towards the frontiers of scientific research. In living this adventure I discovered that the greatest potentialities for making progresses in scientific research are often hidden in the subtle folds connecting close disciplines. The interaction among different but not far apart fields appears to me as a prolific playground in which my research activities will be pointing in the next years.

The studies described in these chapters are joined by the concept of the shape reconstruction, which is symbolically evoked by the well-known picture of the Little Prince book representing at the same time a hat or a boa constrictor digesting an elephant. The Little Prince hat represents the comprehensive vision of reality I gained during my PhD: what appears as a unique spectral shape from a global point of view can be deciphered into fundamental components which allow to go beyond the hat itself and perceive the elephant inside the boa. The profile of the hat can camouflage a variety of shapes that during my PhD I recognized as reactor antineutrino spectra, gamma-ray spectra and probability density functions.

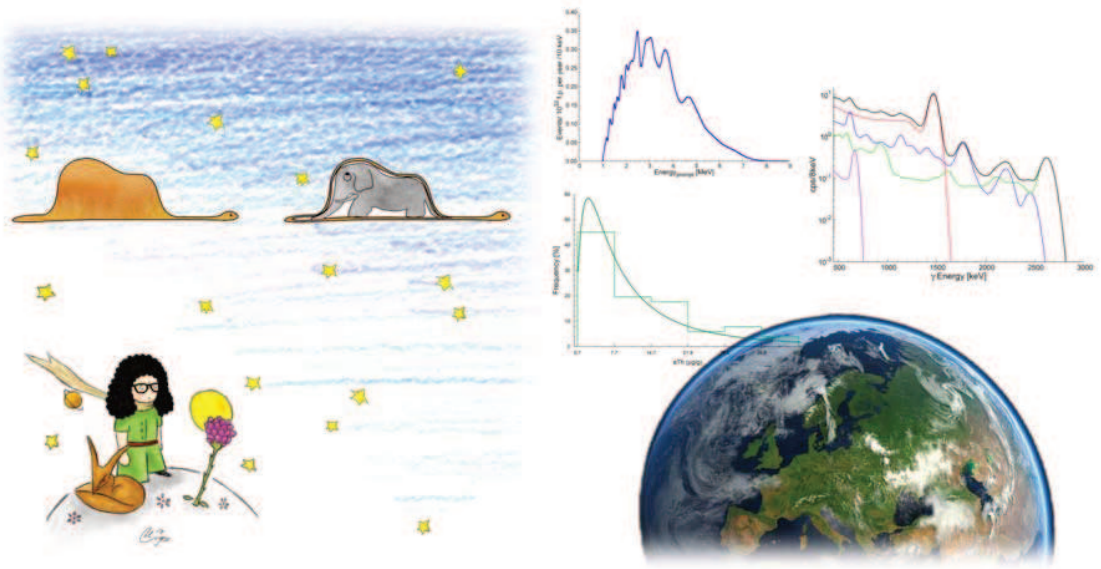

Decomposing an overall shape into underlying structures is the challenging way for uncovering gaps of knowledge, that is where the sources of uncertainties live. Fundamental shapes are responsible for the big picture, providing us the RGB color palette of the kaleidoscope: profiling them is essential in order to make minor shades of the kaleidoscope emerge.

The reactor antineutrino spectral shape has been reconstructed as the superposition of the individual components generated by ^{235}U, ^{239}Pu, ^{238}U and ^{241}Pu, which are the 4 fissile isotopes responsible for the emission of almost all antineutrinos above the Inverse Beta Decay (IBD) threshold. Provided to know the effective thermal power at which a reactor core is operating at a given time, the temporal evolution of the reactor spectral shape is affected by the variability of the fissile isotopes fission fractions and by the off-equilibrium corrections to the reference spectra. During a reactor burning cycle, the fuel composition and hence the power fractions of the fissile isotopes change as plutonium isotopes are bred and uranium is consumed. As each isotope produces a unique antineutrino spectrum through the decay of its fission fragments and their daughters, the reactor antineutrino shape will inevitably change in time. This point could be a source of concern for the SNO+ experiment which will be the first long baseline experiment to measure a reactor signal dominated by CANDU cores whose functioning over time is currently a missing piece of knowledge for the scientific community.

In reference uranium and plutonium antineutrino spectra long-lived fission fragments having half-lives longer than 10 hours and maximum antineutrino energy above the IBD threshold did not reach equilibrium yet. Their accumulation during the reactor operation as well as the storage of spent nuclear fuels in water pools can threaten the reconstruction of the reactor spectral shape in the energy region below ∼3.5 MeV. This is a delicate aspect for the JUNO experiment as the low energy region is the one in which the highest sensitivity to interference effects related to the neutrino mass hierarchy is foreseen. At the same time this is a crucial point also for geoneutrino measurements as the maximum

geoneutrino energy is 3.27 MeV, corresponding to the ^{214}Bi beta decay to the ^{214}Po ground state. In the framework of the JUNO Collaboration I recently joined, I will give my contribution in the modeling of the expected geoneutrino signal which will require a refinement of the regional crustal model. Moreover, I will spend the knowledge I gathered on the reconstruction of spectral structures on the base of individual templates for what concerns the shape of waveforms acquired by fast digitizers connected to large area photomultiplier tubes, which is one of the challenges posed by the JUNO experiment in opening the scenario of neutrino calorimetry.

The fundamental blocks building the geoneutrino spectrum are the spectral shapes associated with the ^{238}U and ^{232}Th decay chain, each one resulting from the superposition of the components arising from two beta decays above the IBD threshold. Half of the detected geoneutrino signal coming from the Earth's crust is typically generated within 200 km from the detector, which implies that refined regional crustal models are crucial for the modeling of the expected signal at a given experimental site. In the case of the SNO+ detector, the high uncertainty associated to the prediction of the signal generated by the Huronian Supergroup geological reservoir drives the development of a higher resolution geochemical and geophysical model. In particular, a better geochemical characterization of the reservoir is demanded for putting constraints on the expected geoneutrino spectral shape, which can in principle provide a direct measurement of the Th/U ratio in the Earth. I am currently involved together with colleagues of the University of Maryland in the development of a refined model in 50 km $\times$ 50 km region centered at the SNO+ location, which will be published in the next months.

Informations on the radioactive content of the Earth's surface can come from the reconstruction of measured gamma-ray spectra. The Full Spectrum Analysis (FSA) with Non Negative Least Square (NNLS) constraint has been applied to the sensitivity calibration of in-situ and airborne sodium iodide scintillators. With the FSA approach the gamma-ray spectrum is modeled as a linear combination of the spectral shapes generated by individual radionuclides, where the contribution given by each isotope is obtained weighting the fundamental spectrum (i.e. the detector response to a unitary isotope concentration) by the abundance of the specific isotope in the environment. For the ZaNaI, CavaRad and AGRS_16L detectors the ^{40}K, ^{238}U, ^{232}Th and ^{137}Cs fundamental spectra have been determined, which are the essential components required for the reconstruction of environmental gamma-ray spectra.

In order to address this challenge natural calibration sites have been identified and characterized by means of laboratory gamma-ray spectroscopy measurements performed with the MCA_Rad system on collected soil samples. The MCA_Rad system plays in this game the role of an independent instrument of known response function. The full efficiency calibration of the MCA_Rad system has been performed by using certified reference materials and by estimating a series of correction factors related to the intrinsic features of the specific gamma decay as well as to the characteristics of the source material itself. The separate treatment of corrections and sources of uncertainty allowed to quantify for the most intense gamma lines the individual contribution each input quantity has on the total uncertainty budget. In the perspective of adopting multisensorial detection systems, e.g. in the case of nuclear proliferation monitoring, having a full understanding of the range of reliability of each

detector component will be of crucial importance.

These studies highlighted the importance of performing dedicated instrumental calibrations and cross-validation tests, which often involve dealing with experimental measurements characterized by different sources of uncertainty and different fields of view. Issues related to spectral fitting can affect gamma-ray spectroscopy measurements as the reliability of the estimated radioactive contents is strictly correlated with the reliability of the templates used in the reconstruction of experimental gamma-ray spectra. This point allowed me to focus on problematic aspects related to detector calibrations and background radiation assessment which can easily introduce systematic biases in the estimation of radionuclide abundances and which will be the subject of a future publication.

It is not uncommon that the treatment of uncertainties arising from spectrometers calibrations is just lightly touched, especially for what concerns airborne measurements where the Poisson statistical uncertainty typically takes over other sources of uncertainty due to the small number of observed events. The use of Monte Carlo simulations can be strategic in order to address this delicate point, but provides also an extraordinarily powerful tool for the spectral reconstruction of airborne measured spectra. Traditionally ground concentrations are determined by applying height scaling factors to airborne measured abundances: in this scenario, the power of Monte Carlo simulations is the modeling of detector responses at different survey heights, which in principle does not result in a simple scaling but produces modifications in the spectral shapes due to the attenuating effect of air layers of different thicknesses. Moreover, the employment of Monte Carlo simulation can deeply help in understanding detector performances, allowing to explore different detection technologies (e.g. LaBr3 and CZT) as well as different detector geometries in the light of gamma-ray directional measurements.

In this complex puzzle, a strong joining link is represented by the study of probability density functions (pdf) describing the underlying statistical distribution of a given observable. In this thesis pdfs have been employed in uncertainty propagation methods, determination of central values, statistical analysis, representing an essential and versatile know-how for the elaboration of models and algorithms as well as for the interpretation of experimental data. Many other elephants will be discovered inside the stomach of a boa, having the spectral shape of a hat!

Appendix A

Table A.1: Predicted antineutrino signals (in TNU) from nuclear power plants in the FER (R_{FER}) and in the LER (R_{LER}) obtained with 2014 reactor operational data, together with the expected geoneutrino signals (G) and R_{LER}/G ratios at current and proposed neutrino experimental sites. Antineutrino signals in the FER and in the LER include the off-equilibrium contribution due to the accumulation of the LLIs during the running of the reactor.

Site	Experiment	Coordinates	G [TNU]	R_{FER} [TNU]	R_{LER} [TNU]	R_{LER}/G
Gran Sasso (IT)[a]	Borexino	42.45 N, 13.57 E[b]	$40.3^{+7.3}_{-5.8}$	$85.3\ ^{+2.1}_{-1.9}$	$23.0^{+0.6}_{-0.6}$	0.6
Sudbury (CA)	SNO+	46.47 N, 81.20 W[b]	$45.4^{+7.5}_{-6.3}$	$192.6^{+4.7}_{-4.4}$	$48.5^{+1.8}_{-1.5}$	1.1
Kamioka (JP)	KamLAND	36.43 N, 137.31 E[b]	$31.5^{+4.9}_{-4.1}$	$27.4^{+0.7}_{-0.6}$	$7.4^{+0.2}_{-0.2}$	0.2
DongKeng (CH)	JUNO	22.12 N, 112.52 E[c]	$39.7^{+6.5}_{-5.2}$	214^{+11}_{-11}	$53.9^{+3.0}_{-2.8}$	1.4
GuemSeong (SK)	RENO-50	35.05 N, 126.70 E[c]	$38.3^{+6.1}_{-4.9}$	1177^{+75}_{-72}	191^{+22}_{-20}	5.0
Hawaii (US)	Hanohano	19.72 N, 156.32 W[b]	$12.0^{+0.7}_{-0.6}$	$3.4^{+0.1}_{-0.1}$	$0.9^{+0.02}_{-0.02}$	0.1
Pyhäsalmi (FI)	LENA	63.66 N, 26.05 E[b]	$45.5^{+6.9}_{-5.9}$	$69.5^{+1.7}_{-1.6}$	$18.0^{+0.5}_{-0.5}$	0.4
Boulby (UK)	LENA	54.55 N, 0.82 W[b]	$39.2^{+6.3}_{-4.9}$	1053^{+30}_{-29}	209^{+10}_{-10}	5.3
Canfranc (SP)	LENA	42.70 N, 0.52 W[b]	$40.0^{+6.4}_{-5.1}$	$237.9^{+5.7}_{-5.5}$	$67.8^{+1.6}_{-1.7}$	1.7
Fréjus (FR)	LENA	45.13 N, 6.68 E[b]	$42.8^{+7.6}_{-6.4}$	558^{+12}_{-11}	$129.2^{+5.5}_{-5.0}$	3.0
Slănic (RO)	LENA	45.23 N, 25.94 E[b]	$45.1^{+7.8}_{-6.3}$	$115.0^{+2.8}_{-2.7}$	$31.3^{+0.8}_{-0.7}$	0.7
Sieroszowice (PL)	LENA	51.55 N, 16.03 E[b]	$43.4^{+7.0}_{-5.6}$	$154.7^{+3.8}_{-3.5}$	$42.2^{+1.0}_{-1.0}$	1.0
Homestake (US)	/	44.35 N, 103.75 W[b]	$48.7^{+8.3}_{-6.9}$	$31.8^{+0.8}_{-0.7}$	$8.5^{+0.2}_{-0.2}$	0.2
Baksan (RU)	/	43.20 N, 42.72 E[b]	$47.2^{+7.7}_{-6.4}$	$37.4^{+0.9}_{-0.8}$	$10.0^{+0.3}_{-0.3}$	0.2

[a] IT: Italy, JP: Japan, CA: Canada, CH: China, SK: South Korea, US: United States of America, FI: Finland, UK: United Kindom, SP: Spain, FR: France, RO: Romania, PL: Poland, RU: Russia.
[b] Huang et al. 2013
[c] Ciuffoli et al. 2014

Table A.2: Predicted antineutrino signals (in TNU) from nuclear power plants in the FER (R_{FER}) and in the LER (R_{LER}) obtained with 2015 reactor operational data, together with the expected geoneutrino signals (G) and R_{LER}/G ratios at current and proposed neutrino experimental sites. Antineutrino signals in the FER and in the LER include the off-equilibrium contribution due to the accumulation of the LLIs during the running of the reactor.

Site	Experiment	Coordinates	G [TNU]	R_{FER} [TNU]	R_{LER} [TNU]	R_{LER}/G
Gran Sasso (IT)[a]	Borexino	42.45 N, 13.57 E[b]	$40.3^{+7.3}_{-5.8}$	$83.5\ ^{+2.0}_{-1.8}$	$22.5^{+0.6}_{-0.6}$	0.6
Sudbury (CA)	SNO+	46.47 N, 81.20 W[b]	$45.4^{+7.5}_{-6.3}$	$193.4^{+4.7}_{-4.4}$	$48.7^{+1.7}_{-1.5}$	1.1
Kamioka (JP)	KamLAND	36.43 N, 137.31 E[b]	$31.5^{+4.9}_{-4.1}$	$30.2^{+0.7}_{-0.7}$	$8.2^{+0.2}_{-0.2}$	0.3
DongKeng (CH)	JUNO	22.12 N, 112.52 E[c]	$39.7^{+6.5}_{-5.2}$	328^{+19}_{-18}	$80.3^{+6.3}_{-5.7}$	2.0
GuemSeong (SK)	RENO-50	35.05 N, 126.70 E[c]	$38.3^{+6.1}_{-4.9}$	1124^{+71}_{-66}	184^{+21}_{-20}	4.8
Hawaii (US)	Hanohano	19.72 N, 156.32 W[b]	$12.0^{+0.7}_{-0.6}$	$3.5^{+0.1}_{-0.1}$	$0.9^{+0.02}_{-0.02}$	0.1
Pyhäsalmi (FI)	LENA	63.66 N, 26.05 E[b]	$45.5^{+6.9}_{-5.9}$	$69.1^{+1.7}_{-1.5}$	$17.9^{+0.5}_{-0.5}$	0.4
Boulby (UK)	LENA	54.55 N, 0.82 W[b]	$39.2^{+6.3}_{-4.9}$	1103^{+32}_{-31}	219^{+11}_{-11}	5.6
Canfranc (SP)	LENA	42.70 N, 0.52 W[b]	$40.0^{+6.4}_{-5.1}$	$245.2^{+5.9}_{-5.6}$	$70.3^{+1.6}_{-1.7}$	1.8
Fréjus (FR)	LENA	45.13 N, 6.68 E[b]	$42.8^{+7.6}_{-6.4}$	565^{+12}_{-11}	$130^{+5.6}_{-4.9}$	3.0
Slănic (RO)	LENA	45.23 N, 25.94 E[b]	$45.1^{+7.8}_{-6.3}$	$113.3^{+2.7}_{-2.6}$	$30.8^{+0.7}_{-0.7}$	0.7
Sieroszowice (PL)	LENA	51.55 N, 16.03 E[b]	$43.4^{+7.0}_{-5.6}$	$146.8^{+3.6}_{-3.4}$	$40.0^{+1.0}_{-1.0}$	0.9
Homestake (US)	/	44.35 N, 103.75 W[b]	$48.7^{+8.3}_{-6.9}$	$31.8^{+0.8}_{-0.7}$	$8.5^{+0.2}_{-0.2}$	0.2
Baksan (RU)	/	43.20 N, 42.72 E[b]	$47.2^{+7.7}_{-6.4}$	$39.2^{+0.9}_{-0.9}$	$10.4^{+0.3}_{-0.3}$	0.2

[a] IT: Italy, JP: Japan, CA: Canada, CH: China, SK: South Korea, US: United States of America, FI: Finland, UK: United Kindom, SP: Spain, FR: France, RO: Romania, PL: Poland, RU: Russia.
[b] Huang et al. 2013
[c] Ciuffoli et al. 2014

Appendix B

Table B.1: The table reports the critical values of the vertical distances $D^*_{n,\alpha}$ of the Kolmogorov-Smirnov statistical test, as described in Chapter 2.

	Level of significance α				
Sample size n	0.20	0.15	0.10	0.05	0.01
3	0.565	0.597	0.642	0.708	0.828
4	0.494	0.525	0.564	0.624	0.733
5	0.446	0.474	0.510	0.565	0.669
10	0.322	0.342	0.368	0.410	0.490
15	0.266	0.283	0.304	0.338	0.404
20	0.231	0.246	0.264	0.294	0.356
30	0.190	0.200	0.220	0.240	0.290
35	0.180	0.190	0.210	0.230	0.270
40	0.170	0.180	0.190	0.210	0.250
45	0.160	0.170	0.180	0.200	0.240
50	0.150	0.160	0.170	0.190	0.230
over 50	$\frac{1.07}{\sqrt{n}}$	$\frac{1.14}{\sqrt{n}}$	$\frac{1.22}{\sqrt{n}}$	$\frac{1.36}{\sqrt{n}}$	$\frac{1.63}{\sqrt{n}}$

Appendix C

Table C.1: The K, U, Th and Cs concentrations of all the samples collected at calibration sites for the sensitivity calibration of the AGRS_16L system are listed in the table.

Site	Sample ID	m [g]	K [%]	eU [ppm]	eTh [ppm]	Cs [Bq/kg]
KCl	KCl_1	210.27	54 ± 3.0	2 ± 1	6.0 ± 0.5	< 1
ASIAGO	CAL_ASIAGO_N	146.76	0.67 ± 0.06	6.4 ± 0.6	7.3 ± 0.9	279 ± 16
	CAL_ASIAGO_C	167.90	0.62 ± 0.05	1.6 ± 0.2	4.8 ± 0.7	196 ± 11
	CAL_ASIAGO_S	130.80	1.21 ± 0.09	3.4 ± 0.3	7.8 ± 0.9	178 ± 10
	CAL_ASIAGO_1	129.50	0.76 ± 0.06	3.2 ± 0.3	5.5 ± 0.8	221 ± 12
	CAL_ASIAGO_2	131.46	0.84 ± 0.07	2.8 ± 0.3	5.8 ± 0.8	250 ± 14
	CAL_ASIAGO_3	140.29	0.84 ± 0.07	2.7 ± 0.3	6.2 ± 0.8	193 ± 11
	CAL_ASIAGO_4	134.14	0.83 ± 0.07	2.7 ± 0.3	5.8 ± 0.8	270 ± 15
	CAL_ASIAGO_5	134.02	0.80 ± 0.07	3.1 ± 0.3	5.6 ± 0.8	264 ± 15
LOCALITA' OSTERIA	CAL_AURORA_EXT	108.39	1.08 ± 0.09	10.8 ± 0.9	10.9 ± 1.3	210 ± 12
	CAL_AURORA_C	108.94	0.94 ± 0.08	9.7 ± 0.8	9.3 ± 1.2	360 ± 20
BAONE	BAONE_1	236.53	2.54 ± 0.15	2.8 ± 0.3	29.9 ± 2.0	4.3 ± 0.8
	BAONE_2	244.12	2.71 ± 0.16	2.8 ± 0.3	29.3 ± 2.0	4.2 ± 0.8
	BAONE_3	235.9	2.69 ± 0.16	2.8 ± 0.3	27.4 ± 1.9	2.0 ± 0.7
MONSELICE	CAL_IVAN_II_C	204.29	2.78 ± 0.17	24.9 ± 2.0	20.7 ± 1.6	4.8 ± 1.1
	CAL_IVAN_II_E	211.83	2.67 ± 0.16	25.8 ± 2.0	22.5 ± 1.7	7.1 ± 1.1
	CAL_IVAN_II_N	200.85	2.81 ± 0.17	25.3 ± 2.0	20.8 ± 1.6	6.7 ± 1.1
	CAL_IVAN_II_NE	199.52	2.77 ± 0.17	26.5 ± 2.1	21.1 ± 1.6	6.2 ± 1.1
	CAL_IVAN_II_NE_EXT	205.19	2.70 ± 0.17	25.8 ± 2.0	19.3 ± 1.5	7.1 ± 1.1
	CAL_IVAN_II_NW	185.37	2.90 ± 0.18	24.8 ± 2.0	16.5 ± 1.4	6.6 ± 1.2
	CAL_IVAN_II_NW_EXT	201.46	3.04 ± 0.18	27.5 ± 2.2	20.8 ± 1.6	8.6 ± 1.2
	CAL_IVAN_II_S	209.11	2.78 ± 0.17	24.9 ± 2.0	19.3 ± 1.5	7.7 ± 1.1
	CAL_IVAN_II_SE	215.41	2.97 ± 0.18	26.0 ± 2.0	19.9 ± 1.5	6.4 ± 1.1
	CAL_IVAN_II_SE_EXT	219.81	2.71 ± 0.16	25.0 ± 2.0	20.4 ± 1.5	8.1 ± 1.1
	CAL_IVAN_II_SW	214.10	2.81 ± 0.17	23.8 ± 1.9	20.3 ± 1.5	8.0 ± 1.1
	CAL_IVAN_II_SW_EXT	188.54	2.84 ± 0.17	24.8 ± 2.0	22.7 ± 1.7	7.7 ± 1.1

	CAL_IVAN_II_W	193.36	2.66 ± 0.16	21.9 ± 1.7	18.0 ± 1.4	6.6 ± 1.1
RAPOLANO	CAL_RT_BULK_1	252.07	0.05 ± 0.01	7.9 ± 0.7	< 0.9	8.5 ± 0.8
	CAL_RT_BULK_2	262.89	0.05 ± 0.01	7.6 ± 0.6	1.06 ± 0.3	4.8 ± 0.6
	CAL_RT_BULK_3	255.00	0.04 ± 0.01	8.1 ± 0.7	< 1.0	2.1 ± 0.5
	CAL_RT_BULK_4	264.08	0.05 ± 0.01	8.0 ± 0.7	< 0.9	3.8 ± 0.6
	CAL_RT_BULK_5	255.91	< 0.03	8.3 ± 0.7	< 1.0	2.0 ± 0.5
	CAL_RT_BULK_6	274.87	< 0.03	8.1 ± 0.7	1.0 ± 0.3	4.9 ± 0.6
	CAL_RT_UP	255.03	< 0.03	8.1 ± 0.6	1.6 ± 0.4	4.9 ± 0.6
	CAL_RT_DOWN	256.96	< 0.03	7.9 ± 0.7	< 0.9	< 1.2
SAN CASCIANO	CAL_SAN_CASCIANO_SW	198.00	1.77 ± 0.11	4.8 ± 0.4	65.3 ± 4.0	4.9 ± 1.0
	CAL_SAN_CASCIANO_S_EXT	195.70	1.68 ± 0.11	4.3 ± 0.4	61.8 ± 3.8	4.8 ± 1.0
	CAL_SAN_CASCIANO_W	206.62	1.82 ± 0.12	5.4 ± 0.5	65.2 ± 4.0	3.7 ± 1.0
	CAL_SAN_CASCIANO_W_EXT	190.82	1.69 ± 0.11	5.6 ± 0.5	64.6 ± 3.9	5.1 ± 1.0
	CAL_SAN_CASCIANO_N_EXT	212.48	1.74 ± 0.11	4.1 ± 0.4	63.6 ± 3.9	7.1 ± 1.0
	CAL_SAN_CASCIANO_N	208.17	1.82 ± 0.12	5.5 ± 0.5	64.0 ± 3.9	4.1 ± 1.0
	CAL_SAN_CASCIANO_E	197.32	1.78 ± 0.11	5.5 ± 0.5	62.9 ± 3.9	4.9 ± 1.0
	CAL_SAN_CASCIANO_C	210.93	1.80 ± 0.11	4.7 ± 0.4	61.9 ± 3.8	5.9 ± 1.0
	CAL_SAN_CASCIANO_S	204.60	1.78 ± 0.12	4.6 ± 0.4	65.1 ± 4.0	2.7 ± 1.0
	CAL_SAN_CASCIANO_E_EXT	196.9	1.75 ± 0.11	4.7 ± 0.4	62.5 ± 3.9	6.7 ± 1.0
SCHIO	SCHIO_1	191.11	1.84 ± 0.12	23.4 ± 1.9	17.0 ± 1.4	37.7 ± 2.5
	SCHIO_2	181.74	1.83 ± 0.12	22.6 ± 1.8	16.7 ± 1.4	35.7 ± 2.5
	SCHIO_3	191.36	1.91 ± 0.12	23.7 ± 1.9	17.7 ± 1.4	43.3 ± 2.8
	SCHIO_4	185.77	1.84 ± 0.12	22.9 ± 1.8	17.8 ± 1.4	38.8 ± 2.6
	SCHIO_5	186.01	1.79 ± 0.12	23.1 ± 1.9	17.5 ± 1.4	41.8 ± 2.8
	SCHIO_6	188.85	1.80 ± 0.12	24.6 ± 1.9	17.1 ± 1.4	47.5 ± 3.1
	SCHIO_7	190.76	1.80 ± 0.12	24.1 ± 1.9	17.8 ± 1.4	40.5 ± 2.7
	SCHIO_8	193.13	1.72 ± 0.11	23.5 ± 1.9	16.3 ± 1.3	36.0 ± 2.5
	SCHIO_9	186.63	1.71 ± 0.11	23.9 ± 1.9	17.3 ± 1.4	35.8 ± 2.5
	SCHIO_10	176.36	1.87 ± 0.12	22.5 ± 1.8	17.5 ± 1.4	38.7 ± 2.6
	SCHIO_11	169.98	1.79 ± 0.12	17.6 ± 1.4	14.8 ± 1.3	40.8 ± 2.7
	SCHIO_12	177.00	1.80 ± 0.12	24.1 ± 1.9	17.5 ± 1.4	39.4 ± 2.7
	SCHIO_13	177.60	1.74 ± 0.11	22.5 ± 1.8	16.3 ± 1.4	42.8 ± 2.9
SORANO	CAL_SORANO_SE	178.73	2.69 ± 0.17	6.2 ± 0.6	36.5 ± 2.4	12.1 ± 1.3
	CAL_SORANO_C	166.41	2.84 ± 0.18	7.3 ± 0.6	40.3 ± 2.6	13.2 ± 1.4
	CAL_SORANO_E	168.07	2.82 ± 0.17	7.7 ± 0.7	37.4 ± 2.5	11.8 ± 1.3
	CAL_SORANO_N_EXT	185.77	2.77 ± 0.17	7.3 ± 0.6	36.3 ± 2.4	15.2 ± 1.4
	CAL_SORANO_W_EXT	163.45	2.85 ± 0.18	7.2 ± 0.6	37.7 ± 2.5	11.3 ± 1.3
	CAL_SORANO_N	160.25	2.88 ± 0.18	6.8 ± 0.6	40.2 ± 2.7	13.5 ± 1.4
	CAL_SORANO_NE	165.85	2.79 ± 0.17	6.6 ± 0.6	41.0 ± 2.7	16.3 ± 1.5
	CAL_SORANO_SW	164.72	2.80 ± 0.17	7.3 ± 0.6	40.3 ± 2.6	16.3 ± 1.5
	CAL_SORANO_E_EXT	174.82	2.77 ± 0.17	6.6 ± 0.6	38.6 ± 2.6	14.9 ± 1.4

	CAL_SORANO_W	176.92	2.66 ± 0.16	6.8 ± 0.6	39.0 ± 2.6	11.7 ± 1.3
	CAL_SORANO_NW	185.45	2.79 ± 0.17	6.7 ± 0.6	38.6 ± 2.5	11.8 ± 1.3
	CAL_SORANO_S	174.64	2.68 ± 0.17	7.2 ± 0.6	38.4 ± 2.5	14.4 ± 1.4
	CAL_SORANO_S_EXT	176.61	2.90 ± 0.18	6.9 ± 0.6	38.3 ± 2.5	12.2 ± 1.3
SORDINO	CAL_SORDINO_C	215.02	1.98 ± 0.12	3.01 ± 0.3	14.9 ± 1.1	6.1 ± 0.8
	CAL_SORDINO_E	193.52	1.94 ± 0.12	3.0 ± 0.3	15.0 ± 1.2	6.0 ± 0.8
	CAL_SORDINO_E_EXT	179.62	2.10 ± 0.13	3.0 ± 0.3	13.7 ± 1.1	7.8 ± 0.9
	CAL_SORDINO_N_EXT	206.46	2.03 ± 0.13	3.3 ± 0.3	12.4 ± 1.0	6.9 ± 0.8
	CAL_SORDINO_NE	210.15	2.00 ± 0.12	2.7 ± 0.3	13.7 ± 1.1	7.4 ± 0.8
	CAL_SORDINO_NW_EXT	175.67	1.83 ± 0.12	2.8 ± 0.3	14.1 ± 1.2	8.1 ± 0.9
	CAL_SORDINO_S	210.21	2.06 ± 0.13	3.2 ± 0.3	13.9 ± 1.1	7.2 ± 0.8
	CAL_SORDINO_S_EXT	210.44	2.11 ± 0.13	2.9 ± 0.3	13.4 ± 1.1	7.1 ± 0.8
	CAL_SORDINO_SE	201.50	2.12 ± 0.13	2.9 ± 0.3	13.9 ± 1.1	7.1 ± 0.8
	CAL_SORDINO_SW	207.27	1.99 ± 0.12	3.4 ± 0.3	13.5 ± 1.1	6.3 ± 0.8
	CAL_SORDINO_W	220.31	2.03 ± 0.13	3.3 ± 0.3	13.6 ± 1.1	7.3 ± 0.8
	CAL_SORDINO_W_EXT	195.15	2.00 ± 0.13	3.2 ± 0.3	13.7 ± 1.1	6.8 ± 0.9
	CAL_SORDINO_N	198.69	2.02 ± 0.13	3.3 ± 0.3	13.4 ± 1.1	9.0 ± 0.9
PORTO GARIBALDI	CAL_MATTEO_C	278.35	1.32 ± 0.08	1.33 ± 0.14	4.2 ± 0.5	< 1
	CAL_MATTEO_O	270.78	1.56 ± 0.10	1.02 ± 0.13	3.8 ± 0.5	< 1
	CAL_MATTEO_E	273.46	1.57 ± 0.10	< 0.3	4.3 ± 0.5	< 1
	CAL_MATTEO_SO_C	282.74	1.42 ± 0.09	1.00 ± 0.12	3.7 ± 0.5	< 1
	CAL_MATTEO_SE	256.79	1.53 ± 0.10	1.27 ± 0.14	4.0 ± 0.5	< 1
	CAL_MATTEO_NE	263.19	1.42 ± 0.09	1.31 ± 0.15	3.9 ± 0.5	< 1
	CAL_MATTEO_SO	264.78	1.49 ± 0.09	1.15 ± 0.13	4.0 ± 0.5	< 1
	CAL_MATTEO_O_C	274.58	1.40 ± 0.09	1.22 ± 0.14	3.8 ± 0.5	< 1
	CAL_MATTEO_E_C	293.34	1.35 ± 0.09	1.26 ± 0.14	3.5 ± 0.5	< 1
	CAL_MATTEO_NO	277.68	1.49 ± 0.09	1.24 ± 0.14	3.6 ± 0.5	< 1
	CAL_MATTEO_SE_C	268.56	1.38 ± 0.09	1.05 ± 0.13	3.4 ± 0.5	< 1
	CAL_MATTEO_NE_C	283.18	1.37 ± 0.09	1.15 ± 0.13	3.5 ± 0.4	< 1
	CAL_MATTEO_NO_C	267.74	1.40 ± 0.09	1.19 ± 0.14	3.0 ± 0.4	< 1